What happened to rocky planets?

An atmosphere-interior perspective from numerical modelling

Harrison Nicholls
University of Oxford

A thesis submitted for the degree of
Doctor of Philosophy

February 2026

Tell all the truth but tell it slant—
Success in Circuit lies
Too bright for our infirm Delight
The Truth’s superb surprise
As Lightning to the Children eased
With explanation kind
The Truth must dazzle gradually
Or every man be blind —

Emily Dickinson

Acknowledgements

This thesis is the product of my DPhil itself, but also of my years in Oxford and the many academic and personal relationships which have shaped me. It would not exist without the guidance of my mentors, nor without the unwavering support of my friends and family.

To my supervisor, Ray Pierrehumbert: thank you for sharing some of your wisdom on the physics of planetary atmospheres with me, and for your infectious enthusiasm for ‘anything with an atmosphere’.

To Tim Lichtenberg, I am deeply grateful for your abundant support and kind mentorship. I look forward to our continuing discussions, shared endeavours, and satisfactions from these deep problems for many years to come.

The broader Oxoplanets and Planetary Climate Dynamics communities have made each week in AOPP my pleasure. To Jayne Birkby, Luke Parker, Claire Guimond, and Richard Chatterjee in particular: thank you for the many vibrant discussions.

I would also like to extend my sincere appreciations to Tad Komacek for his thoughtful support, and to Paolo Sossi for his dedication to reading and assessing this thesis.

To Shirin, thank you for your DPhil comradeship since its very beginning, and to Charlotte and Tom, for your company during the close of my Oxford years. Stef and Harry: thank you, both, for your sustained confidence in me and unflagging humour.

To Amy, thank you for your warm commitment over these many years. From shared lunchtime commiserations to our more cultured adventures, your friendship has brought me so much happiness.

To Tom, to whom I do not express this directly often enough: I thank you for your brotherly, loving reminders that there is truly much more to Life than work. I will not ask you to mark this thesis.

Lastly – and foremost – to my parents: with your unreserved love, tender care, and homeward prompting. This thesis is dedicated to you both, to whom I could write reams of ‘thank you’s which would still not do justice to all that you have done for me.

Declaration

I declare that this thesis is entirely my own work and, except where stated, describes my own research. A portion of this work corresponds to research in peer-reviewed scientific journals:

- Chapter 2 – Journal of Geophysical Research: Planets (Nicholls et al. 2024),
- Chapter 3 – Mon. Not. R. Astron. Soc (Nicholls et al. 2025c),
- Chapter 3 – Journal of Open Source Software (Nicholls et al. 2025b),
- Chapter 4 – Mon. Not. R. Astron. Soc (Nicholls et al. 2025a),
- Chapter 5 – Nature Astronomy (Nicholls et al. 2026).

Word count: 60156.
Page count: 224.
Figure count: 46.
Table count: 7.
Compiled on February 3, 2026.
This document is typeset in Merriweather, Erewhon Math, and Noto Sans Mono.

Abstract

A satisfactory model describing why Earth, Venus, and Mars, differ so substantially is yet to be described; centuries of planetary science have yielded insightful – but incomplete – explanations. Meanwhile, observations of planets beyond the Solar System are revealing novel environments which raise challenges to our existing theories.

Multiple lines of evidence suggest the presence of ‘magma oceans’ early in rocky planets’ lifetimes. During these important natal periods, planet-scale feedbacks emerge via exchange of energy and material between mantles and atmospheres. Some magma oceans are sustained indefinitely; others solidify, providing initial conditions for solid-body geodynamics, secondary atmospheres, and the potential for habitability. Both scenarios are observable on exoplanets today.

I present a numerical framework for modelling planetary evolution over deep time, capturing the physics of mantle dynamics, tides, volatile partitioning, atmospheric chemistry, convection, radiative transfer, and escape. Applying this holistic model resolves the history of rocky (exo)planets from their birth to the present.

Diverse atmospheres are formed in equilibrium with deep magma oceans: from H_2- to CO_2-dominated compositions, beyond previously-adopted simplified mixtures. Corresponding radiative properties can sustain magma oceans for billions of years. Atmospheric temperature structure, tied to the efficacy of energy transport, regulates planet-scale evolution – including that of the deep interior. Tidal feedbacks, from interior-atmospheric coupling, further regulate magma ocean longevity. My simulations show that global physical-chemical interactions set exoplanets’ observables, making a connection between measurable atmospheric properties and otherwise hidden processes. Evolution tracks of L 98-59 d (a case study) are consistent with recent JWST & TESS observations: L 98-59 d formed volatile-rich, with a substantial atmosphere and a reducing interior – a scenario inaccessible to simplified models, pointing to a continuum of atmospheric evolution scenarios.

Space missions, ground-based telescopes, and lab experiments are expanding the horizon of planetary science. The interdisciplinary modelling framework developed here provides a connection between these missions and experiments – yielding a comprehensive picture of the geological, chemical, physical, and climatic evolution of rocky planets in the Solar System and beyond.

Contents

1 Introduction **1**
1.1 Planetary evolution 1
1.1.1 Things newborn 1
1.1.2 Expectations from the physics 4
1.1.3 Expectations from the Earth 10
1.2 Ad astra 13
1.2.1 Measuring exoplanets 13
1.2.2 Exoplanet populations and individuals 17
1.3 Theoretical approaches 25
1.3.1 Early terrestrial models 25
1.3.2 Recent generalised models 26
1.3.3 Retrieval methods and static-structure calculations 30
1.4 Targeted science questions 32

2 Factors regulating early magma ocean evolution **37**
2.1 Introduction 37
2.2 Modelling framework 38
2.2.1 Module roles 39
2.2.2 Dummy modules 43
2.2.3 Termination criteria 45
2.2.4 Volatile partitioning 46
2.2.5 Interior dynamics module 50
2.2.6 Convective atmosphere module 55
2.2.7 Radiative transfer in principle 58
2.2.8 Radiative transfer in practice 63
2.2.9 Gas opacities and parametrisations thereof 68
2.2.10 Stellar evolution, briefly 70
2.3 Model validation and benchmarking 75
2.3.1 Validation of radiative transfer calculations 75
2.3.2 Pure-steam runaway greenhouse behaviour 80
2.3.3 Fiducial H_2O-only evolutionary simulation 81
2.4 A range of evolutionary outcomes 86
2.4.1 Outgassed atmospheric compositions 87
2.4.2 Ensemble statistics and distributions 88
2.4.3 Hydrogen and water greenhouse effects 92
2.5 Shallow magma ocean states 94
2.6 Local radiative heating of the atmosphere 97
2.7 Discussion on implications 98
2.8 Discussion on limitations 102
2.9 Chapter conclusions 105

3 Convective shutdown in outgassed atmospheres **107**
3.1 Introduction 107
3.2 A model for extreme atmospheres on rocky exoplanets 109
3.2.1 Mixing-length theory of convection 110

3.2.2 Sensible heat and conduction 112
3.2.3 Volatile phase changes and latent heat 113
3.2.4 Numerical optimisation solver 115
3.2.5 Atmospheric thermochemistry 118
3.2.6 Thermodynamic properties 120
3.3 Validation of my new atmosphere model 124
3.3.1 Fiducial H_2O-only atmosphere calculations 124
3.3.2 An example in the case of K2-18 b 126
3.4 Outgassing of oxidised sulfur species 129
3.5 Two exoplanets as case studies 130
3.5.1 Modelled evolutionary outcomes with PROTEUS 132
3.5.2 Temperatures and convection in the atmosphere 134
3.5.3 Probing magma ocean redox with emission spectra 136
3.6 The 1D thermochemical speciation of an oxidised atmosphere 140
3.7 Chapter discussion 141
3.7.1 Importance of convective stability 141
3.7.2 Observational prospects for HD 63433 d and TRAPPIST-1 c 143
3.7.3 Compositional inhomogeneity in early atmospheres 144
3.7.4 Limitations and future work 146
3.8 Chapter conclusions 148

4 Tides regulated by atmospheres and rheology 151
4.1 Introduction 151
4.2 Outline of modelling approach and case studies 154
4.3 Simulations with a semi-analytic thermal model 157
4.3.1 Evolutionary tracks and hysteresis 157
4.3.2 A ‘blue sky catastrophe’ at later ages 161
4.4 Simulations with viscoelastic mantle tidal heating 162
4.4.1 Implementation within PROTEUS 162
4.4.2 Expectations for the tidal power-density 165
4.5 Emergence of tidally-supported worlds 166
4.5.1 Evolution neglecting tides 166
4.5.2 Evolution with tides 169
4.6 Sensitivity of outcomes to orbital eccentricity 171
4.7 Sensitivity of atmospheric convection to interior heating 173
4.8 Discussion on tides and their role 175
4.8.1 Negative feedback and stable equilibria 175
4.8.2 Evolution of L 98-59 b/c/d 178
4.8.3 Tidally-driven atmospheric convection 183
4.9 Chapter conclusions 184

5 The life and times of L 98-59 d 187
5.1 Introduction 187
5.2 A more realistic atmospheric height structure 190
5.3 Parametrisation of hydrodynamic escape 194
5.4 H_2S, and NH_3, kinetics, and photochemistry 196
5.5 Neither a gas-dwarf nor a water-world 197
5.5.1 Description of parameter grid 198

5.5.2 Modelled evolutionary tracks 200
5.5.3 Scenarios constrained by JWST observations 201
5.6 Thermo-compositional case study 203
5.7 Which physics drives the evolution of observables? .207
5.8 Sensitivity tests to other physics 209
5.9 Indication of sulfur photochemistry 211
5.10 Chapter conclusions 214

6 Conclusions **217**
6.1 How atmospheric physics shapes rocky planets 217
6.2 Suggested lines of further investigation 219
6.3 A perspective on the future 223

A Volatile solubilities and thermochemistry

B Derivation of time-average orbital separation

C Gibbs free energy and the equilibrium constant of reaction

D Derivation of the Clapeyron and Clausius-Clapeyron relations

E Derivation of the dry adiabatic lapse rate

F Derivation of the convective heat flux with MLT

G Supplementary emission spectra from the JANUS model

Chapter 1
Introduction

1.1 Planetary evolution

1.1.1 Things newborn

To understand how rocky planets change over deep time, we must first consider their initial conditions (McPhee 1998). There are multiple lines of evidence for large-scale melting during the planet formation process (Elkins-Tanton 2012; Schaefer and Elkins-Tanton 2018). Early molten states are important because they facilitate the efficient exchange of energy and material between planetary interiors and overlying atmospheres (Lichtenberg et al. 2025). For solidified planets like the Earth, the process of cooling and solidification from an initially-molten state thereby represents the initial condition for all subsequent solid-state evolution and climate scenarios (Bower et al. 2019). Sequential giant impact events may also 'reset' a given planet towards a partially-molten state (Tonks and Melosh 1993; Elkins-Tanton 2012). Meanwhile, ultra-short period 'lava world' exoplanets keep indefinitely-molten surfaces by absorbing stellar radiation, and are an observable connection to these otherwise-universal initial conditions (Meier et al. 2023).

Large reservoirs of molten material within young planets has been recognised since Leibniz's *Protogaea* – written in the late-1600s – proposed an early episode of global melting on the Earth. Such states are now termed 'magma oceans': regional or global reservoirs of (partially) molten silicate which comprise some part of a rocky body[1] (Taylor and Norman 1992). A mantle locally melts when its temperature exceeds the material's 'solidus': the temperature at which some components of the material begin to melt, which is $\sim$ 1300 K at zero pressure for anhydrous peridotite (Herzberg et al. 2000). Since not all mantle components melt at the same temperature, small solids may be entrained in the liquid phase, giving rise to partial-melt phases. The mantle material will locally become entirely molten when the temperature exceeds the 'liquidus' tempera-

---

[1] The term 'magmasphere' has also been proposed (Warren 1985).

ture, $\sim$ 2000 K at zero pressure for a chondritic composition (Andrault et al. 2011). The solidus and liquidus temperatures both increase as a function of pressure, but also depend on the mantle composition and the presence of any dissolved volatiles (Katz et al. 2003). They are usually compiled for Earth-like interior conditions through lab experiments and ab-initio simulations (Mosenfelder et al. 2007; Spera et al. 2011a; Wolf and Bower 2018). A magma ocean may exist at the surface – permitting direct interaction with an overlying atmosphere (Walbecq et al. 2025) – within the upper mantle layers, or as a *basal* magma ocean in contact with a metallic core (Schaefer and Elkins-Tanton 2018; Boukaré et al. 2022).

We can readily motivate the ubiquity of early magma oceans by considering that the kinetic and potential energy stored within planetesimals is converted to substantial amounts of thermal energy during the planet-formation process (Tonks and Melosh 1993). Additionally, giant impact events will cause substantial melting and the redistribution of material (Matsui and Abe 1986). For example, the canonical theory for the formation of Earth's moon is an impact between the proto-Earth and a Mars-sized body ('Theia') which would have ejected material that later coalesced to form the Moon (Daly 1946; Cameron and Ward 1976). This energetic event would have generated global magma oceans on both bodies (Sleep et al. 2014; Barr 2016). Thus, the modern 'magma ocean' concept originates from Apollo 11 soil samples found to contain anorthosite, a mineral which is known to form on Earth through the fractional crystallisation of lavas (Wood et al. 1970; Elkins-Tanton 2012). An early lunar magma ocean is primarily evidenced by the enhancement of so-called KREEP material[2] in samples from the lunar surface. The incompatible elements contained within KREEP (notably europium) readily partitioned into the melt phase of a lunar magma ocean, so they separated into a surface component compositionally distinct from the bulk Moon (Taylor and Norman 1992; Korotev and Gillis 2001; Borg et al. 2004; Elkins-Tanton 2012). Figure 1.1a shows an example of KREEP-rich basalt obtained during the Apollo 15 mission. Recent radioisotope dating has placed lunar crystallisation and the differentiation of KREEP at $\sim$ 140 Myr after the formation of the Solar System (Dauphas et al. 2025). Similarly, Venus' present slow

---

[2] The 'KREEP' acronym refers to this material containing potassium, rare-earth elements, and phosphorus.

rotational state may be justified by an early giant impact (Bussmann et al. 2025) and Mercury's internal structure can be theoretically reproduced by a series of giant impactors (Franco et al. 2025). Dissipation of the Solar Nebula and the stabilising effect of its drag would have destabilised the orbits of the young planets, likely making giant impacts commonplace within young planetary systems (Halliday and Canup 2023). Even if we did not appeal to these giant impact events, planet formation and accretion processes alone would be sufficient to melt young planetary embryos (Abe and Matsui 1986; Elkins-Tanton 2008). Lastly, seismic measurements of the compositions of low-velocity zones in the deep mantles of Earth and Mars provide additional evidence for primordial magma oceans on these planets (Williams and Garnero 1996; Labrosse et al. 2007; Debaille et al. 2009; Brown et al. 2014). It is therefore expected that rocky bodies are born in a partially molten state with the potential to cool down[3] (Hamano et al. 2015; Zahnle et al. 2015).

The effects of tidal heating may also keep some rocky bodies in a molten state. Gravitational perturbation of Jupiter's moon Io by Ganymede and Europa keeps Io on an eccentric orbit. In passing through a changing gravitational potential around Jupiter, Io experiences tidal deformation which frictionally dissipates heat within its interior (Peale et al. 1979; Segatz et al. 1988; Hay et al. 2020). A tidal heat source can explain the hot spots, volcanic activity, and outgassing of SO_2 observed by Juno (Pettine et al. 2024), Voyager (Smith et al. 1979), and from the Earth (Spencer et al. 1990). Tides are estimated to dissipate more than 100 TW of heat within Io's interior – far exceeding Earth's geothermal heat flux – and may even support a basal magma ocean within the moon (Khurana et al. 2011; Miyazaki and Stevenson 2022; Aygun and Cadek 2024; Davies et al. 2024; Park et al. 2024). Tides acting on Io are analogous to hypothetical tides raised within a rocky planet of a multi-planet star system, where companion planets sustain its non-zero orbital eccentricity through their gravitational perturbations. Io represents an environment in the Solar System where extreme heating is persistent and measurable, and where conditions are potentially comparable to those present during the early lives of rocky plan-

---

[3] However, we may still respectfully re-consider this foundational assumption, of complete early-stage melting, upon which my work and the broader literature rests. If some rocky planets are in fact *not* born mostly molten, then the implications for their lifetime evolution would be profound (Taylor and Norman 1992).

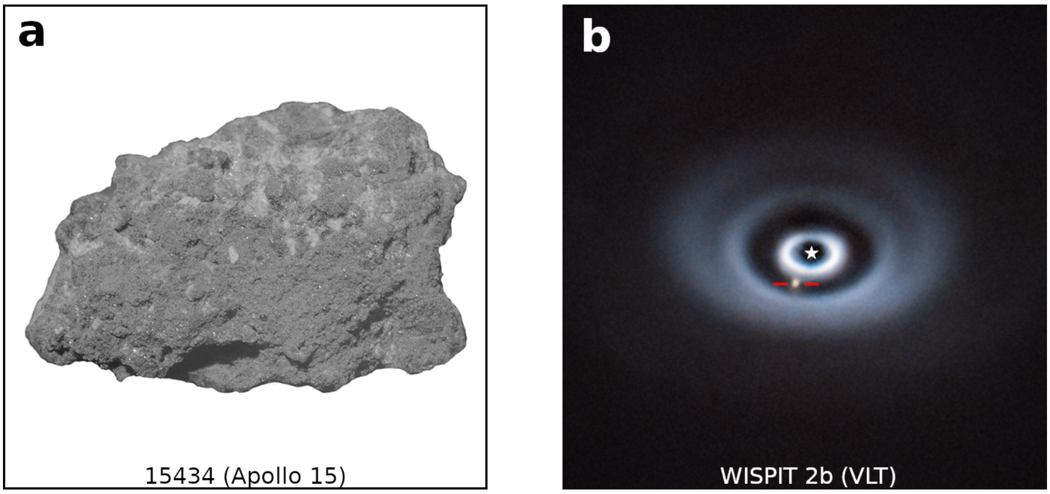

Figure 1.1: Lunar samples and disk observations provide evidence for melting of planetary bodies. **Left**: sample of lunar KREEP basalt obtained during Apollo 15 (`virtualmicroscope.org`). **Right**: a VLT-SPHERE image of the protoplanet WISPIT 2 b orbiting within a gap of its star's protoplanetary disk (Capelleveen et al. 2025; Close et al. 2025). The host star (white star symbol) is masked by a coronagraph. The red lines identify the young planet in the image.

ets. Simultaneously, heat is produced by the decay of short-lived radioisotopes in young systems (e.g. ^{26}Al Lee et al. 1976; Lichtenberg et al. 2019b), while electromagnetic induction has been considered as an additional source of energy (Kislyakova et al. 2017; Kislyakova et al. 2023).

1.1.2 Expectations from the physics

The processes of planet accretion and formation are expected to yield a range of thermal, compositional, and structural outcomes. Depending on their initial and migratory (Grewal et al. 2024) locations within the protoplanetary disk, planetary embryos can accrete a range of elemental (both volatile and refractory) compositions which are different to that of Earth, their star, and meteorites (Lammer and Blanc 2018; Jorge et al. 2022; McDonough 2025). For example, the small size of Mars may be a result of the early inward migration of Jupiter which depleted the protoplanetary disk of material in the vicinity of Mars (Walsh et al. 2011; Halliday and Canup 2023). The timing and timescale of planet formation is important; the Earth and Moon's enhanced Hf/W ratios indicate that they formed relatively late compared to Mars (Schoenberg et al. 2002; Kleine et al. 2009; Thiemens et al. 2019; Sossi et al. 2022). Venus' crustal resurfacing processes mean that we lack useful estimates for its formation timescale (Lammer et al. 2020; Gillmann et al.

2022). It was during this time, prior-to and contemporaneous-with the Moon-forming impact, that Earth obtained most of its present-day volatiles (Norris and Wood 2017; Nakajima and Stevenson 2018). Computer simulations can reproduce the present Earth-Moon orbital configuration under the canonical giant impact scenario (Barr 2016), but cannot account for the compositional similarity between the Earth and the Moon[4] (Sossi et al. 2024). Uncertainties in the processes of planet formation, migration, and material delivery clearly complicate the picture of planetary evolution (Rubie et al. 2007; Kimura and Ikoma 2020; Sossi et al. 2022).

One result of this complexity is that we do not know how much water is contained within the Earth (Peslier et al. 2017). Some fraction was likely delivered from chondritic impactors during the later-stages of planet formation, (Chyba 1990; Peslier et al. 2017) while it is also possible that some of Earth's water formed endogenously by oxidation reactions of nebular H_2 (Ikoma and Genda 2006; Halliday 2013; Kite and Schaefer 2021; Raymond and Morbidelli 2022). Earth's current oceans were likely sourced from multiple reservoirs, evidenced by isotopic measurements suggested to arise via mass-dependent fractionation processes. Endogenously-produced Earth water would have a low isotopic D/H ratio $\sim 2 \times 10^{-5}$, while enstatite chondrites – with a composition similar to Earth's mantle – have an intermediate ratio, and comets and carbonaceous chondrites have a large $\mathrm{D/H} \sim 3 \times 10^{-4}$ (Javoy 2005; Peslier et al. 2017). Earth's surface water, $\mathrm{D/H} \sim 1.56 \times 10^{-4}$, sits between these end-members (Javoy 2005; Genda and Ikoma 2008; Dauphas 2017). Impactor comets and chondrites delivered during the late veneer may have also modulated the Earth's redox state (Dauphas 2017; Lichtenberg and Clement 2022; Halliday and Canup 2023). A snapshot of the planet formation process imaged by the VLT (Figure 1.1b) shows the active accretion of H_2 onto the 5.1 Myr young protoplanet WISPIT 2 b embedded within its birth disk (Capelleveen et al. 2025; Close et al. 2025). Other young exoplanets can offer insight into the early stages of planetary formation; e.g. TOI-1227 b (8 Myr), HD 109833 b/c (27 Myr), and HD 63433 d (414 Myr) (Wood et al. 2023; Capistrant et al. 2024; Varga et al. 2025). Observing and

---

[4] One alternative model is the 'synestia' hypothesis: where a single impact (or multiple) caused the Earth to spin-up to a sufficiently rapid rate that it generated a circumplanetary disk, from which the Moon was eventually formed (Lock et al. 2018; Lock and Stewart 2024).

modelling young planets can then provide insight into how and when such bodies gain their volatile inventories, and in which regimes their volatiles can be retained over long timescales (Schlichting and Young 2022; Zahnle and Kasting 2023).

A planet without an atmosphere will thermally radiate energy directly to space, and potentially solidify. However, thick atmospheres can substantially limit the cooling rate of a planet by absorbing thermal radiation emitted by its surface and re-radiating it downwards. Models suggest that this effect would extend the lifetimes of primordial magma oceans, depending on atmospheric composition (Abe and Matsui 1986; Elkins-Tanton 2008; Hamano et al. 2015). It is therefore essential that we can understand – and develop models for – the exchange of energy and mass between planetary interiors and atmospheres (Lichtenberg et al. 2025).

Volatile CHNOPS elements have the capacity to dissolve into magma oceans in a manner analogous to the dissolution of CO_2 and NH_3 into our water oceans. Aqueous partitioning of gas species is classically described by Henry's law, which relates the aqueous concentration of a dissolved species to its gas-phase partial pressure using a solubility constant. Similarly, volatile species can partition across an atmosphere-magma ocean interface (a planet's surface) according to equilibrium solubility relationships (Kite et al. 2016; Gaillard et al. 2021; Gaillard et al. 2022; Schlichting and Young 2022). For example, H_2O is highly soluble in melt but not so-much in solid silicate phases, so it is expected that H_2O will be efficiently degassed during magma ocean solidification (Sossi et al. 2023). This expectation gave rise to predictions of large steam-dominated atmospheres for recently-solidified planets (see Section 1.3.2). Solubility can be represented using empirical relationships, although the dissolution mechanism is usually heterogeneous, since the chemistry *within* the melt often means that a dissolved species is different to its counterpart in the atmosphere; e.g. CO_2 dissolves as carbonate CO_3^{2-} (Dixon 1997).

Atmosphere-forming volatiles may be sequestered within the solid phase of the mantle during the course of mantle solidification by (i) directly partitioning into the solid phase, or (ii) being dissolved within trapped pockets of melt (Hier-Majumder and Hirschmann 2017; Kite and Barnett 2020; Schlichting and Young 2022; Sim et al. 2024). The latter mechanism is thought to be more efficient at keeping volatiles, subject to the timescale of mantle solidification (Lichtenberg et al. 2025). Volatile elements may also readily bond to iron, such as FeO alloyed with metallic Fe, so the formation of a metallic core provides a further pathway for the storage of light elements deep within planetary interiors (Dreibus and Palme 1996a; Guimond et al. 2024). FeO will be the primary bearer of iron atoms at high pressures and temperatures in the planet's deep interior, which could inhibit the segregation of a distinct metallic core (Huang et al. 2021; Huang and Dorn 2025).

Another family of processes also factor into the complexity of planetary evolution: atmospheric escape. These are a set of physical and chemical mechanisms by which atoms are removed from a planet's gravitational well. The potential for hydrogen loss from the Earth was first mentioned by Waterson (1851) and later formulated more rigorously (Jeans 1904). We have since directly observed escape processes occurring on Earth, Mars, Venus, Titan, and Pluto (Brain et al. 2016; Gunell et al. 2018), although the rate of escape on these bodies is relatively low ($\sim$ 1 kg s^{-1} on Earth) compared to what might be expected on some exoplanets (Ehrenreich et al. 2015; Owen 2019). Escape processes are categorised (Hazra 2025) as 'thermal' (driven by thermal processes, usually enabled by absorption of stellar radiation) and 'non-thermal' (interactions – sometimes magnetic – between the stellar wind and planetary atmospheres). The trivial type of thermal escape is 'Jeans escape', where atoms in the upper atmosphere leave the planet by simply having a kinetic energy greater than the gravitational binding energy, on the understanding from kinetic theory that the gas contains particles with a Maxwellian distribution of energies (Jeans 1904; Gronoff et al. 2020). Further to Jeans escape is 'hydrodynamic escape', where the gas fluid escapes as a transonic wind rather than particle-by-particle. Absorption of X-ray and ultraviolet (XUV) radiation supplies energy to support the escaping flow at some energy efficiency η, so hydrodynamic escape is expected to be the dominant process for planets exposed to large radiation fluxes, such as those around young stars (Zahnle and Kasting 1986; Johnstone 2020). The 'true' value of η in the energy-limited regime is poorly constrained due to multiple disequilibrium processes factoring into the energy balance (Johnstone 2020; Ito and Ikoma 2021). For example, some XUV energy is effectively lost due to photon emission when electrons transition between energy levels in excited atoms, inducing a cooling effect ('atomic line cooling'; Nakayama et al. 2022; Yoshida et al. 2024). Lighter species may more readily escape because of their weaker gravitational attraction to the planet, giving rise to compositionally *fractionating* hydrodynamic escape (Zahnle and Kasting 1986; Odert et al. 2018). An atmosphere may become preferentially enriched in relatively heavier species, such as oxygen, due to fractionation over long periods of time (Hunten et al. 1987; Luger and Barnes 2015; Zahnle and Kasting 2023). An atmosphere composed of hydrogen and heavier elements will experience compositional fractionation at varying degrees depending on the XUV irradiation, collisional coupling between species, and gravity (Odert et al. 2018). Hydrodynamic simulations in the limit of rapid escape have previously shown that the out-flowing fluid is may instead escape in bulk without fractionating because H atoms drag heavier atoms along with them (Johnstone 2020). We can trace escape rates on exoplanets by measuring absorption by metastable helium, excited by the same radiation which drives hydrodynamic escape (Owen 2019; Yan et al. 2024). Hubble Space Telescope observations of metastable helium absorption support treatment of exoplanetary escape as being within the energy-limited hydrodynamic regime (McCreery et al. 2025). Complete atmosphere stripping is an extreme scenario which may eventually come about in some cases; suggested to explain observations of LHS 3844 b and TRAPPIST-1 b (Kreidberg et al. 2019; Ducrot et al. 2024), although these 'bare rocks' have also been suggested to arise from extremely volatile-poor formation scenarios (Kane et al. 2020).

In parallel to escape processes, the redox state of planetary mantles is another factor controlling the chemical speciation of volatile elements, and therefore the composition of a planet's atmosphere (Kasting et al. 1993a; Hirschmann 2012; Sossi et al. 2020; Gaillard et al. 2022). Variations in mantle redox primarily arise from the capacity for iron to take-on different oxidation states (metallic Fe^{0+}, ferrous Fe^{2+}, and ferric Fe^{3+}), usually when reacting with oxygen to generate various planet-forming compounds (Frost 1991). Oxygen is the most abundant element in the Earth by mass. So, because of oxygen's abundance and chemical relationship to iron, the oxygen fugacity $f\mathrm{O}_2$ – is used as a measure for the chemical potential of oxygen, and thereby for the mantle's redox state (Eugster 1957; Frost 1991; Guimond et al. 2023a). The fugacity of a species i is formally related to its chemical potential μ_i as $\mathrm{d}\mu_i = RT\,\mathrm{d}(\ln f_i)$, but can be intuitively interpreted as the measure of a given species' real-gas contribution to the total pressure of a mixture, accounting for deviations from non-ideality through some fugacity coefficient $\psi_i = f_i / p_i$. Rather than quoting values with dimensions of pressure, the oxygen fugacity $f\mathrm{O}_2$ can be readily expressed relative to a temperature-dependent buffer reaction that is *assumed* to be representative of the redox chemistry of iron in the mantle (Frost 1991). We may then use relative terminology to describe an environment as being 'reduced' (when $f\mathrm{O}_2$ is smaller) versus being 'oxidised' (when $f\mathrm{O}_2$ is larger). For example, the net reaction between metallic iron and free oxygen to form wüstite, $2\,\mathrm{Fe} + \mathrm{O}_2 \rightleftharpoons 2\,\mathrm{FeO}$. This net reaction will generate different amounts of O_2 depending on the temperature, pressure, and the activity and oxidation state of iron. The oxygen fugacity can then be written as $\log_{10}(f\mathrm{O}_2) = \log_{10}(f\mathrm{O}_2{}^{\mathrm{IW}}) + \Delta\mathrm{IW}$, where the dimensionless quantity $\Delta\mathrm{IW}$[5] quantifies the oxygen fugacity relative to that of the iron-wüstite buffer, in logarithmic units. It must be noted that oxygen does not exist freely as O_2 within planetary interiors, but this buffer is useful for representing the redox state of iron; $f\mathrm{O}_2$ is not *identical* to the mantle redox state because other present minerals will also take up oxygen atoms. So, while a cooler environment at chemical equilibrium does shift the iron-wüstite reaction towards FeO (Hirschmann 2021) at thermochemical equilibrium, this process will be occurring across an inhomogeneously-composed mantle where the Fe content – and its oxidation state – vary with depth (McCammon 1997; Itcovitz et al. 2022; Schaefer et al. 2024; Zhang et al. 2024b). Mantles are expected to become more reducing with depth, so that the regions most strongly interacting with an overlying atmosphere are the most oxidised; in part because Fe^{3+} is less reactive within garnet phases at high-pressure (Ballhaus 1995; Yaxley et al. 2012; Gaetani 2016). Since I am concerned with the time-evolution of these systems, I would ideally consider the processes by which Fe droplets – initially suspended in the convective cells of the mantle following planet formation – would segregate to the deep interior of the planet, forming a metallic core while also oxidising its mantle (Wade and Wood 2005; Wordsworth et al. 2018). However, the particulars of core formation depend on mantle dynamics and the size of the Fe droplets, in their capacity to become entrained within these overturning cells (Karato and Rama Murthy 1997; Ichikawa et al. 2010; Qaddah et al. 2019). For these

---

[5] It is also common to use the notation $\mathrm{IW} + x$, equivalent to writing $\Delta\mathrm{IW} = x$.

reasons – in that a planet is not wholly in thermodynamic equilibrium and I will not directly model mantle fluid dynamics – expressing upper-mantle redox state in terms of fO_2 is an important and useful modelling tool (Frost 1991; Schaefer et al. 2024). Other mineral redox buffer reactions could be chosen, such as the fayalite-magnetite-quartz buffer: $3\,Fe_2SiO_4 + O_2 \rightleftharpoons 2\,Fe_3O_4 + 3\,SiO_2$.

We can then expect that young planets with primordial atmospheres accreted from the Solar Nebula ($\sim$ IW $-$ 7) initially have reducing interiors with low fO_2 (Grossman et al. 2008; Sharp 2017; Cartier and Wood 2019). Earth's *bulk* oxygen fugacity is now approximately IW $-$ 2 (Kress and Carmichael 1991; Aulbach and Stagno 2016), which represents the conditions of core-mantle equilibration (Frost and McCammon 2008), while isotopic measurements of zircon crystals and komatiite rocks provide evidence for Earth's *upper mantle* having been relatively oxidised to IW + 4 since shortly following its formation (Trail et al. 2011; Nicklas et al. 2018; Zhang et al. 2024a). So, Earth's primitive mantle may have been initially reduced, and then oxidised primarily during the process of core segregation, cooling, and magma ocean solidification (Kasting et al. 1993a; Wade and Wood 2005; Armstrong et al. 2019; Deng et al. 2020). The redox state of the lunar mantle is estimated as $\sim$ IW $-$ 1 (Wadhwa 2001). Measurements of Mercury's crustal composition have established that it has a reducing mantle – between IW $-$ 7 and IW $-$ 4 – rich in sulfide minerals (Zolotov et al. 2013; Namur et al. 2016). A wide range of mantle redox states are demonstrably feasible depending on these chemical and dynamic processes acting across different planetary contexts, meaning that a broad diversity of outgassed *atmospheric* compositions are possible (Ortenzi et al. 2020; Sossi et al. 2020). This thesis will explore this potential for compositional diversity.

1.1.3 Expectations from the Earth

To collectively contextualise the key interior and atmospheric processes outlined in the previous section, the next paragraph will briefly outline the timeline of Earth's relevant history – for which we benefit from in-situ measurements. A consideration of these events within a shared context provides a benchmark to calibrate our *generalised* expectations from planetary formation and evolution processes.

The Sun began fusing hydrogen into helium 4.6 billion years ago (Gudel 2007). The first solid materials within the Solar System (Ca-Al-rich inclusions) formed thereabouts, at around 4.57 Ga[6] (Baker et al. 2005; Connelly et al. 2012). The Earth itself then formed at $\sim$ 4.54 Ga in the presence of the Solar Nebula, from which the Earth obtained some of its volatiles (Dalrymple 2001; Sossi et al. 2022; Savignac and Lee 2025). The Moon formed shortly afterwards, at $\sim$ 4.34 Ga; likely contemporaneous with substantial (re-)melting of the Earth's interior (Borg et al. 2014). An early giant impact to the Earth would have removed its primary nebula-derived atmosphere, which is evidenced by Earth's depletion in inert heavy noble gases relative to other volatile elements (Aston 1924; Pepin 2000). Earth's primordial magma ocean solidified at some point during the Hadean, the first eon of Earth's history, which lasted until the Eoarchaen at 4.03 Ga. The oldest terrestrial rocks to have survived billions of years of crustal recycling are dated from $\sim$ 4.33 to 4.20 Ga (during the Hadean) which is the latest point by which the Earth's early magma ocean can have solidified (Cavosie et al. 2005; O'Neil et al. 2008; Sole et al. 2025). These ages allow an approximately $\sim$ 100 Myr duration for solidification of Earth's magma ocean. Solid-phase mantle convection has since been sustained for $\gtrsim$ 3.8 Gyr up to the present day (Wilson 1965; Cates et al. 2013; Caro et al. 2025). There is evidence for surface water oceans on Earth at ages between $\sim$ 4.4 and $\sim$ 3.8 Ga, although liquid water oceans can only be stable after a crust has formed (Wilde et al. 2001; Genda and Ikoma 2008). The point at which life first arose is poorly constrained, but can be traced to the Hadean (Betts et al. 2018; Pearce et al. 2018; Westall 2025). The *last* universal common ancestor of all Life potentially existed as early as $\sim$ 4.2 Ga (Crapitto et al. 2022; Moody et al. 2024). Our ancestor lived in an environment which was historically thought to have been chemically reducing (H_2-rich; Zahnle et al. 2020), although more recent work now favours an oxidised (CO_2-rich) environment during this time (Paschek et al. 2025). Habitability is maintained in part due to weathering and crustal recycling, which regulates the atmosphere's composition and its greenhouse effect (Kasting and Catling 2003; Korenaga 2012; Trapp-Muller et al. 2025). In particular, the presence of liquid water on a planet's surface efficiently facilitates the draw-down and regulation of

---

[6] 'Ga' is an absolute measure of time, indicating billion-year units *into the past* from the present day. 'Gyr' is a measure of duration in billions-year units.

CO_2 (Sleep et al. 2001). An atmospheric greenhouse has been necessary for maintaining habitable conditions on Earth, potentially through 'snowball' periods whilst the Sun was less luminous (by $\sim 20\%$) earlier in its lifetime (Sagan and Mullen 1972; Sagan and Chyba 1997). And, while Earth's bulk redox state has been approximately constant for most of its lifetime (Trail et al. 2011), a protracted 'Great Oxidation Event' occurred on its surface environment between 2.5 and 2.2 Ga (Ligrone 2019). The GoE is coincident with the Makganyene snowball periods, during which atmospheric CH_4 declined, oxygenic photosynthesis flourished, and atmospheric O_2 rose [7]; atmospheric oxygen further rose by $\sim 100\times$ during the Cambrian explosion, bringing its concentration to its substantial present-day levels (Poulton et al. 2021; Donoghue et al. 2025; Wang et al. 2025a). The Earth's biosphere is a key component of the broader Earth climate system (Lyons et al. 2024), so whether life arose on Earth in an oxidising or reducing environment, and the conditions under which it initially thrived, depend directly on the atmospheric composition during the Hadean (Pearce et al. 2018; Bower et al. 2025). The timing of magma ocean crystallisation, cooling, and ocean formation is thus highly sensitive to the physics occurring within the Earth's interior and its atmosphere. These processes are then directly responsible for the resultant climate states, and to potential habitability and the origin of life.

Could a subset of the above-described events, which collectively shaped the Earth, also have occurred on other planets? The present state of the Earth stands in contrast to those of its neighbours, not least because of its cosy separation from the Sun, but also possibly by its relatively late formation and large moon (Zahnle et al. 2007; Halliday and Canup 2023). On Earth, CO_2 is efficiently scrubbed from the atmosphere by surface water and weathering processes. But, in comparison, Venus' hot runaway state precludes surface water; its atmosphere remains dominated by CO_2 (Nakajima et al. 1992; Turbet et al. 2021). Venus probably never initiated plate tectonics and has remained in a 'stagnant lid' regime where sequestration of carbon is inefficient (Schubert et al. 2001; Tackley 2023). Measurements of Venus's enhanced D/H ratio do provide evidence for past and current hydrogen loss from the planet – suggesting an early water ocean or continued

---

[7] Aerobic metabolisms are thought to be necessary for the proliferation of complex life (Runge et al. 2025).

cometary delivery (Grinspoon 1993). On the other hand, we have direct evidence for fluvial activity on ancient Mars (Carr 2012; Losekoot et al. 2025) and some suggestions for a more Earth-like atmosphere in Mars' recent past (Kite et al. 2020; Joiret et al. 2025). These suggestions exist despite Mars' presently uninhabitable surface and it being located outside the Sun's habitable zone (Carr 1996; Lunine et al. 2003). How did the environments of these three neighbouring bodies diverge? The answer to this question depends strongly on the specifics of the earliest stages of their evolution (Farcy et al. 2025), the distribution of their volatiles (Hamano et al. 2024; Jakosky and Byrne 2025), the geodynamics of their interiors (Gillmann et al. 2024), and atmospheric escape processes (Kasting and Catling 2003; Nakayama et al. 2022).

Strong physical and chemical interactions between interiors, atmospheres, and the space environment apparently define the initial conditions for later-stage planetary evolution, and then continuously act to shape planets throughout their lifetimes (Schaefer and Elkins-Tanton 2018). Moving beyond Earth and the Solar System leaves us with similar physics in completely different contexts, with additional questions to be asked and (ideally) answered. In the next sections, I illustrate the diversity of exoplanetary climates, outline prior attempts at modelling these systems, and then identify the particular science questions which will be addressed in this thesis.

1.2 Ad astra

1.2.1 Measuring exoplanets

As of February 2026, three decades after the first detection of an exoplanet orbiting a Sun-like star, we have > 6200 confirmations of planets beyond the Solar System (Schneider et al. 2011). Detecting and characterising exoplanets is primarily an indirect affair, as they are small and dim compared to their hosts (Seager 2011; Fischer et al. 2014; Perryman 2018). The three main methods for measuring exoplanets are illustrated in Figure 1.2: Doppler spectroscopy, transmission measurements, and emission measurements. Emission measurements are typically applied for characterisation of already-known exoplanets, although direct-imaging can be used for discovery.

A fraction of a star's light is blocked when an orbiting planet passes between it and an observer, resulting in a decrease in apparent brightness of the star due to absorption of stellar radiation by the planet and its atmosphere. This blocking geometry is known as a 'primary eclipse' or a 'transit', so measurements of this blocking of starlight are referred to as 'the transit method'. The transit method is responsible for the detections and the characterisations of much of the surveyed exoplanet population (Charbonneau et al. 1999; Schneider et al. 2011). Green circles in Figure 1.2 show the geometry of a planet performing a single transit (T1, T2, T3). The magnitude of this absorption ('transit depth', δ_t) is related to the ratio of planet and stellar radii: $\delta_t = (R_p/R_\star)^2$. Spectroscopic measurement of δ_t provides information on the composition of the planet's upper atmosphere, as R_p depends on the atmosphere's temperature structure and wavelength-dependent opacity. The transit method probes the atmospheric composition at pressure levels between 10^{-3} and 10^{-5} bar where photochemical and aerosol processes are important (Venot et al. 2012; Wogan and Catling 2020; Lee et al. 2021; Benneke et al. 2024). The formation of spectral absorption features and the physics of radiative transfer are discussed in Sections 2.2 and 3.2. Unfortunately, the transit method is sensitive to the so-called 'transit light source effect', where processes occurring on the photosphere of the host star complicate inferences of planetary properties from measurements of δ_t. For example, the detection of a H_2O feature in a transmission spectrum may be attributed to water in a transiting planet's atmosphere – but in reality, we could instead be detecting molecular features arising from within the star's photosphere itself (Rackham et al. 2018; Rackham et al. 2019). The effects are stellar activity are an active point of research, and thought to be especially problematic for planet's orbiting cooler late-type stars which have molecules in their atmospheres (Reiners et al. 2010; Haywood et al. 2014). The interpretation of transmission measurements is stymied by a degeneracy between metal-rich atmospheres of high-molecular weight and the presence of aerosols: both of which act to reduce spectroscopic feature depths (Kreidberg et al. 2014; Helling 2019).

Similarly to the transit method, changes in apparent brightness also occur when a planet passes *behind* its host star from the viewpoint of an observer. This configuration is referred to as a 'secondary eclipse' (Figure 1.2, orange circles). By comparing the measured radiation during (E2) and outside (E1, E3) of eclipse, we obtain an emission spec-

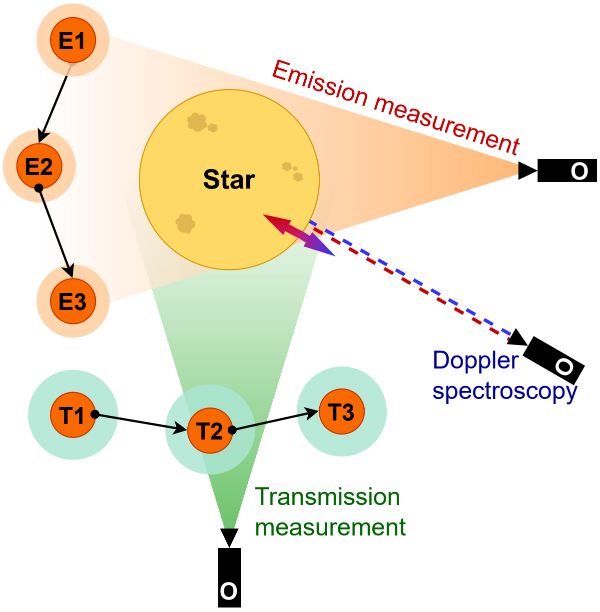

Figure 1.2: Thousands of exoplanets have been discovered using three main techniques. This cartoon illustrates the three geometries of emission, transmission, and Doppler spectroscopy. Each technique allows characterisations of different planetary properties, although each with its own individual complexities.

trum of the radiation emitted from a planet (Swain et al. 2010). These spectra can contain molecular features due to the absorption of radiation passing through the planet's atmosphere, enabling similar characterisations to the transit method. However, the viewing geometry of emission spectroscopy allows measurements to probe comparatively deeper regions of the planet's atmosphere, between 10^{-1} and 10^{-3} bar (Piette et al. 2023). Emission measurements are particularly sensitive to the planet's atmospheric temperature structure, which can provide insight into its dynamics. However, there are substantial degeneracies in interpreting these measurements because different physical scenarios can equally explain a particular brightness temperature derived from emission fluxes (Line et al. 2019; Hammond et al. 2025).

The two observational techniques described above can also be applied photometrically. Spectral data may be binned down, or an instrument may use filters with a particular bandpass to focus on a particular wavelength region, usually centred around a molecular feature of interest (Gordon et al. 2022b). Photometry can offer relatively improved signal-to-noise sensitivity at the cost of marginalising over spectroscopic information, such as narrow absorption lines (Bowman et al. 2020; Libralato et al. 2024).

For a synchronously rotating tidally locked exoplanet, stellar radiation is always absorbed by a single *dayside* hemisphere. Any atmosphere present on a planet would then act to redistribute some amount of heat from the dayside to the nightside through large-scale circulations, cooling the dayside temperature compared to an atmosphere-less body (Kempton and Knutson 2024). Secondary eclipse observations have used this physical reasoning to infer the absence of atmospheres around Earth-sized exoplanets through photometry; e.g. TRAPPIST-1 b, TRAPPIST-1 c, LHS 1140 c, and LTT 3780 b (Zieba et al. 2023; Ducrot et al. 2024; Allen et al. 2025; Fortune et al. 2025). Measuring the changing brightness of the planet-star system over an entire orbit produces a 'phase curve', which can more reliably infer the presence of an atmosphere and break some of the degeneracies in interpreting photometric eclipse measurements (Hammond et al. 2025; Maurel et al. 2025).

Doppler spectroscopy (the 'radial velocity method', RV) is used to measure the combined orbital parameters and masses of exoplanets (Reiners et al. 2010). Mutual gravitational attraction between a star and an orbiting body results in the star moving on an elliptical orbit around their barycentre, so by observing Doppler-shifts to the stellar emission lines, we can determine its motion relative to an observer: the star's radial velocity. Conservation of momentum and knowledge of the star's own mass allows a solution to be obtained for the orbital configuration of the system and quantify the minimum mass, $M_p \sin(i)$, of orbiting planets (Seager 2011). Orbital inclination i is not constrained by radial velocity measurements; absolute estimates for planet mass M_p require follow-up transit measurements. Doppler spectroscopy is usually performed using high-resolution spectrographs connected to ground-based telescopes (Birkby 2018). Extracting parameters from spectroscopic measurements requires simultaneously accounting for the motions of multiple orbiting planets, but also for Doppler shifts introduced by motions within the star itself, such as from convective granules and star spots (Reiners et al. 2012; Haywood et al. 2014; Fischer et al. 2016). It was through the RV method that Mayor and Queloz (1995) made the first detection of an exoplanet orbiting a main-sequence star, to later win the 2019 Nobel Prize in Physics.

Direct imaging methods are generally only possible for exoplanets on sufficiently wide orbits, but they can avoid the problem of separating stellar and planetary signals (Zurlo 2024). The upcoming Habitable Worlds Observatory (Feinberg et al. 2024), Extremely Large Telescope (Padovani and Cirasuolo 2023), and LIFE mission (Quanz et al. 2022) will all directly image exoplanets to search for signs of life elsewhere in the universe. Gravitational microlensing, pulsar timing, disk kinematics, and astrometry are examples of other observational techniques (Perryman 2018; Zang et al. 2025).

Observing a given exoplanet with more than one technique provides constraints on multiple properties. In knowing both a planet's mass (from RV) *and* radius (from transit), we can estimate its bulk density and attempt to infer its bulk composition (Luque and Palle 2022). However, we must keep in mind that uncertainties and errors in stellar parameters then factor into the parameters of orbiting planets. There may also be various degenerate structures and compositions compatible with a planet's bulk characteristics (Turbet et al. 2020). Careful application of theoretical models is therefore necessary for determining which structural, compositional, and chemical configurations are compatible with combined observations (Lichtenberg and Miguel 2025). The next section overviews our present understanding of the exoplanet populations, and highlights specific cases which have been characterised using these observational techniques.

1.2.2 Exoplanet populations and individuals

The exoplanet census has overturned our understanding of planetary environments and system architectures, compared to prior assumptions informed by the Solar System. We have discovered Earth-sized planets orbiting small M-type stars, including some within their star's habitable zone (Kopparapu et al. 2013; Agol et al. 2021). However, terrestrial-sized planets orbiting small stars are intrinsically more difficult to characterise (Seager 2011). Figure 1.3 plots all the surveyed small exoplanets, with a handful of systems highlighted (coloured circles) alongside the Solar System planets (black circles). The exoplanet population also contains several types of 'small' planet which have no solar-system analogues. Notably, super-Earths ($1.0R_\oplus \lesssim R \lesssim 1.7R_\oplus$; Kempton and Knutson 2024), and sub-Neptunes ($1.7R_\oplus \lesssim R \lesssim 4.0R_\oplus$; Fulton and Petigura 2018). Both of these populations sit in a regime between the canonical 'terrestrial' planets (e.g. Mars, Earth) and the 'ice giants' (e.g. Neptune, Uranus). These new sub-Neptune and super-Earth planets are especially relevant because their large radii and small orbits (Figure 1.3a) enable high signal-to-noise measurements with current instruments, and thereby allow detailed characterisation of their properties (Lichtenberg and Miguel 2025; Valencia et al. 2025).

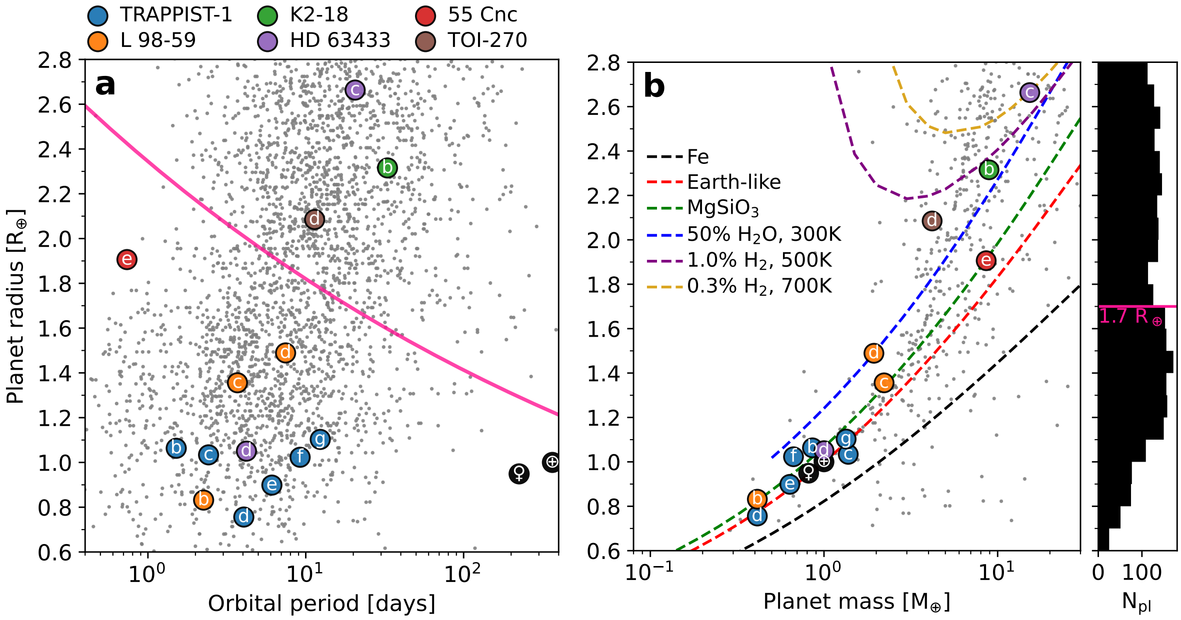

Figure 1.3: Projections of exoplanet parameters shows a range of potential compositional and thermodynamic regimes. Left: planet radius versus orbital period for exoplanets in general (grey) and in particular (colours). The pink line shows an empirical fit to the radius valley (Ho and Van Eylen 2023). **Right**: planet radii versus their masses. Different theoretical mass-radius relations are plotted as dashed lines (Zeng et al. 2019). A flattened histogram of exoplanet radii is shown in the auxiliary axis. These exoplanet data were obtained from `exoplanet.eu`. Solar system data were obtained from the NASA Space Science Data Coordinated Archive.

We do not know how super-Earths and sub-Neptunes originate, nor if their formation is fundamentally related. Across the literature, two competing scenarios are often considered for explaining these two categories (Zeng et al. 2019; Valencia et al. 2025): they may form jointly as *gas-dwarfs* with large envelopes (primarily H_2-He comprising ∼ wt% fractions of a planet's mass) and eventually diverge due to long-term atmospheric escape processes (Lopez and Fortney 2014; Lopez 2017; Owen and Wu 2017; Owen 2019), or they could be *water-worlds* of layered rock- and H_2O-phases that differ primarily by the water content arising from their formation context within the protoplanetary disk (Mousis et al. 2020; Lacedelli et al. 2022; Luque and Palle 2022; Burn et al. 2024). The water-world scenario is justified in that planets forming beyond the system's 'snow line'[8] may readily gain large amounts of water ice during accretion (Bitsch et al. 2019). The gas-dwarf scenario has generally been favoured (Rogers 2025; Valen-

---

[8] This conceptual boundary is also referred to as the 'ice line' or 'water ice line', and is traditionally defined by the condensation temperature of H_2O at 0.1 mbar (Sossi et al. 2022).

cia et al. 2025) because a primordial H_2-dominated envelope can be easily gained during planet formation (Rogers 2015), and because this scenario generally explains the population-level trends in the current exoplanet census better than the water-world case (Lopez 2017; Rogers 2025). However, it should be noted that the condensation lines are not discrete boundaries, but *regions* representing the onset of a material's condensation and its efficient adsorption to grains within the protoplanetary disk (Boitard-Crepeau et al. 2025; Wang et al. 2025b). Planets forming outside the water snow line must necessarily also form outside the 'soot line'; these water worlds would necessarily accrete substantial amounts of C via organic (hydro)carbon compounds, raising the possibilities of soot-worlds and water-soot-worlds (Bergin et al. 2023a; Li et al. 2025; Lin and Seager 2025). It may be possible for water-rich planets to form *interior* to the systems' snow line, through the endogenous oxidation of nebular hydrogen to H_2O at high pressures within sub-Neptune interiors (Horn et al. 2025). Modelling is likely necessary for connecting these early processes shape to observable planets at the present-day.

The exoplanet census can be projected over different observable variables. Consideration of planet radius versus orbital period shows a distinct and statistically significant dearth of planets around the 'radius valley' (pink line in Figure 1.3). This radius valley was theoretically predicted to arise from photoevaporative escape processes before it was observationally confirmed (Lopez and Fortney 2013). The width and location of the radius valley depend on orbital period and host-star mass, leaving it poorly resolved unless these axes are flattened as in Figure 1.3 (Fulton and Petigura 2018; Venturini et al. 2020; Ho et al. 2024). This is important because the radius valley distinguishes super-Earths from sub-Neptunes, although it has been suggested (Luque and Palle 2022) that bulk density may be a better discriminator of these putative classifications. There are also several planets better suited to a 'super-Earth' label, but which sit on the sub-Neptune side of the 1D radius valley (e.g. 55 Cancri e). Both the gas-dwarf and water-world paradigms are put-forth to theoretically justify the presence and shape of the radius valley, with the gas-dwarf scenario relying on long-term atmospheric photoevaporation (energy-limited hydrodynamic escape) to explain the valley's current morphology. The California-Kepler survey of 1385 planets and their stars has shown that sub-Neptune planet tend to orbit younger stars than super-Earth planets

(David et al. 2021; Sandoval et al. 2021), which would be consistent with planet evolution theories which suggest that super-Earths come about from long term photoevaporation (Ginzburg et al. 2016; Lopez 2017). In which case, young sub-Neptune planets may represent a reservoir for potential future super-Earths. If true, this transformation would intimately link the observed sub-Neptune and super-Earth populations by their evolution over time (David et al. 2021), so studying these planets' present-day states can provide direct insight into their histories. I undertake such a study in Chapter 5. While simplified models of the proposed gas-dwarf and water-world scenarios have seen success in reproducing demographic features, comprehensive multi-physics models are still necessary, not least because simplified models cannot reproduce observational characterisations of *specific* planets (Schaefer and Elkins-Tanton 2018; Kite et al. 2020; Kite and Schaefer 2021; Lichtenberg and Miguel 2025; Rogers 2025). Better understanding the nature of the radius valley will require further large-scale surveys, such as PLATO (Rauer et al. 2025), alongside sufficiently comprehensive modelling to target and explain these observations. Another feature of the exoplanet census is the general absence of planets in the 'Neptunian desert', which exists at approximately sub-Jovian masses and orbital periods < 2 days (Mazeh et al. 2016; West et al. 2019), potentially shaped by planet migration alongside rapid escape processes. Understanding how these features arise, how they connect bridge different planetary populations, and the fundamental processes involved are all important problems of planetary science readily distilled in the National Academies decadal survey (National Academies of Sciences, Engineering, and Medicine 2023):

- Which physical processes govern a planet's interior structure?
- How does a planet's interior structure and composition connect to its surface and atmosphere?
- What fundamental planetary parameters and processes determine the complexity of planetary atmospheres?
- How does a planet's interaction with its host star and planetary system influence its atmospheric properties over all time scales?

The 'habitable zone' (HZ) of orbital distances around a given star is often used to highlight planets which may have conditions amenable to life. The HZ is defined by the amount and spectral distribution of stellar radiation a planet would receive at a given distance from its host, and therefore whether liquid water could be stable on the planet's surface (Maunder 1913; Dole 1964; Kasting et al. 1993b; Ware et al. 2022). Receiving too much radiation when interior to the inner edge of the HZ causes a planet to *runaway* towards a hot greenhouse regime and potentially desiccate, while too little radiation causes water to freeze-out onto the surface as a solid (e.g. Venus and Mars respectively, by their isotopic D/H ratios). The HZ concept provides a flexible metric by which to distinguish *potentially* habitable planets from those which are inhospitable to life as we know it, requiring only the knowledge of a planet's equilibrium temperature and host star type. The HZ concept must be held tentatively, in part because its boundaries are dependent on processes which are poorly understood and/or inconsistent with each other, particularly across a range of potential exoplanetary contexts. When and whether a planet undergoes a runaway greenhouse transition to an inhospitable regime depends on the spectral type of its host star (Ware et al. 2022), the atmospheric composition (Ramirez and Kaltenegger 2017), cloud radiative properties (Turbet et al. 2023), assumed initial conditions (Leconte et al. 2013), and the dynamics of its atmosphere (Turbet et al. 2023). Radiative blanketing of a planet's surface by an atmospheric greenhouse can induce melting of its interior, given sufficient irradiation and atmospheric thickness (Hamano et al. 2013). The outer edge of the HZ is sensitive to regulation by silicate weathering feedbacks (Graham and Pierrehumbert 2020; Hakim et al. 2021), land-albedo and ice-albedo feedbacks (Zsom et al. 2013; Abbot et al. 2018), and the potential for thick greenhouse atmospheres to maintain temperate surfaces even at extremely low instellations (Pierrehumbert and Gaidos 2011). The importance of atmospheric temperature structure in more generally setting planetary thermal evolution over geological timescales is discussed and modelled in Chapter 3.

With these caveats to the HZ noted, confirmed detections of rocky bodies in their star's HZ are still exciting. An Earth-sized exoplanet orbiting a Sun-like star in its HZ would naturally be a prime target for studies with the aim of detecting extraterrestrial life (Seager 2013). We have already detected Earth-sized planets around M-type stars, such as TRAPPIST-1 e and Proxima Centauri b (Barnes et al. 2016; Wolf 2017). Furthermore, there is the potential for exo-moons orbiting giant planets in their star's HZ; e.g. Alpha Centauri A (Williams et al. 1997; Sanghi et al. 2025). The deep oceans of Enceladus could harbour life similar to 'extremophiles' on the Earth (Pikuta et al. 2007; Deamer and Damer 2017; Postberg et al. 2018; Kahana et al. 2019). It has even been suggested life could thrive within organic-ionic liquids on the surfaces of atmosphere-less exoplanets (Agrawal et al. 2025). Regardless, the presence of life on an extra-solar body would necessarily be inferred indirectly through the detection of biosignatures: observational markers which can be strongly linked to biological activity rather be preferentially explained by abiotic processes alone (Seager 2013; Harman et al. 2019). A comprehensive picture of the true range of possible planetary environments and their *abiotic* processes is therefore crucial for establishing a null-hypothesis in the search for life (Catling and Kasting 2017; Harman et al. 2019). Atmospheric photochemistry, escape, and volcanic outgassing are all thought to generate false-positive biosignatures (Wordsworth and Pierrehumbert 2014; Krissansen-Totton et al. 2018; Lincowski et al. 2018; Wogan and Catling 2020). The recently claimed detection of dimethyl sulfide (DMS) on the HZ sub-Neptune exoplanet K2-18 b (Madhusudhan et al. 2023b; Madhusudhan et al. 2025) is controversial because DMS is a potential biosignature produced by algae in Earth's oceans (Stefels et al. 2007). However, DMS can also be produced photochemically (Hu et al. 2025) and its claimed detection rests on questionable statistical grounds (Stevenson et al. 2025; Taylor 2025; Welbanks et al. 2025). Sophisticated climate models also rule against a surface ocean on this planet, since K2-18 b's thick H_2-greenhouse atmosphere may raise its surface beyond the critical point of water (Luu et al. 2024; Shorttle et al. 2024; Wogan et al. 2024; Liu et al. 2025). K2-18 b remains an important case study because multiple structural and compositional scenarios are commensurate with its bulk density, and a non-detection of NH_3 provides insight into its deep dynamics (Tsai et al. 2021b; Yu et al. 2021). These ongoing problems are consolidated in the Decadal Survey (National Academies of Sciences, Engineering, and Medicine 2023):

- How are potentially habitable environments formed?
- What processes influence the habitability of environments?
- How will we interpret the biosignatures that we see?

The TRAPPIST-1 system of planets (blue circles in Figure 1.3) has received much attention because it contains seven Earth-sized exoplanets. Secondary eclipse observations of the innermost planets (b/c/d) have previously been used to infer that these planets lack substantial atmospheres (Greene et al. 2023; Zieba et al. 2023; Ducrot et al. 2024; Piaulet-Ghorayeb et al. 2025). These indications have more recently been supported by full phase curve observations of TRAPPIST-1 b/c (Gillon et al. 2025). Alternatively, an anti-greenhouse effect induced by the radiative properties of photochemically-produced atmospheric hazes could explain these planets' high brightness temperatures measured using photometry (Maurel et al. 2025). The extended 7.7 Gyr age of the TRAPPIST-1 system provides sufficient time for atmospheric escape processes to strip these inner planets of their volatiles (Burgasser and Mamajek 2017), so it may also be the case that the outer planets in their star's HZ may have also lost their atmospheres. We may use theoretical computer models to link the observed states of b/c to the potential present-day states of e/f/g through comparative planetology (Krissansen-Totton 2023). I study the early evolution of TRAPPIST-1 c in Chapter 3, by which I place constraints on the solidification timescale of its early magma ocean and explore a range of compositions that its early atmosphere may have had before it was lost. Quantifying the solidification timescale of primordial magma oceans is important in understanding when and why rocky planets may lose their atmospheres, through the capacity for their interiors to dissolve volatiles and shield them against hydrodynamic escape processes (Dorn and Lichtenberg 2021; Lichtenberg and Miguel 2025). The architecture of the TRAPPIST-1 system stands in contrast to that of the Solar System. The diversity of exoplanetary systems more broadly suggests that the Solar System may be atypical – for example, in that there are no planets orbiting interior to Mercury – potentially making the Solar System especially amenable to life (Winn and Fabrycky 2015; Halliday and Canup 2023).

In the spirit of the HZ concept, consideration of planets which receive extremely large amounts of stellar radiation (i.e. $> 100\times$ Earth's) has revealed a population of 'lava planets' on short orbital periods (Zilinskas et al. 2023). Even in the absence of an atmospheric greenhouse, these planets are sufficiently irradiated to induce melting of their day-side hemispheres, assuming a rocky composition. The prototypical lava planet, 55 Cancri e, has been observed several times over the last decade, although a confident assessment of its present day conditions remains elusive. This planet is shown by the red circle in Figure 1.3. Recent JWST and previous Spitzer observations of 55 Cancri e both point to a volatile-rich atmosphere composed of CO_2 or CO in contrast to an expected rock-vapour atmosphere (Demory et al. 2016; Hu et al. 2024; Zilinskas et al. 2025). In comparison, the smaller lava world K2-141 b may lack an atmosphere entirely or, indeed, host a tenuous envelope composed of evaporated rock vapours (Barragan et al. 2018; Zieba et al. 2022). Whether such planets can theoretically retain their volatiles over Gyr-timescales is currently uncertain, and necessitates further investigation in parallel to more temperate worlds.

The simultaneous consideration of multiple measured properties permits a finer characterisation of a given exoplanet. These may be derived from several observations which use different techniques; e.g. radial velocity and transmission spectroscopy together (Section 1.2.1). Projecting exoplanets onto mass-radius space allows a comparison of their *bulk* properties against isolines of potential compositions and layer-structures, known as 'mass-radius curves'. Figure 1.3b plots known exoplanets alongside theoretical mass-radius curves from Zeng et al. (2019), which allows a comparison against feasible compositions and structures (Valencia et al. 2007). The models used to generate these curves are highly simplified and contain no notion of planetary evolution, but simply serve to indicate which structural scenarios *might* be compatible with the bulk properties of a given planet (Lichtenberg and Miguel 2025). To further understand which structure-scenario is more likely, it is necessary (Madhusudhan 2019) to turn to spectroscopic characterisation methods; e.g. transmission spectroscopy. The sub-Neptune K2-18 b is also a famous case of degeneracy in planetary structure (shown in Figure 1.3 with a green circle). This planet's mass and radius are compatible with several layer structures including: a gas-dwarf scenario of an H_2 envelope atop a rocky interior (purple line; Shorttle et al. 2024; Wogan et al. 2024), a supercritical water-rich scenario atop a smaller core (blue line; Luu et al. 2024), and a habitable 'hycean' configuration (Madhusudhan et al. 2021). So, uncertainty in the planetary-scale structure of K2-18 b factors directly into the debate on its surface habitability. Similarly, the sub-Neptune TOI-270 d may incorporate mixed silicate-volatile layers, where these phases are able to miscibly mix at high temperatures deep within the planet (Benneke et al. 2024).

Lastly, I would like to briefly describe the L 98-59 system of five exoplanets (Kostov et al. 2019; Demangeon et al. 2021). Their host is a bright M3V star hosting three transiting exoplanets and two outer non-transiting planets. The inner planets are plotted in Figure 1.3 with orange circles. The innermost planet (b) is smaller than Venus and *may* host a volcanically sustained atmosphere rich in SO_2 (Bello-Arufe et al. 2025). Planet c is a super-Earth which may have lost its atmosphere entirely (Zhou et al. 2023). Planet d's low bulk density (Figure 1.3b) means that it *must* contain a significant amount of light volatile elements, reinforced by recent JWST transit observations which point to sulfur-bearing species in a H_2-dominated gaseous envelope (Banerjee et al. 2024; Gressier et al. 2024). Recent radial-velocity measurements have shown that the outer non-transiting planets (e/f) orbit within their star's habitable zone (Cadieux et al. 2025; Schwarz et al. 2025). The L 98-59 system is similar to TRAPPIST-1 (Gillon et al. 2017) in that the presence of several highly observable planets orbiting a shared star enables a comparative analysis which can marginalise over differences between systems (Seager 2011). However, unlike those of TRAPPIST-1, the planets of L 98-59 are of distinctly different sizes. I study the role of tidal heating during the early evolution of L 98-59 b/c/d in Chapter 4, and the complete history of planet d up to the present day in Chapter 5.

These planetary systems are a few examples of the thousands we have discovered so far. Over the course of this thesis, I consider some of these as test cases to probe planetary evolution more generally and to study the physics of their atmospheres and interiors. Numerous prior studies have compared interior and atmosphere models against measurements of Earth and observations of exoplanets, although we are yet to paint a comprehensive self-consistent picture. I review these previous modelling attempts and highlight important theoretical gaps in the next section.

1.3 Theoretical approaches

1.3.1 Early terrestrial models

Early work on the evolution of Earth's first atmosphere was qualitative (Kaula 1969), usually with the suggestion of CO_2-H_2O atmospheres formed by impactor degassing and serpentinisation reactions (Lange and Ahrens 1982). These works correctly proposed that geochemical cycling of CO_2 could explain the differentiation of Earth and Venus, and that the greenhouse properties of these gases could shape these first environments.

In the following decades, pioneering studies by Takafumi Matsui and Yutaka Abe considered a numerical solution for the coupled interior-atmospheric evolution of the early Earth shortly following a large impact (Abe and Matsui 1985). They highlighted the importance of atmospheric blanketing of the Earth's interior; the modelled greenhouse effect of H_2O was found to maintain a surface temperature sufficient to keep Earth's interior molten for some time (Matsui and Abe 1986; Abe 1993). Given the amount of H_2O suggested in their degassing models, Matsui and Abe (1986) proposed a giant impact as the origin of Earth's present surface water. Zahnle et al. (1988) highlight several deficiencies in these early Abe papers; in particular their spectrally-grey treatment of radiative transfer and their subsequently inaccurate estimates of the expected runaway greenhouse behaviour (Kasting 1988). With the introduction of a moist atmospheric convection scheme, and simplification to pure-H_2O atmospheric compositions, Zahnle and Kasting both emphasised the role of the runaway greenhouse limit in setting the thermal evolution of the early Earth and the exposure of its hydrogen inventory to escape processes (Kasting et al. 1984; Zahnle and Kasting 1986).

Teller (1973) undertook similar work, but instead focussed on refractory rock-vapour atmospheres generated shortly following a presumed Moon-forming impact. Teller solved the equations of stellar structure (applied to the Earth) and provided evolutionary tracks of surface temperature and radius over time; see also a discussion by Cameron (1983). These works gave rise to an early understanding of the primordial Earth, with an atmosphere modelled as isothermal or fully convective and composed primarily of H_2O (sometimes also CO_2). They find that the young Earth spent some time in a runaway regime during which a fraction of its hydrogen inventory escaped, but it eventually cooled to form oceans.

1.3.2 Recent generalised models

The following decades lead to further development of planetary evolution models, with extensions to cases beyond the Earth and the Solar System. These works continued with an emphasis on H_2O saturation in setting atmospheric structure, and subsequently in controlling the thermal evolution of young planets. After an earlier discovery of a stratospheric limit to a planet's outgoing longwave radiation by Ingersoll (1969), the Simpson-Nakajima runaway radiation limit (Nakajima et al. 1992) in the asymptotic regime of a saturated upper atmosphere has become an established benchmark in the literature (Goldblatt et al. 2013; Leconte et al. 2013; Turbet et al. 2019; Turbet et al. 2020; Boukrouche et al. 2021). The apparent universality of this limit has been reinforced by its application in defining the inner edge of the habitable zone (Kopparapu et al. 2013; Ramirez and Kaltenegger 2014). The origin of the runaway greenhouse radiation limit is discussed and demonstrated in Section 2.3.2.

Attempts to trace rocky planet evolution over deep time have largely adopted numerical modelling approaches. The work of Elkins-Tanton (2008) represents the first modern attempt at simulating the coupled problem of interior-atmosphere physics. Elkins-Tanton provided estimates of CO_2 and H_2O partitioning at the point of magma ocean solidification, which set the initial conditions for the origin of life and Earth's present-day atmosphere. Similar coupled interior-atmosphere calculations were applied by Hamano et al. (2013) and Hamano et al. (2015), although they instead considered planets at a range of orbital separations and volatile endowments. Hamano et al. (2013) propose classifying outcomes into types I and II, where the latter cases sustain their primordial magma oceans for $\sim$ 100 Myr (see also Lebrun et al. 2013). The behaviours demonstrated by these models are strongly regulated by the runaway limit, and therefore the assumed convective atmospheric structure and simplified gas compositions.

Long-term fractionating escape processes may leave behind $\sim$ 1000 bar O_2-dominated atmospheres on highly irradiated exoplanets (Wordsworth and Pierrehumbert 2014). For example, those orbiting Proxima Centauri, GJ 667C, TRAPPIST-1, and L 98-59 (Luger and Barnes 2015; Barnes et al. 2016; Bolmont et al. 2017; Meadows et al. 2018; Fromont et al. 2024). These predictions of O_2-rich envelopes arise from a principle that XUV photons photolyse H_2O into H and O in the upper atmosphere; H then readily escapes while the O remains to form molecular O_2 (Chassefiere 1996). The oxygen could then stay in the atmosphere and/or be 'locked up' in the planet through oxidation of its surface and/or interior, accounting in-part for the oxidation of Earth's early mantle (Catling et al. 2001; Catling 2014). When accounting for the dissolution into H_2O and oxidation of a terrestrial magma ocean by residual O_2, Schaefer et al. (2016) instead found that 'tenuous' $\lesssim 1$ bar O_2 partial pressures are formed unless extreme initial H_2O inventories are considered. These works rest heavily on the presumption of initially H_2O-dominated atmospheres on young planets, and that any liberated atomic oxygen does chemically speciate into heavier O-bearing molecules such as CO or SO_2 (Gaillard et al. 2022; Sossi et al. 2023). However, it may still be the case that atmospheric processes occurring far above the surface, such as escape, can act to shape planetary interiors over time, influencing the observations we make at the present day.

The generation of high molecular-weight atmospheres composed of CO_2 and H_2O has often been considered because of their predicted formation as a result of magma ocean solidification (Sossi et al. 2020; Salvador et al. 2023), in addition to degassing from impactors (Schlichting and Mukhopadhyay 2018; Kite and Schaefer 2021) and by heterogeneous reactions with hot rocks (e.g. serpentinisation; Moody 1976). Later-stage cooling to more temperate conditions would eventually rain-out H_2O to leave behind a CO_2-N_2 secondary atmosphere (Sleep et al. 2001; Zahnle et al. 2007; Way et al. 2016; Sossi et al. 2020; Gillmann et al. 2024). The additional potential for heavy SO_2-rich compositions supplied by volcanism is raised by Io, and also by tentative inferences from JWST spectroscopy of L 98-59 b (Bello-Arufe et al. 2025).

However, primary atmospheres of near-Solar elemental composition have usually been considered for exoplanets larger than the Earth (Fortney et al. 2021). These H_2-He dominated compositions are also motivated by the application of models originally developed for stellar applications, and more recently motivated by exoplanet surveys of low density sub-Neptune exoplanets (Figure 1.3; David et al. 2021; Vach et al. 2024). Lopez and Fortney (2014) modelled the thermal evolution of planets with primary atmospheres, neglecting escape, and provided an early framework for mapping mass-radius relationships (for $M_\oplus \leq M_p \leq 10 M_\oplus$) to planetary compositions depending on their age. Importantly, Lopez and Fortney (2014) showed that gas-dwarfs cool and contract over a range of timescales, with their specific behaviour depending on the atmospheric molecular weight due to its impact on the scale height. Their model does not reproduce population-level trends (e.g. the radius valley, which was not confirmed until Fulton et al. 2017), but it does highlight that planets are entities which *evolve* over Gyr timescales in-parallel with stars. Similarly, both Kubyshkina et al. (2020) and Misener and Schlichting (2021) used planetary evolution models to simulate the thermal contraction of exoplanets *with* coupled atmospheric escape, although both models are limited to low-metallicity H_2-rich primordial compositions and do not consider partitioning of volatiles into deep interior reservoirs. Several works have been successful in reproducing the radius valley by including photoevaporative escape processes into simplified evolution models (Lopez and Fortney 2013; Owen and Wu 2017; Rogers 2025).

Recent planetary evolution models incorporate a wide range of physics, with a view of capturing of most important interactions. These include the VPLanet code (Barnes et al. 2020) in which planets are not spatially resolved; a host of physical processes are expressed together as a system of differential equations that are integrated over time to simulate a box-model planet alongside its potential neighbours and their host star. Barth et al. (2021) incorporated a simple 1D-mantle model into VPLanet, with which they suggest that mantle tidal heating could sustain the early magma oceans within the TRAPPIST-1 planets for 100s of Myr (c.f. Schaefer et al. 2016). The PACMAN evolution code has been applied to Venus (Krissansen-Totton et al. 2021) and the TRAPPIST-1 planets (Krissansen-Totton 2023) to map potential present and historical oxygen budgets against formation pathways, leveraging isotopic fractionation of Ar and He by escape. With PACMAN, Krissansen-Totton et al. (2024) showed that numerical models can capture the transition from a primary atmosphere towards a volatile 'secondary' atmosphere, yielding large surface water inventories ($\gtrsim 7\times$ Earth's oceans) and conditions potentially compatible with life. These models assume atmospheric compositions of H_2O and its atoms, with the occasional inclusion of CO_2 on the basis of its infrared absorption properties.

Other examples of planetary evolution models are described by Nikolaou et al. (2019), Katyal et al. (2020), Herath et al. (2024), and Sahu et al. (2025). Prior to the work in this thesis, the most comprehensive planetary evolution model was that of Lichtenberg et al. (2021), who considered CHNO volatile atmospheres formed on Earth-sized planets, with a comprehensive interior dynamics code. Lichtenberg et al. highlighted the importance of atmospheric composition, set by outgassing, in controlling the sequence of magma ocean crystallisation. Their radiative transfer calculations showed that observable spectral features may be linked to planetary interior properties through their physical interactions (see also Piette et al. 2023; Seidler et al. 2024).

Some recent works have considered more diverse elemental mixtures shaped by escape processes alongside magma ocean outgassing, although not self-consistently with the thermal evolution (e.g. Bower et al. 2025; Cherubim et al. 2025; Heng et al. 2025; Zilinskas et al. 2025). These studies have also highlighted the potential for exoplanets with more exotic atmospheric compositions such as 'helium worlds' (Lammer et al. 2025). Cherubim et al. (2025) also show that there may exist a gradient of planetary oxidation states across the radius valley, where photoevaporatively-produced super-Earths are more oxidised than their sub-Neptune counterparts due to the removal of hydrogen atoms.

1.3.3 Retrieval methods and static-structure calculations

Comparing models to measurements is fundamental to science. In astronomy, one approach has been to use complex physically representative models (e.g. MESA and PHOENIX) in a 'grid-search' (Allard and Hauschildt 1995; Paxton et al. 2011; Goyal et al. 2017). In a grid-search, we define some parameter space and construct a multidimensional grid of points in which we sample every combination of the desired parameters. A 'forward model' is then run at each grid point so that we can compare its predictions against some observations (Barstow and Heng 2020). Grid-searches can be inefficient because the number of grid points N scales rapidly with the dimensionality of the problem. With n samples in d dimensions, the grid size scales as $N = n^d$, which limits the number of parameters that can be easily explored. For example, the PHOENIX stellar models are tabulated on only four axes due to the expensive nature of the model (Husser et al. 2013).

Since Madhusudhan and Seager (2009) it has been common to instead use statistical 'retrieval' methods to infer planetary parameters (Barstow and Heng 2020). These methods use Bayesian statistics to carefully sample a higher-dimensional parameter space, eventually converging upon a region which best fits some observation (Aigrain and Foreman-Mackey 2023). However, these methods require that the forward model used in the retrieval be fast, since the result of each model evaluation is necessary for determining the next iteration of the retrieval process (Madhusudhan 2018). A popular approach has been to use iterative Monte-Carlo Markov Chain algorithms (Foreman-Mackey et al. 2013), although Nested Sampling methods have been applied to address some of the weakness of MCMC algorithms (Skilling 2006; Ashton et al. 2022). The iterative nature of retrieval methods is a weakness which may be mitigated by using simplified, highly parametrised, forward models. An example of this is a retrieval based on 'free chemistry', where atmospheric chemical abundances are inferred as free parameters without a complete consideration of the natural feasibility of a potential best-fitting solution. Retrievals with parametrised forward models may result in multiple degenerate scenarios to explain a given observation; infamously the degeneracy between high metallicity compositions and low-pressure aerosols (Wakeford and Sing 2015; Mai and Line 2019; Barstow 2020).

Rather than directly considering the time-evolution of planets, steady state equilibrium models have seen widespread application in the literature. These steady state models include static 'structure models' which calculate planetary temperature-, density-, and pressure-profiles as a function of radius by solving a system of equations defined by hydrostatic equilibrium, mass conservation, and energy transport[9] (Valencia et al. 2007; Haldemann et al. 2024; Gkouvelis et al. 2025; Werlen et al. 2025). Neglecting time-evolution allows obtaining a solution for planetary composition and structure for a given mass and bulk-composition such as those from radial velocity and transit measurements. These models provide computational efficiency, allowing them to be readily applied through statistical retrieval frameworks (Barstow et al. 2020; Haldemann et al. 2024). Equilibrium chemistry and volatile solubility is readily incorporated (Kite et al. 2016; Schlichting and Young 2022) into these equilibrium models, allowing atmospheric and interior composition to be obtained self-consistently with their structure. Since these models have no notion of planetary evolution, they cannot represent time-dependent processes (e.g. escape; Krissansen-Totton et al. 2018) and the hysteresis that is likely important to these complex systems (Zahnle et al. 2015; Lichtenberg 2021; Turbet et al. 2023).

---

[9] Usually defined by an adiabatic, radiative, or conductive temperature profile.

1.4 Targeted science questions

In this thesis, I aim to resolve the important mechanisms involved in setting rocky planet evolution, and to describe particular evolutionary pathways which link the past states of exoplanets to their observables. To do this, I will develop numerical tools that address some of the key modelling deficiencies within the prior literature, with a particular focus on the atmospheric physics. Such numerical models are the most promising approach for resolving the unknowns of planetary evolution (Lichtenberg and Miguel 2025). A close comparison of theoretical modelling and actualised observations of (exo)planets is central to understanding how planets change over time, and the diversity of environments which may exist at the present day. By making these comparisons, we can identify the important physical processes which secularly shape planets and their present observable characteristics. For example: the timing of the formation of Earth's oceans and the origin of life is strongly bounded by the cooling of Earth from its initially hot state (Hamano et al. 2013). Similarly: the atmospheric conditions which arose from early thermochemical evolution and geochemical cycling are poorly constrained, but understanding this environment is critical for setting the origin of life. Gaps in knowledge exemplified on Earth also apply to extra-terrestrial contexts (Madhusudhan et al. 2016).

A first-order modelling assumption highlighted in Section 1.3.2 is to simplify the assumed atmospheric compositions to a single component, or to a binary mixture. Boer et al. (2025) recently showed that the runaway greenhouse is not a universally determining factor in controlling the cooling of young planets, because H_2O-poor secondary atmospheres may be readily generated. Only Lichtenberg et al. (2021) explicitly considered a diverse range of gas mixtures in controlling early planetary evolution, although their modelling was also limited to simplified atmospheric structures and Earth-sized planets. The first investigation undertaken in this thesis is to test how a range of atmospheric compositions and radiation environments shape early planetary-scale cooling. Chapter 2 introduces a modular numerical framework for simulating rocky planet evolution in general. I use a volatile outgassing model to self-consistently calculate atmosphere compositions for a range of redox states and post-accretion scenarios. Poly-component gas mixtures and spectroscopic radiative transfer raises the potential for different evolutionary pathways compared to those previously considered, accessible by accounting for the unique radiative properties of different volatile gases (Chen et al. 2011), and the strong coupling between atmospheres and underlying interiors (Wordsworth and Kreidberg 2022; Acuna et al. 2023). I apply this framework to Earth-sized planets, discuss the role of volatile chemistry and solubility on controlling atmospheric composition, and study the impact of atmospheric blanketing on their thermal evolution, to test which cases solidify and which may retain permanent magma oceans.

The planetary bodies in the Solar System with thick atmospheres broadly exhibit deep convective regions with radiative regions aloft (e.g. Earth, Titan, Jupiter, Saturn; Robinson and Catling 2014). It is convenient to adopt this atmospheric configuration, as it permits an analytic prescription of a planet's temperature profile. As such, deep tropospheres extending upwards from rocky surfaces have been broadly adopted in magma ocean planetary evolution models, with a some also considering fully-isothermal atmospheres (e.g. Abe and Matsui 1986; Elkins-Tanton 2008; Kopparapu et al. 2013; Lebrun et al. 2013; Hamano et al. 2015; Schaefer et al. 2016; Lehmer and Catling 2017; Salvador et al. 2017; Boukrouche et al. 2021; Lichtenberg et al. 2021; Misener and Schlichting 2021; Krissansen-Totton et al. 2024). However, atmospheres may not always be convective. The Sun's temperature structure has the opposite configuration: its outer layer comprises a convective zone (giving rise to observable cells – 'granules') while its deeper regions are fully radiative (Miesch 2005; Beeck et al. 2013). The shear dynamics occurring at the interface between the Sun's convective zone and radiative core are central to controlling its magnetic dynamo (Parker 1993), highlighting the potential for deep radiative regions and that we may expect interactions with related physical processes. Of course, one important difference being that stars derive their own source of energy from fusion, while older planets *primarily* derive theirs by absorbing stellar radiation. So, what about young, cooling planets with hot interiors? It is known for giant (exo)planets and brown dwarfs that the presence of deep convection depends on their internal heat production (Guillot 2010; Parmentier et al. 2015; Goyal et al. 2017). However, modelling and observations of Uranus also point to deep stable layers where convection is inhibited by a vertical gradient in gas composition (Scheibe et al. 2021). Earth's own atmosphere is largely convectively stable, and especially so at high latitudes where radiative-advective balance sets the energy budget (Cronin and Jansen 2016). We must therefore also consider the potential for deep radiative regions in the atmospheres of rocky exoplanets, which has been recently suggested (Selsis et al. 2023) to occur in the simplifying case of pure-steam compositions.

Chapter 3 addresses the potential role of atmospheric convective stability by developing a new atmosphere model and incorporating it into my wider modelling framework. I consider a range of gas compositions to test the conditions in which outgassed volatile atmospheres may be convective. I discuss the implications of convective shutdown, and also search for observational markers of magma ocean redox state which may be leveraged by emission spectroscopy (Katyal et al. 2020).

Atmospheric convection is typically powered by the absorption of stellar radiation, but it may also be driven by heat released within the interior of a planet. Such is the case for the atmospheres of Jupiter and Saturn (Guillot 1999; Vazan et al. 2016). Tidal interactions represent another potential source of internal heating. Alongside the evidence for substantial tidal heating on Io (Peale et al. 1979; Hay et al. 2020) and suggestions for the early Earth (Zahnle et al. 2015), there have recently been several calculations of exoplanetary tidal heating (Henning et al. 2009; Seligman et al. 2024; Farhat et al. 2025). However, it should be noted that the tidal heat fluxes estimated by Seligman et al. (2024) and Farhat et al. (2025) are simply 'treated as an extra luminosity source' alongside stellar irradiation, despite indications from Zahnle et al. (2015) that atmosphere-interior processes strongly shape the behaviours of tidal effects. While neglecting the probable presence of atmospheres, Herath et al. (2024) found that tidal heating of their mantles may efficiently maintain night-side magma oceans on some rocky exoplanets. The coupled behaviour of interior-atmosphere interactions, when shaped by tidal heating, has not yet been directly tackled in the literature.

I address this gap in Chapter 4 by including orbital eccentricity-driven tidal interactions within my modelling framework. Focussing on the L 98-59 system, I simulate the early evolution of three rocky exoplanets while self-consistently accounting for heating of their interiors. I test whether feedback between tides, mantle rheology, and atmospheric blanketing can keep planets permanently molten, and whether tides can indirectly drive atmospheric convection. To test the robustness of these behaviours, I compare physically-informed viscoelastic tidal heating models to a heuristic semi-analytic description.

We know that escape processes shape planets over long timescales (Brain et al. 2016). This is exemplified by the radius valley between the sub-Neptune/super-Earth populations, for which photoevaporative hydrodynamic escape may be responsible (Owen and Wu 2017). It is therefore necessary to account for escape processes when making direct comparisons between theoretical calculations and present-day measurements of exoplanets. However, previous modelling on escape has generally been limited to low-metallicity atmospheres (Lopez and Fortney 2014; Lehmer and Catling 2017; Kubyshkina et al. 2020; Misener and Schlichting 2021) or volatile-rich atmospheres with simplified structures (Wordsworth and Pierrehumbert 2013; Krissansen-Totton et al. 2024; Rogers 2025). As yet, no previous works (which make direct comparisons with observations) have simultaneously considered escape processes acting alongside magma ocean evolution while also making a comprehensively self-consistent treatment of atmospheric structure and climate.

Chapter 5 studies the exoplanet L 98-59 d in detail. With the introduction of atmospheric escape into my modelling, I simulate the complete lifetime of L 98-59 d while considering a range of potential post-formation scenarios. I use a grid-search approach to compare my theoretical predictions against recent observations of this planet. I test whether the canonical water-world and gas-dwarf scenarios are consistent with the physics and the observational constraints, and whether photochemical processes are necessary to explain the transmission features of SO_2 indicated by recent JWST observations of this planet.

My concluding chapter (6) reviews the implications of my results and potential future directions arising from the work presented in this thesis.

Chapter 2

Factors regulating early magma ocean evolution

This chapter explores the diversity of atmospheric compositions which arise from magma ocean outgassing and their control over their planet's thermal evolution. For this purpose, I introduce a flexible numerical modelling framework designed to simulate the coupled interior-atmosphere evolution of rocky (exo)planets. Here, the operation of the framework's individual components is described in detail. It is then validated against established behaviours from the literature. My simulations show that the atmospheric composition in inherently linked to bulk planetary parameters and strongly controls planetary thermal evolution. I also assess the potential for convective stability in outgassed atmospheres.

A portion of the research presented in this chapter is published in the Journal of Geophysical Research: Planets (Nicholls et al. 2024). However, the modelling methodology described in Section 2.2 is afforded greater detail in this thesis, and Section 2.3.1 is not included in the published article.

2.1 Introduction

Current models of planetary evolution suffer from a range of potential over-simplifications and deficiencies, which limits the validity and scope of their application. In this chapter, I review the important physical processes involved in setting the early evolution of rocky planets. I introduce a modular computational framework for simulating planetary evolution, and detail the implementation of the physics within my model. This framework is then applied to simulate a range of evolutionary pathways for an Earth-sized planet, which are then compared against previous modelling results in the literature. I consider several parameters which are expected to vary depending on the outcome of planetary accretion and core formation, and study which resultant evolutionary scenarios an Earth-sized planet may follow, with the consideration of this expected diversity in volatile inventories and redox states.

2.2 Modelling framework

George Box famously put that ‘all models are wrong, but some are useful’. He further elaborated that ‘since all models are wrong the scientist cannot obtain a ‘correct’ one by excessive elaboration’ so ‘the scientist must be alert to what is importantly wrong’ (Box 1976). We must bear this in mind when developing a tool that claims to self-consistently treat the multiple and complex physical processes of planetary evolution, which inherently span orders of magnitude across spatial- and time-scales. I therefore leverage a modular and hierarchical modelling approach.

PROTEUS[1] is a modular framework for simulating the time evolution of rocky (exo)planets. This new modelling framework is designed to be flexible, in a sense reflecting the broad diversity of planetary conditions that we have already discovered, with the view of being updated to incorporate additional physics as the need arises. This approach stands in contrast to otherwise monolithic models in the literature; e.g. GOOEY (Schaefer et al. 2016) and PACMAN (Krissansen-Totton et al. 2024). Furthermore, PROTEUS is free and open-source, which permits external scrutiny of its workings and ensures that conclusions derived from its calculations do reasonably reflect the assumptions involved. PROTEUS may be considered a ‘re-write’ of the Python codebase developed for Lichtenberg et al. (2021) – which itself was inspired by Elkins-Tanton (2008) – although PROTEUS now exceeds both of these previous models in physicality, robustness, and usability.

Although PROTEUS aims to treat the problem of *planetary* evolution, it must necessarily also handle external processes which act upon the planet (e.g. tides). I therefore solve for the combined physical system of a planet, its interactions with neighbouring planets, its orbital mechanics, and the evolution of its host star. The planet itself is conceptually subdivided into a volatile *atmosphere* component, which sits above an *interior* component containing a silicate mantle and metallic core. Figure 2.1 schematically illustrates the problem under consideration and its algorithmic solution, depicting the most important physical processes. The schematic flowchart in Figure 2.1b outlines the main time-stepping loop within PROTEUS, which connects all the modules together and allows them to causally interact. In subdividing the system, PROTEUS acts to facilitate

---

[1] `https://github.com/FormingWorlds/PROTEUS`

communication between individual software *modules*, which each implement a model for a specific part of the overall physical system. For example: the `interior` module of PROTEUS simulates the time-evolution of the planet's mantle and core, their cooling, and potential solidification. Conceptually, modules are slots which are filled by specific implementations 'models'. PROTEUS and the individual models all benefit from software unit tests, ensuring that the codes behave appropriately and to prevent systematic errors from being introduced in the course of continuous development (Whittaker 2000).

Table 2.1 outlines the modules within PROTEUS in its current formulation and the model implementations currently available for each module. Implementations marked with a dagger† are derived from previously-existing codes, although these have all been modified for the purposes of inter-compatibility. Modularity makes PROTEUS more robust, as each model can be independently validated and tested. Alongside the available documentation, modularity also makes the tool more accessible to new users and critics. Hierarchical modelling allows an inter-comparison of simple and complex models, taking advantage of the easy comprehension of the Simple to diagnose and validate the qualitative behaviour of the Complex. Below, I start by describing the role of each module within the framework and the simplified 'dummy' implementations of each. I emphasise that the dummy modules are not designed to make quantitatively meaningful calculations of planetary evolution, but only to qualitatively capture end-member behaviours and set expectations from the physically-representative implementations. Support for relatively simplified models in PROTEUS, alongside more comprehensive treatments, will eventually allow the application of PROTEUS as a forward-model within a retrieval approach while still retaining a rigorous treatment of the physics.

Note that the following regimes are currently outside the scope of my modelling: brown dwarves, gas giants, protoplanetary disks, circumplanetary disks, asteroids, moons, geochemical cycling and volcanism, aerosolised hazes, and life.

2.2.1 Module roles

I now outline the specific role that each module plays within the framework.

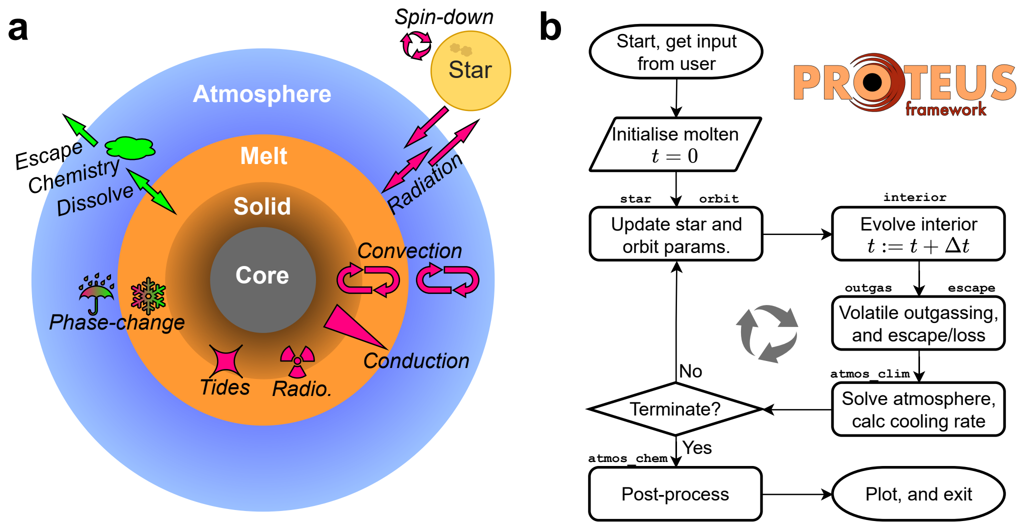

Figure 2.1: Schematic of the problem modelled in this thesis. Left: cartoon of the assumed planet structure. The most important energy (pink) and mass (green) transport processes are indicated. **Right**: flowchart outlining the time-integration simulation loop within PROTEUS, with module placement indicated by monospaced text.

Module	Model	Thesis reference	Primary literature reference
`atmos_clim`	AGNI	Section 3.2	Nicholls et al. (2025c)
	JANUS†	Section 2.2.6	Graham et al. (2021)
	dummy	Section 2.2.2	Nicholls et al. (2024)
`atmos_chem`	VULCAN†	Section 5.4	Tsai et al. (2021a)
`star`	MORS†	Section 2.2.10	Johnstone et al. (2021)
	dummy	Section 2.2.2	Nicholls et al. (2024)
`escape`	ZEPHYRUS	Section 5.3	Postolec et al. (Submitted)
	dummy	Section 5.3	Nicholls et al. (2026)
`outgas`	CALLIOPE	Section 2.2.4	Nicholls et al. (2024)
	Atmodeller	—	Bower et al. (2025)
`interior`	SPIDER†	Section 2.2.5	Bower et al. (2018)
	Aragog	—	Bower et al. (In prep.)
	dummy	Section 2.2.2	Nicholls et al. (2025a)
`tide`	LovePy†	Section 4.4	Hay and Matsuyama (2019)
	dummy	Section 2.2.2	Nicholls et al. (2025a)

Table 2.1: PROTEUS modules and their various model implementations. The role of each module can be fulfilled by several possible models, each with their own advantages and limitations. This table will expand as PROTEUS continues to develop in the years to come.

The `atmos_clim` module must calculate the surface temperature T_s, surface and top-of-atmosphere (TOA) energy fluxes, bulk observable metrics, and bond albedo. These are calculated at each point in time subject to a given top-of-mantle temperature T_m, instellation F^{ins}, atmospheric composition, surface pressure P_s, and surface reflectivity. In all cases, atmospheric energy fluxes are split into upwelling and downwelling components, as well as shortwave (SW) and longwave (LW) components. These components of the radiation field may spectroscopically overlap, so these terms refer to the different processes which emit and absorb radiation rather than a specific spectral domain. Broadly speaking, however, SW radiation encompasses X-ray and UV and optical wavelengths, while LW radiation encompasses the optical and infrared.

The top-of-mantle temperature T_m calculated by the `interior` module provides a lower-boundary condition for the `atmos_clim` module. The outgoing flux F^{atm} calculated by `atmos_clim` then provides an upper-boundary condition for the `interior` module, effectively setting the rate at which energy is removed from the planet. It is thought that magma oceans are covered in a thin conductive boundary layer (CBL), which limits heat transport through the surface (Solomatov 2007; Lebrun et al. 2013; Schaefer et al. 2016; Lichtenberg et al. 2021). This conductive boundary layer is analogous to those which form on terrestrial lava ponds, but here in the context of a magma ocean occurring on a global or hemispherical scale. I parametrise this boundary layer using Fourier's law,

$$F^{\text{CBL}} = \kappa_c (T_m - T_s)/d_c \tag{2.1}$$

assuming a constant thermal conductivity $\kappa_c = 2\,\text{W}\,\text{K}^{-1}\,\text{m}^{-1}$ and thickness $d_c = 1$ cm. Then, T_s is less than T_m for a net positive conductive heat flux F^{CBL}. Equation 2.1 is used to determine the temperature at the base of the atmosphere T_s by ensuring that F^{CBL} is equal to the net flux F^{atm} for a given top-of-mantle temperature T_m. Equation 2.1 is adopted throughout this thesis because it conserves energy between the planet's interior and atmosphere (by construction) and permits steep temperature gradients across a thin surface boundary layer which is not readily resolved by models. Several previous works have applied a formulation for parametrising the physics of the surface boundary layer (Elkins-Tanton 2008; Hamano et al. 2015; Schaefer et al. 2016; Bower et al. 2019).

In this thesis, I keep d_c and κ_c fixed at the values above. In reality, we might expect

d_c to increase in thickness as a primordial magma ocean cools and mantle convection becomes less vigorous. It is difficult to quantify d_c because the CBL is affected by multiple dynamical and thermal effects that are not resolved in my simulations. For example, shear stresses from fluid motions against the CBL could break it up – analogous to mobile versus stagnant tectonic regimes (Meier et al. 2023; Tackley 2023). Substantial zonal variations in the CBL thickness are also a reasonable expectation in tidally-locked scenarios. The conductivity κ_c would depend on the composition of the boundary layer, which may contain substantial amounts of graphite (Sossi et al. 2020; Bower et al. 2025).

The `interior` module drives the time-evolution of the planet's interior, stepping over a time interval Δt during each PROTEUS iteration. By the end of each iteration, it calculates a new top-of-mantle temperature T_m and mantle melt fraction Φ subject to the flux boundary condition F^{atm}.

At the start of each new iteration, the `star` module updates the host star's bolometric luminosity $L_\star$, emission spectrum, rotation rate, and radius. Similarly, the `orbit` module updates the orbital semi-major axis a, period p, eccentricity e, and the corresponding average planet-star distance d. It is also responsible for handing tidal heating, calculating the power that is instantaneously generated within the planet's interior based on information from the `star` about its orbital parameters and `interior` module about its mantle properties. These stellar and orbital quantities are evolved during the course of planetary evolution assuming a fixed stellar mass $M_\star$ and some initial age t_{ini}, which represents the age of the star at the point when a simulation is initialised.

Atmospheric escape processes act to remove volatiles from the planet over time, depending primarily on the atmospheric structure and the amount of ionising stellar radiation (X-ray plus UV, 'XUV') received by the planet. The `escape` module determines the escape rate [$\mathrm{kg\,s^{-1}}$] of atoms based on information from the `star` and `atmos_clim` modules, removing some mass of volatile elements (CHNOS) from the planet during the time-interval Δt in each time-step. With an updated inventory of volatiles, the `outgas` module calculates the instantaneous interior-atmosphere partitioning of CHNOS elements at each point in time, assuming some initial inventory of elements set by the user.

I emphasise that only the `interior` and `star` modules have an explicit notion of time-evolution. All other modules are applied at equilibrium, such that the quantities calculated by these modules are effectively updated instantaneously at each PROTEUS time-step. I am assuming that the physical processes handled by these equilibrium modules are able to reach steady-state on timescales shorter than Δt, governed by the interior and stellar evolution models. In each run, Δt is initially set to a small value $\sim 10^2$ yr, but increases to $\sim 10^5$ or $\sim 10^6$ yr as the simulation progresses.

2.2.2 Dummy modules

I now describe the simplified dummy implementations for the different modules, starting with `atmos_clim`. This dummy model which does not vertically resolve the atmosphere and instead calculates 0-dimensional energy fluxes. The net upward-directed radiative flux is then expressed as

$$F^{\text{atm}} = F^{\uparrow L} + F^{\uparrow S} - F^{\downarrow L} - F^{\downarrow S} \tag{2.2}$$

while at the top of the atmosphere, the downwelling shortwave $F^{\downarrow S}$ is calculated as

$$F^{\downarrow S} = F^{\text{ins}} f_s \cos\theta_z \tag{2.3}$$

where the *zenith angle* θ_z represents the angle of the modelled atmospheric column relative to the zenith, and f_s is a scale factor accounting for the fact that only one hemisphere is illuminated by the star at a given point in time. Together, θ_z and f_s capture the radiative character of the *whole* atmosphere, given that we are treating the (fundamentally 3-dimensional) planet with a lower-dimensionality model. A substellar column would be represented by $\theta_z = 0$ and $f_s = 0$; see Section 2.2.7. The instellation F^{ins} is calculated from the bolometric stellar luminosity $L_\star$, scaled to the time-average separation d between the planet and its host:

$$d = a(1 + e^2/2) \tag{2.4}$$

Large orbital eccentricities e act to increase the average planet-star separation, and correspond to a decreased instellation F^{ins}, compared to a circular orbit with the same semi-major axis a. A derivation of Equation 2.4 may be found in Appendix B.

The shortwave fluxes absorbed and reflected by the surface are

$$F^{\downarrow S} = F^{\text{ins}} \cdot (1 - \alpha_s) \tag{2.5}$$

$$F^{\uparrow S} = F^{\text{ins}} \cdot \alpha_s \tag{2.6}$$

where α_s is the specular albedo of the surface material. The planet's shortwave albedo is then $\alpha_b = F^{\uparrow S}/F^{\downarrow S}$. Here, for the dummy atmosphere model, the outgoing longwave flux is modelled as

$$F^{\uparrow L} = \sigma(T_s - \gamma T_s)^4 \tag{2.7}$$

where σ is the Stefan-Boltzmann constant (such that the surface radiates as a blackbody). The atmospheric radiative effects are parametrised by γ, which for $\gamma = 1$ acts to set the outgoing longwave component to zero, and for $\gamma = 0$ represents a transparent atmosphere scenario in which the surface radiates directly to space. For this dummy model, the downward-longwave flux component $F^{\downarrow L}$ is zero. Equations 2.6 and 2.7 are used to calculate the net energy flux F^{atm} via equation 2.2, which is solved-for alongside equation 2.1 for a given T_m.

Like its atmospheric counterpart, the *dummy* `interior` module does not spatially resolve the interior of the planet. It simply applies conservation of energy to evolve the mantle temperature through each iteration:

$$T_m(t + \Delta t) = T_m(t) + 4\pi R_{\text{int}}^2 \frac{F^{\text{atm}} - F^{\text{tide}} - F^{\text{radio}}}{c_m M_m + c_c M_c} \Delta t \tag{2.8}$$

where c_m and c_c are the specific heat capacities of the mantle and core (1792 and 880 J K^{-1} kg^{-1} respectively, for an Earth-like composition; Lodders and Fegley 1998; Bower et al. 2018), while M_m and M_c are their masses. R_{int} is the radius of the planet's surface. The mantle melt fraction is a monotonic function of surface temperature:

$$\Phi = \begin{cases} 1 & \text{if } T_m > T_{\text{lq}} \\ (T_m - T_{\text{sol}})/(T_{\text{liq}} - T_{\text{sol}}) & \text{if } T_{\text{liq}} \geq T_m \geq T_{\text{sol}} \\ 0 & \text{if } T_{\text{sol}} > T_m \end{cases} \tag{2.9}$$

where T_{liq} and T_{sol} are representative liquidus and solidus temperatures (2700 and 1700 K respectively; Wolf and Bower (2018)). The mantle and core masses, and the radius of the planet's interior R_{int}, are calculated such that the interior structure satisfies the core radius fraction r_c and total planet mass M_p as provided as input parameters by the user; i.e. $M_p = M_{\text{volatiles}} + M_c + M_m$. In the case of this dummy interior model, the core and mantle densities are fixed such that Earth's structure is reproduced. However, while M_p and r_c remain as fixed input parameters, a realistic structure calculation is applied in my main simulations (see Section 2.2.5).

The *dummy* `star` module treats the star as a blackbody emitter with a fixed effective temperature and radius. Its luminosity is then set by the Stefan-Boltzmann law: $L_\star = 4\pi R_\star^2 \sigma T_{\text{eff}}^4$. The dummy `escape` and `orbit` modules simply apply a constant bulk escape rate to the planet's total inventory of volatile elements and use fixed orbital parameters provided by the user. PROTEUS does not currently implement a dummy outgassing module, but the physical outgassing model described in the next section can be optionally simplified to consider single-gas compositions.

2.2.3 Termination criteria

PROTEUS currently has seven termination criteria which are enabled by the user as appropriate. Calculations are performed up to a non-zero numerical precision, primarily from floating-point arithmetic, so these criteria are expressed as inequalities with relative and absolute tolerances. Each criterion is individually sufficient for stopping the simulation.

The **solidification** criterion is triggered when the planet's mantle has effectively solidified: $\Phi \leq \Phi_{\text{crit}}$, where the absolute tolerance Φ_{crit} is typically $\sim 1\%$. This criterion can bracket the modelling regime to partially- and fully-molten planets.

The **energy balance** criterion represents an *energetic* steady state, where the net energy flux F^{atm} carried to space by the atmosphere balances the energy released within the planet's interior: $|F^{\text{atm}}| \leq \varepsilon_{\text{rtol}}(F^{\text{tide}} + F^{\text{radio}}) + \varepsilon_{\text{atol}}$. Typical values for these tolerances are $\varepsilon_{\text{rtol}} = 0.2$ and $\varepsilon_{\text{atol}} = 1\ \text{mW}\,\text{m}^{-2}$. In a case without tidal or radiogenic heating, this represents radiative equilibrium. In the absence of atmospheric escape or substantial stellar/orbital evolution, this then also represents the final steady state of the planet.

The **desiccation** criterion tests when the planet's atmosphere has been removed by escape, proxied by the total surface pressure: $p_s \leq p_{\text{crit}}$. PROTEUS does not currently account for volatiles within the solid-phase of the mantle or within the metallic core, so this represents the removal of the planet's total volatile inventory.

The **time** criterion stops the simulation when a total integration time has been attained: $t \geq t_{\text{max}}$. This acts to stop the simulated evolution at an age of $t_{\text{max}} + t_{\text{ini}}$, allowing comparison to be made against observed planets with observationally-derived age estimates.

The **breakup** criterion stops the simulation when the planet's orbital separation d moves interior to the star's Roche limit: $d \leq R_p (2M_\star / M_p)^{1/3}$. This represents when tidal forces generated across the planet exceed the binding force of gravity.

Two final criteria are not physically motivated: the **iters** criterion is triggered when a set number of iterations have been performed, and the **keepalive** criterion is triggered when the user manually requests that the model terminate.

2.2.4 Volatile partitioning

Volatile elements contained within a planet can speciate into various compounds and partition between the different reservoirs of the planet. For a given mass [kg] of atoms of each element contained across the whole planet, we must calculate how these atoms partition and into which form they speciate to determine the composition of the atmosphere. For this I introduce CALLIOPE[2], an equilibrium outgassing model which calculates atmospheric gas partial pressures from whole-planet elemental mass inventories. This code is based on the scheme described by Bower et al. (2022) and Sossi et al. (2023). Independently of PROTEUS, this code has been applied to the case of K2-18 b (Shorttle et al. 2024). Since I neglect the explicit partitioning of volatiles into the planet's metallic core and into the entirely-solid phase of its mantle in this thesis, there are only two reservoirs to consider: the semi-molten mantle and the atmosphere. There are then two key pieces of physics occurring at the atmosphere-mantle interface which we must consider: volatile dissolution into the melt and gas-phase thermochemistry.

Dissolving gases into molten silicate is somewhat analogous to dissolving gases into water. Here, we may draw an analogy with ammonia dissolving into the ocean ($NH_3(g) \rightleftharpoons NH_3(aq)$). The gas phase does not necessarily correspond to the formation of a single solvated phase. In this example case, dissolved ammonia can react with the water ($NH_3 + H_2O \rightleftharpoons NH_4^+ + OH^-$) to form ammonium anions. At the same time, we must also consider that the gaseous phase (here $NH_3(g)$) can react with other atmosphere components within a complex *network* of chemical reactions in the atmosphere. For example,

---

[2] `https://github.com/FormingWorlds/CALLIOPE`

reactions between NH_3 and H_2O in Earth's atmosphere plays a key role in the nucleation of cloud droplets (Renard et al. 2004), while the non-detection of NH_3 in the atmosphere of K2-18 b has been used to suggest the presence of a surface water ocean acting as a solubility 'sink' (Tsai et al. 2021b; Yu et al. 2021; Luu et al. 2024).

CALLIOPE solves a system of equations defined by volatile dissolution (heterogeneous gas-solute reactions) and equilibrium chemistry (homogeneous gas-gas reactions). Conservation of mass requires that the mass of each volatile element e in the atmosphere and in the melt phase must sum to the total amount of e in the whole planet:

$$M_e^{\text{tot}} = M_e^{\text{atm}} + M_e^{\text{liq}} \tag{2.10}$$

I aim to solve for the partial surface pressures of the gas species such that Equation 2.10 is satisfied for HCNS. The total amount of oxygen is not tracked in this manner, as I instead fix the oxygen fugacity at the surface relative to the iron-wüstite buffer, which depends on temperature. Fixing the oxygen fugacity in this way implicitly captures the disproportionation of Fe, assuming that core segregation has completed before $t = t_{\text{init}}$ (Lichtenberg et al. 2021; Sossi et al. 2023). I find that the total amount of O in the system does not significantly change throughout each simulation.

For the atmosphere (denoted 'atm') and magma ocean ('liq') reservoirs, I obtain the total mass of each element e by summing over all species j containing e. Assuming a compositionally homogeneous gas phase interacting with a magma ocean, the mass of each species j in comprising the atmosphere can be determined from its partial surface pressure p_j via

$$M_j^{\text{atm}} = 4\pi R_{\text{int}}^2 \frac{p_j}{g} \frac{\mu_j}{\bar{\mu}} \tag{2.11}$$

where μ_j is the molar mass of j and $\bar{\mu}$ is the molar mass (or mean molecular weight, MMW) of the whole gas mixture (Bower et al. 2019). Chemical equilibrium is also applied to the gas phase, such that for a reversible reaction aA + bB $\rightleftharpoons$ cC + dD (lowercase letters are stoichiometric coefficients) we may ideally relate the partial pressures of species ABCD as:

$$(p_C)^c (p_D)^d = K_{\text{eq}} (p_A)^a (p_b)^b \tag{2.12}$$

Through Equation 2.12, the partial pressures of products C and D are calculated from reactants A and B.

The position of this homogeneous reaction at equilibrium is described by K_{eq}, which can also be related to the difference in free energy between the products and reactants,

$$K_{\text{eq}} = -\frac{\Delta G^\circ}{RT_m} = -\frac{G^\circ_{\text{products}} - G^\circ_{\text{reactants}}}{RT_m} \tag{2.13}$$

We can see that this equation explicitly depends on temperature T_m, but also implicitly because the species' free energy G° may have an empirically-derived temperature dependence.

To capture this behaviour, I apply the power law fit

$$\log_{10} K_{\text{eq}} = r_1/T_m - r_2 \tag{2.14}$$

to express the empirical nature of these reactions, taking r_1 and r_2 from the literature when available. Otherwise, I obtain G°_j from the JANAF database (Chase 1986), tabulate Equation 2.13 as a function of temperature, and then use a Levenberg-Marquard least-squares minimisation algorithm to determine the best-fitting values for r_1 and r_2 (Sections 3.4 and 5.4). Similarly, the amount of volatile elements in the magma ocean M_e^{liq} are calculated by summing over the corresponding solvated phases of each gas species j that contains e. The canonical relationship between dissolved and exsolved components is Henry's law, which may be expressed in this context as

$$M_j^{\text{liq}}/M_{\text{liq}} = \mathcal{H}_j p_j \tag{2.15}$$

where $M_{\text{liq}} = \Phi M_m$ is the total mass of molten silicate in the magma ocean, and $\mathcal{H}_j$ is the solubility constant for j. However, in CALLIOPE, I apply empirically-derived solubility relationships $M_e^{\text{liq}}(\vec{p}, \ldots)$ which capture non-ideal effects, dependency on oxygen fugacity, dependency on the refractory composition of the mantle itself, and also account for cases where a given gas species j maps to multiple solvated phases carrying volatile elements e. For brevity here, the specific solubility laws and equilibrium reactions used in CALLIOPE may be found in Appendix A. While we must note that these solubility laws are not fully-consistent with each other – since they were not necessarily derived using the same mineralogical compositions – they were all obtained using (ultra)mafic melts that have relatively low SiO_2 content comparable with Earth's mantle (Lodders and Fegley 1998; Schubert et al. 2001). Recently, Thompson et al. (2025) showed that hydrogen capacity[3] depends on the composition of the melt phase, especially through variations

---

[3] Here, 'capacity' refers to the ratio between the dissolved hydrogen content and the gas-phase

in SiO_2 content, so further experiments are required in order to fully understand how solubilities may vary based on melt composition.

In summary... The input quantities to the CALLIOPE outgassing model are the total amount of HCNS volatiles in the *bulk* planet, outgassing temperature T_m, surface gravity g, mantle mass M_m, mantle melt fraction Φ, mantle oxygen fugacity fO_2, solubility coefficients, and reaction coefficients. The output quantities are the volatile surface partial pressures, and the amount of atoms of each element in each reservoir. I solve for these quantities by invoking conservation of mass, applying a numerical root-finding method (`scipy.optimize.fsolve`) to determine the partial pressures which satisfy Equation 2.10 for a given set of M_e^{tot}.

In practice, I express the bulk elemental inventories M_e^{tot} with more intuitive quantities. For hydrogen, I use units of 'equivalent Earth oceans' (denoted [H]): $M_H^{\text{tot}} = 2\mu_H n_{\text{oc}}[\text{H}]$, where n_{oc} is the total number of moles of H_2O in Earth's surface water inventory ($\approx 7.68 \times 10^{22}$ mol; Clark (1982)). I primarily express the bulk inventory of C-N-S elements relative to that of hydrogen; e.g. $M_C^{\text{tot}} = [\text{C/H}] M_H^{\text{tot}}$. Formulating the amount of C-N-S in this manner is useful for exploring various *total* volatile budgets while keeping elemental (metallicity) ratios constant, in which case the total amount of volatile elements is proxied by M_H^{tot}. Alternatively, the abundances of CHNS elements may be expressed simply relative to the mass of the dry mantle; e.g. $M_H^{\text{tot}} = M_m[\text{H}_{\text{ppmw}}] \times 10^{-6}$.

It should be noted that Equation 2.12 is only strictly true for ideal conditions where Dalton's law is valid, since I have substituted species concentrations for partial pressures (McQuarrie and Simon 1997). Furthermore, for real mixtures, an exact treatment would express these reactions in terms of *activities* a_i rather than *concentrations* (or mole fractions χ_i), relating them through empirically-determined activity coefficients $\gamma_i = a_i/\chi_i$ (Sossi et al. 2023; Bower et al. 2025). The ideal gas regime takes the limit of $\gamma_i = 1$; deviation from non-ideality is expected at conditions within sub-Neptune size planets (Bower et al. 2025). Although Chapter 5 considers derivation from ideal equations of state in the context of atmospheric structure, I will assume ideal *outgassing* behaviour throughout this thesis.

In the magma ocean context there are processes for which we cannot draw a sim-

---

fugacity of H_2O.

ple analogy to the Earth climate system. Water and hydrogen can become miscible with the molten silicate at high temperatures ($\gtrsim 4000$ K) in the deep mantle, so rather than chemically dissolving into the melt it could form mixtures with volatile mass-fractions far exceeding the capacity of silicate as a solvent (Shen and Keppler 1997; Keppler and Bolfan-Casanova 2006; Kovacevic et al. 2022; Rogers et al. 2025). Similarly, pockets of melt intrusions trapped within the solid phase of the mantle – entrained during the process of solidification – could store volatiles deep within the planet alongside volatiles which are chemically bound within the solid-phase of the mantle itself (Hier-Majumder and Hirschmann 2017; Sim et al. 2024). Furthermore, precipitation of mineral pockets within the solidified phase could also trap volatiles in excess of the amount taken-up by chemical dissolution (Gehlen 1992). And finally, the planet's metallic core can store large amounts of volatile-bearing components (e.g. FeO, FeS; Dreibus and Palme 1996b; Dasgupta et al. 2009; Ebel 2011). We may therefore view my calculations of volatile interior-atmosphere partitioning as *conservative*; for a given amount of volatile atoms in the *bulk* planetary inventory, I probe the regime in which the planet's interior has a conservatively small capacity for storing volatile elements, by only considering their partitioning into the molten phase of the mantle (Dorn and Lichtenberg 2021; Huang and Dorn 2025).

2.2.5 Interior dynamics module

The interior component of the system contains the magma ocean and the core. It is nominally evolved using a previously-established 1D mantle dynamics model, SPIDER[4] (Bower et al. 2018; Bower et al. 2019; Bower et al. 2022). At each level of the planet's mantle with pressure p and specific entropy S [$\mathrm{J\,K^{-1}\,kg^{-1}}$], the melt fraction of the mantle material is calculated according to

$$\phi = \begin{cases} 1 & \text{if } S > S_l \\ (S - S_s)/(S_l - S_s) & \text{if } S_l \geq S \geq S_s \\ 0 & \text{if } S_s > S \end{cases} \tag{2.16}$$

where S_l and S_s are the specific entropies of the liquidus and solidus melting curves at pressure p. This prescription effectively treats the mantle material as a two-phase sys-

---

[4] `https://github.com/djbower/spider`

tem: either liquid or solid, or a mixture of the two phases. I do not consider spatial variations in elemental abundance throughout the mantle. Modelled properties of the solid and liquid phases, including their melting curves and equations of state, are interpolated internally in SPIDER using look-up data tables derived from high-pressure experiments and molecular dynamics simulations (Mosenfelder et al. 2009; Andrault et al. 2011; Wolf and Bower 2018). The resulting behaviour is constructed to be consistent with peridotite in the upper mantle limit and with chondritic material in the deep mantle high-p limit. These thermodynamic tables are validated for pressures up to $\sim$ 200 GPa (Spera et al. 2011b). The planet's mantle is treated as hydrostatic, such that the radius R_{int} is calculated from the total mantle mass M_m and core radius fraction r_c. The interior radius R_{int} is held constant throughout each simulation, since thermal contraction is known to have a minimal effect on the specific volume of silicate mantles because their density primarily depends on pressure (Unterborn and Panero 2019; Boley et al. 2023; Lichtenberg and Miguel 2025).

In my modelling, any dissolved volatiles do not directly interact with the silicate components. In reality, dissolved volatiles are known to 'depress' both the solidus and liquidus to lower entropies for a given pressure (Katz et al. 2003; Saracino et al. 2025), potentially making magma oceans more widespread than my modelling will generally predict. It should also be noted that these melting curves generally result in bottom-up crystallisation, but other crystallisation modes may be possible, resulting in basal magma oceans containing a segregated reservoir of dissolved volatiles (Labrosse et al. 2007; Bajgain et al. 2022). Additionally, entrainment of high-density FeO into deep melt layers may stabilise them against mixing with solidified regions, and thus yield basal magma oceans – representing a deep reservoir for sequestering volatiles – in some planets (Boukaré et al. 2022).

To evolve the interior of the planet over time, SPIDER solves for energy conservation at each layer i of the mantle,

$$\int_V \rho_i T_i \frac{\partial S_i}{\partial t} \,\mathrm{d}V = -\int_A F_i^{\mathrm{int}} \,\mathrm{d}A + \int_V \rho_i (H_i^{\mathrm{radio}} + H_i^{\mathrm{tide}}) \,\mathrm{d}V \tag{2.17}$$

where T is the temperature, ρ is the mass density, F^{int} is the net heat flux through each layer [$\mathrm{W\,m^{-2}}$], and H is the internal heat generation [$\mathrm{W\,kg^{-1}}$] from radioactive decay and tidal heating within each layer. As for other PROTEUS modules, positive fluxes are measured in the upward direction. In the mantle, the flux term F^{int} represents the sum of energy transport by convection F^{conv}, solid-liquid phase mixing (latent heat) F^{mix}, thermal conduction F^{cond}, and gravitational settling F^{grav}.

Heat from the radioactive decay of ^{40}K, ^{232}Th, ^{235}U, and ^{238}U is also included; the abundances of these radioisotopes are calculated by scaling measured concentrations for modern Earth ($t = 4.55$ Gyr) to the system's age t_{ini} at the start of the simulations (Turcotte and Schubert 2002; Ruedas 2017).

I will now briefly summarise the calculation of each term contributing to the net interior flux F^{int} at each layer of the mantle (Abe 1993; Abe 1997; Bower et al. 2019). The subscript for model layer i is left-out for brevity.

Convection is a fundamentally multidimensional and turbulent motion which occurs across a range of spatial- and time-scales in fluids (Shestakov et al. 2017). Mixing-length theory (MLT) is a parametrisation of such motion to a single 1D column model, with the important characteristic of providing the momentum- and heat-transport fluxes associated with convective turbulence (Prandtl 1925; Vitense 1953; Joyce and Tayar 2023). MLT has been successfully applied across the physical sciences (Chan and Sofia 1987) and is more thoroughly discussed in Chapter 3.2.1 in the context of planetary atmospheres. Since SPIDER uses entropy as the primary thermodynamic variable, MLT enables us to express the mantle convective heat flux as

$$F^{\text{conv}} = -\rho T \kappa_h (\partial S / \partial r), \tag{2.18}$$

where κ_h is the eddy diffusivity of the fluid. Here, I take $\kappa_h = u\lambda$, where u is the characteristic velocity of the flow (depending on its Reynolds number[5]) and λ is the assumed mixing length. The calculation of u switches between the inviscid and viscous regimes on either side of a critical Reynolds number (Abe 1997), but itself also depends on the entropy gradient $\partial S / \partial r$. The mixing length λ is calculated as the distance from the nearest thermal boundary layer (Bower et al. 2019).

The latent heat (mixing) contribution to the energy flux is calculated in SPIDER as

$$F^{\text{mix}} = -\rho T (S_l - S_s) \kappa_h \frac{\partial \phi}{\partial r} \tag{2.19}$$

---

[5] The Reynolds number is defined as the ratio of inertial and viscous forces.

which assumes that the melt undergoes a *fractional* mode of crystallisation, in which solid crystals formed by cooling of the melt phase become gravitationally separated rather than being (semi-)permanently entrained in the turbulent flow (Solomatov and Stevenson 1993a; Solomatov and Stevenson 1993b; Schaefer and Elkins-Tanton 2018). The F^{mix} term acts to transport heat energy downwards, partially offsetting the other energy flux terms' contributions to the interior energy balance.

Gravitational separation of the melt and solid phases realises their gravitational potential energy as a net heat flux. The amount of heat transported depends on the nature of the separating flow, and the dominant phase in at each region of the planet's mantle. The melt can permeate through a solid matrix in regions where the mantle is primarily solidified, while solid crystals can settle-out of the melt in primarily molten regions. The highly complex process of gravitational separation and percolation occurs on an unresolved sub-grid scale, so it is parametrised in SPIDER as

$$F^{\text{grav}} = a^2 g \rho T \frac{[\rho_l - \rho_s] \cdot [S_l - S_s]}{\eta} \zeta(\phi) \tag{2.20}$$

where $a = 10\,\text{cm}$ is the characteristic grain size, η is the dynamic viscosity, and ζ is a 'flow mechanism factor' representing the unresolved dynamics of the phase separation which depends on the local melt fraction (see Abe 1997; Bower et al. 2018). The F^{grav} term can also be negative-valued in cases where the density of melt is larger than the density of solid due to its compressibility at high pressures, but is only non-zero in the mixed phase region of the mantle.

Throughout this thesis, I use a single fixed value for the grain size a. However, the literature has established that our choice for a will strongly influence modelled magma ocean crystallisation behaviours (Abe 1997; Lichtenberg et al. 2019a; Lichtenberg 2021). Smaller grains may can remain entrained in the liquid phase, leading to a batch crystallisation mode, and a potential basal magma ocean (Elkins-Tanton 2012). In comparison, larger grains may settle-out, leading to the fractional bottom-up crystallisation modes presented in my models (Bower et al. 2022).

Thermal conduction is expressed by Fourier's law relative to the adiabatic temperature gradient,

$$F^{\text{cond}} = -\rho \kappa_t \Big(T \frac{\partial S}{\partial r} + c_p \frac{\partial T}{\partial r}\Big|_S \Big) \tag{2.21}$$

where κ_t is the thermal diffusivity. Entropy is not the natural variable for expressing thermal conduction, giving rise to the additional terms in Equation 2.21 not seen in the usual formulations of Fourier's law.

The planet's metallic core is not spatially resolved by SPIDER and is parametrised via a core-mantle boundary entropy, which corresponds to a core temperature T_c. The CMB entropy represents the bottom boundary condition on the numerical solution for the mantle entropy. The CMB entropy decreases over time – as core heat is released into the bottom of the mantle and the planet cools – at a rate dependent on the local entropy gradient $\mathrm{d}S\ \mathrm{d}r$ in the bottommost layer of the mantle. The core thereby acts as a reservoir of heat determined by its density ($10\,738\ \mathrm{kg\,m^{-3}}$) and heat capacity ($880\ \mathrm{J\,kg^{-1}\,K^{-1}}$). I do not account for radiogenic or tidal heating in the core, nor for thermal boundary layer effects on either side of the CMB.

The mantle is initialised on an adiabat with a specific entropy $S(t=0)$, corresponding to an initial surface temperature > 3000 K such that all of my simulations begin with a 'hot start' fully-molten mantle which then cools and potentially solidifies after some time.

The flux boundary condition used to solve the interior at a time $t = t_n$ is placed at the top-most layer of the mantle based on calculations of F^{atm} from the `atmos_clim` module (Figure 2.1b). Equation 2.17 is numerically integrated over a time-interval Δt using a fifth-order ODE solver[6], acting to evolve the mantle's specific entropy, temperature, and melt fraction profiles across each PROTEUS time-step to a new time $t_{n+1} = t_n + \Delta t$. The temperature at the top of the interior T_m is then used to set the lower-boundary condition for the `atmos_clim` solver for the next PROTEUS iteration (Equation 2.1) starting at this new time t_{n+1}.

The length Δt of each PROTEUS time-step is determined dynamically throughout the simulation. If the absolute changes in whole-mantle melt fraction Φ or net flux F^{atm} are within the user-provided absolute and relative tolerances, then Δt is increased by a scale-factor of 1.5 for the next iteration, but otherwise is decreased by a scale-factor of 0.8 in order to stabilise the model.

---

[6] `CVODE` via the PETSc library (Hindmarsh et al. 2005; Gardner et al. 2022).

2.2.6 Convective atmosphere module

Atmospheric convection is driven by locally heating deeper layers of the column, driving a vertical temperature gradient to exceed the critical lapse rate ($\mathrm{d}T/\mathrm{d}z$) required for triggering convection. In the case of planetary atmospheres, radiation is the primary source of local heating. In the case of Earth: solar radiation passes through the atmosphere and is absorbed at the surface, this energy is transported to the lower layers of the atmosphere[7], heating it, and driving convection.

The lowest layer of Earth's atmosphere, the troposphere[8], is shaped by convection occurring from the surface upwards(Pierrehumbert 2010). Above Earth's troposphere is the stratosphere, where the atmosphere is thermally inverted (i.e. $\mathrm{d}T/\mathrm{d}z > 0$) due to absorption of shortwave radiation by O_3 (see Section 2.2.7). The stratosphere is defined by convective stability; energy balance is then set mainly by radiative and conductive processes. More generally, stratospheres can also be near-isothermal or slightly uninverted depending on the balance of shortwave and longwave opacities to radiation (Guillot 2010; Pierrehumbert 2010). The configuration of deep convection below and radiative layers aloft extends to other Solar System bodies with thick atmospheres and may be a general trend for planetary atmospheres more broadly (Robinson and Catling 2014). As highlighted in Section 1.4, it has thus been common in the literature to assume that planetary atmospheres exhibit deep convective zones *a priori*; this assumption has come under recent scrutiny (Selsis et al. 2023; Cmiel et al. 2025) and is explicitly investigated in Chapter 3, but is adopted for the investigation in this chapter.

The critical lapse rate required to trigger convection depends on the *type* of convection involved. Dry convection is taken to be an adiabatic process, meaning that no energy or mass is exchanged between a rising/sinking parcel and the surrounding atmosphere during its motion (Pierrehumbert 2010). Radiative heating can then only drive the atmospheric lapse rate up to that of a dry adiabat,

$$\nabla_{\mathrm{ad}} := \left.\frac{\mathrm{d}\ln T}{\mathrm{d}\ln p}\right|_{\mathrm{ad}} = \frac{R}{c_p} \tag{2.22}$$

---

[7] Energy is transported through the lowermost layers by combination of thermal radiation, sensible heating (usually turbulence and conduction), and latent heat from H_2O evaporation.

[8] Except at high latitudes, which are set by radiative-*advective* balance (Cronin and Jansen 2016).

in the case of an ideal gas (see Appendix E for derivation). $R = 8.314\,\mathrm{J\,K^{-1}\,mol^{-1}}$ is the ideal gas constant and c_p is the molar heat capacity of the gas mixture. The Schwarzschild criterion for determining convective instability is then,

$$\left|\frac{\mathrm{d}\ln T}{\mathrm{d}\ln p}\right|_{\mathrm{atm}} > \left|\frac{\mathrm{d}\ln T}{\mathrm{d}\ln p}\right|_{\mathrm{ad}}, \tag{2.23}$$

which also sees wide application in stellar astrophysics (Gabriel et al. 2014; Anders et al. 2022). The temperature profile $T(p)$ in a convective region will then tend towards the integral of Equation 2.22. We thus have an analytic form for $T(p)$.

Similar to crystallisation within a planet's interior, atmospheric volatiles can begin to condense in the atmosphere when they become 'saturated' – when the temperature decreases below their dew point temperature T_{dew}, which depends on the volatile's partial pressure. The dew point of a single species may be readily calculated using the Clausius-Clapeyron relation in the ideal gas regime,

$$\frac{\mathrm{d}p_{\mathrm{sat}}}{\mathrm{d}T_{\mathrm{dew}}} = \frac{p_{\mathrm{sat}}L}{T_{\mathrm{dew}}^2 R}, \tag{2.24}$$

where L is the molar latent heat of phase change [$\mathrm{J\,K^{-1}\,mol^{-1}}$]. Equation 2.24 may be integrated from a reference point (usually the triple point) to obtain the dew point temperature (or saturation pressure) elsewhere along the phase coexistence curve which it defines. The latent heat L depends on temperature, and tends to zero at the critical point (Pierrehumbert 2010). A derivation of Equation 2.24 is described in Appendix D.

With phase change occurring, convection then becomes a *pseudo*-adiabatic process in that some change $\mathrm{d}S$ in entropy occurs upon ascent as latent heat is released within the parcel. Various formulations exist for expressing moist convection with *dilute* condensable components, which is applicable to H_2O in Earth's atmosphere (Miyawaki et al. 2022). The moist lapse rate is less steep than that of the dry adiabat; i.e. the temperature profile will be closer to isothermal.

Alternatively, rather than being dilute, a condensable gas instead may be the dominant component of a gas mixture. For this end-member regime where the atmosphere effectively comprises a single condensing species, the lapse rate instead tends to the Clausius-Clapeyron relation (Equation 2.24). In the case of H_2O condensation, a temperature profile in this limit gives rise to the canonical runaway greenhouse behaviour defined by the vapour-liquid coexistence curve for water (Section 2.3.3; Kasting 1988; Kopparapu et al. 2013).

The intermediate regime is more complicated: where *multiple non-dilute* gases condense upon parcel ascent, releasing latent heat and decreasing in abundance as they rain-out from the mixture. In this case, convection is pseudoadiabatic because heat is released within the parcel, but it still assumed to not exchange energy with its surroundings. There are several analytical formulations for pseudoadiabatic convection of somewhat unsightly construction: e.g. Graham et al. (2021) derived a pseudoadiabatic lapse rate,

$$\nabla_{\mathrm{G21}} = \left(x_d + \sum_i x_{v,i}\right) \div \left(x_d \frac{c_d x_d + \sum_i \left[x_{v,i} \left(c_{v,i} - R\beta_i + R\beta_i^2 \right) + \alpha_i x_{c,i} c_{c,i} \right]}{R \cdot \left(x_d + \sum_i \beta_i x_{v,i} \right)} + \sum_i \left[\beta_i x_{v,i} \right] \right) \tag{2.25}$$

applicable to an idealised atmosphere composed of a dry background component $\square_d$, multiple non-dilute condensable vapours $\square_v$, and their corresponding condensates $\square_c$. $\beta_i = L_i/(RT)$ and α_i is the 'retention fraction' of condensate, such that a mole fraction α_i of the condensate produced is rained-out while the remainder is retained as cloud. See also Li et al. (2018) and Peters et al. (2022), although their lapse rate formulas are less generalised than Equation 2.25. An attractive feature of these formulations is that they reduce to the usual moist adiabat when only a single component is condensing, and also reduce to the phase coexistence curve (Equation 2.24) when the mixture comprises only a single condensing component.

The convective lapse rates exhibit $T \to 0$ as $p \to 0$, which is an unrealistic behaviour for the upper atmosphere since absorption of stellar radiation – or even a planet's own thermal radiation – will act to heat this region above $T = 0\,\mathrm{K}$. We can make the approximation of a radiative stratosphere which is assumed to be transparent to shortwave radiation but a grey absorber of longwave radiation by imposing $T(p) \geq T_r$, where

$$T_r = \left(\frac{f_s F_\star}{2\sigma_{\mathrm{SB}}} \right)^{1/4} \tag{2.26}$$

is the radiative skin temperature of the planet, set by the bolometric instellation stellar flux $F_\star$ (Pierrehumbert 2010). Radiative transfer is further discussed in the next section (2.2.7).

To simulate a range of planetary atmospheres in this chapter, I apply the JANUS[9] atmosphere model which implements a pseudoadiabatic temperature structure and spectral radiative transfer (Graham et al. 2021). JANUS simulates volatile atmospheres of arbitrary composition without the requirement of specifying a dominant 'background' gas or the specification of each component's diluteness in the mixture. For a given surface temperature T_s and surface gas composition, JANUS integrates Equation 2.25 upwards in pressure-space from the surface p_s to some user defined top-of-atmosphere. The temperature profile $T(p)$ follows the dry adiabat in regions without condensation, the multispecies pseudoadiabat where component(s) undergo phase change, and is set to T_r in the uppermost regions to represent a radiatively-heated isothermal stratosphere. This means that, in this chapter, as in the prior literature, I enforce a critically-stable atmospheric temperature profile which sits directly on the pseudoadiabatic convective profile. In making this assumption, I neglect the potential for purely-radiative layers that are *stable* to convection, and largely neglect the role of radiative energy transport within convective regions. With atmospheric composition and temperature defined at each pressure level, radiative transfer calculations are performed to determine the planet's top-of-atmosphere energy balance and thus the cooling rate of the planet as a whole.

2.2.7 Radiative transfer in principle

Radiative transfer is the absorption, emission, and scattering of electromagnetic radiation as it propagates through a region. Radiation is usually the dominant form of energy transport in a planetary atmosphere so it is important to understand its role in setting a planet's energy balance and therefore its climate (Pierrehumbert 2010). I begin this section with a qualitative description of radiative transfer and describe my specific implementation in Section 2.2.8. Atmospheres are composed of several gases (e.g. H_2O, H_2, CO_2) which have wavelength-dependent radiative absorption cross-sections and which may not be spatially well-mixed. A beam of radiation travelling through a slab of material (e.g. atmospheric gas) will be attenuated by absorption and scattering processes, but also enhanced by thermal emission and scattering processes.

---

[9] `https://github.com/FormingWorlds/JANUS`

A photon can be probabilistically absorbed when encountering a molecule, subject to conservation laws, resulting in the excitation of roto-vibrational modes in the molecule, and thereby warming the gas (Stamnes et al. 2017). Photons with wavenumbers ν in the ultraviolet and x-ray regimes and above may impart sufficient energy to also *photolyse* the molecule, splitting it into multiple fragments that have a net electric charge (e.g. OH^-), or instead to *photoionise* the atoms and cause electrons to transition to higher energy levels (Sharp and Burrows 2007; Huebner and Mukherjee 2015; Nakayama et al. 2022). The photon energy $E_\nu = hc\nu$ does not need to exactly correspond to the energy of the molecular modes or atomic transitions, as the absorption properties of the gas is modified by line broadening processes such a natural-, pressure-, collisional-, and Doppler-broadening (Frommhold 1993; Stamnes et al. 2017). As a result, the absorption cross-section κ_ν of the gas at a given wavenumber ν depends on the local pressure and temperature. In this thesis I make the assumption of *local thermodynamic equilibrium*, meaning that I do not explicitly resolve the electron transitions in atoms or modes in molecules, and assume that they are generally in their ground state (López-Puertas et al. 1986). In addition to the absorption of photons governed by electron transitions in lone molecules and atoms, collisions between molecules in the atmosphere lead to the brief formation of multi-species complexes with their own opacity to radiation (Pierrehumbert 2010). This 'collisional' source of absorption (abbreviated CIA) introduces a spectrally continuous and varying source of opacity – since the exchange of particle kinetic energy and photon energy is bounded only by classical conservation laws – and thus requires special semi-empirical treatment in modern radiation schemes (Amundsen et al. 2014; Stamnes et al. 2017). Gases emit their own thermal radiation through de-excitation and the corresponding emission of a photon, producing unique and characterisable absorption features. We leverage these features when making spectroscopic observations of exoplanets and stars (Birkby 2018; Madhusudhan 2019). However, at local thermodynamic equilibrium, this also gives rise to the famous Stefan-Boltzmann law describing the bolometric radiative energy flux emitted by a surface, $F = \sigma T^4$, where σ is the Stefan-Boltzmann constant. Opacities are further discussed in the next Section (2.2.9).

Absorption of radiation due to some opacity κ_ν [m^2/kg] also allows us to define an optical depth

$$\mathrm{d}\tau_\nu = \kappa_\nu \rho \, \mathrm{d}l \tag{2.27}$$

as a measure of the attenuation along a path length $\mathrm{d}l$. For a directly collimated beam we must retain here some angular information describing the beam geometry, since it scales the path length relative to a vertical beam, and because scattering processes depend on the beam angle relative to an observer (Stamnes et al. 2017). We then have a path length $\mathrm{d}l = \mathrm{d}z / \cos\theta_z$ through the slab of gas of vertical thickness $\mathrm{d}z$, for a path angled at θ_z from the zenith. $\theta = 0^\circ$ at the substellar point (noon) and 90° at the terminator (dawn/dusk). Choice of the most appropriate beam zenith angle depends on the modelling context (Cronin 2014). No particular choice needs to be made for global climate models that spatially resolve the planet in three dimensions, since a global model will naturally adopt an appropriate θ_z at each point on a planet's surface (Datseris and Stevens 2021). However, when attempting to represent the *general* radiative character of an entire planet with a single one-dimensional column, we must take care when choosing θ_z. It is usually selected alongside some scaling factor f_s applied to the entire spectrum of incoming stellar radiation (Equation 2.3); I describe my choices of θ_z and f_s in later sections.

Scattering processes contribute to the transfer of radiation. Here I only consider Rayleigh scattering, whereby the polarised oscillating electric field of a passing photon induces an electric dipole in nearby molecules, causing their electrons to also oscillate (and therefore accelerate), resulting in the emission of radiation across a spectral continuum in the optical and ultraviolet regimes (Stamnes et al. 2017). The intensity of Rayleigh scattering depends on the angle between a directly incoming beam of stellar radiation and an observer, here represented by our zenith angle θ_z. In the case of downwelling stellar radiation, Rayleigh scattering generally acts to diffusely redirect some fraction of the radiative energy upwards, and therefore increases the Bond albedo of the planet (John 1869; Lord Rayleigh 1881; Pierrehumbert 2010). Note that here and throughout, I use the term 'shortwave radiation' to refer to both the direct downwelling stellar radiation and its diffusely scattered component. However, for cooler stars, such as M-dwarfs, the downwelling SW component may primarily sit within the infrared regime and spectrally overlap with planetary thermal radiation (France et al. 2016). Aerosols such as water droplets (clouds) and hazes also scatter and absorb radiation with a strong angular-dependence, generating broad absorption features in observations of exoplanet spectra (Mackwell et al. 2014). The resultant effects on a planet's radiation balance depends on the distribution, altitude, and type of aerosol present (Jordan et al. 2025; Mak 2025). I do not model the radiative properties of aerosols in this thesis.

I have written in terms of arbitrary gas mixtures, but also suggested that atmospheric temperature profiles can be shaped by the presence of particular species. An example of this is O_3 in Earth's atmosphere, which drives a temperature inversion due to its absorption cross-section being $\gtrsim 1000\times$ larger within the SW ultraviolet compared to the thermal infrared regime, so local balance between absorbed flux (from the Sun, primarily at shorter wavelengths) and emitted flux (thermal emission, longer wavelengths) is only achieved by raising the temperature of the atmosphere where O_3 is present (Gorshelev et al. 2014). The presence of shortwave absorbers (potentially TiO and VO) in giant hot-Jupiter exoplanets drives thermal inversions similarly to O_3 on Earth (Fortney et al. 2008; Piette et al. 2020).

When stellar radiation is instead mainly deposited in the deeper atmosphere (or at the surface), it locally heats these layers rather than driving an upper-atmosphere inversion. Since the planet primarily radiates thermally in the infrared regime, this absorbed energy is then re-emitted as part of the thermal longwave component of the radiative budget. The balance between the near-surface absorption of SW radiation and the emission of thermal LW radiation gives rise to a greenhouse effect when the atmosphere is composed of gases which absorb strongly in the infrared regime, because the thermal emission is strongly inhibited from escaping to space. Examples of these 'greenhouse' gases are H_2O, CO_2, and CH_4; the H_2-H_2 continuum also has significant greenhouse properties (Pierrehumbert and Gaidos 2011). The greenhouse effect of CO_2 is central to Earth's present habitability and Venus' presently uninhabitable conditions (Trenberth 1992; Lodders and Fegley 1998). The capacity for an atmosphere to thermally 'blanket' the interior of a planet is subject to filling gaps ('windows') in the atmospheric thermal absorption spectrum, which may be achieved through the combination of multiple absorbing gases and gas CIA-pairings.

A wavelength-dependent treatment of the radiative transfer problem is clearly necessary (Edwards and Slingo 1996). One type of approach to describing radiative transfer is via line-by-line methods, which use a list of energy transitions (a linelist) to calculate the absorption of a gas mixture for each transition across a desired range of wavenumbers $\Delta\nu$. Although line-by-line methods provide high accuracy and fine spectral resolution, they require large linelist files and significant computing power per unit $\Delta\nu$ (Dudhia 2017; Stamnes et al. 2017). Instead, tabulating the absorption spectrum into spectral bands – which we assume contain some large ($\gtrsim 100$) number of randomly distributed lines – allows the efficient treatment of $\Delta\nu$ as a single entity with its opacity set by the combination of individual line opacities. Pre-processing a linelist to generate band absorption cross-sections is slow and lossy to fine spectral information, but then allows high performance radiative transfer calculations (Goody and Yung 1989). These 'band' methods include double-grey and picket-fence approaches (Lee et al. 2021; Malsky et al. 2024). As a third category of approach, k-distribution methods also split the absorption spectrum into bands $\Delta\nu$, but take advantage of the fact that any given value of the radiative absorption cross-section κ_ν will be encountered several times within each band (Lacis and Oinas 1991; Edwards and Slingo 1996). These k-distribution methods then bin κ_ν within each band and sort the bins in ascending κ magnitude to allow for more efficient calculations by more readily allowing wider, and thus fewer, bands to be used (Amundsen et al. 2014). Whichever method is applied, the final result from all of these radiative transfer methods is a determination of radiative fluxes as a function of wavelength, directed along a beam through a region of an atmosphere. With these fluxes, we may solve for the climate state of a planet subject to some boundary conditions, and make comparisons to telescope observations (Madhusudhan 2019). Computational efficiency is an important consideration because systematically faster calculations permit a favourable compromise between accuracy and the liberal application of numerical models (e.g. in retrievals and as forward-models; Barstow and Heng 2020). I make a direct comparison between correlated-k and line-by-line radiative transfer in Section 2.3.1.

2.2.8 Radiative transfer in practice

I will now detail the primary approach to radiative transfer applied in this thesis, which is based on SOCRATES: a suite of software tools developed for modelling radiation in planetary atmospheres using the correlated-k method (Edwards and Slingo 1996; Manners et al. 2017; Sergeev et al. 2023; Manners 2024). I have redistributed SOCRATES on GitHub[10] with some modifications, where I have also included the Python tools for running my custom opacity pipeline (Section 2.2.9).

In SOCRATES, bolometric radiation fluxes are determined by summing over some set of spectral regions ('bands'). These bands are then split into sub-bands, which are treated mono-chromatically. Each monochromatic calculation is performed under a two-stream approximation, in which we integrate over the angular component of the radiation field to use a single column with multiple upward- and downward-directed beams (Lee 2024). We can therefore write the bolometric radiation flux as a sum over bands and monochromatic sub-bands,

$$F^{bol} = \sum_j F_j^{\text{band}} = \sum_j \sum_k w_{jk} F_{jk}^{\text{mono}} \tag{2.28}$$

The weights w and k-terms (factoring into F_{jk}^{mono}) describing the optical properties of each monochromatic calculation are stored in a pre-computed table of values known as a 'k-table', which I will describe below.

These monochromatic fluxes are calculated at edges of each layer of the atmosphere, each of which is treated as compositionally and thermally homogeneous. In this chapter, the composition and thermodynamic properties of each layer are calculated from the temperature profile $T(p)$ obtained from JANUS' integration of the pseudoadiabat. SOCRATES then solves for three sets of monochromatic radiation fluxes in both the LW and SW regimes:

- U_ν the upward flux
- V_ν the downward flux (diffuse and direct contributions combined),
- Z_ν the downward flux directly originating from the star.

Any other components of the flux field may be obtained from these three terms by subtraction, eliminating the other components as required. These three fields are evaluated

---

[10] `https://github.com/nichollsh/SOCRATES`

for both the SW and LW regimes with appropriately differing boundary conditions, and for each spectral band, which yields a spectroscopic solution to the radiation field. The *net* radiation flux at wavenumber ν transported through each layer is then

$$F_\nu^{\mathrm{rad}} = U_\nu^{\mathrm{LW}} + U_\nu^{\mathrm{SW}} - V_\nu^{\mathrm{LW}} - V_\nu^{\mathrm{SW}} \tag{2.29}$$

so that positive flux values represent a net-upward transport of energy due to radiation around wavenumber ν. Note that V terms include contributions from Z, and that this formulation is directly comparable to Equation 2.2 used in the dummy `atmos_clim` model.

With the model discretised into N levels indexed from $l = 0$ at the top of the atmosphere, we can relate the fluxes to each other and between adjacent layers:

$$U_{l-1} = \mathcal{T}_l U_l + \mathcal{R}_l V_{l-1} + \mathcal{S}_l^+ \tag{2.30}$$

$$V_l = \mathcal{T}_l V_{l-1} + \mathcal{R}_l U_l + \mathcal{S}_l^- \tag{2.31}$$

$$Z_l = \mathcal{T}_l Z_{i-1} \tag{2.32}$$

$$\tag{2.33}$$

where $\mathcal{T}_l$ and $\mathcal{R}_l = 1 - \mathcal{T}_l$ are the transmission and reflection coefficients (Equation 2.39), and $\mathcal{S}_l$ is the source term in each layer. The boundary condition for the upward part is set by emission and reflection at the surface (U_N). The boundary conditions for the downward parts are set from the instellation flux scaled by f_s and θ_z in the SW case ($V_0 = Z_0$), and set to zero in the LW case. In my calculations, the instellation is given by Equation 2.3 and in this thesis is calculated spectroscopically from the stellar spectrum synthesised according to the methodology in Section 2.2.10. SOCRATES expresses the flux components in this manner since it can form a matrix of banded flux terms that is otherwise largely zero-valued, thereby permitting an efficient numerical solution for obtaining U, V, and Z(Edwards and Slingo 1996). Furthermore, from Equations 2.33 we can see that in the optically-thick limit ($\mathrm{d}\tau \gg 1$) the radiative transfer effectively reduces to a diffusion problem, since photons emitted by a layer l are readily absorbed in neighbouring regions $l \pm 1$. An example of this is Venus' thick CO_2-dominated atmosphere, which is within the radiative-diffusion regime near the surface (Pollack and Young 1975; Pierrehumbert 2010).

As with the boundary conditions, the form of the source terms is different in the SW and LW regions. For the two-stream formulation used in my calculations, in the LW these are

$$\mathcal{S}_l^{\pm\mathrm{LW}} = \pm c_l^{\mathrm{LW}}[B(T_l) - B(T_{l-1})] \tag{2.34}$$

where $B(T)$ is the Planck function representing thermal blackbody emission at temperature T, under the assumption of local thermodynamic equilibrium. Similarly in the SW we have,

$$\mathcal{S}_l^{+\mathrm{SW}} = c_l^{(1,\mathrm{SW})} Z_{l-1} \tag{2.35}$$

$$\mathcal{S}_l^{-\mathrm{SW}} = c_l^{(2,\mathrm{SW})} Z_{l-1} \tag{2.36}$$

where the coefficients c_l at each layer represent the radiative properties of the layer; their calculation depends on the particular approximation applied to represent integration of the radiation field over solid angle. For example, to easily perform this integration, the classical 'Eddington approximation' assumes that beam intensity is a linear function of its angle. I apply SOCRATES under the 'practical improved flux method' (Zdunkowski et al. 1980; Zdunkowski and Korb 1985) where the diffusivity factor $\mathcal{D} = 1.66$ (Elsasser 1938). This method is recommended by the SOCRATES user guide, and represents an approximation of the complete radiative transfer equation that incorporates higher-order Legendre terms than the Eddington approximation. Alternative formulations are the discrete ordinate and hemispheric mean approximations of the angular integration (Amundsen et al. 2014; Stamnes et al. 2017). Whichever angular integration method is used, the physically meaningful quantities which factor into c, $\mathcal{T}$ and $\mathcal{R}$ are the optical depth $\Delta\tau$ (from the extinction coefficient k in the layer; Equation 2.27), the single-scattering albedo (ω, the ratio of scattering and extinctions), and the scattering asymmetry (g, the directional-average of the scattering phase function; Ehlers and Moosmuller 2023). These quantities are spectrally variant and depend on the gas composition. The total extinction coefficient k_l in each layer is a combination of the individual gas extinctions, weighted by their mass mixing ratio, each of which is a continuous function of T and p via a scaling function with coefficients determined from their absorption cross-sections κ (Manners et al. 2017). Furthermore, numerical scalings are applied within SOCRATES to τ, ω, and g to maintain good accuracy given limited numerical precision (Joseph et al. 1976). A keen reader may refer to the SOCRATES user guide and technical documentation[11] for specific algebraic details. The scattering and extinction coefficients of aerosols, such as clouds, can also readily factor into the correlated-k parameterisation within SOCRATES.

Correlated-k methods efficiently express the absorption of *individual* gases, avoiding expensive line-by-line calculations to permit accurate flux computations with relatively few spectral bands (Stamnes et al. 2017). Within a spectral region ($\Delta\nu = \nu_2 - \nu_1$), a given value of the extinction will be encountered multiple times, as the absorption lines rapidly peak and trough in ν-space (Lacis and Oinas 1991). So rather than express the absorption as a function of ν – as in a line-by-line approach – we can instead determine some statistical *distribution* of extinction coefficients within a spectral band, which is then discretely binned into monochromatic (Equation 2.28) sub-bands as

$$f_j^{\text{band}}(k) = \frac{1}{\nu_2 - \nu_1} \sum_i \left| \frac{\delta \nu_i}{\delta k_i} \right| \Pi(k_i, k_i + \delta k_i) \tag{2.37}$$

where Π is a top-hat window function equal to unity in the region of k-space between k_i and $k_i + \delta k_i$. A sum can then readily express this as a cumulative distribution across each spectral band,

$$g^{\text{band}}(k) = \sum_i f(k_i)\delta k_i \tag{2.38}$$

The inverse of this cumulative distribution yields the so-called ‘k-distribution’ of terms in each spectral band: $k(g) = g^{-1}(k)$. So far, this algebra has simply re-ranked extinction coefficients within a given band, itself binned into monochromatic intervals, which retains the absorption properties of the original absorption cross-section data without loss of generality. The important result of this reshuffling of $\kappa(\nu)$ is that we can tabulate $k_n(g)$ as a function of g (in the interval $[0, 1]$), which yields sets of ‘g-terms’ and ‘k-terms’ describing the absorption properties of a *single* gas across a *single* spectral band, at a particular temperature T and pressure p. The transmission coefficient within a band j is then the weighted average of k-terms in its monochromatic sub-bands,

$$\mathcal{T}(u) = \sum_i e^{-k_i u} f(k_i)\delta k \tag{2.39}$$

$$= \sum_i e^{-k_i u} \delta g_i \tag{2.40}$$

for a mass path $u = \rho \cdot \mathrm{d}l$. This is a simple k-distribution method, known as the ‘ex-

---

[11] https://github.com/nichollsh/SOCRATES/tree/main/docs

ponential sum-fitting technique' (ESFT).

This description of parametrised absorption must be extended to mixtures of multiple absorbers. If we assume that the absorption lines of various components which are active in a particular band are randomly correlated in k-space, then the combined transmission is simply the product of their individual transmissions: $\mathcal{T} = \mathcal{T}_A \cdot \mathcal{T}_B \cdots$ equivalent to computing the convolution of their $f(k)$ distributions (Amundsen et al. 2017). However, since we have information about each absorber's k-distribution over ν-space, we can more accurately write the combined transmission (for two gases, A and B) as

$$\mathcal{T}(u_A, u_B) = \sum_{i}^{N_A} \sum_{j}^{N_B} \left[\exp(-k_i u_A) \cdot \delta g_i \times \exp(-k_j u_B) \cdot \delta g_j \right] \tag{2.41}$$

summing over the monochromatic sub-bands of both absorbers, yielding the 'random overlap' method, which is a type of correlated-k method. The random overlap formulation has been benchmarked to provide good accuracy and can be readily extended to N arbitrary absorbers, although with additional sums, the computation time expensively scales as $\mathcal{O}^N$ (Amundsen et al. 2014).

A more efficient technique for mixing absorbers is the 'equivalent extinction' method, (Edwards 1996) which is an extension of the ESFT method (Ritter and Geleyn 1992). Equivalent extinction discriminates between major and minor gases in each band, taking a single gas to be the main absorber depending on its abundance and opacity. In this case, for each minor gas we first calculate the weighted-sum of k-terms in each band j *before* performing steps to combine gas opacities (Manners et al. 2017). The equivalent extinction method treats minor gases as grey absorbers across each band, but major absorbers retain their fully spectroscopic treatment. Equivalent extinction significantly improves computational performance, with some losses in accuracy (Amundsen et al. 2014; Amundsen et al. 2017). I make a comparison between the equivalent extinction and random overlap schemes against a line-by-line baseline in Section 2.3.1.

A final option for calculating the transmittances of mixtures is to simply pre-mix gas opacities; an approach adopted by HELIOS and PICASO (Malik et al. 2017; Mukherjee et al. 2023). In this case, the k- and g-terms in each band $\Delta\nu$ are calculated for every combination of the gas mixing ratios, rather than calculating k and g for individual gases and then combining them later (with mixing ratios instead propagating-through to their mass path u; Equation 2.41). Pre-mixing opacities is fast and accurate *in principle* (Malik et al. 2017). However, the k-table dimensionality then scales as $\mathcal{O}^N$ with the number of absorbers since we must include an additional axis for each absorber to tabulate potential values of its mass mixing ratio. Even with modern computing resources, these additional dimensions mean that it is not possible to construct k-tables with sufficient resolution to reliably maintain good accuracy when using pre-mixed opacities (Amundsen et al. 2017).

2.2.9 Gas opacities and parametrisations thereof

SOCRATES parametrises gas opacity in a file format referred to as a ‘spectral file’, in which k-coefficients of each absorber are stored in a ‘k-table’ of wavenumber intervals (bands and sub-bands), temperatures, and pressures. The k-terms in these spectral files are fitted to pre-computed data tables of gas absorption cross-section κ_ν. As long as these cross-section data are tabulated at wavenumber intervals comparable to the line width, tabulated values of $\kappa_\nu(T, p)$ will still capture the particular shape of each line and aggregate spectral features; a resolution of $0.01\,\mathrm{cm}^{-1}$ is typical (Grimm et al. 2021; Selsis et al. 2023). Computing absorption cross-sections κ_ν and fitting k-coefficients to them are computationally expensive processes because the number of transitions included in a molecular linelist can be large. So, when fitting k-coefficients using SOCRATES’s utilities, the number of the sub-bands within each spectral band are determined such that transmittances $\mathcal{T}_j^{\text{band}}$ calculated from k-coefficients are accurate (to a tolerance) compared to line-resolution calculations using the tabulated cross-sections (Amundsen et al. 2014; Manners et al. 2017). Alongside k-coefficients, additional data are included in these spectral files: water droplet absorption and scattering properties (Slingo and Schrecker 1982), continuum absorption coefficients (Karman et al. 2019), Rayleigh scattering depolarisation factors (Parthasarathy 1951), the incoming stellar spectrum binned to each band (Section 2.2.10), and other important metadata required for using SOCRATES. Once a k-table has been generated, it may be re-used indefinitely to provide quick and flexible calculations of radiative fluxes.

The number of transitions in a molecular linelist is limited by theoretical and numerical studies of gases. Line locations and strengths are numerically derived from quantum-mechanical molecular dynamics simulations which approximately solve the Schrödinger equation (Rothman et al. 1992; Rothman et al. 2010; Stamnes et al. 2017). Numerical approaches to linelist generation are particularly desirable as they avoid the reproduction of extreme temperatures and pressures in a laboratory (Tennyson and Yurchenko 2012). Furthermore, computational advancements have enabled significant improvement to linelists over the last two decades. For example, the HITEMP2010 H_2O linelist[12] (Rothman et al. 2010) contains 320 thousand transitions, while the later H_2O linelist (Barber et al. 2006) 'BT2' contains 500 million transitions, and the latest ExoMol H_2O linelist 'POKAZATEL' contains 5 billion transitions with significant updates to the optical and ultraviolet regimes (Polyansky et al. 2018).

So, rather than dealing with these comprehensive (and correspondingly cumbersome) linelists directly, I utilise pre-computed absorption cross-sections $\kappa_\nu(T, p)$ available from the DACE Opacity Database[13] (Malik et al. 2017; Grimm et al. 2021). Where possible, DACE uses the latest and most complete linelists available in the literature, and then applies the GPU-accelerated HELIOS-K code to calculate opacities at a wavenumber resolution of 0.01 cm^{-1} as a function of temperature and pressure. Line wings are cut off at a fixed distance of 25 cm^{-1} from line centres, which is consistent with SOCRATES internal calculations that determine k-coefficients from these pre-computed cross-section data. The process of generating a SOCRATES spectral file is outlined by Figure 2.2. Table 2.2 outlines the included absorbers, their literature sources, and corresponding collisional pairings for the spectral files used in this chapter. With the capacity for generating spectral files with various numbers of spectral bands and spacings, I perform sensitivity tests to the number of bands required to obtain sufficient performance and accuracy from my models (Sections 2.3.1 and 5.8).

The continuum opacity induced by collisional interactions between gases, as described in Section 2.2.7, is treated separately but similarly to the absorption by single gases in SOCRATES. The absorption cross-section of two gases with number densities n_A and n_B

---

[12] `https://hitran.org`

[13] `https://dace.unige.ch/opacityDatabase/`

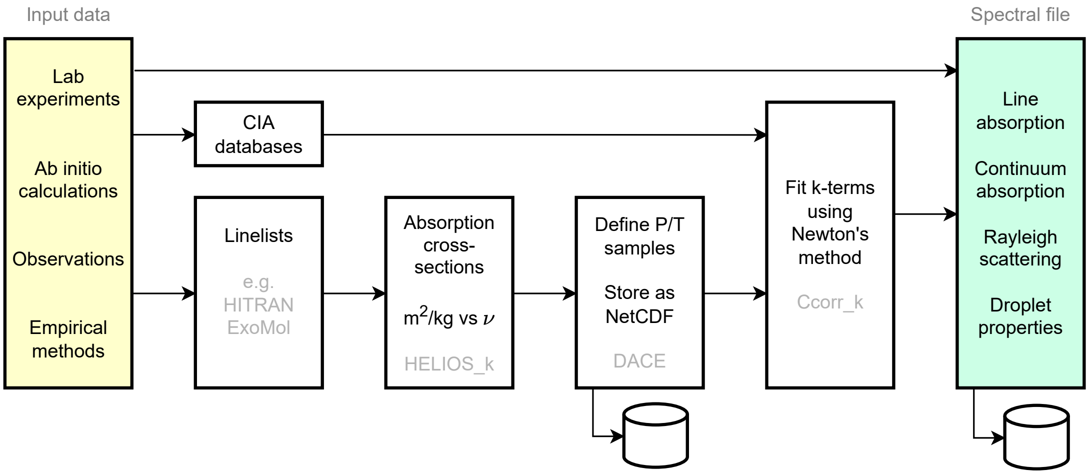

Figure 2.2: Flowchart showing the process to create a SOCRATES spectral file. Once opacity data are obtained from DACE for a given T-P grid, they may be stored locally and re-used multiple times. This approach allows the efficient generation of spectral files with various numbers of spectral bands and absorber combinations. The program `Ccorr_k` is a component of SOCRATES which fits k- and g-terms to spectroscopic absorption data, as a function of temperature and pressure.

is nominally parametrised as

$$k(\nu) = b_\nu^{(A-A)} n_A^2 + b_\nu^{(A-B)} n_A n_B + b_\nu^{(B-B)} n_B^2 \tag{2.42}$$

where the binary absorption coefficients b are numerically calculated with ab-initio methods, and here taken from opacity databases (e.g. HITRAN; Karman et al. 2019). Obtaining absorption coefficients for the collisional self-continuum of water molecules is not yet tractable, but the water vapour continuum represents an important source of opacity, so I use the empirical MT_CKD continuum derived from laboratory experiments and observations of Earth's atmosphere (Mlawer et al. 2012; Mlawer et al. 2023). MT_CKD has only been validated around Earth-like conditions, but is adopted here and elsewhere in the literature for lack of alternative prescriptions.

2.2.10 Stellar evolution, briefly

Stars are very important to planets and their inhabitants because the absorption of stellar radiation is their primary source of energy. For example, Earth's instellation (set by the solar constant $S_0 = 1360.8 \pm 0.5\,\mathrm{W\,m^{-2}}$) is about four orders of magnitude larger than Earth's present-day internal heat flux of $0.1\,\mathrm{W\,m^{-2}}$ (Davies and Davies 2010; Kopp and Lean 2011). Both of these fluxes have evolved over time: the former driven by stel-

Gas	References	Collisional pairings
H_2O	POKAZATEL – Polyansky et al. (2018)	H_2O, N_2
H_2	RACPPK – Roueff et al. (2019)	H_2, CH_4, CO_2, N_2
N_2	WCCRMT – Shemansky (1969), Barklem and Collet (2016), Western (2017), and Western et al. (2018)	N_2, H_2, H_2O
CO_2	UCL-4000 – Yurchenko et al. (2020)	CO_2, H_2, CH_4
CH_4	YT34to10 – Yurchenko and Tennyson (2014) and Yurchenko et al. (2017)	CO_2, H_2
CO	HITEMP2019 – Li et al. (2015)	None

Table 2.2: Sources of line-absorption and corresponding collisional absorption pairings used in this chapter. Absorption from the water self-continuum is calculated using Version 3.2 of the MT_CKD model (Mlawer et al. 2012; Mlawer et al. 2023). All other collisional absorption is calculated using the HITRAN collisional absorption database (Karman et al. 2019). The DACE opacity database derives cross-sections using HELIOS-K (Grimm et al. 2021) to parse linelists.

lar evolution, and the latter by metallic core formation and decay of radiogenic isotopes (Turcotte and Schubert 2002; McDonough 2025). However, we must bear in mind that stars are highly complex entities; *comprehensively* modelling them is generally outside the scope of this thesis.

The proto-Sun formed via direct gravitational collapse from the solar nebula, rapidly contracted, and spun-up its rotation alongside the formation and flattening of the surrounding protoplanetary disk (Gough 1980; Bonanno et al. 2002). Such young 'T Tauri' stars are initially fully convective and luminous, emitting strongly in the X-ray regime (Bertout 1989; Kippenhahn et al. 2012); a visual example is provided by WISPIT 2 in Figure 1.1b. A deep radiative zone developed in the star's core as its internal temperature increased, due to steady hydrostatic gravitational contraction through its pre-main sequence phase. After 10 – 100 Myr, the Sun's internal temperature was sufficient to overcome electrostatic repulsion between protons and initiate their fusion into helium nuclei through the first branch of the $p-p$ nuclear reaction chain (Salaris and Cassisi 2005). Onset of fusion placed the Sun on its main sequence evolution track. This point is referred to as a star's 'zero-age main sequence'[14]. The $p-p$ chain has several branches of fusion reactions, but its initial step to form deuterium

$$p^+ + p^+ \rightarrow {}^2_1\mathrm{H}^+ + e^+ + \nu_e \tag{2.43}$$

is rate-limiting because of the β^+ decay involved in converting a proton into a neutron

---

[14] This is not necessarily the point from which we date a star's age, since this would assign pre-main sequence stars with negative ages. There is no consensus on point at which to measure the 'birth' of a star.

for the deuterium nuclear product. The deuterium and positron are rapidly consumed to form $^{3}_{2}\mathrm{He}^{+}$ (Adelberger et al. 2011; Kippenhahn et al. 2012). Conversion to 'normal' helium can occur through various branches of the $p-p$ chain, and thenceforth to heavier nuclei of lithium, beryllium, and boron. This process of hydrogen burning will remain the primary source of energy throughout most of the Sun's lifetime, and also for similar FGK stars. For stars more massive than 1.3 $M_\odot$, the CNO cycle is also an important factor in their energy budget (Salaris and Cassisi 2005). Stars 'turnoff' from the main sequence when their core is entirely composed of helium; accumulated helium and heavier elements are then consumed in a post-main sequence stage (Burbidge et al. 1957; Salaris and Cassisi 2005). It is by the triple-alpha process – which fuses three helium nuclei into ^{12}C via beryllium – during stellar post-main sequence phases that the majority of the carbon in the universe is synthesised. Evolutionary timescales, and the main sequence lifetime in particular, are a strong function of stellar mass: cool M-type stars (e.g. TRAPPIST-1 and L 98-59; Section 1.2.2) spend a long time in their pre-main sequence phase and then evolve slowly along the main sequence, providing a different environment to their orbiting planets than the Sun does for the inner Solar System.

The luminosity of stars of all types evolves over time in both bolometric and spectroscopic terms. Most stars emit enhanced rates of X-ray and ultraviolet radiation compared to their bolometric luminosity during their pre-main sequence phase (Fleming et al. 2020; Namekata et al. 2023). The X-ray luminosity of the Sun may have initially been 1000× larger than it is today (Gudel 2007). Large cumulative doses of photoionising radiation may then be delivered to planetary companions during these early 'saturated' periods when a star's rotation rate is large and approximately constant in time (Luger and Barnes 2015; Wheatley et al. 2017). Eventually a star will spin-down, primarily by shedding angular momentum to stellar winds and through magnetic braking (Kippenhahn et al. 2012; Johnstone et al. 2021), so its XUV luminosity decreases. Capturing these relatively short early periods is important for understanding which planets may retain atmospheres against escape, and what these atmospheres may be composed of (Fromont et al. 2024). This is particularly crucial for planets orbiting cooler low-mass stars, as their saturated periods are longer and habitable zones closer-in compared to planets orbiting larger stars (Lammer et al. 2007; Wordsworth and Pierrehumbert 2014;

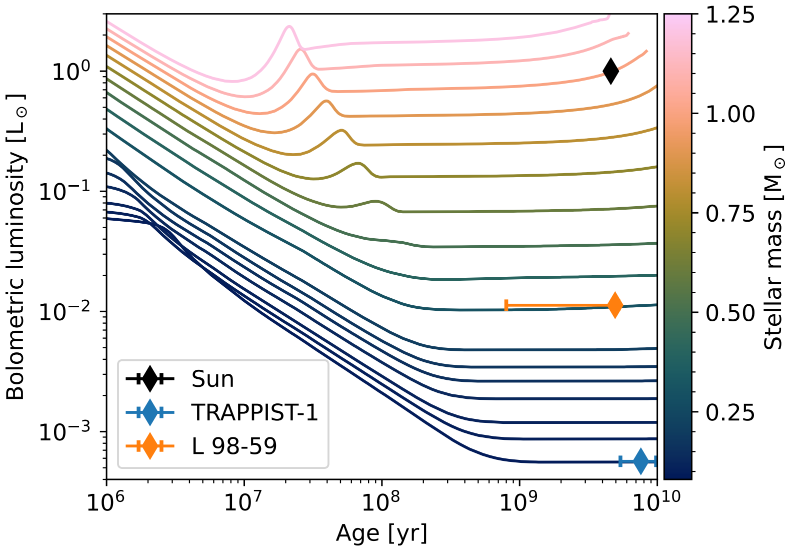

Figure 2.3: Evolution tracks of stellar bolometric luminosity over time. These tracks, taken directly from Baraffe et al. (2015), cover the pre-main sequence and complete main sequence for stars with a range of masses. Overplotted are the observed luminosities and estimated ages of three relevant stars.

Johnstone et al. 2021).

The *bolometric* luminosity of all stars will also typically increase as they evolve along their main sequence. However, since M-type stars may first spend 100s of Myr evolving along their pre-main sequence Hayashi track (Hayashi 1961; Hayashi and Hoshi 1961), their bolometric luminosity will decrease for some time until reaching their zero-age main sequence (Stahler and Palla 2004). I have plotted a series of stellar evolution tracks in Figure 2.3 to demonstrate the changing bolometric luminosity of stars over a range of evolutionary timescales depending on their mass (Baraffe et al. 2015). After performing stellar structure and evolution calculations, Baraffe et al. (2015) obtain radiation fluxes using 1-dimensional PHOENIX (Allard and Hauschildt 1995) stellar atmosphere models. PHOENIX implements a mixing-length convection parameterisation and spectral radiative transfer. Free parameters in the PHOENIX model (e.g. the mixing length α value) are calibrated against hydrodynamic and microphysical models, and against colour observations of stellar clusters (Freytag et al. 2012).

These processes, which together shape stellar evolution, also mean that it is difficult to determine the age of a given star, however that quantity is defined (Kippenhahn et al. 2012). Since we cannot directly measure a star's age, there are various methods by which we can attempt to estimate it. We may turn to ratios in its elemental composition via nucleocosmochronometry, since nuclear synthesis within stars is the fundamental mechanism by which metals are produced (Fowler and Hoyle 1960; Soderblom

2010). Cosmochronometry requires measuring a star's composition, which is particularly difficult for low-mass types (Lodders 2003; Reiners et al. 2012). Alternatively, we may compare a star's rotation rate, colour, and luminosity to theoretical isochrones – systematically biased by their modelling uncertainties (Jørgensen and Lindegren 2005; Baraffe et al. 2015). This significant known-unknown is important to consider when referring to an *exoplanet*'s age, which we can only define relative to the age of its host star.

Small M-type stars are fully convective, which keeps them almost chemically homogeneous and thereby avoids segregation of helium in a deep core (Reiners and Basri 2009); this will allow M-stars to continue fusing light isotopes on their main-sequence phase for more than a trillion years (Kippenhahn et al. 2012). M-star planets which manage to retain atmospheres up to their host's zero-age main sequence may therefore represent long-term environments for the maintenance of life, as slow main sequence evolution will leave them unperturbed for long periods of time. In comparison, the Sun will likely have a main sequence lifetime ~ 12 Gyr to eventually become a red giant and engulf the Earth. It has also been suggested that any planetary companions which avoid destruction during the 'death' of their host stars, surviving to their host's white dwarf stage, may be favourable targets for characterisation although they have low prospects for habitability (Agol 2011; Barnes and Heller 2013). Pollution of white dwarf stars with heavy elements derived from accreting of their planetary companions can offer some insight into the bulk composition of exoplanets and their redox states (Doyle et al. 2019a; Xu and Bonsor 2021; Bonsor et al. 2023).

In this thesis, I use the parametrised MORS stellar model (Johnstone et al. 2021) to simulate the evolving properties of a planet's host star alongside the planet itself, capturing the important effects of varying bolometric and spectroscopic radiation fluxes impinging upon a planet throughout its lifetime. MORS calculates the evolving band-integrated X-ray ($0.5 - 12.5$ nm), extreme UV ($12.5 - 92.0$ nm), UV ($92.0 - 400.0$ nm), and bolometric luminosities of stars over time using empirical scaling laws between these bands, which depends on the stellar mass and rotation rate (Reiners et al. 2014). The model parametrises rotational evolution by considering angular momentum transport within the star (Gallet and Bouvier 2015), and angular momentum losses to stellar winds and magnetic braking (Kippenhahn et al. 2012; Matt et al. 2015). MORS obtains stellar structures from pre-computed tracks for a given age and mass (Spada et al. 2013).

My simulations of planetary evolution in this chapter are initialised at $t_{\mathrm{ini}} = 100$ Myr relative to stellar $t = 0$ in MORS' modelling[15], allowing the integration time from PROTEUS to be directly mapped to stellar age. With this, I make the assumption of neglecting to model planetary accretion processes and early orbital migration in this thesis. At each time-step of PROTEUS, spectral regions of a high-resolution template stellar emission spectrum are scaled such that each spectral region in the template corresponds to the band-integrated luminosities calculated by MORS. The user must pre-determine if the star is a relatively fast or slow rotator compared to the population of comparable-mass stars.

The template spectrum used in each simulation is chosen case-by-case as appropriate to the modelling scenario. I use the Gueymard (2004) solar spectrum when considering a Sun-like host. Otherwise, I generally use the MUSCLES and Mega-MUSCLES synthetic stellar spectra (France et al. 2016; Loyd et al. 2018; Behr et al. 2023). MUSCLES spectra are carefully compiled from 1D PHOENIX stellar models for the optical-infrared regime, alongside XMM-Newton observations in the X-ray, and reconstruction of stellar emission in the ultraviolet regime from Hubble observations [16]. Together, the result of my parametrised stellar modelling is a calculation of a planet's exposure to stellar radiation across the electromagnetic spectrum, over time, allowing me to simulate its climate state and escape rate simultaneously together self-consistently.

2.3 Model validation and benchmarking

2.3.1 Validation of radiative transfer calculations

In order to verify the functionality of my opacity pipeline and radiative transfer calculations, I calculate three k-tables for O_2 absorption using data from two databases. Firstly with cross-sections derived from DACE according to the pipeline outlined by Figure 2.2,

---

[15] Stellar $t = 0$ in MORS, via the Yale Isochrones, is when a protostar begins to fuse deuterium nuclei; the so-called 'stellar birthline' (Yi et al. 2001).

[16] Reconstruction of UV fluxes is complicated by absorption in the interstellar medium.

with which I use SOCRATES to generate two spectral files that have different numbers of correlated-k bands. I use O_2 here because the DACE cross-section data provided to SOCRATES are themselves calculated from the HITRAN linelist (Gordon et al. 2022a). I then also generate a third k-table with the standard SOCRATES routine, not based on my above pipeline, which parses HITRAN linelist `.par` files directly without using cross-sections from DACE. These three spectral files, containing the k-tables, are then applied to the same atmospheric profile to perform a check on my opacity pipeline. I consider a physically extreme case of a 270 bar pure O_2 atmosphere above a 2200 K surface on an Earth-sized planet. This scenario could represent a planet which has built-up significant amounts of O_2 via fractionating escape processes (Wordsworth and Pierrehumbert 2014; Luger and Barnes 2015) but here primarily serves the purposes of a benchmarking scenario. The emission spectra of outgoing longwave radiation from this test are plotted in Figure 2.4, which shows good agreement between the three calculations (line colours). The bolometric fluxes are 644, 633, and 637 $\mathrm{kW\,m^{-2}}$ respectively for the cases of DACE-4096 bands, DACE-256 bands, and HITRAN-318 bands. These variations of $\sim 10\ \mathrm{W\,m^{-2}}$ are an acceptable level of accuracy for my work, corresponding to a relative error of 0.16%. There are minimal differences in the bolometric outgoing longwave flux ($< 1\,\mathrm{W\,m^{-2}}$) when I test fitting k-terms with a tighter transmission tolerance of 5×10^{-6} compared to my nominal value of 5×10^{-3}.

I now calculate emission spectra for an atmosphere of *mixed* composition to test the sensitivity of the radiative flux calculations to the number of spectral bands. Similarly to the O_2 test above, I model an Earth-sized planet, but now with an atmosphere of equal parts H_2O, CO_2, CH_4, HCN, SO_2, and H_2. This test is necessary because I must compromise between performance (fewer bands) and accuracy (more bands). Figure 2.5 plots emission spectra calculated by SOCRATES for four different k-tables with different numbers of bands, using the opacities described by Table 2.2. The 256-band result shows good performance and converges upon the fluxes calculated using 4096-bands, so I use 256-band spectral files for the remainder of this chapter. The 48-band result would also be a reasonable standard choice. The 16-band spectral file is useful for testing/debugging my models, while the 4096-band file can be used for comparison with telescope observations (in emission spectroscopy). The bolometric emission fluxes for the spectra in Figure 2.5 are 290, 290, 289, and 293 W m^{-2} in order of descending band number.

Finally for this section, I compare SOCRATES longwave emission spectrum calculations against an entirely independent line-by-line radiative transfer model: the Reference Forward Model[17] (Dudhia 2017), using linelist data from HITRAN. This serves the purposes of further validating my opacity pipeline, but also validating SOCRATES's solution to the radiative transfer problem while providing a benchmark against which to compare the assumptions two common opacity overlap schemes. Figure 2.6 shows calculated thermal emission spectra from a convective saturated atmosphere composed of 90% H_2O and 10% CO_2 by mole fraction, with a 270 bar surface pressure and 647 K surface temperature. The top panel of the figure shows that combining gas opacities with the random overlap method (blue line) compares well with the Reference Forward Model (black line), and that there is minimal error associated with this technique despite my approximation of separately fitting k-table for the gases and then combining them at runtime (Section 2.2.8). The middle panel shows the cumulatively integrated fluxes for the wavenumber range shown, which accounts for the different spectral binning between the models, and highlights that the bolometric fluxes tend towards the same value (rightmost end of the panel). Differences between cumulative integral lines in the middle panel are shown in the bottom panel. The equivalent extinction method (orange line) shows similar accuracy to random overlap, yet it comes a substantially improved computational performance. Both k-distribution methods calculate cumulative fluxes which maximally deviate by $\sim$ 5 W m^{-2} relative to the LBL case (black line, panel b). This offset is generated from differences near the 1500 cm^{-1} feature (panel a), although it is largely cancelled by differences near 2500 cm^{-1} feature. These flux differences arise when spectroscopic feature sizes are comparable to the correlated-k bin widths. Overall, findings presented in Figure 2.6 are in-line with previous inter-comparisons between gas opacity mixing implementations for correlated-k schemes (Edwards 1996; Amundsen et al. 2014). I adopt the random overlap technique as my standard mixture method in this chapter, for completeness.

---

[17] `https://eodg.atm.ox.ac.uk/RFM/`

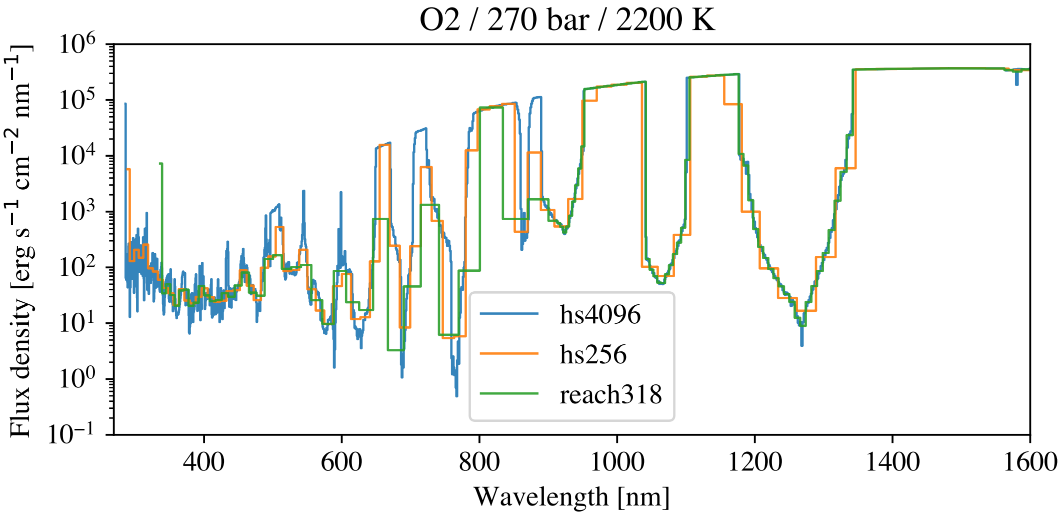

Figure 2.4: Sanity check on my opacity pipeline, showing emission spectra from a pure-O_2 atmosphere. The figure plots the planetary emission spectrum calculated by SOCRATES using three spectral files: hs4096 (4096 bands derived via DACE opacities), hs256 (256 bands derived via DACE opacities), and reach318 (318 bands derived from HITRAN directly).

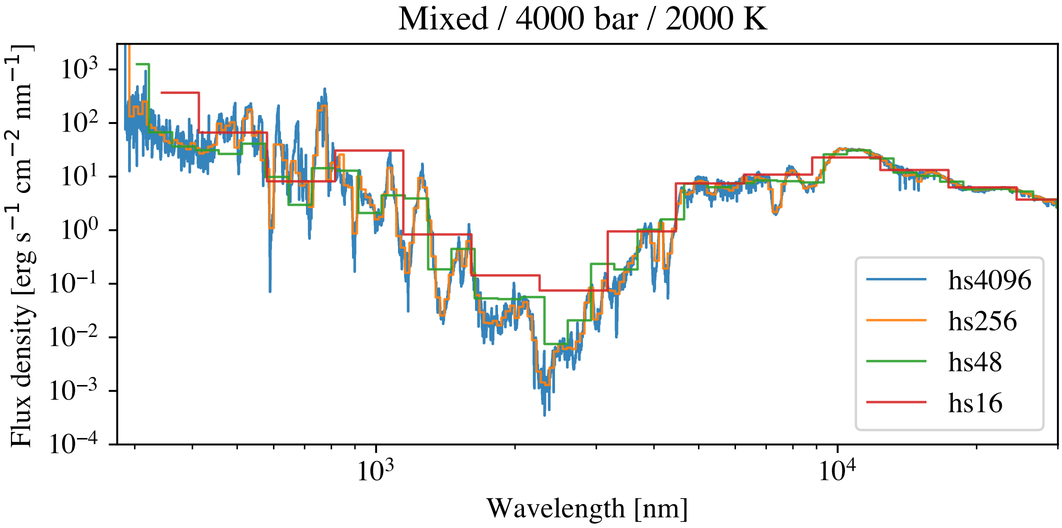

Figure 2.5: Sensitivity test to spectral file band number and placement. This plot shows emission spectra calculated by SOCRATES using four spectral files containing different numbers of spectral bands: 4096, 256, 48, and 16.

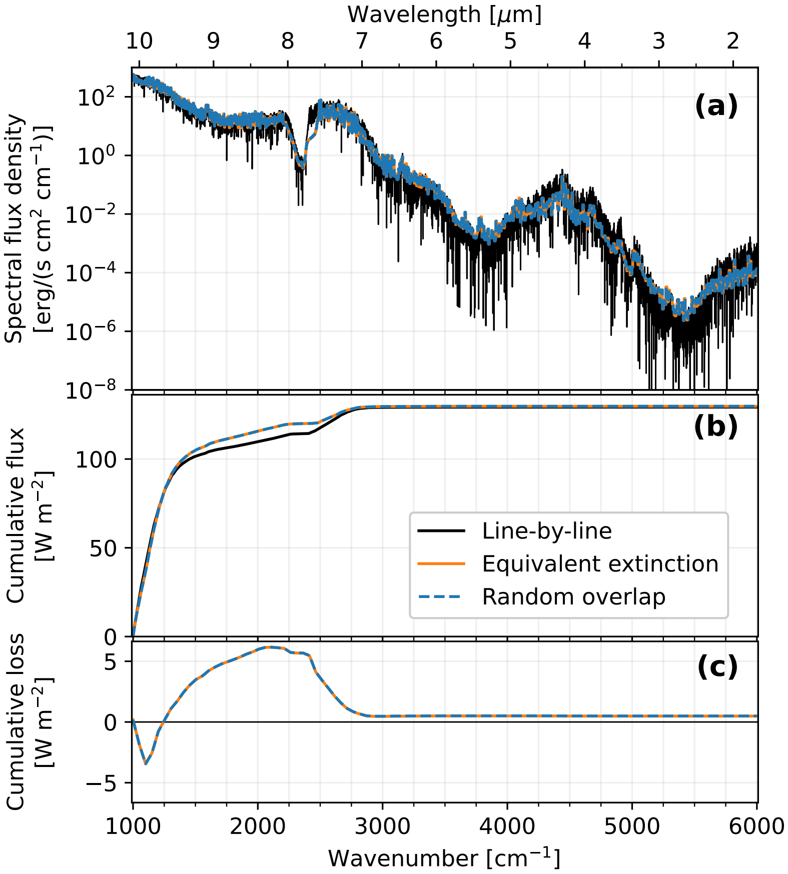

Figure 2.6: Comparison of modelled emission spectra with two opacity-mixing schemes and a line-by-line model. Outgoing longwave fluxes using equivalent extinction (solid orange line) and random overlap (dashed blue line) are compared against those from the RFM (black line). **Top**: the outgoing spectral flux density. **Middle**: cumulative integral of flux over the wavenumber range shown. **Bottom**: flux loss, as the difference between the integrated fluxes.

2.3.2 Pure-steam runaway greenhouse behaviour

A key requirement is that the JANUS atmosphere model is able to reproduce the Simpson-Nakajima limit on the bolometric outgoing longwave radiation (OLR) produced by thermal emission within a runaway greenhouse regime (Nakajima et al. 1992). This is important because Hamano et al. (2015) and Lebrun et al. (2013) have emphasised that the asymptotically-limited OLR within the runaway greenhouse regime acts to determine when a planet can support a permanent magma ocean. This limit is also the basis for some calculations of habitable zone boundaries (e.g. Kopparapu et al. 2013).

The limiting value of OLR$\approx$ 282 W m^{-2} comes about because, under the assumption of a pure-H_2O pseudoadiabatic structure, the temperature in the upper atmosphere becomes independent of the surface temperature T_s within a particular regime. For a sufficiently large $T_s \gtrsim 2000$ K, most of a pure-H_2O atmosphere will lie on the dry adiabat (Equation 2.22) as each layer will have a temperature in excess of the H_2O dew or critical points (post-runaway; Boukrouche et al. 2021). At somewhat cooler T_s, parts of the upper atmosphere will condense H_2O because their temperature decreases to the dew point. These regions then have a temperature set by the saturation curve of H_2O via the Clausius-Clapeyron relation (Equation 2.24), and do not cool below it because latent heat release from H_2O condensation dominates the energy balance. As a result, the OLR then becomes decoupled from T_s because the photosphere of the planet is within this condensing region, which has a temperature defined only by the thermodynamic properties of H_2O. This means that changes to T_s have no impact on the ability for the planet to cool, giving rise to a seemingly runaway limit on the OLR. When the surface temperature is cold, the atmosphere can rain-out, become optically thinner, and allow direct emission from the surface to space which physically couples the outgoing radiation to the T_s in a pre-runaway regime.

An additional factor is that emission from the atmosphere and surface is set by the Planck function, so hotter T_s leads to emission at shorter wavelengths, allowing for increased emission through relatively transparent windows between H_2O absorption features (Pierrehumbert 2010).

Figure 2.7 plots OLR versus surface temperature, calculated for an atmosphere of pure-H_2O composition. JANUS is demonstrated to compare well against previous studies when calculating fluxes using HITRAN-derived opacities (dashed line). The DACE opacities derived from ExoMol are more complete at shorter wavelengths compared to HITRAN, since the ExoMol linelist (Polyansky et al. 2018) was computed across a larger range of electronic energy levels. Due to this increased line absorption below 500 nm, the calculations using DACE-derived opacities (Table 2.2) find a lower OLR limit and a hotter T_s at which the planet transitions into the post-runaway regime. This is because higher T_s are required to emit through the comparatively narrower windows between absorption bands, and more importantly, the increased opacity shifts the photosphere to lower pressures with lower temperatures. There are minimal differences between the two linelists at lower temperatures because HITRAN is sufficiently complete in this regime (Figure 2.6; Polyansky et al. 2018).

The OLR arising from this atmosphere scenario is also controlled by continuum absorption from H_2O-H_2O collisions. The continua databases (i.e. MT_CKD for H_2O) used in this thesis were originally developed for application alongside HITRAN opacities. I have tested whether the OLR differences in Figure 2.7 could be attributed to continuum incompatibility with the linelists I have used. In line with the predictions of Mlawer et al. (2023), I have found that the relative flux differences between HITRAN and DACE are present even with the CIA continua disabled, meaning that these differences can be attributed to improvements in quantifying line absorption rather than misbehaviour in my treatment of the continuum. Furthermore, a comparison between calculations using HITRAN2008 to those using HITEMP2010 was previously undertaken by Kopparapu et al. (2013): the more-complete HITEMP2010 linelist required $\gtrsim 300$ K larger T_s before the modelled atmosphere entered into a post-runaway state, compared to HITRAN2008, all else equal.

2.3.3 Fiducial H_2O-only evolutionary simulation

With my atmosphere modelling established, I now turn to the problem of coupled interior-atmosphere evolution. As a test case for simulating planetary evolution in this manner, I consider an Earth-analogue planet initialised as fully molten and endowed with

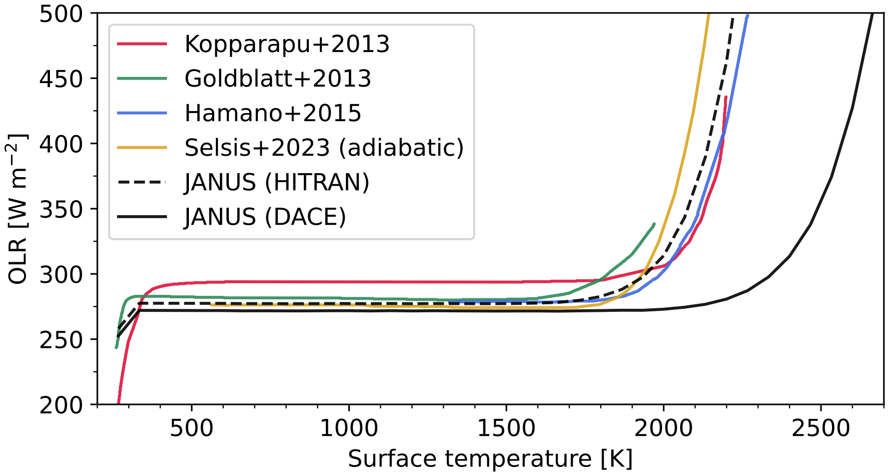

Figure 2.7: Outgoing longwave radiation versus surface temperature for adiabatic steam atmospheres. SOCRATES-JANUS radiative transfer calculations of OLR are compared against curves from the literature: Goldblatt et al. (2013), Hamano et al. (2015), and Selsis et al. (2023) with HITEMP2010 and Kopparapu et al. (2013) with HITRAN2008. I find an OLR limit of 277 W m^{-2} using HITRAN-derived opacities (dashed black line), close to the canonical Simpson-Nakajima limit of 280 W m^{-2} (Komabayasi 1967). Using DACE-derived opacities (solid black line) yields an OLR limit of 272 W m^{-2}. With the DACE opacities, the post-runaway transition shifts from 1800 K to higher temperatures at 2100 K.

an arbitrary 10 bar pure-steam atmosphere in solubility equilibrium with H_2O dissolved into the underlying melt, so that the total water content in the bulk planet is equivalent to 8.5 times that presently on Earth's surface. The planet is placed around a 100 Myr young Sun at a distance of 1 AU. I set its mass, radius, and core fraction to Earth's values: $M_\oplus = 5.972 \times 10^{24}$ kg, $R_\oplus = 6.335 \times 10^6$ m, and $r_c = 0.550$ respectively (Lodders and Fegley 1998).

The modelled surface temperature is initially very large ($T_s = 3023$ K) which places the planet into a post-runaway state that enables large outgoing fluxes $F^{\text{atm}} = 10.6\,\text{kW}\,\text{m}^{-2}$.

Figure 2.8 shows the evolution of this planet's atmosphere and interior temperatures (panels a and c), energy fluxes (panel b), and mantle melt fraction (panel d). The surface temperature of 1615 K at the point of solidification is within the runaway greenhouse regime indicated by Figure 2.7 due to the region of H_2O-condensation between pressure levels of 100 bar and 0.01 bar. The modelled planet spends most of its time in the runaway greenhouse regime which limits the OLR to around 273 W m^{-2}, which, minus the incoming stellar radiation and the Rayleigh scattering contribution, results in a net outgoing flux of only 74 W m^{-2} (panel b). The planet does not attain radiative equilibrium because solidification occurs rapidly, which causes the simulation to terminate. The non-zero net upward energy flux at solidification (panel b) indicates that the planet would continue to cool below the surface solidus temperature. The interior cools rapidly from its initial state to below the liquidus (panel c). It then spends a comparatively longer period with a mushy mantle until solidification occurs (panel d). Panel d also shows the ascent of the rheological front (defined here as $\phi_{\text{crit}} = 40\%$; Costa et al. 2009), which tracks where the mantle undergoes a rheological transition between dynamics characteristic of a melt to those of a solid (Bower et al. 2022). The black triangle in panel b indicates the time at which the rheological front begins its ascent from the core-mantle boundary, at which point mixed-phase energy transport processes enter into the system.

The grey and orange curves in Figure 2.8b overlap continuously, demonstrating that my method for iteratively coupling the interior and atmosphere modules of PROTEUS is reasonable. The contribution from Rayleigh scattering is small (34 W m^{-2}) but not insignificant compared to the 273 W m^{-2} OLR at solidification. The isothermal stratosphere (235 K) has a small presence, although it has little impact on the simulation due to the small opacity at such low pressures.

The time taken for complete mantle solidification is 4.7 Myr. This is too short for significant stellar evolution to occur (Baraffe et al. 2015), and is within the $\sim$ 100 Myr period bounded by the formation of the Moon and evidence of Earth's solid crust (Section 1.1). This solidification time is comparable with the 3.9 Myr calculated by Hamano et al. (2015). The 0.8 Myr difference may be reasonably accounted for by their slightly different total reservoirs of hydrogen and oxygen compared to my case, different opacities and mantle melting curves, and the inclusion of Rayleigh scattering and non-zero surface albedo in my simulations. Hamano et al. (2015) concluded that the modelled solidification time of an Earth-like planet strongly depends on its initial water inventory, varying from 0.7 to 630 Myr for 0.1 and 10 oceans respectively (their Figure 4b), the latter case only being able to cool due to slow atmospheric escape. Lebrun et al. (2013) found that magma ocean duration is 'quite sensitive' to the planet's H_2O endowment due to the large radiative opacity of H_2O gas. Lebrun et al. (2013) also found that the magma ocean duration could vary in length by 0.8 to 2 Myr depending on the choice of mantle solidus

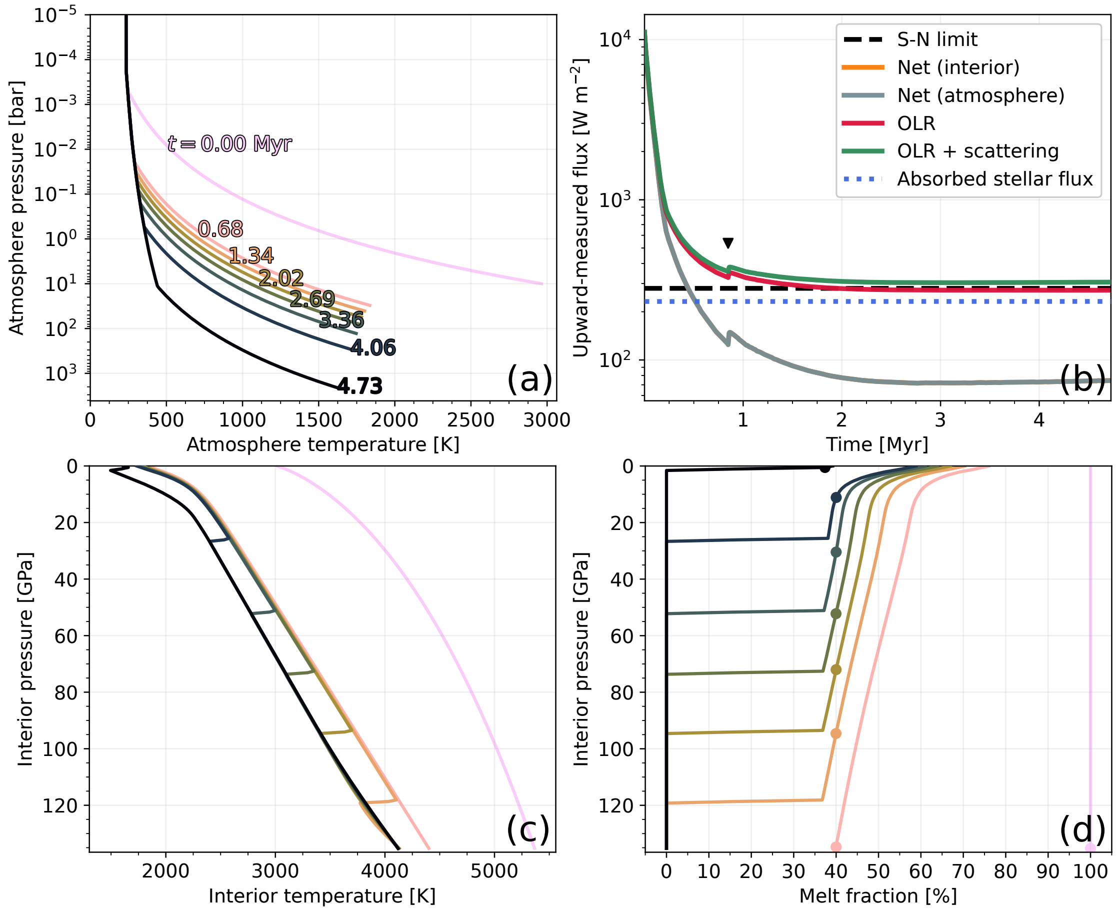

Figure 2.8: Evolution of the fiducial model until mantle solidification occurs. Panel a: atmosphere temperature profiles, with simulation time [Myr] indicated by the coloured text. **Panel b**: upward-measured energy fluxes, with the Simpson-Nakajima limit indicated by the dashed black line. The black triangle indicates the time at which the mantle rheological front begins its ascent from the core-mantle boundary. **Panel c**: mantle temperature profiles. **Panel d**: mantle melt fraction profiles, with the rheological front ($\phi = 40\%$) on each profile indicated by a dot.

and liquidus curves; this factor being particularly important when comparing my results with the literature given that PROTEUS is able to model multiple energy flux terms in the magma ocean. In comparison, previous works have typically used parametrised adiabatic mantles, which assume that convection is the only energy transport process and effectively makes them a zero-dimensional problem defined by a potential temperature and Nusselt number[18]. With these modelling differences under consideration, my calculated solidification time from this test case is reasonable.

Solidification is bottom-up, so the surface layer is the last to begin to solidify (Figure 2.8d). This occurs at 0.2 Myr, at which point crystals are forming within the melt and settling at the bottom of the magma ocean (Solomatov and Stevenson 1993a; Solomatov and Stevenson 1993b; Solomatov 2000; Bower et al. 2022). While convection rapidly transports energy upwards ($\sim 10^{10}\,\mathrm{W\,m^{-2}}$), this flux is largely offset by the effective downward transport of energy by latent heat ($\sim -10^{10}\,\mathrm{W\,m^{-2}}$). Additionally, gravitational settling acts to transport energy upwards ($\sim 10^{7}\,\mathrm{W\,m^{-2}}$). Inclusion of these additional energy transport processes alongside convection reduces the net upward energy transport, and correspondingly increases the magma ocean cooling time. Although I include radiogenic heating, the simulated global heat flux through the surface of the planet arising from radioactive decay is initially $0.282\,\mathrm{W\,m^{-2}}$ and then decreases by 0.27% over the course of the simulation. This radiogenic flux is negligible compared to the other heat transport processes in this case.

As described in Section 2.2.5, I have adopted radionuclide abundances equivalent to Earth's budget: scaling their initial fertile concentrations such that their decay leads to present-Earth abundances at Earth's present-day age. It is reasonable to expect that some exoplanets have non-terrestrial radionuclide abundances, giving them different in geothermal heat fluxes. Perhaps a planet which forms with super-terrestrial amounts of lighter elements could also be enhanced in radioactive uranium, thorium, and potassium.

Solidification of the mantle leads to significant outgassing of water, with the surface partial pressure monotonically increasing from 10 to 2054 bar in this simulation. The

---

[18] The Nusselt number of a fluid is the ratio of the total heat transfer to the conductive heat transfer.

Parameter	Symbol	Points	Range or values
Orbital separation	a	7	0.105, 0.316, 0.527, 0.737, 1.054, 2.108, 3.162
Oxygen fugacity	fO_2	7	-5, -3, -1, 0, 1, 3, 5
C/H ratio	C/H	7	0.01 to 2.0 logarithmically spaced
Total H inventory	[H]	3	1, 5, 10

Table 2.3: Parameter axes used to construct my grid of models. There are 1029 grid points in total. Orbital separation is measured in AU from the Sun (Equation 2.3). The other three parameters relate to the outgassing (Section 2.2.4) of volatiles: oxygen fugacity fO_2 is measured in $\log_{10}$ units relative to the iron-wüstite (IW) buffer, C/H is the ratio of the total mass of carbon to the total mass of hydrogen in the mantle and atmosphere combined, the total hydrogen inventory $[H]$ is measured in units of the total amount of hydrogen in all of Earth's oceans (hereafter abbreviated to 'oceans').

'catastrophic' outgassing of steam-rich atmospheres, as a result of mantle solidification, is an established theoretical behaviour (Nikolaou et al. 2019; Barth et al. 2021).

2.4 A range of evolutionary outcomes

I have established that a magma ocean on an Earth-sized planet at 1 AU, with a pure-steam atmosphere, can rapidly solidify. However, we may readily apply the same modelling approach to other similar cases. How does variation in atmospheric composition control cooling of the planet? This can be parametrised through the redox state of the mantle and the volatile endowment resulting from planet formation. How does the control of these parameters compare to differences arising from the planet-star separation?

To approach these questions, I run PROTEUS across a grid of parameters. With these models I am then able to explore the impact of these parameters on the composition of the atmosphere, the phase state of the mantle at model termination (i.e. solidified or molten), and the cooling timescale. This grid of models is configured according to the parameters in Table 2.3. All cases consider an Earth-sized planet. The nitrogen content of the planet is set based on a dissolved concentration of 2 ppmw relative to the mantle mass (Wang et al. 2018).

The range of a bounds the habitable zone (roughly 0.95 to 2.4 AU) and extends to small separations for applicability to Venus and highly irradiated exoplanets (Kasting et al. 1993b; Ramirez and Kaltenegger 2017). Bulk elemental endowment depends on the location and timing of planetary formation (Drążkowska et al. 2023; Krijt et al. 2023), so I use a broad range of [H] and C/H which encompass concordant estimates for primitive Earth (Wang et al. 2018). Mineralogical variations and differences in planetary bulk elemental composition will introduce a spread of at least 4 log units to fO_2 (Spaargaren et al. 2020; Guimond et al. 2023a; Spaargaren et al. 2025). Inferences as to the compositions of planetary material accreted onto white dwarf stars indicates that some exoplanets may have an oxygen fugacity comparable to asteroids within the solar system (Doyle et al. 2019a). Constraints on Mars' redox state derived from measurements of Martian meteorites imply a variation of at least 3 log units between samples (Wadhwa 2001). Observations of Mercury's surface by the MESSENGER spacecraft have been used to infer a highly reduced composition (Cartier and Wood 2019). I therefore explore a range of fO_2 from comparatively reduced to more oxidised across my grid of models.

2.4.1 Outgassed atmospheric compositions

Figure 2.9 plots the atmospheric composition for highly-irradiated planet outcomes across two slices of the parameter space (1 ocean and 10 oceans of hydrogen). Pie slices correspond to the volume mixing ratios of outgassed volatiles; white numbers show the *total* surface pressure in $\log_{10}(p_s/\text{bar})$. While the atmospheric composition depends on fO_2 and the C/H ratio, the total hydrogen content [H] exerts the most control over the dominant gas. CO- and CO_2-dominated atmospheres are produced for $\text{C/H} > 0.1$ and $fO_2 \gtrsim \text{IW} - 1$, inline with Bower et al. (2022) and Sossi et al. (2020). H_2- and CO-dominated atmospheres are common, particularly under reducing conditions, inline with the results of Maurice et al. (2024). The mole fraction of H_2O is typically small across all cases plotted in Figure 2.9 because it is primarily dissolved into the molten mantles. Methane remains a minor component in all of these hot cases due to the exothermic nature of its thermochemical formation from CO_2, with the CH_4 mixing ratio being maximised for the most reducing and hydrogen-rich cases. The total surface pressure p_s varies by approximately 2 log units in both parameter slices shown in Figure 2.9, with larger p_s typically found for larger [H] and larger C/H. There is a broader range of p_s at oxidising conditions than at reducing conditions, corresponding to a larger diversity of compositions.

Figure 2.10 plots atmospheric composition for two slices of the parameter space at 3.162 AU, probing the atmospheres of cases which have solidified. The diversity of composition is smaller than for molten cases (Figure 2.9). This is primarily because the high solubility of H_2O leads to a large fraction of the hydrogen being dissolved in the magma ocean in molten cases, whereas in these solidified cases it is primarily partitioned into the atmosphere since the mass of melt is small. Lower surface temperatures also disfavour the endothermic formation of CO, decreasing its abundance relative to CO_2 in these cases. These atmospheres typically have higher surface pressures than in the molten cases of Figure 2.9 because of the outgassing which occurs due to mantle solidification. Because the majority of volatiles have been outgassed, there is a much smaller range of p_s in these cases, which is instead set primarily by [H], fO_2, and C/H and not the variable melt fraction.

2.4.2 Ensemble statistics and distributions

Across my parameter grid of 1029 cases, 413 (40%) result in complete solidification, while 616 (60%) reach radiative equilibrium and thereby retain permanent magma oceans of various depths. The minimum, median, and maximum times to solidify are 0.4, 3, and 110 Myr respectively. In comparison, the maximum time for a case to attain a steady state at radiative equilibrium without solidifying is 140 Myr. Figure 2.11 plots distribution functions for all cases explored, which statistically represents how four dependent output variables (columns) vary according to the four independent variables which define the grid (rows). A broad range of evolution pathways are demonstrated to be possible for a given planet, even at a fixed orbital separation.

The solidification time is sensitive to the orbital separation (panel i), typically decreasing for larger separations. This is because the incoming stellar flux is smaller at larger distances, so the outgoing thermal flux becomes increasingly dominant in the total energy balance. The solidification time is shortest (median value of $\sim$ 3 Myr) at the largest separation considered, of 3.162 AU. As demonstrated by the fiducial case in Section 2.3.3, complete solidification leads to significant outgassing of volatiles (panel j) and large surface pressures. The longest solidification time is larger than that found by the fiducial pure-steam case, indicating that the lifetimes of magma oceans may be extended by atmospheres of mixed compositions due to the additional sources of opac-

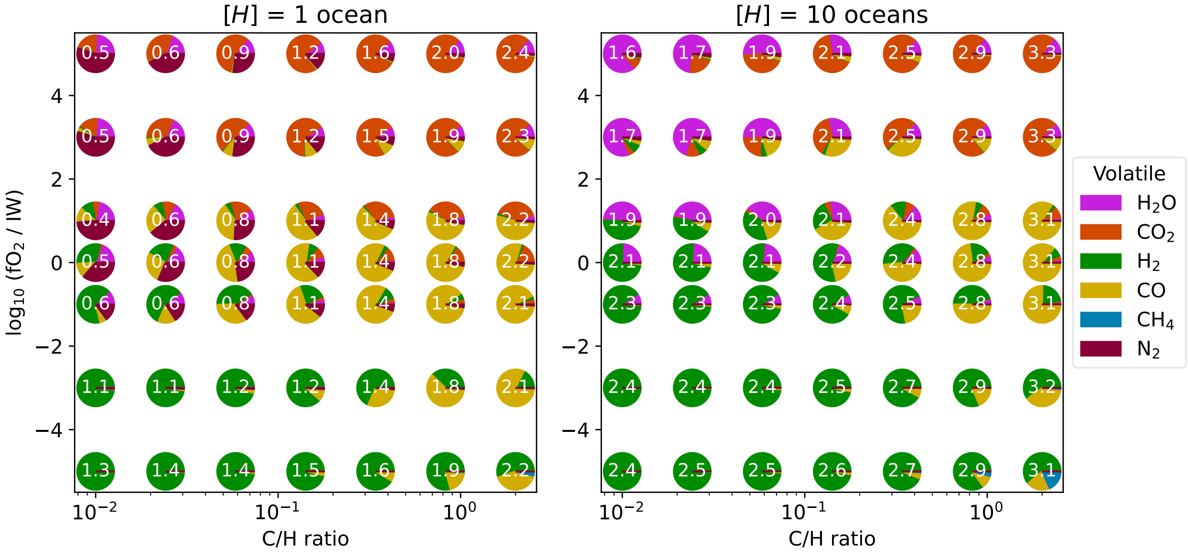

Figure 2.9: Atmospheric composition for planets which do not solidify. Pie charts display the atmosphere mole fractions χ_i (equivalently, volume mixing ratios $n_i/n_{\text{tot}} = p_i/p_s$) for all six included volatiles across the parameter space at 0.105 AU. The white numbers enumerate the total surface pressure as $\log_{10}(p_s/\text{bar})$, rounded to 1 decimal place. Note that mole fraction is a relative measure of molecule number density, so even at C/H = 2 (a measure of mass ratio) it is possible for there to be more H_2O than CO_2.

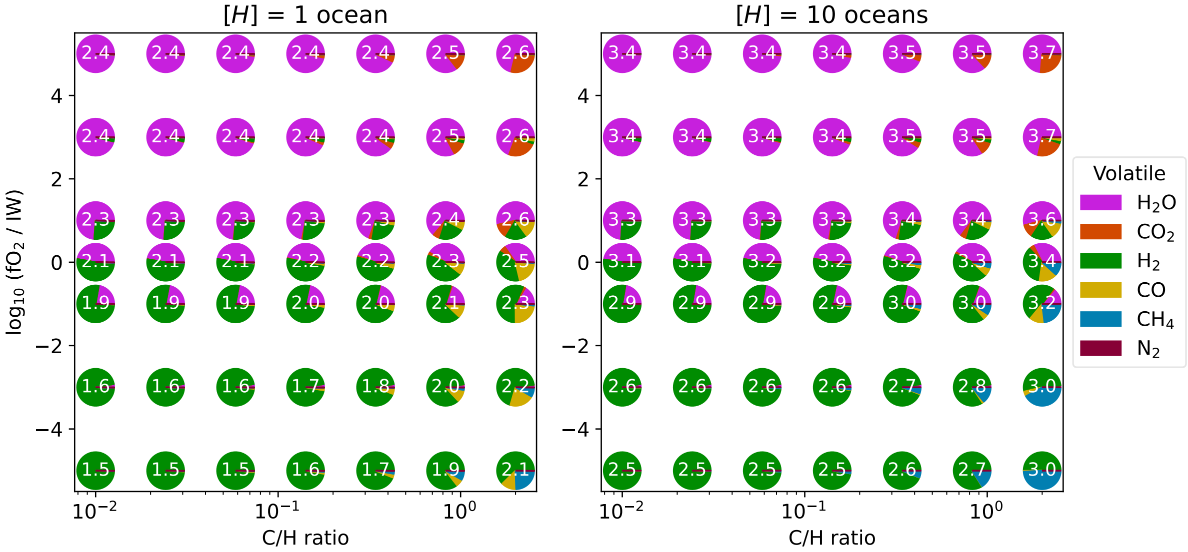

Figure 2.10: Same as Figure 2.9, but for cases at 3.162 AU, which are solidified.

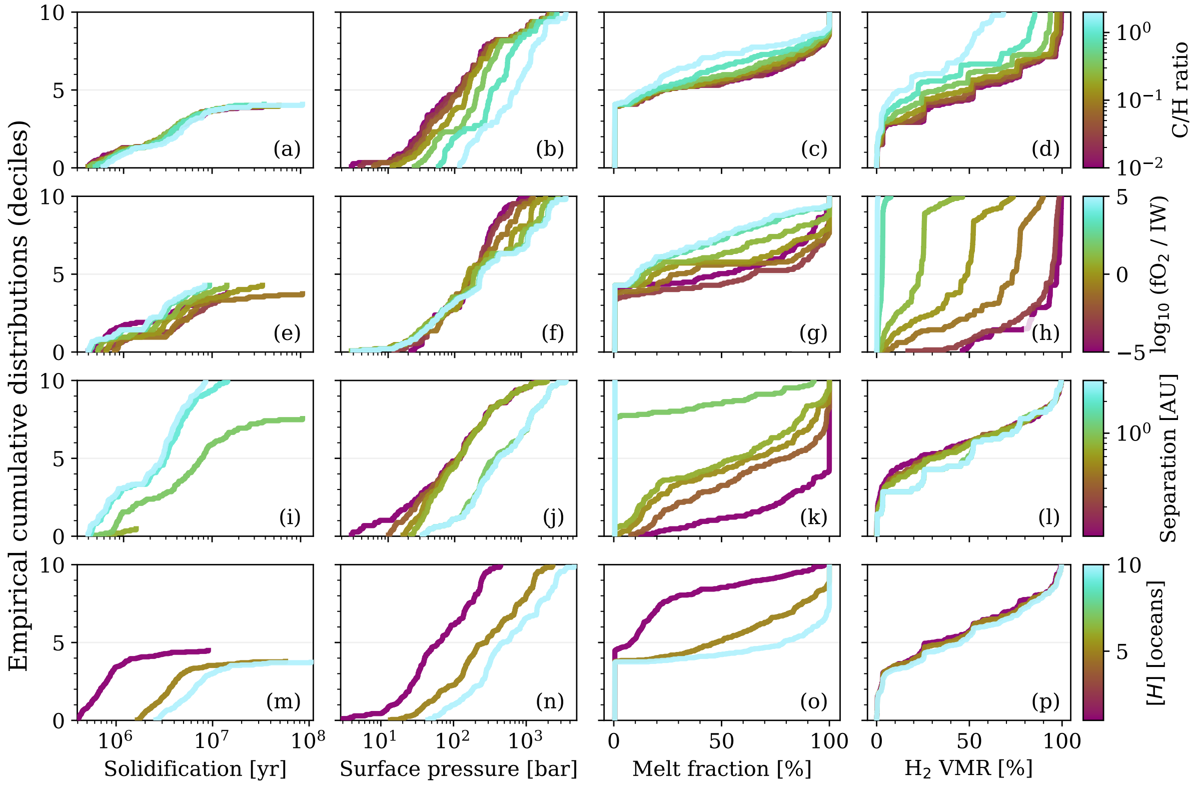

Figure 2.11: Empirical cumulative distribution functions for four independent variables (colourbars) and four dependent variables (x-axes). Curves are produced for an independent/dependent variable combination (v_i, v_d) by filtering grid cases to each value of v_i (rows), extracting the corresponding v_d (columns) values at model termination, and then sorting the v_d values in ascending order. For a given curve the corresponding v_i is held constant while all other independent variables are allowed to vary, thereby producing the distribution. If a variable v_d has a strong dependence on a variable v_i, then the distributions in the corresponding panel will tend not to overlap. Steep curves (in the $\mathrm{d}y/\mathrm{d}x > 0$ sense) correspond to v_d being distributed around a small range of values, while shallower curves correspond to a wider distribution. The data are plotted for all four axes of the parameter space (Table 2.3) and a selection of four dependent variables (solidification time, total surface pressure, interior melt fraction, and H_2 mole fraction). Cases which reach radiative equilibrium are treated as having an infinite solidification time, and thus do not appear explicitly in panels a, e, i, and m.

ity. The global melt fraction is directly tied to the orbital separation (panel k) since less irradiated cases more commonly solidify. Complete solidification only occurs for a small fraction of cases for $a \leq 0.7$ AU (panel i).

Across all cases and times across my grid of simulations, the surface pressure is maximised at 4711 bar by a H_2O- and CO_2-dominated outgassed atmosphere produced by a solidified mantle after 4.7 Myr of evolution. Some non-solidifying cases attain global radiative equilibrium very slowly due to the imbalance of outgoing and incoming radiation F^{atm} being near zero. The most extreme example of this (case 635) evolved with a thick H_2 dominated atmosphere for 142 Myr before satisfying my termination criterion for radiative equilibrium.

Alongside the orbital separation, the hydrogen inventory of the planet [H] exerts significant control over the solidification time (panel m). The solidification time increases with [H]. The oxygen fugacity and C/H ratio have a smaller but non-zero impact on the solidification time (panels a and e). The ensemble-median melt fraction varies from 10% to 80% depending on the value of [H] (panel o). [H] is important in regulating partially molten cases because the speciation of hydrogen atoms into H_2, H_2O, and CH_4 upon outgassing contributes significant radiative opacity to the atmosphere, slowing energy loss to space, and prolonging the evolution of the planet or potentially preventing solidification entirely.

There is a large range of H_2 mole fraction across the parameter space (panel h), with it primarily being controlled by the oxygen fugacity of the mantle. H_2 is consistently dilute (maximum mole fraction <5%) under the most oxidising conditions ($fO_2 \geq \mathrm{IW}+3$), but is consistently dominant (median mole fraction >50%) in reducing cases ($fO_2 \leq \mathrm{IW}-1$; see also Figure 2.9). This is because larger fO_2 promotes the outgassing of oxygen-bearing molecules (such as H_2O) over deoxygenated ones (such as H_2), with variability depending on the temperature via the gas-phase thermochemistry. Since the model terminates at solidification or radiative equilibrium, surface temperatures always remain high and the abundances of themochemically disfavoured species (e.g. CH_4) remain small. The production of H_2 dominated atmospheres under reducing conditions are inline with the findings of Schaefer and Fegley (2017) and Ortenzi et al. (2020), although these previous works did not directly model the evolving atmospheric composition of a particular planetary scenario *over time*.

While C/H has a smaller impact on the solidification outcome of the planet (panels a and c), it does yield changes to the total surface pressure (panel b). A large C/H promotes carbon-bearing molecules (such as CO_2) over hydrogenated species (such as H_2, panel d), resulting in significant changes to the mean molecular weight μ of the atmosphere. Surface pressure increases with μ, through its relationship to the atmosphere mass loading [kg/m^2], yielding higher pressures at larger C/H. This has less impact in solidified cases where outgassing is complete, and the total pressure is large, where the atmosphere is typically dominated by steam. At the largest C/H the partial pressure of CO_2 approaches 1800 bar, but H_2O typically remains a dominant or major component of the atmosphere under more oxidising conditions, when the planet's mantle solidifies.

2.4.3 Hydrogen and water greenhouse effects

Figure 2.11 shows that the total hydrogen inventory and redox state of a magma ocean planet exerts control over its evolution but does not explain the mechanism behind this relationship. Vibrational modes within triatomic H_2O and collisional absorption of H_2 make both of these molecules effective greenhouse gases (Borysow and Frommhold 1991; Abel et al. 2011; Chen et al. 2011; Pierrehumbert and Gaidos 2011). Similarly, Nikolaou et al. (2019) and Katyal et al. (2019) found that planetary volatile endowment is linked to magma ocean cooling and spectral response through the outgassing of greenhouse gases. Figure 2.12 plots the mole fractions of H_2 and H_2O for cases at 1.054 AU, which probes the parameter subspace where either outcome of solidification or radiative equilibrium is quite possible. All cases solidify for $[H] = 1$ oceans, independent of the oxygen fugacity and C/H ratio (left panels). The top-right panel shows that molten cases have an increased mole fraction of H_2, affirming the indications of Figure 2.11 that the H_2 greenhouse effect is key to preventing/slowing planetary solidification.

For $[H] = 10$ oceans, the mantle melt state is more sensitive to C/H and fO_2, although comparison of the two columns indicates that [H] still exerts the most control over the planet's melt state (at 1.054 AU). Cases more oxidising than the iron-wüstite buffer always solidify, while more reducing cases become subject to the planet's C/H ra-

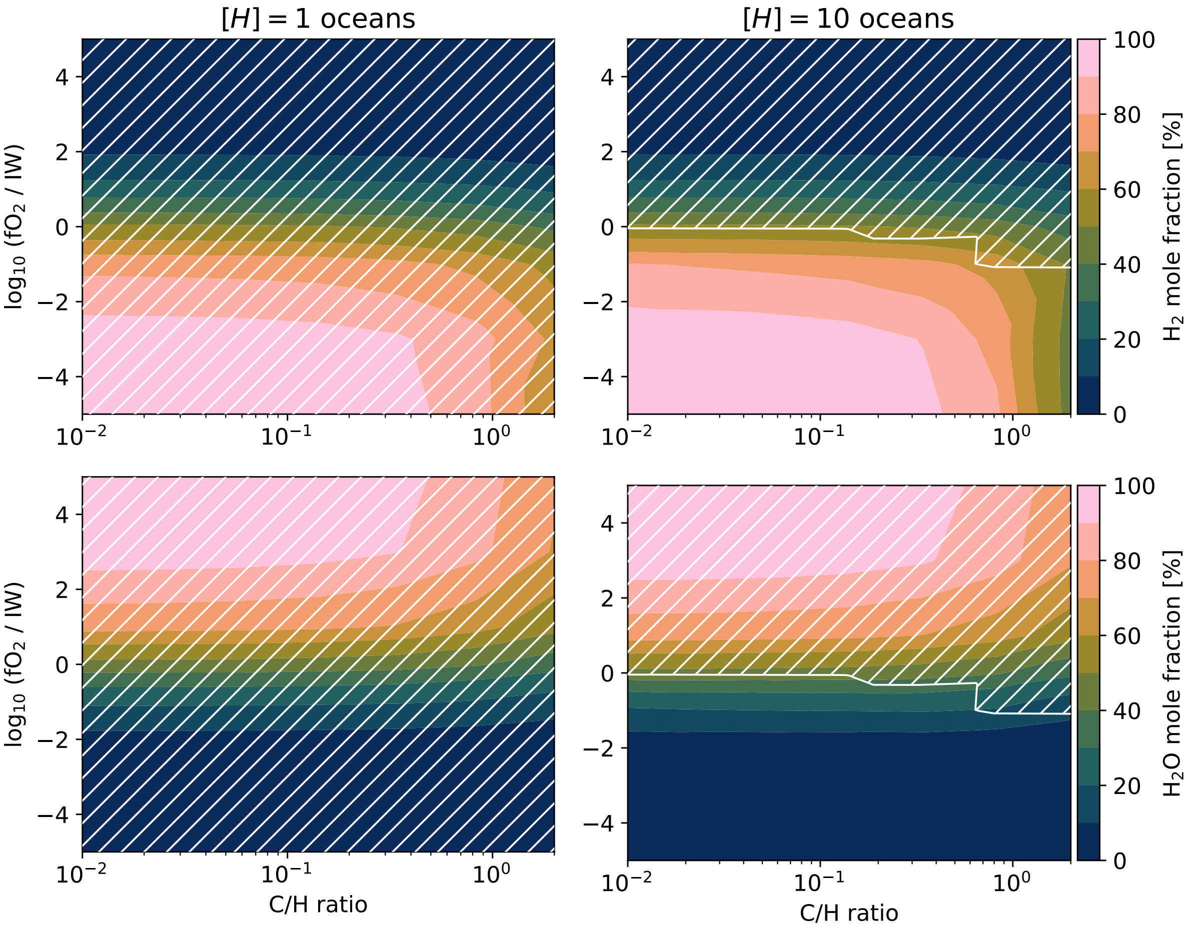

Figure 2.12: Outgassed mole fractions of H_2 and H_2O plotted versus oxygen fugacity and planetary C/H mass ratio. Here I consider two values of planetary hydrogen inventory [H] (columns). The white hatched regions indicate fully solidified cases. Orbital separation is fixed at 1.054 AU for these cases.

tio. An oxidation state comparable to modern Earth (~ IW+4) falls within the solidifying regime for all cases of [H] explored in this chapter.

What do these models say for a Venus-like scenario, given the Venus is solidified at the present day but retains a thick CO_2-dominated atmosphere? The cases at a Venus-like orbital separation of ~ 0.737 AU (not plotted in Figure 2.12) vary between fully molten and mostly solidified in my grid of models, depending on the total hydrogen content considered. At this distance, the models typically enter into a protracted mushy state following rapid initial solidification, which compares well with previous studies (e.g. Lebrun et al. 2013). Early Venus probably produced at least 2 oceans of H_2O by oxidising nebular H_2, placing $[H] \geq 2$ oceans and ruling out the $[H] = 1$ oceans case (Lammer et al. 2020; Salvador et al. 2023). Assuming that H capture and oxidation was a viable avenue of water generation in the young Venus, at least 8 oceans of H_2O are expected to have been endogeneously if the planet formed before protoplanetary disk dispersal (Williams and Mukhopadhyay 2019; Kimura and Ikoma 2020; Salvador et al. 2023). This leaves the $[H] = 10$ oceans cases in my grid, which requires highly oxidising conditions ($\geq$ IW + 5) and sufficiently high metallicities ($C/H > 0.5$) in order to avoid large amounts of remnant melt at steady state. This case (index 587) terminates within a pseudo-runaway greenhouse regime (OLR = 364 W m^{-2}) with a thick ($P_s = 2472$ bar) CO_2 dominated atmosphere which contains large amounts of steam (H_2O mole fraction of 31%). The high surface temperature ($T_s = 1740$ K) could cause most of the H_2O to escape during continued evolution, allowing the planet to desiccate and thereby replicate modern Venus-like conditions (Salvador et al. 2023).

The incorporation of parametrised atmospheric escape and aerosol formation into PROTEUS is necessary for a more direct and meaningful comparison with Venus, for which we know that clouds strongly affect the planet's current Bond albedo, and thus its radiative energy budget. An investigation into aerosols is left for future endeavours.

2.5 Shallow magma ocean states

Surfaces do not cool below the surface solidus temperature in these models because they do not evolve past the point of mantle solidification. Across fully solidified cases, final net top of atmosphere fluxes F^{atm} range between approximate radiative equilibrium ($\lesssim 3\,\mathrm{W\,m^{-2}}$) and rapid energy loss ($259\,\mathrm{W\,m^{-2}}$). Further cooling could allow for rainout of more volatile components, reducing the optical depth and radial extent of the atmosphere.

The calculation of chemical and dissolution equilibrium of volatiles can yield relatively transparent atmospheres, enabling large F^{atm} and thus rapid cooling. These atmospheres initially contain little H_2O as it is dissolved in the magma, and in some cases, such as case 714 below, are initially N_2 dominated. A form of self-regulation then occurs because H_2O (along with other volatiles) is outgassed due to bottom-up crystallisation of the mantle, which increases the radiative opacity of the atmosphere. This means that the majority of the mantle first begins to rapidly crystallises until the opacity of the atmosphere becomes large enough to stall – or prevent, in radiative equilibrium cases – complete mantle solidification. One example of this behaviour is Case 714, which is plotted in Figure 2.13.

Solidification starts from the bottom of the mantle (Section 2.2.5), with crystals forming at the core-mantle boundary and then at successively shallower layers. In this case, the rheological front lifts off the core-mantle boundary after 48.9 kyr and exceeds $0.95R_{\mathrm{p}}$ by 185.0 kyr (Figure 2.13c). Crystallisation begins at the top-most layer of the mantle after 26.7 kyr of evolution, so the magma ocean spends very little time in a completely liquid state, instead spending a significant period of the time with a shallow mixed-phase magma ocean.

Outgassing of H_2O is sufficient to shift the atmosphere from an N_2 dominated composition into a H_2O dominated one (panel e). This also leads to increased abundances of H_2 in the atmosphere through equilibrium chemistry. The radiative opacity of the atmosphere keeps the planet in a runaway regime ($T_{\mathrm{s}} \sim 1700$ K, panels b), with the OLR approximately equal to the Simpson-Nakajima limit (panel a) until solidification. The timescales for CO_2 and CO outgassing are shorter compared to H_2O due to their lower solubility in the mantle. Case 714 would continue to cool after mantle solidification, which can be inferred by the simulation terminating with a non-zero net positive top of atmosphere flux, of $72.6\,\mathrm{W\,m^{-2}}$ (Figure 2.13a). This case could then remain within the runaway greenhouse regime for some period of time until the surface cools to a sufficiently low temperature (Figure 2.7).

During the final stages of solidification ($\Phi < 1\%$) the shallow magma ocean near the surface exhibits non-linear variability on a short timescale of 18 kyr, causing the surface temperature to oscillate between 1640 and 1700 K (panel b) and outgassing to repeatedly pause and resume (panel f) due to the changing melt fraction. As the average melt fraction of the upper layers decreases, convection in the magma ocean becomes sluggish, leading to inefficient upward energy transport. These dynamics trap heat energy below the planet's surface. The local temperature increases as energy accumulates, eventually re-melting the layer and allowing convection to resume, cooling then continues once more. This behaviour is also seen in other interior evolution models (e.g. Barth et al. 2021; Herath et al. 2024; Krissansen-Totton et al. 2024) and is common to cases that fully solidify among my grid in this chapter.

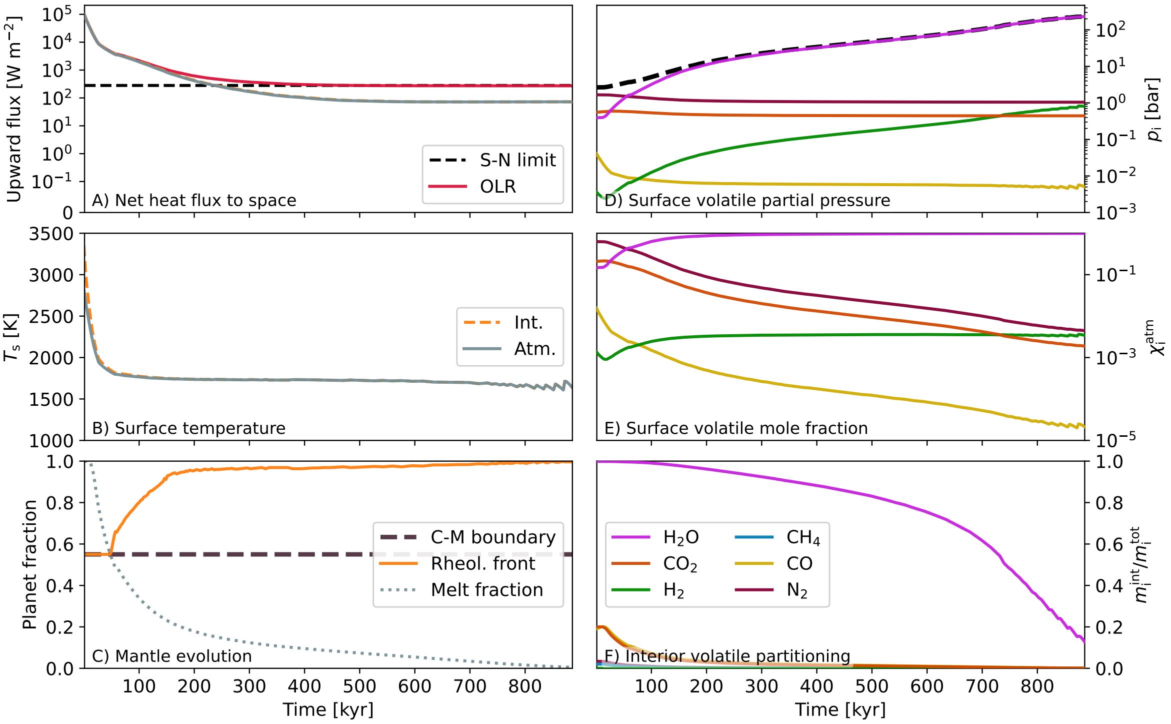

Figure 2.13: Time evolution of simulation case 714 from my grid of models, which results in solidification. Parameters: a = 1.054 AU, fO_2 = IW + 5, C/H = 0.01, [H] = 1.0 ocean. This corresponds to the upper-left corner of the left-column panels of Figure 2.12, deep within the solidifying region of the grid. All panels share the same x-axis. **Panel a**: interior (orange line) and atmospheric (grey line) net heat fluxes alongside the OLR. **Panel c**: 'C-M boundary' plots the location of the core-mantle boundary ($0.55R_p$) as to show the initial location of the rheological front.

2.6 Local radiative heating of the atmosphere

Like most previous works, the JANUS atmosphere model applied in this chapter uses a prescribed temperature structure where convection is assumed to be the main mechanism setting $T(p)$ in the atmosphere (Kopparapu et al. 2013; Hamano et al. 2015; Lichtenberg et al. 2021). However, in the case of pure steam atmospheres in equilibrium with incident stellar radiation, Selsis et al. (2023) showed that convection typically shuts-down in deep optically-thick atmosphere regions because where there is insufficient stellar flux to drive the atmosphere superadiabatic. These atmospheres develop a nearly isothermal layer near the planet's surface: similar to isothermal layers which appear in analytic radiatively-grey solutions, when neglecting the effects of pressure broadening on gas opacity (Guillot 2010; Pierrehumbert 2010; Robinson and Catling 2012). The findings of Selsis et al. (2023) are subject to uncertainties in water vapour opacities at high pressure and temperature, but nonetheless require that the shutdown of convection be considered as a possibility. When shutdown of convection in the lower atmosphere occurs, the surface temperature becomes lower than it would be on an adiabat. However, Selsis et al. (2023) did not consider the case of cooling of a primordial magma ocean; in the context of a time-dependent calculation, convective shutdown could lead to *earlier* solidification of a magma ocean than the adiabatic calculations predict, or could ultimately lead to the solidification of mantles which were otherwise predicted to be permanently molten on the basis of a fully convective atmosphere calculation. In addition to considering the transient case where a hot interior can provide a sufficient flux to maintain atmospheric convection, the atmospheres I treat also differ from those considered by Selsis et al. (2023) in that I incorporate additional opacity sources beyond H_2O that may block water vapour window regions and help maintain atmospheric convection.

Ultimately, the possibility of convective shutdown needs to be addressed in a radiative convective model that allows for radiative layers to appear self-consistently with the other physics. But as a first test of potential convective shutdown in mixed- and cooling-atmospheres, here I check whether the assumed pseudoadiabatic profiles could be maintained by looking at vertical profiles of the radiative heating rate calculated from SOCRATES. Specifically, I can test whether my computed atmospheres would be unstable to convection by analysing the radiative heating rate

$$\frac{\mathrm{d}T}{\mathrm{d}t} = \frac{g}{c_p} \cdot \frac{\mathrm{d}F}{\mathrm{d}p} \tag{2.44}$$

at each layer of the atmosphere. Radiative heating at deeper levels and cooling at adjacent upper levels would act to increase the lapse rate and promote convective instability, while the inverse configuration would act to decrease the lapse rate and lead to a convectively stable region. Figure 2.14 plots per-level radiative heating rate profiles, over time, for two of the grid cases explored in this chapter. The tropopause marked in the figure indicates the boundary of the idealised isothermal stratosphere (Equation 2.26) whereas actual radiative equilibrium could yield non-isothermal stratospheres and shift the tropopause location. The left panel indicates that Case 714 may still initially maintain strong convection from the surface, as a result of the large surface temperature, but a radiative layer may be present at lower pressures aloft (at $p < 0.1$ bar). At solidification, Case 714 may not maintain convection from the surface due a small amount of radiative heating near 0.5 bar, although greater heating at lower pressures (0.01 bar) could trigger convection aloft. The centre panel indicates that Case 205 ($a = 0.316$ AU, $fO_2 = \mathrm{IW}-1$, $C/H = 0.83$, $[\mathrm{H}] = 5$ oceans) likely could remain convectively unstable near the surface and above the nominal tropopause throughout the simulation, including when it reaches global radiative equilibrium (rightmost panel). This suggests that the presence of additional opacity sources (in this case, primarily 205 bar of CO and 57 bar of H_2 at the surface) may allow a permanent magma ocean to exist, though this suggestion must be directly tested with more complete radiative-convective equilibrium calculations. The right panel shows the radiative heating rate profile for the final iteration of Case 205, in which we can see that the layer between roughly 10 bars and 1 bar tends to be stabilised, while convection can be maintained near the surface and above the tropopause.

2.7 Discussion on implications

From these trends, I highlight a hierarchy of parameters to which early planetary magma ocean evolution is sensitive. Orbital separation is the most important factor, followed by total volatile inventory (via [H]), mantle oxygen fugacity, and finally the C/H ratio. It is possible that other factors not explored in this chapter would fit within this hierarchy:

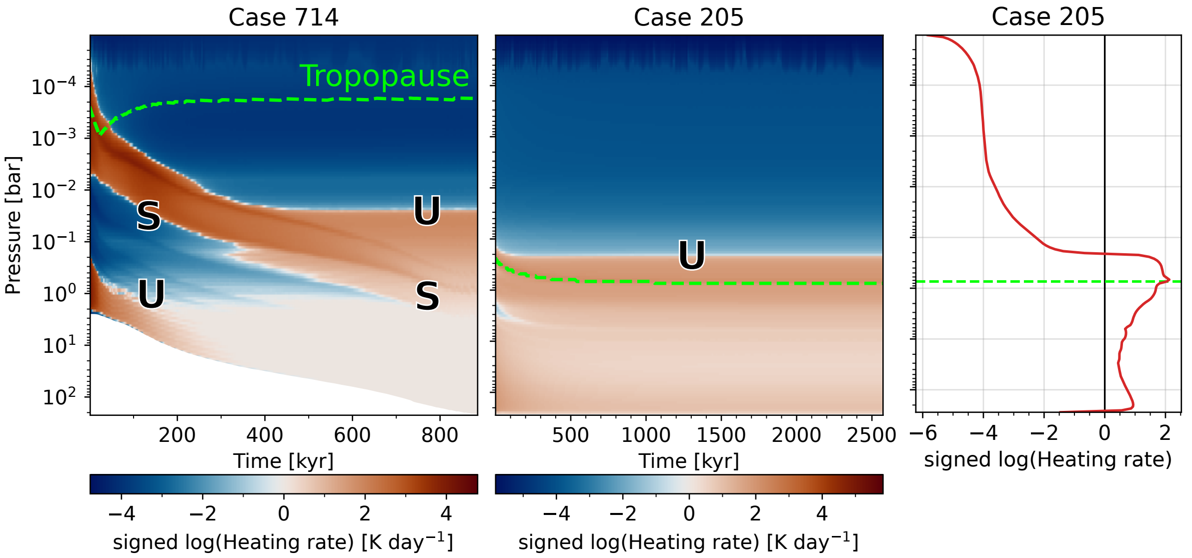

Figure 2.14: Atmospheric radiative heating profiles versus pressure and time for two cases. Case 714 (left) fully solidifies, and was discussed in Section 2.5. Case 205 (centre) reaches global radiative equilibrium while maintaining a significant melt fraction of 97.6% under a CO- and H_2-dominated atmosphere. The dashed green lines indicate the tropopause. Regions of relative radiative heating and cooling are labelled 'U' and 'S', corresponding to whether or not they are unstable or stable to convection. The rightmost panel plots the radiative heating profile at the final timestep of Case 205.

- Surface gravity. For hydrostatically supported atmospheres, scale height is inversely proportional to the gravity; so denser planets may have shallower atmospheres which are maintained against escape and blanket their atmospheres for longer times.
- Cloud parameterisation. Formation of water clouds would reflect stellar flux and also induce additional greenhouse forcing, modulating the rate at which energy can escape the planet.
- Stellar spectral class and age. Both of these factors can lead to variations in stellar emission, which directly impacts the cooling rate of orbiting planets.
- Metallic core size, r_c. This is directly tied to the volume of the mantle, for a given planet mass, and therefore relates to the inventory of dissolved volatiles, the surface pressure, and the corresponding atmospheric opacity.
- Evolution of mantle redox, proxied by $f\text{O}_2$. Multiple physical processes drive inhomogeneous changes to mantle redox state, outlined in Section 1.1.2. We expect that planets become more oxidised with age, with corresponding changes in their atmospheric composition.

There is potential for a very wide range of atmospheric compositions on rocky planets, beyond even those exhibited by this investigation. I find that atmospheres on molten planets typically have a more diverse composition than on solidified planets (which are typically composed of H_2 and/or H_2O at the end of the simulations). Additional post-solidification processes such as volcanism and in-gassing will complicate this picture further, but my results remain applicable for young planets such as TOI 1807 b and HD 63433 d (Hedges et al. 2021; Capistrant et al. 2024). Telescope observations which constrain the atmospheric composition of short-period planets could therefore be used to probe their interior properties and mantle melt state. Observations by Hu et al. (2024) indicate a carbon-rich CO_2-CO atmosphere on the ultra-short period exoplanet 55 Cancri e, a composition which corresponds to a subset of the models explored here. Not only does this observation represent the first tentative evidence of a volatile-rich secondary atmosphere on a rocky exoplanet, it shows that secondary atmospheres may be maintained for Gyr periods despite the potential for ongoing escape processes. Resolving escape and compositional fractionation of initially H-rich atmospheres may also be key to resolving the link between a planet's primordial magma ocean stage and its current conditions (Wordsworth and Kreidberg 2022).

With solidification comes outgassing of water (among other volatiles), shown in the bottom row of Figure 2.12 in which solidified cases have steam-rich atmospheres. Across solidified cases, the H_2O mole fraction varies smoothly with the oxygen fugacity and C/H ratio (bottom left panel) since atmospheric composition is no longer buffered by large amounts of melt. This behaviour is also present at higher [H], but only in the absence of any significant amount of silicate melt since the H_2O will otherwise favourably dissolve into the interior of the planet. This may make a high mole fraction of H_2O a useful tracer for a recently solidified surface, despite not being the sole driver behind early planetary evolution.

Gases beyond H_2O contribute to the opacity of these atmospheres, thereby impacting their cooling times or relaxation to radiative equilibrium. However, even for a pure-steam case I find that the post-runaway transition occurs at higher temperatures when modelled with the most up-to-date linelists, in contrast to models using HITRAN-derived opacities. Future work should explore the impacts of additional sources of atmospheric opacity. For example, CO and H_2-H_2O collisional continua at high pressure and temperature (Karman et al. 2019).

It has been previously suggested that the mass, radii, and spectroscopic observations of sub-Neptune planets can be explained by the presence of magma oceans underneath thick H_2 dominated atmospheres (Benneke et al. 2024; Luu et al. 2024; Shorttle et al. 2024). H_2 dominated atmospheres are common on permanently molten cases arising from my grid, so it may be possible that some sub-Neptunes have maintained molten surfaces since their formation, with energy loss and cooling limited by atmospheric blanketing and sufficient instellations (Vazan et al. 2018). For example, case 608 has a reducing mantle and large hydrogen inventory ($a = 1.054$ AU, $fO_2 = \mathrm{IW} - 5$, $C/H = 2$, $[\mathrm{H}] = 10$) which allows it to reach a steady state at radiative equilibrium with an H_2-dominated atmosphere ($p_{\mathrm{H}_2} = 1038$ bar) containing significant amounts of CO (329 bar) and CH_4 (103 bar). It is possible that such an atmosphere – particularly one buffered by volatiles dissolved in the mantle – could resist escape if formed around a sufficiently massive interior (Dorn and Lichtenberg 2021; Misener and Schlichting 2021). In such a case, the redox evolution of the interior would dictate the post-H-escape composition of its secondary atmosphere (Lichtenberg 2021; Lichtenberg and Miguel 2025).

It is unreasonable to assume that all planets (both within and external to the Solar System) have a similar or Earth-like mineralogy, redox state, and volatile endowment (Doyle et al. 2019a; Putirka and Rarick 2019; Gaillard et al. 2021; Guimond et al. 2023a; Lichtenberg and Miguel 2025). My simulations show that – at a fixed planet mass, instellation, and radius – the evolution of a magma ocean planet is strongly dependent on the properties of its semi-molten interior (Meier et al. 2023). This is directly reflected in the composition of the overlying atmosphere, both before and after the magma ocean solidifies. It is therefore also not possible to determine whether a given planet (with properties of its mass, instellation, etc.) will be solidified or molten without sufficient knowledge of these other parameters. However, polluted white dwarfs provide an opportunity to probe the mineralogy and elemental compositions of exoplanets and can therefore provide insight into which evolutionary pathways are compatible with contemporary observations of exoplanets (Doyle et al. 2019b; Xu and Bonsor 2021). Observations of multiple exoplanets orbiting the same host star may also be helpful in lifting this degeneracy, since they have closely related compositions but different instellations; characterising their present states and comparing with evolutionary models (such as PROTEUS) may thereby constrain their interior properties.

2.8 Discussion on limitations

My simulations show that cases modelled at orbital separations of ≤ 0.527 AU have atmospheres which are completely dry (i.e. not condensing) at termination due to the combinations of high temperatures and relatively low surface pressures resulting from volatile dissolution into their mantles. This means that volatile condensation does not occur, which precludes cloud formation but leaves open the possibility of photochemical haze production (Bergin et al. 2023b; Maillard et al. 2023). Similarly, Lebrun et al. (2013) found that rainout is unlikely to occur at $a < 0.66$ AU for planets orbiting a Sun-like star. Shallow regions of moist H_2O convection occur for a subset of my cases at 0.737 AU. At $a \geq 1.054$ AU, moist convection and/or equilibrium saturation occurs in the upper atmosphere for almost all cases. This corresponds to solidified planets (panel k of Figure 2.11) where the mole fraction H_2O of water is large.

Optically thick water clouds would reflect stellar radiation and absorb upwelling radiation, so it is unclear when they induce a net greenhouse or net anti-greenhouse effect (Pierrehumbert 2010; Salvador et al. 2017). Furthermore, clouds are expected vary in both latitude and longitude, depending on the convective dynamics of the atmosphere (Komacek et al. 2019a; Turbet et al. 2021; Turbet et al. 2023). Rainout of H_2O could allow sufficient infrared transmission such that these planets escape the runaway greenhouse regime after some time. It is unintuitive as to whether clouds generally prolong or foreshorten magma ocean solidification. Future work should explore the role of aerosols in regulating magma ocean thermal evolution – particularly if comparisons with Venus and Earth – potentially via a comparison against global circulation models.

The results presented in Section 2.6 indicate that the atmospheres of young rocky worlds may present radiative layers, despite my assumption that they are fully convective below the stratosphere. However, it is also shown that some planets which maintain permanent magma oceans (e.g. case 205 - Figure 2.14) may still able to remain convectively unstable in near-surface layers. Calculation of an energy-conserving atmospheric temperature structure (and resultant energy fluxes) would provide more accurate estimates for energy loss to space, potentially changing the solidification times calculated in this chapter (see also Salvador et al. 2017). Although JANUS prescribes a temperature profile for the atmosphere similarly to previous works (e.g. Lebrun et al. 2013; Hamano et al. 2015; Nikolaou et al. 2019; Lichtenberg et al. 2021), it is possible that cases in the grid which remain molten at steady state would instead solidify in reality. My prediction that some planets orbiting within the habitable zones of Sun-like stars may maintain permanent magma oceans at steady state is in line with previous predictions (e.g. Hamano et al. 2015), although this finding may not hold when accounting for convective shutdown.

Atmospheric escape would act to remove volatiles from the system over extended periods. However, due to the prescriptive nature of the JANUS atmosphere model, calculations of escape rate would offer little investigative value and are thus neglected. The equilibrium chemistry calculated for Case 714 (Figure 2.13) yields only minor abundances of low molecular weight species (H_2, CO), so it is possible that this atmosphere would be maintained against significant escape. However, more complete calculations of the chemistry would be required to determine the speciation of elements in the regions of the upper atmosphere from which escape is occurring (Odert et al. 2018; Tsai et al. 2021a). Together, chemistry and escape could influence outgassing rates – subject to sufficient mixing – through transport of volatiles from the surface into the aloft regions, which is then compensated by further outgassing (Wordsworth et al. 2018; Cherubim et al. 2024). Together, chemistry and escape are expected to shorten magma ocean lifetimes compared to the calculations made in this chapter. Uncertainties in volatile accretion, however, could partially compensate for these processes (Venturini et al. 2020; Zahnle et al. 2020; Lichtenberg and Clement 2022).

In this chapter, I do not include tidal effects on the interior which could be a significant source of heating for planets within tightly packed systems or on elliptical orbits (Bolmont et al. 2013; Bower et al. 2019; Hay and Matsuyama 2019; Seligman et al. 2024). The effects of tidal heating are modelled and discussed in Chapters 4 and 5. The SPIDER interior model, which is able to resolve melt-crystal separation as the magma ocean evolves, shows that interior energy transport by convection is largely offset by other transport processes. In the case of tidal stresses dissipated near the surface, additional heating could act to extend magma ocean lifetimes and to influence the composition and structure of overlying atmospheres.

In these simulations, I have used a mass-balance approach to simultaneously solve for chemical and dissolution equilibrium, but only for a small set of volatiles. Vapour species bearing refractory elements (e.g. SiO, SiH_4) may be present in the atmospheres of hot rocky planets to various degrees (Wolf et al. 2023; Hakim et al. 2025), impacting their radiation environment and inducing atmosphere thermal inversions through their large optical opacity (Piette et al. 2023; Zilinskas et al. 2023). These latter two works solve for chemical and dissolution equilibrium as separate processes, obtaining the total gas budgets by adding the results of each calculation. Falco et al. (2024) self-consistently solved for chemical and dissolution equilibrium of rock vapours and volatiles, finding that it is necessary to solve for the whole chemical system of volatiles plus refractory vapours simultaneously. Falco et al. (2024) and Zilinskas et al. (2023) found that only small amounts of hydrogen are required to prevent the formation of a thermal inversion in the atmosphere; quantified as χ_{H_2} and bulk planet H, respectively. Increased amounts of hydrogen in the atmosphere necessarily raise the abundance of H_2O, which has a strong infrared absorption cross-section, so the transition between inverted and non-inverted temperature profiles is narrow in the phase-space of atmospheric composition. Using the empirical fit for the transition derived by Falco et al. (2024) I find that all cases explored in the grid fall deep within the non-inverted regime. It is therefore expected that the inclusion of rock vapours would have a negligible impact on the results presented in this chapter.

In reality, condensation does not necessarily occur exactly when $T = T_{\mathrm{dew}}$; the microphysics of droplet formation is often enabled by the presence of condensation nuclei which provide surfaces onto which a saturated mixture condenses liquid and/or solid phases (Farmer et al. 2015; Helling 2019; Lee and Ohno 2025). Theoretical models suggest that mineral vapour clouds may form near the surfaces of hot sub-Neptune exoplanets, which would substantially impact their energy balance through additional opacity and scattering effects (Bower et al. 2025; Hakim et al. 2025). I neglect aerosol microphysics in this thesis and always assume that condensation occurs upon saturation. Further to complications from aerosol microphysics, we must recall that convection is fundamentally driven by buoyancy gradients. So, potentially countering buoyancy driven by decrease in gas density caused by radiative heating, compositional gradients in the atmosphere may act to prevent convection, despite the temperature gradient exceeding the usual critical lapse rate (Equation 2.23). We may instead substitute the Schwarzschild criterion for the Ledoux et al. (1961) criterion to capture the stabilisation against convection by molecular weight gradients, although this does not account for moist processes (Joyce and Tayar 2023). Simultaneously accounting for condensation and compositional stabilisation, through the Guillot (1995) criterion, has recently found application in planetary atmospheres (Leconte et al. 2017; Tremblin et al. 2019; Habib and Pierrehumbert 2024). Furthermore, ab initio simulations have shown that H_2O can demix from an H_2 background at low temperatures in a manner similar to condensation rain-out of H_2O (Bergermann et al. 2024; Howard et al. 2025).

2.9 Chapter conclusions

I have introduced a modular numerical framework designed to simulate coupled interior-atmosphere evolution of small (exo)planets across a range of early conditions. In this chapter, I explore the particular effects of differences in whole-planet volatile inventories and upper-mantle redox state. These variations result in cases which either fully solidify, or reach global radiative equilibrium while maintaining some amount of interior melt.

The main conclusions from this chapter are as follows.

1. Atmospheres which overlie magma oceans can have diverse compositions ranging from H_2- to CO_2-dominated, while recently solidified planets typically have atmospheres composed of H_2 and/or H_2O (by mole fraction).
2. Thermal blanketing by radiatively opaque atmospheres means that magma oceans may spend most of their lifetime in a semi-molten mushy state, with significant energy transport generated by crystallisation and gravitational settling. The opacity of H_2 – in part due to its collision-induced continuum absorption – moderates

early magma ocean cooling by 10s to 100s of Myr, even for planets orbiting Sun-like stars at relatively temperate distances.

3. Whether a magma ocean solidifies depends not only on its planet's instellation flux, but also on other planetary properties; e.g. bulk C/H ratio, mantle oxygen fugacity, and volatile inventory. It is critically important to consider a wide range of initial conditions when using present-day observations of a planet to constrain its historical evolution.
4. Radiative heating rates within my simulated atmospheres indicate that they may maintain strong atmospheric convection while initially hot and molten. However, it is possible that atmospheric convection shuts down at later (cooler) stages in their evolution. Chapter 3 will explore this possibility in detail.

PROTEUS enables future modelling to incorporate a range of additional physical processes as necessary, such as: radiative-convective energy balance and chemical kinetics in the atmosphere, volatile escape processes, interior tidal heating, giant impacts and volatile delivery, and late-stage geochemical cycling and weathering. Inclusion of the relevant processes, where necessary, can enable a complete exploration of the geophysical history of exoplanets in diverse regimes.

Chapter 3

Convective shutdown in outgassed atmospheres

Following the results presented in Chapter 2, this chapter develops a novel radiative-convective atmospheric model and incorporates it within the wider PROTEUS framework. With these tools, I investigate dry convective (in)stability within the volatile atmospheres of two recently-observed rocky exoplanets, and discuss observable emission features that arise from these environments. A portion of the results presented in this chapter are published in the Mon. Not. R. Astron. Soc (Nicholls et al. 2025c) and the numerical tooling in the Journal of Open Source Software (Nicholls et al. 2025b).

3.1 Introduction

Across the literature, theoretical studies of younger planets and those in long-term runaway greenhouse states often make the assumption that their atmospheres are fully convective, *viz.*, that they are unstable to convection from the surface upwards. This means that the corresponding atmospheric temperature profiles are prescriptively set by dry convection in dry regions, moist convection in regions where volatiles condense, and in some cases through a parametrized isothermal stratosphere (e.g. Abe and Matsui 1986; Elkins-Tanton 2008; Kopparapu et al. 2013; Lebrun et al. 2013; Hamano et al. 2015; Schaefer et al. 2016; Salvador et al. 2017; Boukrouche et al. 2021; Zieba et al. 2023; Krissansen-Totton et al. 2024). This assumption of convective instability is central to our current understanding of the behaviour of planets within the runaway greenhouse regime (Goldblatt et al. 2013; Graham et al. 2021). In the previous chapter, I studied the time-evolved behaviour of young Earth-sized planets at arbitrary redox state. I did this by introducing and employing PROTEUS, also while making the assumption of complete atmospheric convective instability under the JANUS atmosphere model. The JANUS model generates atmosphere temperature structures by integrating a generalised moist pseudoadiabatic lapse rate (Equation 2.25; Graham et al. 2021) and then performs spectral radiative transfer calculations using SOCRATES (Manners 2024). However, my analysis of atmospheric radiative heating rate profiles in Section 2.6 strongly indicates that atmospheres overlying early magma oceans may be conditionally stable to convection. Convection can be triggered under various criteria, but it's possible that insufficient near-surface absorption of stellar radiation or dominant absorption in the upper atmosphere may lead to deep layers which are stable to convection.

Selsis et al. (2023) used a radiative-convective model of *pure*-H_2O atmospheres to test the assumption of convective instability, finding that deep isothermal layers – stable to convection – can form. Zilinskas et al. (2023) and Piette et al. (2023) modelled atmospheres containing rock vapours of refractory elements, yielding a range of near-isothermal and inverted atmospheres, which also contrasts with the previously-held assumption of convective stability. Neglecting scattering processes and assuming spectrally-grey absorption allows analytical solutions to the radiative transfer equation. These solutions yield deep isothermal (i.e. not convective) layers when the internal heat production from the planet is small or zero, which is represented in the literature by $T_{\mathrm{int}} \approx 0$ which corresponds to $F^{\mathrm{atm}} \approx 0$ in the nomenclature of this thesis (Guillot 2010; Pierrehumbert 2010). The presence of these layers means that some planets may be able to reach radiative equilibrium at lower surface temperatures than under the simplified fully-convective paradigm, potentially precluding magma oceans in some cases. Furthermore, shutdown of convection may inhibit the vertical transport of gases – chemical kinetics models often relate mass diffusion coefficients and fluxes to measures of convective vigour (Parmentier et al. 2013; Lee et al. 2024).

In this chapter I explore whether the planetary atmospheres of mixed volatile composition overlying magma oceans can remain convectively unstable, and the implications that potential convective stability (shutdown) has for planetary cooling and magma ocean solidification. To make this investigation, I present a new atmosphere model which is coupled into an updated version of the PROTEUS framework. I apply this modelling setup to the cases of two exoplanets (HD 63433 d and TRAPPIST-1 c), make assessments about their potential evolutionary histories, and probe the range of evolutionary pathways that Earth-mass planets could exhibit more generally. Non-grey radiative transfer allows a calculation of outgoing emission spectra and the identification of potentially-observable molecular features.

3.2 A model for extreme atmospheres on rocky exoplanets

AGNI[1] is a new 1D numerical model designed to efficiently simulate the atmospheres of planets under extreme conditions. Unlike JANUS, it is able to account for the possibility of convectively stable regions in the atmosphere. AGNI is written in the Julia programming language (Bezanson et al. 2017) and implements SOCRATES to simulate radiative transfer (Edwards and Slingo 1996; Sergeev et al. 2023; Manners 2024). This is the same radiative transfer scheme as used in the JANUS atmosphere model, and was described in Section 2.2.7. Building upon the work of the previous chapter, I also include the additional sources of opacity in my radiative transfer calculations, which are outlined in Table 3.1.

The atmosphere is constructed with N layers (cell-centres), corresponding to $N + 1$ interfaces (cell-edges). The radiative transfer calculation takes cell-centre temperatures T_l, pressures p_l, geometric heights z_l, densities ρ_l, and gas volume mixing ratios as input variables to each layer l, as well as flux boundary conditions described in Section 2.2.8. Cell-edge thermodynamic quantities in the bulk atmosphere are interpolated from cell-centres (Section 3.2.6) to cell-edges. In return from the radiative transfer – Equations 2.28, 2.33, and 2.29 – we obtain spectroscopic radiation energy fluxes F_l^{rad} at all $N + 1$ interfaces. This accounts for the absorption of radiation within each layer, its thermal emission, Rayleigh scattering, water cloud radiative effects, and surface reflection.

Gas	Linelist	References
NH_3	CoYuTe	Al Derzi et al. (2015) and Coles et al. (2019)
SO_2	ExoAmes	Underwood et al. (2016)
N_2O	HITEMP2019	Hargreaves et al. (2019)
O_3	HITRAN2020	Gordon et al. (2022a)
H_2S	AYT2	Azzam et al. (2016) and Chubb et al. (2018)
HCN	Harris	Harris et al. (2006) and Barber et al. (2013)

Table 3.1: Additional sources of opacity introduced in this chapter. All opacities are derived from the DACE database (Grimm et al. 2021). Other sources of opacity included in my models are described in Table 2.2.

---

[1] `https://h-nicholls.space/AGNI`

3.2.1 Mixing-length theory of convection

AGNI employs a parameterisation of atmospheric convection to obtain an estimate of the vertical energy flux associated with convection. Convection is fundamentally a process which occurs across more than one spatial dimension in a fluid, although it plays a critical role in setting a planet's climate, and so must be included within my otherwise one dimensional models in a parametrised form. I apply mixing length theory (MLT) to directly calculate the energy flux F^{cvt} associated with convective heat transport in planetary atmospheres (Vitense 1953; Robinson and Marley 2014; Joyce and Tayar 2023; Lee et al. 2024). Canonical MLT neglects to resolve the full spectrum of turbulence associated with real convection, and instead implicitly considers only a single convective eddy, represented by a rising parcel of air which diffuses energy over some *mixing length* λ (Joyce and Tayar 2023). This is analogous to only treating the dominant wavenumber of turbulence (Canuto and Mazzitelli 1991). With this assumption, we can derive an equation which allows a calculation of the energy flux associated with convection that is induced by the local lapse rate ∇_T exceeding that of an adiabat ∇_{ad}. This derivation is undertaken in Appendix F, so only the most important equations are presented here.

The convective heat flux is given by,

$$F^{\mathrm{cvt}} = \frac{1}{2}\rho c_{pm} w T \frac{\lambda}{H}(\nabla_T - \nabla_{\mathrm{ad}}), \tag{3.1}$$

where T is the local temperature, c_{pm} is the heat capacity of the gas per unit mass,

$$w = \lambda\sqrt{(g/H)(\nabla_T - \nabla_{\mathrm{ad}})} \tag{3.2}$$

is the characteristic upward velocity, H is the pressure scale-height,

$$\nabla_T = \frac{\mathrm{d}\ln T}{\mathrm{d}\ln p} \tag{3.3}$$

is the lapse rate of the atmosphere, and here I apply the Schwarzschild stability criterion, so

$$\nabla_{\mathrm{ad}} = \frac{R}{\mu c_{pm}} \tag{3.4}$$

is the dry adiabatic lapse rate (Section 2.2.6; Appendix E). μ is the local mean molecular weight of the gas and $R = 8.314\,463\,\mathrm{J\,K^{-1}\,mol^{-1}}$ is the universal gas constant. The Schwarzschild criterion does not account for potential stabilisation against convection caused by vertical gradients in μ, nor by latent heating (Ledoux et al. 1961; Tremblin et al. 2015; Habib and Pierrehumbert 2024).

Convecting parcels of gas transport energy by diffusion over a characteristic mixing length,

$$\lambda = \frac{k_v z}{1 + k_v z/H}, \tag{3.5}$$

where $k_v \approx 1/\sqrt{2\pi}$ is Von Karman's constant and z is the geometrical height above the surface of the planet (Blackadar 1962; Högström 1988). In practice, the resultant temperature structures and convective fluxes have little sensitivity to the specific parametrisation of λ, but it exists to ensure that the convective flux approaches zero close to the surface of the planet (Joyce and Tayar 2023). This expectation that $\lambda \rightarrow 0$ as $z \rightarrow 0$ respects conservation of momentum in the fluid via the 'Law of the Wall' to parametrise the velocity profile in the unresolved near-surface turbulent boundary layer (Von Karman 1930; Blackadar 1962; Högström 1988; Ali and Dey 2020).

Using MLT to parametrise convection also allows AGNI to calculate an estimate for the eddy diffusion coefficient [m^2/kg] associated with convective motions,

$$K_{zz} = w\lambda, \tag{3.6}$$

although this does not capture the mixing effects caused by other dynamical processes, such as gravity wave breaking (Parmentier et al. 2013; Noti and Lee 2024). Even this simple estimate for this coefficient is useful, because profiles of K_{zz} as a function of altitude are used to parametrise the mixing of gases in a compositionally inhomogeneous atmosphere. These profiles are an important – and otherwise unconstrained – input parameter to chemical kinetics schemes, which can then resolve the balance ('quenching') between the timescale of dynamical mixing and the timescale of disequilibrium chemistry (Seinfeld and Pandis 2006; Goyal et al. 2020; Tsai et al. 2021a).

Other parametrisations exist for representing atmospheric convection in 1D. Adjustment schemes are often applied in atmospheric climate models as they are computationally efficient so long as the radiative timescales are short (e.g. Malik et al. 2017; Innes et al. 2023; Selsis et al. 2023; Wogan et al. 2024). These schemes function by timestepping an atmospheric profile according to a radiative heating rate (Equation 2.44), and then forcibly adjusting the temperature profile towards the corresponding (pseudo-)adiabatic lapse rate within unstable regions (Marley and Robinson 2015). However, adjustment schemes are not numerically differentiable, do not explicitly calculate convective heat fluxes, and do not provide any estimates for K_{zz}. There have previously been efforts towards developing 'full-spectrum' turbulence models of stellar convection: Canuto and Mazzitelli (1991) and later Canuto et al. (1996). These 1D models evaluate the energy spectrum of turbulent transport across a wide range of spatial scales, thereby resolving the energy cascade from large convective motions towards the turbulent and dissipative viscous regime (Goldstein et al. 2002; Browning et al. 2004; Young and Read 2017). In directly treating the spectrum of turbulent energy transport, these full-spectrum models yield larger convective heat fluxes compared to canonical MLT formalisms. Full-spectrum models have seen some success in modelling white-dwarves (Benvenuto and Althaus 1997), although the MLT formalism is still more commonly applied to stellar models because of its simplicity and flexibility (Allard and Hauschildt 1995; Paxton et al. 2011; Marley and Robinson 2015). For example, MLT can be readily extended to account for overshooting beyond strictly convectively unstable regions (Grossman 1996; Browning et al. 2004) and to incorporate the diabatic effects of condensation (Tremblin et al. 2015; Tremblin et al. 2019). In this thesis I adopt the canonical MLT formalism for parametrising planetary atmospheric convection with its deficiencies in-mind.

3.2.2 Sensible heat and conduction

AGNI models the sensible transport $F^{\rm sns}$ of heat between the surface $l = N + 1$ and the lowest layer $l = N$ of the atmosphere using a simple turbulent kinetic energy scheme,

$$F^{\rm sns}_{N+1} = c_{pm} \rho C_d U (T_s - T_N) \tag{3.7}$$

where C_d is a heat exchange coefficient, and $U = 2\,{\rm m\,s^{-1}}$ is the surface wind speed (Pierrehumbert 2010; Bonan 2015). I choose a fixed value for the wind speed U because calculating a single representative value for U necessitates resolving the fluid dynamics of the turbulent atmosphere-surface boundary layer – which would depend on atmospheric composition and vary spatially across the planet's surface. The sensible heat component $F^{\rm sns}$ does not encompass latent heat effects, and is usually negligible for my purposes. Qualitatively: the sensible heat flux depends on the temperature difference between the ground T_s and the temperature T_N at the top of the boundary layer. In this thesis, I fix the dimensionless exchange coefficient as 0.001, but it can also be estimated analytically:

$$C_d = \left(\frac{k_v}{\ln(z/\xi)}\right)^2, \tag{3.8}$$

where $z \sim 10$ m is the thickness of the boundary layer and $\xi \sim 0.01$ m is the surface roughness length scale (Nicholson and Benn 2006).

Similarly, AGNI can account for heat transport by thermal conduction through each layer of the atmosphere via Fourier's law,

$$F^{\mathrm{cdt}} = -k\frac{\mathrm{d}T}{\mathrm{d}z} \tag{3.9}$$

where k is the mass-averaged thermal conductivity of the mixture [$\mathrm{W\,m^{-2}\,K^{-1}}$]. This conductive contribution to the atmospheric energy budget is readily negligible except in the ionised upper atmosphere (thermosphere) at pressures less than 0.01 mbar (Gonzalez-Galindo et al. 2009; Gronoff et al. 2020), which is not a focus of the investigations undertaken in this thesis.

3.2.3 Volatile phase changes and latent heat

Volatile phase change (condensation, sublimation, evaporation) and associated energy transport is included in AGNI through a scheme which assumes a fixed condensation timescale t_{cond}. Taking $t_{\mathrm{cond}} = 0$ is physically analogous to an instantaneous moist adjustment scheme. Given a temperature profile, this takes place as follows:

1. A temperature profile is calculated or provided, such as by Equation 3.14.
2. The *surface* partial pressures of super-saturated volatiles are reduced to saturation. The total surface pressure and gas mixing ratios are re-normalised accordingly, and a new pressure grid is generated.
3. Based on the atmosphere temperature-pressure points in the column, condensation of super-saturated condensable volatiles occurs at each pressure level l until the partial pressures p_j of all volatiles j are equal to their saturation pressure $p_j^{\mathrm{sat}}(T_l)$ at the local temperature T_l. The corresponding change in gas mixing ratio is denoted $\delta\chi_j$. Cold-trapping is enforced such that the mixing ratio of condensing volatiles at $\chi_{j,l}$ is always constant or decreasing with height.

4. The mixing ratios of dry (non-condensing) species are increased at each level in order to satisfy the total pressure. The mixing ratios must always sum to unity. This is consistent with the model using a fixed pressure-grid (Innes et al. 2023), and is physically equivalent to adjusting the vertical location of the grid cells in a non-hydrostatic model.
5. For volatiles j which were super-saturated and then set to saturation in the first step, a corresponding yield of condensate [kg m^{-2}] is generated at that condensing level l by mass conservation:
$$\delta m_{j,l} = \delta \chi_j \frac{p_l \mu_j}{g_l \bar{\mu}_l} \tag{3.10}$$
6. The mass per unit area of condensate produced, $\delta m_{j,l}$, is calculated at each layer l. The sum of this quantity for a given species j represents the total amount of its condensate (e.g. rain) produced throughout the column.
7. Through a downward integration, the sum of $\delta m_{j,l}$ over all condensing regions is distributed into dry regions at height levels below the condensing regions, representing re-evaporation of falling precipitate. $\delta m_{j,l}$ is assigned a negative sign in these evaporating regions, also via Equation 3.10. The gas phase mixing ratio of j becomes at-most exactly saturated by evaporation at each level, until all rain is re-evaporated in the atmosphere or reaches the surface, by which the mass balance is closed.
8. The local heating associated with phase change in condensing and evaporating regions is calculated from the enthalpy of phase change as
$$\mathrm{d}F^{\mathrm{lat}}_{j,l} = \delta m_{j,l} L_j(T_l) / t_{\mathrm{cond}} \tag{3.11}$$
9. The total heating rate in each layer $\mathrm{d}F^{\mathrm{lat}}_l = \sum_j \mathrm{d}F^{\mathrm{lat}}_{j,l}$ is integrated from the top of the atmosphere downwards to provide the latent heat component to cell-edge energy fluxes F^{lat} between adjacent layers. This heat flux contributes to the total heat budget, and acts to warm regions of condensation and cool regions of evaporation.

The latent heating rate $\mathrm{d}F^{\mathrm{lat}}$ can take any sign, but the latent heat flux F^{lat} is always positively signed because it has a value of zero at the top of the atmosphere and the mass budget is ensured to be closed. Since condensation is taken to be part of a cycle of upward transport, condensation, precipitation, and evaporation, this latent heat transport is conceptually generated by the motion of condensable gases (Pierrehumbert 2010; Ding and Pierrehumbert 2016). The timescale t_{cond} physically represents the microphysics of condensation; calculating t_{cond} self-consistently with a microphysical model is beyond the scope of this thesis, so I use a representative value of 3×10^4 s (Trenberth 1992) although sensitivity tests show that my calculations are not sensitive to this value. This scheme could also be extended to include a microphysically-informed calculation of t_{cond} (e.g. Lee and Ohno 2025). Overall, this scheme for handling condensation is preferred over direct moist temperature adjustment as it does not require invocation of enthalpy conservation and is numerically differentiable with respect to temperature. Differentiability is a necessary requirement for the numerical method introduced in Section 3.2.4.

Since I typically consider deep and hot atmospheres in this thesis, precipitation is usually found to re-evaporate before reaching the surface; analogous to 'virga' clouds on Earth and the observed behaviour of sulphuric acid rain on Venus (Taylor and Hunten 2014). Precipitation entering supercritical layers from above is miscibly incorporated without releasing latent heat, since $L(T_{\text{crit}})$ equals zero (see Figure 3.2). Ocean formation can occur in my models when precipitation reaches the surface without evaporating or the surface-layer becomes saturated. The surface condensate inventory is then calculated as $\sum_l \delta m_{j,l}$, which is conceptually similar to the method described by Derras-Chouk et al. (2025). In this chapter, the atmosphere is assumed to be a hydrostatically supported ideal gas, although I expand my thermodynamic treatment to a real gas formulation in Chapter 5.

3.2.4 Numerical optimisation solver

The energy flux $F_l = F_l^{\text{up}} - F_i^{\text{down}}$ describes the net upward-directed energy transport [W m^{-2}] from layer l into the adjacent layer $l-1$ above (or into Space for $l = 1$). Taking all the energy transport processes together, this is simply:

$$F_l = F_l^{\text{sns}} + F_l^{\text{cvt}} + F_l^{\text{lat}} + F_l^{\text{rad}} + F_l^{\text{cdt}} \tag{3.12}$$

For energy to be conserved throughout the column, under the plane parallel approximation it must be true that $F_l = F_t \; \forall \; l$ where F^{atm} is the net flux transported through the atmosphere. I use this construction in AGNI to calculate the temperature profile of the atmosphere as an $N+1$-dimensional root-finding problem. Solving for the $T(p)$ profile which conserves energy fluxes in this way avoids having to invoke heating rate calculations, thereby sidestepping slow convergence in regions with long radiative timescales. The temperature structure solution is obtained iteratively from some initial guess. At each iteration of the solver, the residuals vector (length $N+1$) of flux differences

$$\mathbf{r} = \begin{pmatrix} r_l \\ r_{l+1} \\ \vdots \\ r_N \\ r_{N+1} \end{pmatrix} = \begin{pmatrix} F_{l+1} - F_l \\ F_{l+2} - F_{l+1} \\ \vdots \\ F_{N+1} - F_N \\ F_{N+1} - F^{\mathrm{atm}} \end{pmatrix} \tag{3.13}$$

is calculated using the cell-centre temperature guess,

$$\mathbf{x} = \begin{pmatrix} T_l \\ T_{l+1} \\ \vdots \\ T_N \\ T_s \end{pmatrix} \tag{3.14}$$

where T_s is the surface temperature. The top-most cell edge temperature is extrapolated log-linearly with constant $\mathrm{d}T / \mathrm{d}\log p$, although this layer is set to be very small.

The surface temperature T_s can be calculated in three different ways depending on the boundary condition required by the modelling context. Firstly, it may be simply fixed by the user at a constant value – potentially related to some intrinsic temperature as $F^{\mathrm{atm}} = \sigma T_{\mathrm{int}}^4$. Secondly, as is the case when applying AGNI as the `atmos_clim` module within PROTEUS, the surface temperature and net flux will be solved together according to a conductive boundary layer at the mantle-atmosphere interface which introduces the auxiliary Equation 2.1 and a fixed mantle temperature T_m. Thirdly, when the net flux F^{atm} is pre-defined by the user, the surface temperature T_s will be extrapolated log-linearly from T_N.

The Jacobian matrix **J** represents the directional gradient of the residuals **r** with respect to the solution vector **x**. It is a square matrix with elements defined as

$$J_{uv} = \frac{\partial r_u}{\partial x_v} \tag{3.15}$$

AGNI estimates **J** using a 2nd-order central finite-difference: each level v with temperature x_v is perturbed by an amount $\pm\varepsilon x_v$ in order to fill a single column of $\mathbf{J}$. The value of ε must be chosen carefully; small enough to induce an almost-infinitesimal perturbation in $\mathbf{x}$, but large enough to avoid errors arising from floating point precision. I use $\varepsilon = 3 \times 10^{-5}$ in all cases. Forward and backward finite-difference methods yield significant performance improvements at face value, by almost halving the number of radiative transfer calculations, but also lead to poor estimates of J_{uv} and thus poor convergence. I found that 4^{th}-order finite-difference approximations do not improve model convergence or stability.

It can be expensive to construct a full Jacobian and would be wasteful if it were discarded at the end of each iteration, so AGNI retains some of the elements in $\mathbf{J}$ between iterations. This assumes that the second derivative of the residuals is small. A column v is retained only when

$$\max_{l} |r_l| < 0.1 \text{ for } l \in \{v-2, v, v+2\} \tag{3.16}$$

and when the model is globally is not too close to convergence. With a Jacobian constructed, an update $\mathbf{d}$ to the solution vector $\mathbf{x} \rightarrow \mathbf{x} + \mathbf{d}$ is performed. This is nominally calculated using an extension of the Newton-Raphson method to $N+1$ dimensions,

$$\mathbf{d} = -\mathbf{J}^{-1}\mathbf{r} \tag{3.17}$$

Gauss-Newton and Levenberg-Marquardt methods (Press 2007) are also supported by AGNI as alternatives to Equation 3.17, but are generally not found to offer a meaningful improvement to solver convergence.

If the solver enters a local minimum where the residuals are not decreasing from one iteration to the next, the system is nudged by scaling the update $\mathbf{d}$ by a scalar factor s. The non-convexity of the solution space and somewhat discontinuous nature of the physics means that large $\mathbf{d}$ can also be problematic, resulting in model instability. When $|\mathbf{d}| > d_{\text{max}}$, the update is scaled as $\mathbf{d} \rightarrow d_{\text{max}}\hat{\mathbf{d}}$. A value of $d_{\text{max}} = 200$ K generally works well, but may need to be varied depending on the problem under consideration. To improve convergence, the update $\mathbf{d}$ may also be scaled by a line-search method: $\mathbf{d} \rightarrow \alpha\mathbf{d}$. A line-search is applied if the full $\mathbf{d}$ would increase the cost (Equation 3.18) by an unacceptable amount. If the model is close to convergence, then a golden-section search method is used to determine α, otherwise a backtracking method is used with a scale factor $\tau_{\mathrm{BT}} = 0.7$ (Press 2007). All three of these scalings to $\mathbf{d}$ preserve its direction through the solution space.

The model converges upon a solution for the temperature structure when the 'cost function', the 3-norm of the residuals,

$$\mathcal{C}(\mathbf{x}) = \left(\sum_l |r_l|^3 \right)^{1/3} \tag{3.18}$$

satisfies the condition

$$\mathcal{C}(\mathbf{x}) < \mathcal{C}_a + \mathcal{C}_r \max_l |F_l| \tag{3.19}$$

which represents a state where the fluxes are sufficiently conserved. $\mathcal{C}_a$ and $\mathcal{C}_r$ are the absolute and relative solver tolerances. I have found that the model is relatively insensitive to these tolerances; values as large as $\mathcal{C}_a = 2\,\mathrm{W\,m^{-2}}$ and $\mathcal{C}_r = 0.15$ can work reliably.

3.2.5 Atmospheric thermochemistry

In this thesis – as in previous works on the subject – atmospheres are generally modelled with well-mixed compositions. In reality, the chemistry of an atmosphere is complex due to various processes interacting non-linearly to together change the abundances of chemical species at the surface and aloft (Seinfeld and Pandis 2006). Changes in the composition and chemistry of an atmosphere can also impact its opacity to radiation, and thus its temperature structure (e.g. Drummond et al. 2016; Tsai et al. 2022; Nicholls et al. 2023 in an exoplanetary context).

A common assumption is that atmospheres instantaneously maintain *chemical equilibrium*, where all reactions are reversible through some pathway and the forward and backward rates of each are equal (although not necessarily zero). I also applied this assumption to my outgassing calculations previously described in Section 2.2.4.

The Gibbs free energy of a closed thermodynamic system is

$$G = U + pV - TS \tag{3.20}$$

then, by the product rule, its derivative is

$$\mathrm{d}G = \mathrm{d}U + p\,\mathrm{d}V + V\,\mathrm{d}p - T\,\mathrm{d}S - S\,\mathrm{d}T \tag{3.21}$$

where U is internal energy and V is volume. The entropy S of a closed system will increase over time or remain constant. Therefore, at equilibrium (with constant p and V) G is minimised and $\mathrm{d}G = 0$.

From this, we can obtain the relationship between Gibbs free energy and the equilibrium constant of a chemical reaction,

$$\ln K_j(T) = \frac{-\Delta G_j^\circ(T)}{RT} \tag{3.22}$$

which is identical to Equation 2.13 used in my volatile outgassing scheme. A derivation of this relationship is described in Appendix C and by Denbigh (1981).

The equilibrium constant factors into the Law of Mass Action, which describes the relationship

$$n_j = K_j \prod_e [n_e^{\nu_{j,e}}] \tag{3.23}$$

between the number density n_j of gas species j containing elements e. The exponent $\nu_{j,e}$ is the stoichiometric coefficient of element e within gas species j. We can therefore use the empirically-derived Gibbs free energies of each gas species (G_j°) to obtain a solution for the chemical composition of the mixture which is described by the number densities of the gas species (n_j), by searching for the n_j which conserve mass via Equation 3.23 and charge.

Here I am making three important assumptions:

- the atmosphere evolves for sufficient time to reach chemical equilibrium during each PROTEUS iteration,
- the system is isolated and homogeneous, meaning that escape is not as significant as the chemistry,
- time-dependent processes (e.g. photochemistry and dynamics) are ignored.

Given elemental abundances n_e and the temperature T as input parameters, models of equilibrium chemistry have been established to provide good accuracy in conditions which are dominated by thermochemical processes (Kite et al. 2016; Madhusudhan et al. 2016; Woitke et al. 2018). Equilibrium models have been used to investigate the composition of secondary atmospheres of young rocky exoplanets, although the existing literature calls for future works to go further (Kite and Barnett 2020; Spaargaren et al. 2020; Liggins et al. 2022; Misener et al. 2023). While ultra hot Jupiter exoplanets are dominated by thermochemical equilibrium, cooler gas giants and terrestrial-mass planets do not exist deeply within this equilibrium regime (Cooper and Showman 2006; Madhusudhan et al. 2016; Wogan and Catling 2020). For example, photochemistry is key to setting the composition of Earth's upper atmosphere and observations with JWST have detected SO_2 in the atmospheres of giant exoplanets which is suggested to be produced by photochemistry (Tsai et al. 2023). I leave an investigation into photochemical processes for Chapter 5.

FastChem is a computer model which solves for the composition of a gas mixture at chemical equilibrium, by enforcing conservation of element mass and total electric charge as described above (Stock et al. 2018; Stock et al. 2022; Kitzmann et al. 2024). To do this, FastChem uses a Newton-Raphson method with various numerical optimisations, such as switching to the Nelder-Mead optimisation method at low temperatures where solving for mass conservation becomes numerically difficult (Press 2007).

Similarly to the calculation of radiative transfer, AGNI outsources calculations of atmospheric equilibrium chemistry to FastChem in a self-consistent manner. This is done by assuming that the atmosphere is elementally well-mixed. Then, for each estimate of the temperature profile $\mathbf{x}$ obtained via Equation 3.17, FastChem is used to calculate the speciation of the elements (CHNOS) at each pressure level of the column. The additional species modelled by FastChem contribute to the atmospheric mean molecular weight, heat capacity, and radiative opacity where data are available. Energy transport fluxes are still calculated in the manner described above for atmospheres with isochemical compositions, but this coupling allows for feedback between the chemistry, energy transport, and thermodynamic processes.

3.2.6 Thermodynamic properties

Many models assume that the thermodynamic properties of gases are independent of or linear in temperature (e.g. Way et al. 2017; Selsis et al. 2023; Turbet et al. 2023). This is a valid assumption when the temperature range of interest is small. However, it becomes somewhat less reasonable for the systems under consideration here, since there may be temperature contrasts of up to 3000 K.

The molar heat capacity c_p of a gas describes the amount of heat Q required to raise the temperature of n moles of gas by an amount ΔT: $Q = nc_p\Delta T$. The quantity c_p plays several roles within atmospheric models, such as in expressions of the dry adiabatic lapse rate (Equation 3.4; Appendix E), and in calculations of heating rates and fluxes. The behaviour of $c_p(T)$ can be non-linear, and even non-monotonic, as the degrees of freedom within polyatomic molecules participate in the storage of heat energy to various extents (Pierrehumbert 2010). Figure 3.1 compares three methods for expressing $c_p(T)$: a constant value, data from the JANAF database, and an empirical fit with the Shomate equation,

$$c_p(y) = A + By + Cy^2 + Dy^3 + Ey^{-2}, \tag{3.24}$$

where $y = T/(1000\,\mathrm{K})$ is the non-dimensional temperature. Figure 3.1 shows that, while c_p is approximately constant near room temperature, there is otherwise a strong temperature dependence. The heat capacity increases with temperature as more degrees of freedom become available to store heat energy; rotational and then vibrational (Reif 2009). The Shomate equation (dashdot lines) does well at reproducing the experimental JANAF values (solid lines) at high temperatures, but behaves poorly outside the valid range of its fitting coefficients at low temperatures. The heat capacity asymptotically tends to zero as $T \rightarrow 0$, which is an expectation from quantum theory (Klein 1965). I have therefore decided to implement the tabulated JANAF heat capacities in AGNI, which are accessed via interpolation at runtime.

The saturation pressure p_{sat} of a gas species describes the *partial* pressure around which it undergoes a phase transition from a vapour into either a solid or a liquid form; phase change was introduced more generally in Section 2.2.6. The value of p_{sat} as a function of temperature is important in determining which parts of an atmosphere are saturated with a given volatile, which is where vapour condenses, potentially forming clouds, and where rain can evaporate. Critically, these saturated regions are where latent heat is released and absorbed, which contributes to the energy budget in setting the climate state (Kasting 1988; Pierrehumbert 2010). p_{sat} is temperature dependent up to the critical temperature T_{crit}, above which point liquid and gaseous phases become indistinguishable as a supercritical/superionic fluid (Coker 2007).

The JANUS atmosphere model implements condensation with $p_{\mathrm{sat}}(T)$ calculated from

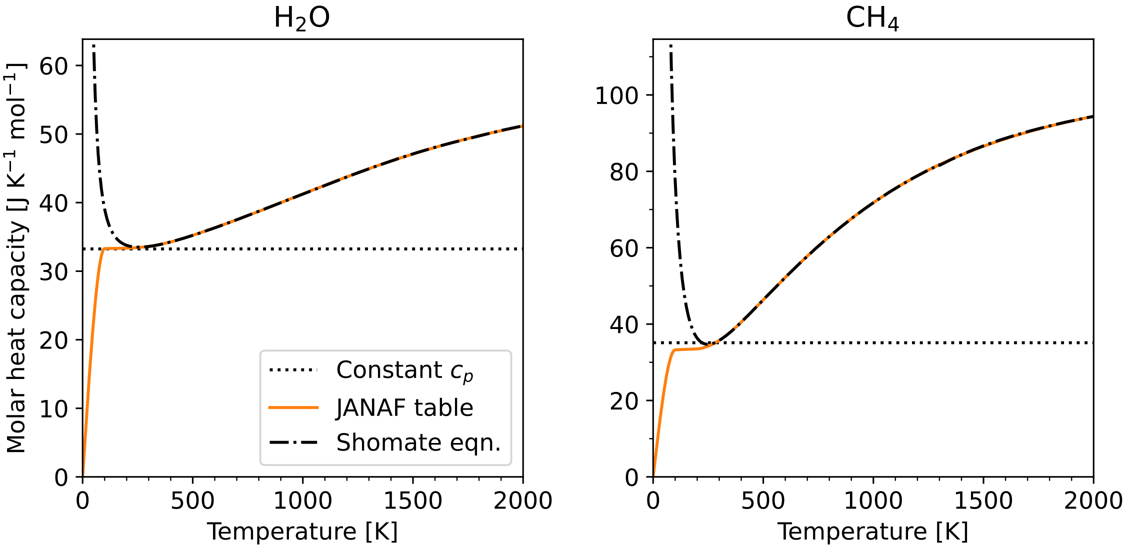

Figure 3.1: Molar heat capacity of gases as a function of temperature, taking H_2O and CH_4 as examples. 'Constant' uses constant values at room temperature and pressure (Pierrehumbert 2010). 'JANAF' is derived from experimental data tabulated in the JANAF database (Chase 1986). 'Shomate' expresses c_p as a function of temperature via Equation 3.24, with coefficients derived from the NIST website.

the Clausius-Clapeyron relation in the ideal regime. This relation, Equation 2.24, makes the assumption that the latent heat L[2] released by the phase change is independent of the temperature. However, this potentially becomes invalid under conditions far from Standard Temperature and Pressure.

Similarly to the Shomate equation applied to gas heat capacities, the Antoine equation,

$$\log_{10}\left(\frac{p_\text{sat}}{\text{bar}}\right) = A - \frac{B}{T + C}, \tag{3.25}$$

is one method for parametrising gas saturation pressure as a function of temperature, with three fitting coefficients (A, B, C). To test the validity of these different calculations of $p_\text{sat}(T)$, I compare various predictions of the H_2O saturation curve against the IAPWS95 standard (Wagner and Pruß 2002), together plotted in the left panel of Figure 3.2.

The A1 curve, which represents one set of the Antoine coefficients from NIST, is an example of the Antoine equation behaving poorly outside its valid range; it blows up at low temperatures. In comparison, the A2 and A7 sets of coefficients generally approach

---

[2] Latent heat is equal to the *enthalpy* difference associated with the phase change, when occurring at constant pressure.

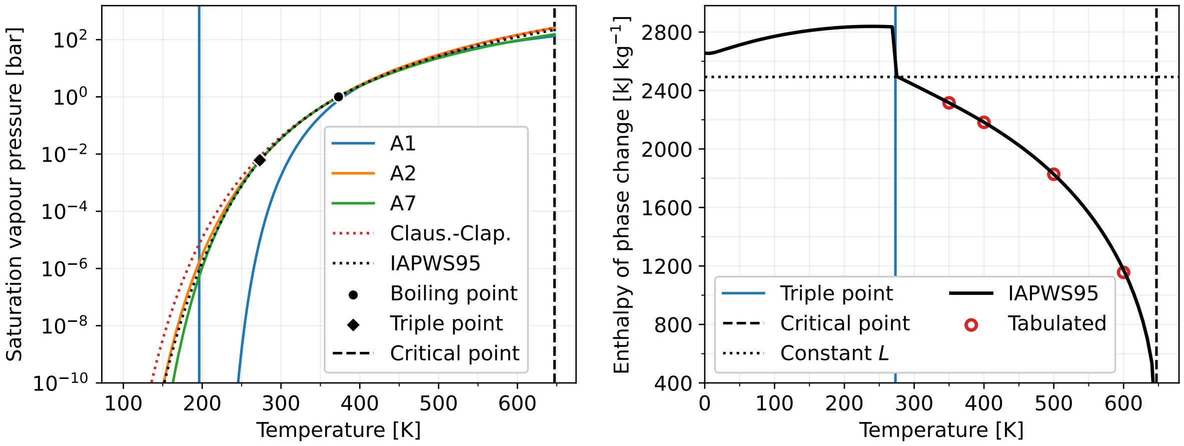

Figure 3.2: Temperature dependence of p_{sat} (left) and L (right) for H_2O. A1, A2, and A7 are calculated using the Antoine equation (Equation 3.25) with coefficients from the NIST website. The saturation curve is also derived using Clausius-Clapeyron, assuming a constant value for L. The IAPWS95 curves are derived from Wagner and Pruß (2002). In the right panel, the IAPWS95 curve is supplemented by data from (Feistel and Wagner 2006) at temperatures below the triple point. The 'Tabulated' L values act as a benchmark, with data taken from `engineeringtoolbox.com`.

the IAPWS standard across a wide range of temperatures. The red curve, calculated using the Clausius-Clapeyron relation, overestimates p_{sat} at low temperatures but generally performs well since it closely matches the IAPWS standard.

The right panel of Figure 3.2 plots $L(T)$ from IAPWS95 and Feistel and Wagner (2006) alongside tabulated values and the constant value adopted of L in JANUS. It is clear that L is strongly temperature dependent, vanishing as $T \to T_{\text{crit}}$ and changing almost discontinuously at the triple point. This means that the lapse rate of condensing regions of the atmosphere, Equation 2.25, also has an additional temperature-dependence through $L(T)$.

I implement phase change thermodynamics in AGNI as follows. A temperature dependent tabulation of $L(T)$ is derived from empirical reference data for H_2O (Wagner and Pruß 2002), C_4H_8, NH_3, CO_2, CO, C_2H_6, C_2H_4, F_2, H_2, HCl, HCN, CH_4, N_2, O_2, and SO_2 (Coker 2007). This list encompasses the most likely abundant species, notably H_2O and CO_2, so any other species are treated with $L = 0$.

The saturation curve, $p_{\text{sat}}(T)$, is nominally calculated using the Clausius-Clapeyron relation (Equation 2.24) which has been demonstrated to generally perform well against the IAPWS standard in Figure 3.2. Since the Clausius-Clapeyron relation only provides the derivative of the saturation curve, it must be integrated from a known point. This known temperature-pressure point on the saturation curve is calculated using Equation 3.25 with coefficients from NIST, ensuring that this point is applied within the valid range of the Antoine coefficients.

All of these thermodynamic data are all tabulated into a NetCDF file for each gas, with temperatures between 0 K and 4000 K at a resolution of 0.1 K. These data are interpolated by AGNI at runtime.

3.3 Validation of my new atmosphere model

3.3.1 Fiducial H_2O-only atmosphere calculations

To test AGNI's ability to resolve convectively stable regions and conserve energy, I first apply the software stand-alone to steam atmospheres similar to those modelled by Selsis et al. (2023). I consider an Earth-sized planet orbiting the Sun, with an atmosphere of 270 bar of H_2O (approximately one evaporated Earth ocean). AGNI is used to solve for radiative-convective equilibrium with $F^{\text{atm}} = 0$ for a range of instellation fluxes F_{ins} between 15 and 45 times Earth's instellation of $S_0 = 1360.8\ \text{W}\,\text{m}^{-2}$ (Kopp and Lean 2011). The opacities are also varied to compare results from calculations using the POKAZATEL/DACE database to those with HITRAN.

Figure 3.3 plots the modelled atmosphere profiles: the leftmost panel shows the temperature profiles calculated by AGNI at various instellation fluxes (coloured lines; solid with POKAZATEL and dashed with HITRAN) compared to Selsis et al. (2023) as the black line. It is clear from the leftmost panel that deep isothermal layers form at pressure levels $p \gtrsim 4$ bar. The AGNI temperature profiles are similar to those calculated by Selsis et al. (2023), particularly in the upper atmosphere. My model finds a surface temperature 35 K hotter than theirs for a comparable $F_{\text{ins}} = 35 S_0$. I take this small difference to be reasonable, given the significant differences between the models: convection parametrisation (AGNI uses MLT instead of their dry convective adjustment), radiative opacity (POKAZATEL/Exomol instead of their HITEMP), spectral resolution (256 instead of their 69 bands), heat capacity (temperature dependent instead of their constant value). The leftmost panel of Figure 3.3 also shows that calculations with my POKAZA-

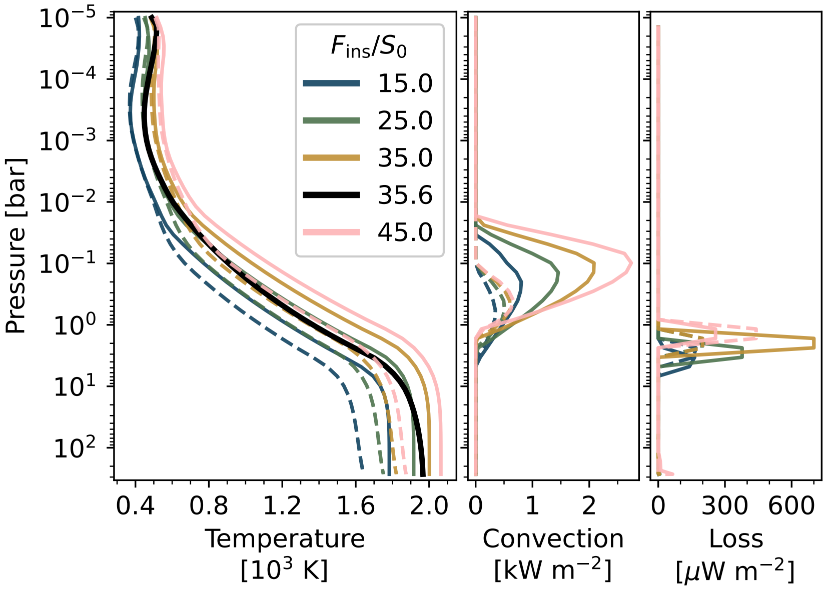

Figure 3.3: Radiative-convective models of a 270 bar pure-steam atmosphere. The Gueymard (2004) solar spectrum is used. Coloured lines plot AGNI atmosphere models calculated using opacities derived from POKAZATEL/DACE (solid lines) and HITRAN (dashed lines), for a range of instellation fluxes (legend). The black line shows the Selsis et al. (2023) model. **Left**: temperature, T in equation (3.14). **Centre**: convective energy flux, F^{cvt} in equation (3.1). **Right**: energy lost across each level, r in equation (3.13).

TEL and HITRAN models show minimal differences at low pressures and temperatures – where HITRAN is sufficiently complete – but deviate under more extreme conditions in the deeper atmosphere and near the surface of the planet.

The middle panel of Figure 3.3 plots convective flux, calculated via Equation 3.1, versus pressure for the different instellations I have considered here. The convection is driven by absorption of shortwave stellar radiation in the middle atmosphere, so it scales with F_{ins} and with the increased shortwave opacity introduced by POKAZATEL over HITRAN. The right panel of the figure plots flux losses (residuals; Equation 3.13) at each level. This shows that per-level flux losses are small in all cases, up to the numerical tolerance set for this calculation (Equation 3.18).

Further to this comparison with the prior literature, I have also compared the numerical $T(p)$ solutions obtained by AGNI against the analytic expectations those calculated from the analytic formulas (Guillot 2010), which shows good agreement although tuning of the double-grey opacities (κ_{th} and κ_{vs}) is necessary and expected. AGNI predicts the formation of deep radiative layers and isothermal stratospheres in the same scenarios as these simplified analytical $T(p)$ solutions. Similarly, I have implemented a double-grey two-stream radiative transfer model directly within AGNI, which may be used as an alternative to SOCRATES, the results of which compare well against otherwise identical scenarios configured to use the full SOCRATES radiative transfer suite.

3.3.2 An example in the case of K2-18 b

A topical sub-Neptune exoplanet is K2-18 b, which has a radius of 2.61 $R_\oplus$ and a mass of 8.63 $M_\oplus$ (Barragan et al. 2018). The planet's host star K2-18 has a spectral type of M2.8 and a bolometric luminosity $L_\star = 0.0234 L_\odot$ (Martinez et al. 2017). Due to the planet's small orbital separation of 0.159 AU, this yields an instellation flux of 1368 W m^{-2}, strikingly similar to the Earth's, so K2-18 b sits within its star's habitable zone and has been suggested to host a habitable surface. It is likely that the planet is synchronously rotating and may host water clouds (Charnay et al. 2021). The bulk properties of this planet are indicated by a green circle in the introductory Figure 1.3.

K2-18 b has a low bulk density compared to terrestrial-sized planets, but is overdense compared to the ice-giants of the Solar System (Madhusudhan et al. 2020). Its structure may be explained by three different scenarios (a gas dwarf, a water world, or a hycean world) described in Section 1.2.2. The latter case describes a surface water ocean underneath a large hydrogen-rich atmosphere, suggested by Madhusudhan et al. (2023b) to support life which actively produces dimethyl sulfide. JWST transit observations of K2-18 b do not detect NH_3, which could readily dissolve into a surface water ocean or, alternatively, be sequestered into the deep interior of the planet (Madhusudhan et al. 2023a; Shorttle et al. 2024). Furthermore, JWST observations do not detect H_2O in its atmosphere, potentially explained by H_2O-raining out in the middle-atmosphere and generating a dry stratosphere in the region probed by transmission spectroscopy (Tsai et al. 2024a).

I use this important planet as a case-study and additional test scenario for AGNI. To do this, I consider two atmospheric compositions from Luu et al. (2024), where the nitrogen abundance is set to 3× and then 100× Solar metallicity while other species are fixed at 100× Solar metallicity by moles (Truong et al. 2024). I also vary the internal temperature, T_{int}, which quantifies the net flux transported by the planet's atmosphere: $F^{\text{atm}} = \sigma T_{\text{int}}^4$ here (Guillot 2010; Marley and Robinson 2015; Hu et al. 2025). Using these compositions and effective temperature scenarios, I compare the temperature profiles calculated by AGNI against those of Luu et al. (2024) which were calculated using PICASO with an *ad-hoc* $T_{\text{int}} = 70$ K(Mukherjee et al. 2023). PICASO uses a time-stepping method to solve for radiative-convective equilibrium in the atmosphere by applying 108-band correlated-k radiative transfer and hard convective adjustment (Lupu et al. 2021).

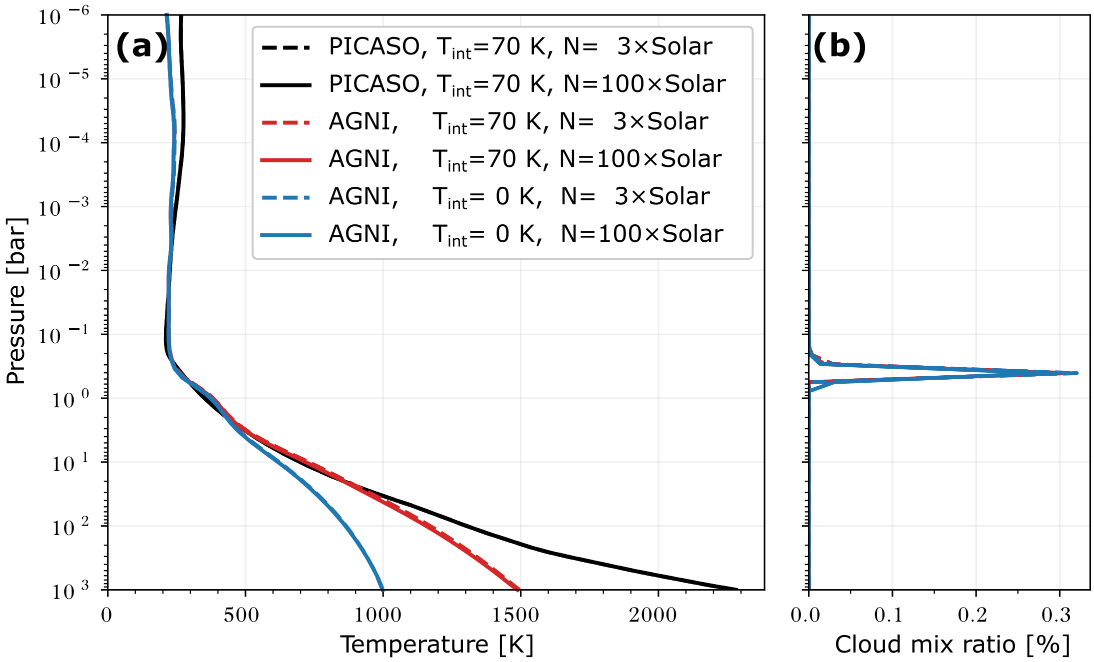

Figure 3.4: Average climate of K2-18 b modelled by AGNI and PICASO. The left panel shows $T(p)$ profiles calculated by AGNI (red and blue lines) compared to those of Luu et al. (2024) (black lines). The right panel shows liquid water cloud mass fractions determined by AGNI, using the condensation scheme described above. Solid and dashed lines correspond to different nitrogen abundances.

We can see from Figure 3.4a that AGNI and PICASO find nearly-identical temperature structures in the middle and upper atmosphere, at pressures < 30 bar. This validates my calculations since they agree with previous modelling in the regions which we can probe with remote sensing, which follows from Section 3.3.1. However, in the deep atmosphere, I find a temperature which is much lower than was calculated by Luu et al. (2024); our profiles diverge at pressures > 30 bar in the comparable cases of $T_{\text{int}} = 70$ K (red and blue lines). The surface temperatures differ by 750 K. A possible explanation for this lies is our different parametrisations of convection: my MLT formulation will generally under-estimate the convective heat flux, compared to reality, while their adjustment scheme will over-estimate the convective heat flux since it forces the profile lie exactly on the dry adiabat in unstable regions. Weaker convection means lower surface temperatures for a given instellation flux and effective temperature. Differences at high pressures and temperatures may also arise from uncertainties in the gas opacity under these conditions, particularly due to continuum absorption (Frommhold 1993; Abel et al. 2011; Karman et al. 2019).

The temperature profiles are highly sensitive to the internal heat flux. I find that increasing the effective temperature from zero to 70 K raises the surface temperature by $\sim$ 500 K (compare red and blue lines in Figure 3.4a). This is important given that several previous studies on K2-18 b have not considered the apparent sensitivity of its climate to the adopted value of T_{int} (e.g. Madhusudhan et al. 2023b; Luu et al. 2024; Wogan et al. 2024; Hu et al. 2025). In these works, the internal temperature represents the continuous release of energy from within the planet's interior due to potential radioactive decay, slow core formation, or tides. These previous studies do not incorporate a self-consistent evolutionary model and thereby have limited constraints on this quantity. However, the application of PROTEUS provides a self-consistent solution to the internal heat production, which is explored directly within Chapters 4 and 5. Both PICASO and AGNI show little sensitivity to the modelled nitrogen abundance, because NH_3 forms in only minor quantities and the opacity of N_2 is small. The modelled atmosphere composition is strongly H_2-dominated for both metallicities probed in this case study.

My modelling predicts the formation of water clouds near the 0.3 bar pressure level in K2-18 b's atmosphere, indicated by Figure 3.4b. The atmosphere becomes saturated in H_2O at the tropopause, where this shallow cloud layer forms and the water becomes cold-trapped, so that the stratosphere is relatively water poor. This prediction of cold-trapping has been previously suggested to explain the water-poor composition inferred from JWST observations of this planet (Rigby et al. 2024). Precipitation from these clouds is evaporated before reaching the surface in my model, which is consistent with prior dynamical studies using a full dynamical 3D-GCM treatment (Charnay et al. 2021).

Overall, my model yields a climate which quantitatively reproduces previous theoretical predictions of the observable upper atmosphere of K2-18 b – including potential formation of water clouds – and also qualitatively reproduces the expected physical behaviour in the lower atmosphere. An important indication from Figure 3.4 is that the surface temperature of this planet likely exceeds the critical point of H_2O, meaning it cannot host a surface water ocean, rendering it uninhabitable.

3.4 Outgassing of oxidised sulfur species

Sulfur geochemistry is thought to play an active and important role within the partitioning of elements between planetary atmospheres and interiors (Kaltenegger and Sasselov 2010; Lichtenberg and Miguel 2025). One example is the observed volcanism on Io which ejects sulfur-bearing species into space (Tyler et al. 2015a; Miyazaki and Stevenson 2022). Additionally, Venus' atmosphere contains sulfur-bearing gases and aerosols, while telescope observations of potentially molten exoplanets have indicated the potential presence of SO_2 and H_2S in their atmospheres (Taylor and Hunten 2014; Banerjee et al. 2024; Gressier et al. 2024; Bello-Arufe et al. 2025). It has been theoretically suggested that SO_2 could be used as a tracer for exoplanetary volcanism (Seligman et al. 2024). I have therefore updated CALLIOPE (Section 2.2.4 to include sulfur degassing: the model implements an S_2 solubility, which is also oxidised into SO_2 in the atmosphere with an equilibrium reaction with O_2 Boulliung and Wood (2022) and Gaillard et al. (2022) – see Appendix A. Chemically, the sulfur dissolves into the silicate as sulfide (S^{2-}), replacing some of the oxygen O^{2-} anions in the matrix. The dissolved sulfur content at sulfide saturation is known to be non-monotonically dependent on the FeO content of the silicate (O'Neill and Mavrogenes 2002), although FeO content is held constant in my models.

To demonstrate the behaviour of sulfur outgassing in the context of all the other modelled volatiles, I calculate the partial pressures of the eight volatiles (previously six) in equilibrium with a magma ocean of fixed Earth-like mass and high temperature, but at variable fO_2. These outgassed atmospheric compositions are plotted in Figure 3.5. I find that CO_2 dominates at oxidising conditions (fO_2 >IW+2), with SO_2 becoming the second most abundant gas in the most oxidising cases ($fO_2 \gtrsim 4.5$). Near IW+0, CO becomes the most abundant gas and its volume mixing ratio is maximised. Under reducing

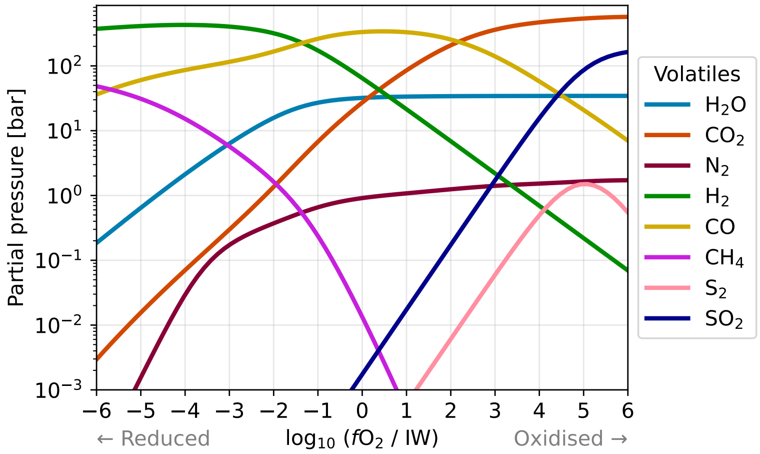

Figure 3.5: Outgassed gas partial pressures at 2500 K versus fO_2. Mid-ocean ridge basalt has an fO_2 approximately equal to the Fayalite-Magnetite-Quartz (FMQ) buffer, equivalent to IW+3.69 (Schaefer and Elkins-Tanton 2018). Observations indicate that Mercury's surface probably erupted with an fO_2 between IW-6.5 and IW-3.5 (Namur et al. 2016), overlapping with the fO_2 of the Solar nebula at approximately IW-7 to IW-6 (Doyle et al. 2019b; Grewal et al. 2024).

conditions ($\lesssim$IW-1.5), H_2 dominates the composition and the partial pressure of CH_4 increases significantly. These behaviours and variety of compositions are consistent with Gaillard et al. (2022), Suer et al. (2023), and Gillmann et al. (2024).

3.5 Two exoplanets as case studies

I now explore whether and when outgassed atmospheres on young rocky planets remain convective. To do this, I use two exoplanets (HD 63433 d and TRAPPIST-1 c) as test cases. Key parameters for these planets and their stars are provided in Table 3.2.

HD 63433 d is a 414 Myr young Earth-sized exoplanet orbiting a G5V star, discovered in transit using TESS (Capistrant et al. 2024). Hydrodynamic models and HST observations indicate that its outer neighbour (HD 63433 b) has already lost its primordial H/He envelope (Zhang et al. 2022). If the more irradiated planet (HD 63433 d) has also lost its envelope, then the composition of an overlying secondary atmosphere is likely to be influenced by mantle degassing or volatile exchange with a permanent magma ocean. This hot planet provides an observable analogue for a young Venus or young Earth, shortly following a giant impact event (Lebrun et al. 2013; Way et al. 2016; Turbet et al. 2021). The properties of HD 63433 d are plotted in the introductory Figure 1.3 as a purple scatter point. Since this planet is young, modelling of its first stages can offer a more direct insight into its present state, given the termination conditions on my simulations (Section 2.2.3).

Planet	HD 63433 d	TRAPPIST-1 c
Mass [$M_\oplus$]	$1.0^\dagger$	1.308
Radius [$R_\oplus$]	1.073	1.097
Semi-major axis [AU]	0.503	0.0158
Eccentricity	0.16	0.00654
Equilibrium temp. [K]	1040	313

Star	HD 63433	TRAPPIST-1
Class	G5V	M8V
Mass [$M_\odot$]	0.99	$0.10^\dagger$
Estimated age [Myr]	414	7600
Spectral analogue	$\text{Sun}^\dagger$	TRAPPIST-1

Table 3.2: Planetary and stellar parameters used for my time-evolved simluations in this section. Sources: Gillon et al. (2017), Grimm, Simon L. et al. (2018), Froning et al. (2019), Agol et al. (2021), Wilson et al. (2021), and Capistrant et al. (2024). Daggers† indicate values for which I have made necessary physical assumptions. The mass of HD 63433 d is currently unknown, so I adopt a value of $1.0 M_\oplus$ for simplicity. It is unlikely that this mass is an underestimate because there are currently no low-density (i.e. sub-Earth) exoplanets with Earth-like radii (Parc et al. 2024). TRAPPIST-1 is modelled with a mass of $0.1 M_\odot$ – rather than $0.0898 M_\odot$ – as $0.1 M_\odot$ is the lower-limit on the stellar masses covered by the Spada et al. (2013) tracks. Equilibrium temperatures taken from the literature are scaled such that they both correspond to a Bond albedo of 30%.

TRAPPIST-1 c is an older Earth-sized exoplanet orbiting the M-dwarf star TRAPPIST-1 (Gillon et al. 2017; Agol et al. 2021). Secondary eclipse observations with JWST/MIRI found a 380 ± 31 K brightness temperature in the 15 μm CO_2 absorption band, which is consistent with emission by a bare rock surface heated by incoming stellar radiation (Zieba et al. 2023; Ducrot et al. 2024). This could indicate that TRAPPIST-1 c has no atmosphere, as heat redistribution by atmospheric dynamics is expected to yield a dayside brightness temperature below the planet's radiative equilibrium temperature. This bare-rock scenario is reinforced by recent JWST phase curve observations (Gillon et al. 2025) which show no offset to the dayside 'hotspot' which would be expected from dynamical heat redistribution; interpretations of the phase curve are not conclusive and leave open the possibility of a thin, potentially O_2-dominated, atmosphere on TRAPPIST-1 c. Observations of its neighbour, TRAPPIST-1 b, more strongly indicate that this inner planet does lack an atmosphere at the present day (Greene et al. 2023; Gillon et al. 2025). It is therefore important to outline potential timescales for the solidification of their primordial magma oceans, and the atmospheres which are predicted to be generated in the process.

3.5.1 Modelled evolutionary outcomes with PROTEUS

I make use of the PROTEUS framework introduced in Chapter 2 to simulate the early evolution of these two planets. These simulations terminate either when the mantle solidifies or when the planet reaches a steady state (i.e. global energy balance, radiative equilibrium). The radius fraction of their metallic cores are fixed at 55% of the atmosphere-mantle interface (Lodders and Fegley 1998). The surfaces are treated with a grey shortwave albedo of 30% (Essack et al. 2020; Fortin et al. 2024). All cases are initialised at a stellar age of $t_{\rm ini} = 100\,{\rm Myr}$, which results in enhanced instellations compared to present-day values for both planets (see Figure 2.3). Both planets are likely to be tidally locked and synchronously rotating, so to represent them with a column model, I use a zenith angle of $\cos^{-1}(1/\sqrt{3}) = 54.74^\circ$ and scale the stellar spectrum by a factor of $1/4$ as per Hamano et al. (2015).

For all cases, I set the planet bulk volatile inventory via the concentrations of elements in the planet's mantle, which are in equilibrium with an overlying atmosphere. I take nitrogen (2.01 ppmw) and sulfur (235.00 ppmw) abundances and C/H mass ratio ($= 1$) consistent with that of Earth's primitive mantle (Wang et al. 2018). The total hydrogen inventory is set equivalent to eight Earth oceans in my models, informed by Chapter 2, although the amount of hydrogen obtained by these particular planets during their formation is entirely unknown (Salvador et al. 2023; Lichtenberg and Miguel 2025).

I otherwise vary the mantle oxygen fugacity ($f{\rm O}_2$) between -5 and +5 log units relative to the iron-wüstite buffer. ΔIW is held constant throughout each simulation relative to IW, although $f{\rm O}_2$ varies in absolute terms [bar] due to the temperature dependence of the buffer (Section 1.1). In total, 44 simulations are run, corresponding to all combinations of: planet (HD 63433 d, TRAPPIST-1 c), atmosphere model (AGNI, JANUS), and ΔIW (11 samples). This allows me to explore the impact of $f{\rm O}_2$ on early planetary evolution, and to explore whether characterisation of the atmospheres of young rocky exoplanets can offer insight into their interiors.

Figure 3.6 plots the whole-mantle melt fractions (Φ, y-axes) calculated at the endpoints of these simulations. The mantle melt fractions depend on its oxygen fugacity (x-axes) and the atmosphere model considered (top and bottom panels). From the top panel of Figure 3.6 we can see that simulations of HD 63433 d with the JANUS atmosphere module (circles) yield an almost fully molten mantle regardless of its mantle's redox state (x-axis) and corresponding atmospheric composition. Simulations of this planet with the AGNI atmosphere module (squares) result in a somewhat smaller melt fraction; that is, the mantles have begun to solidify but attained radiative equilibrium before fully solidifying. All the AGNI cases still maintain a significant amount of melt, which is shown to be maximised at IW-1 by the red line in Figure 3.6. A permanent magma ocean is therefore a possible scenario for HD 63433 d in spite of its 1040 K subsolidus planetary equilibrium temperature (Table 3.2), due to the blanketing provided by the outgassed overlying atmosphere. The upper panel of Figure 3.7 plots the corresponding atmospheric compositions, with fO_2 relative to iron-wüstite varying on the x-axis. Models with AGNI and JANUS both span from H_2 to CO_2 dominated, with little atmospheric H_2O due to its favourable dissolution into the large amount of melt (see discussion in Section 2.3.3). These models show variability of $\sim$ 250 K in the surface temperature of the magma ocean on HD 63433 d. These surface temperatures are plotted as a black line in the top panel of Figure 3.6, which, as with the mantle melt fraction, is maximised near IW-1.

In the case of TRAPPIST-1 c, simulations with AGNI all solidify, which is shown by the square scatter points in the bottom panel of Figure 3.6. This is in complete contrast to the equivalent simulations with JANUS, which yield permanent magma oceans with large melt fractions (circular points). Comparing with the compositions plotted in the bottom panel of Figure 3.7, solidification under reducing conditions (small fO_2) does not yield a steam-dominated atmosphere; degassed hydrogen is primarily speciated into H_2 and CH_4. It is only when the planet solidifies under oxidising conditions that a large H_2O atmosphere is outgassed, which means that it cannot be a general outcome of magma ocean solidification. This result underscores the key weakness of the pure-steam assumption adopted by Selsis et al. (2023), which follows from Chapter 2. The black line in the bottom panel of Figure 3.6 plots solidification time versus fO_2 for the AGNI cases of TRAPPIST-1 c (which all solidify). This shows that the magma ocean on TRAPPIST-1 c may have solidified across a range of timescales from 5.3 to 95.7 Myr depending on the mantle redox state at the time. Modelled solidification time generally increases under more oxidising conditions, where the atmosphere becomes H_2O-dominated and the greenhouse effect is stronger (see Section 2.4.3). This range is too short for significant stellar evolution to occur (Figure 2.3).

3.5.2 Temperatures and convection in the atmosphere

Let us now consider the behaviour of the whole atmosphere column. Figure 3.8 plots atmospheric temperature-pressure profiles for all cases considered: the top panel for HD 63433 d and the bottom for TRAPPIST-1 c. As with the melt fraction, these strongly depend on the mantle redox (fO_2, colourbar) as it exerts significant control over the composition of the atmospheres. Profiles produced by AGNI are shown with solid lines, while the pseudoadiabats produced by JANUS are shown with dashed lines. The square scatter points indicate regions in which convection is occurring in the atmosphere in the AGNI models, with the same colour mapping. At the full square marker size (legend entry), convection is responsible for all upward flux transport at that level, offset by a net-downward radiative flux in these regions. Note that these all correspond to atmospheres in equilibrium with permanent magma oceans, except for TRAPPIST-1 c when modelled with AGNI (Section 3.5.1).

For HD 63433 d, the top panel of Figure 3.8 shows that convection only persists at equilibrium for pressures levels $p < 1$ bar and mantle $fO_2 \geq \text{IW} + 1$. These regions of convection are enabled by the absorption of downwelling stellar radiation, which is otherwise Rayleigh-scattered more strongly for the reducing cases which have greater amounts of H_2 and CO. Convection is the dominant process transporting energy upwards through these regions of the atmosphere (square scatter points in top panel), while energy transport in deeper layers is handled by radiation alone. Under reducing conditions, the atmospheres are entirely radiative. Overall, this shows that convection can shut down even for atmospheres of mixed composition, not just in a pure-steam end member scenario. Despite this convective shutdown, the modelled surface temperatures on HD 63433 d are still sufficiently high to support a permanent magma ocean, even with a sub-solidus equilibrium temperature (Table 3.2). This is possible because the radiative-convective AGNI models have shallower temperature profiles (in $\mathrm{d}T\,/\,\mathrm{d}p$

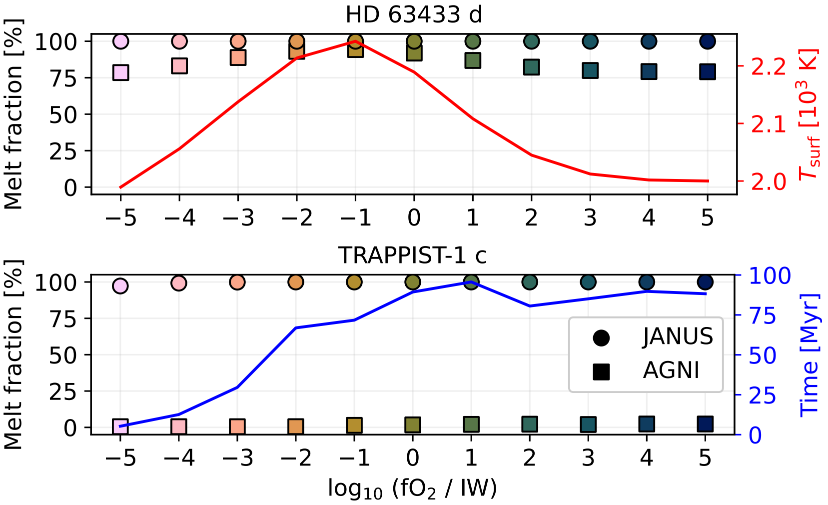

Figure 3.6: Mantle melt fraction Φ at model termination for both planets. Top panel shows final melt fractions for HD 63433 d and bottom panel shows TRAPPIST-1 c, both versus mantle fO_2 relative to iron-wüstite for each of my atmosphere models (marker shape). The red line on the top plot shows the final surface temperature for the AGNI HD 63433 d cases, which all rapidly reach radiative equilibrium. The blue line on the bottom plot shows the time taken for the AGNI TRAPPIST-1 c cases to solidify.

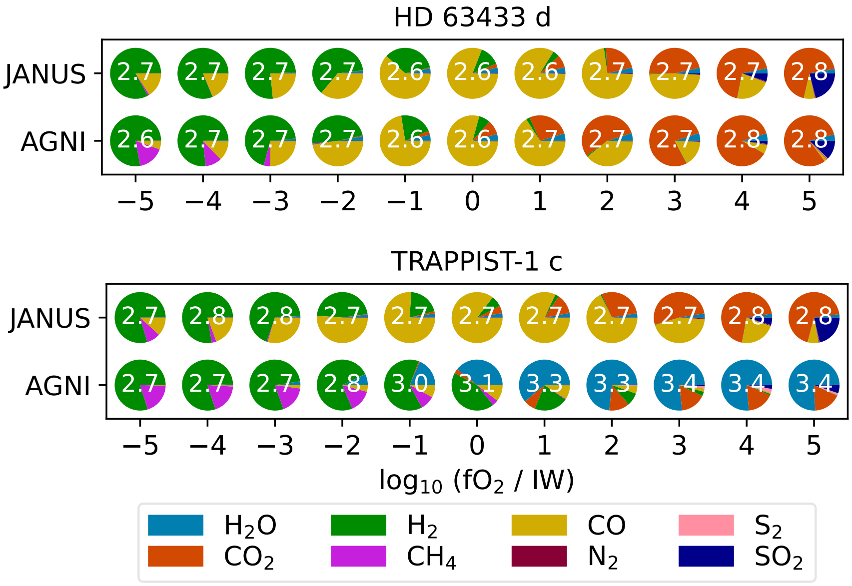

Figure 3.7: Outgassed atmospheric composition at model termination for both planets. Top panel shows compositions for HD 63433 d and bottom panel shows TRAPPIST-1 c, both versus mantle fO_2 relative to iron-wüstite (x-axis), and both planets simulated with my two atmosphere models (y-axis). Pie charts represent outgassed volume mixing ratios, and white numbers show $\log_{10}$ total surface pressures [bar].

terms) than the pseudoadiabatic JANUS models, which allows for smaller temperature contrasts between the planet's surface and the radiating layer aloft, which means that they can still attain radiative equilibrium above a permanent magma ocean. Grey analytic solutions (Guillot 2010; Pierrehumbert 2010) have shown that the temperature of deep isothermal layers depends on the pressure-thickness of the region between the effective shortwave-absorbing layer and the thermal photosphere; when this region is thick, the deep isothermal layer can become very hot. The results presented in Figure 3.8, using my spectrally-resolved radiative transfer calculations, are therefore in line with expectations from grey analytic solutions. The temperature of the upper atmospheres modelled by AGNI are found to increase under more reducing conditions.

The square scatter points in the bottom panel of Figure 3.8 shows that deep convection persists in the models of a young TRAPPIST-1 c under reducing ($\leq$ IW $-$ 1) conditions. These profiles do not sit exactly on the dry adiabat (dashed lines) within convective regions because radiative fluxes are non-zero, and therefore still influence the temperature structures within these regions. It is important to note that the AGNI models (solid lines) of this planet correspond to cases with positive F^{atm} (Equation 2.1) as the planet has not reached radiative equilibrium and would continue to cool post-solidification. This means that the youngest planets may indeed have surface-arising deep convective zones, which then shuts-down at later times as they approach radiative equilibrium. As with HD 63433 d, the upper atmosphere profiles for TRAPPIST-1 c also show a similar trend of increasing temperature under more reducing conditions. Condensation and temperature inversions are both absent, although the reducing cases yield a tall near-isothermal stratosphere which generates a relatively 'flat' emission spectrum (bottom panel of Figure 3.9).

3.5.3 Probing magma ocean redox with emission spectra

The cooling rate of these model planets is determined by radiative transport of energy to space. My calculations of radiative fluxes naturally provide synthetic emission spectra which include the combined contributions of atmospheric thermal emission, backscattered stellar radiation, and surface reflection. Figure 3.9 plots top-of-atmosphere

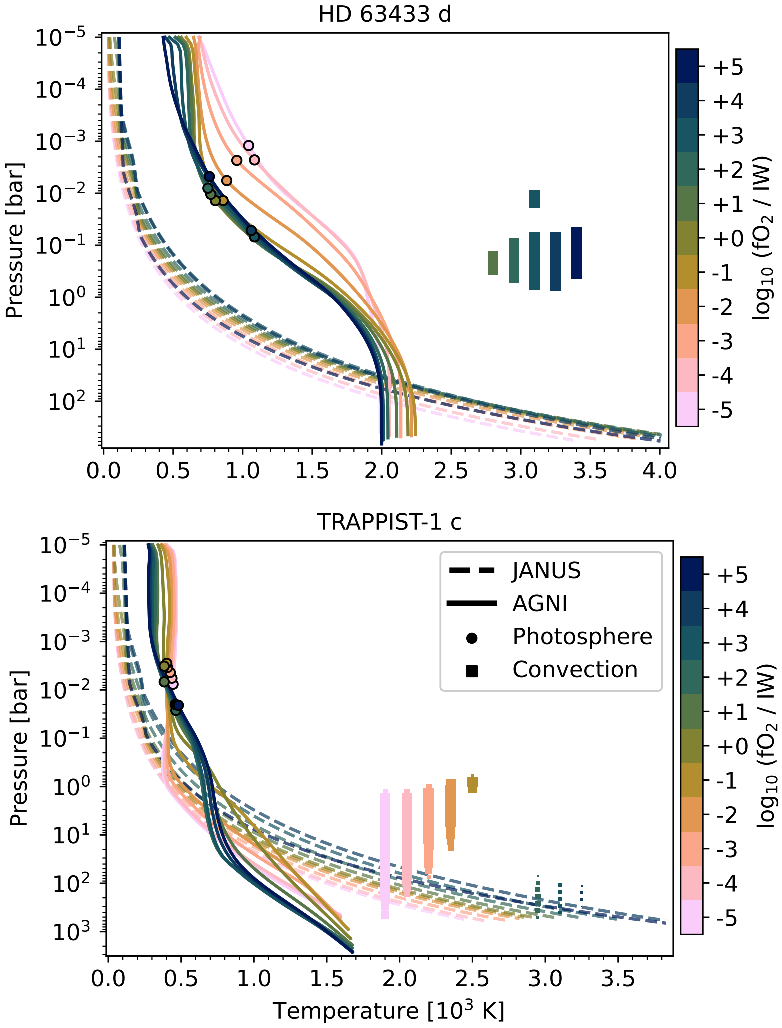

Figure 3.8: Atmospheric temperature profiles at model termination. Modelled for HD 63433 d (top) and TRAPPIST-1 c (bottom), versus mantle fO_2 (line colour), simulated with both atmosphere models (line style). Square markers denote the presence of convective regions in the AGNI cases, where the marker sizes scale with the relative amount of the total flux at each pressure level that is carried by convection; the horizontal positioning of these markers is for visualisation purposes. Circular markers denote the effective photospheres, taken to be the pressure levels at which the contribution functions are maximised in each case (Knutson et al. 2009; Drummond et al. 2016; Boukrouche et al. 2021). Note the different axis limits.

emission spectra for both planets (top and bottom panels) calculated with SOCRATES via AGNI, for each of the eleven oxidation states considered here (colour bar). It is important to note that, because I use a 1D column model, these emission spectra represent the outgoing radiation from the planet *as a whole*, and do not represent the dayside emission that would be observed from a secondary eclipse measurement. Dayside (or even substellar) emission could be more sensitive to the redistribution of heat due to zonal dynamics within the atmosphere, and therefore would require specific modelling that is beyond the scope of this thesis (Hammond and Lewis 2021; Koll 2022). The corresponding emission spectra arising from simulations with JANUS are presented and discussed in Appendix G.

The spectra plotted in Figure 3.9 all show several molecular features; most notably from CO_2, SO_2, and H_2O, which are annotated on the top panel of the plot. These features are all generated by upper atmospheric absorption of radiation produced by the deeper – hotter – atmosphere, as the temperature profiles are uninverted and I assume a grey surface albedo. For both planets (top and bottom panels), the presence and depth of the features varies with fO_2 (colour bar). A smaller upwelling flux within the CO_2 and SO_2 features in Figure 3.9 correlates with an oxidised mantle due to the difference in the composition of the outgassed atmosphere. Oxidising mantles have been shown to yield atmospheres rich in CO_2 and SO_2 (see Figure 3.7) and thus have absorption features associated with these gases. Molecular features are less discernible at wavelengths greater than 20 µm, although outgoing flux generally increases with upper atmosphere temperature (Section 3.5.2).

The absorption features fall within the bandpasses of JWST instruments MIRI (LRS and photometry) and NIRSpec (e.g. F290LP). The SO_2 feature at 7-9 µm corresponds closely with MIRI's F770W filter, and is strongly associated with deviation from the 'flat' Planck function under the oxidising conditions in which sulfur outgassing is favoured. There are also features at shorter wavelengths within the bandpass for direct imaging with HARMONI on the upcoming Extremely Large Telescope (Padovani and Cirasuolo 2023).

The bottom panel of Figure 3.9 shows the synthetic emission spectra for a young TRAPPIST-1 c. Caution should be taken when comparing these to recent observations of this planet (Zieba et al. 2023; Gillon et al. 2025), as Figure 3.9 does not plot dayside emission spectra and the simulations do not account for processes which may have occurred on TRAPPIST-1 c between the solidification of its magma ocean and the present day. However, there are there are clear molecular features associated with mantle redox, as with HD 63443 d. Within the CO_2 feature at 15 μm the brightness temperature varies between ~ 300 and 450 K. Which brackets the 380 K dayside value detected by Zieba et al. (2023).

There are no emission features directly associated with convective shutdown, although Section 3.5.2 showed that convective stability is preferred under reducing conditions for permanent magma oceans. The composition of the atmospheres could be inferred from these emission spectra, and thereby allow inference on the convective regime of these atmospheres.

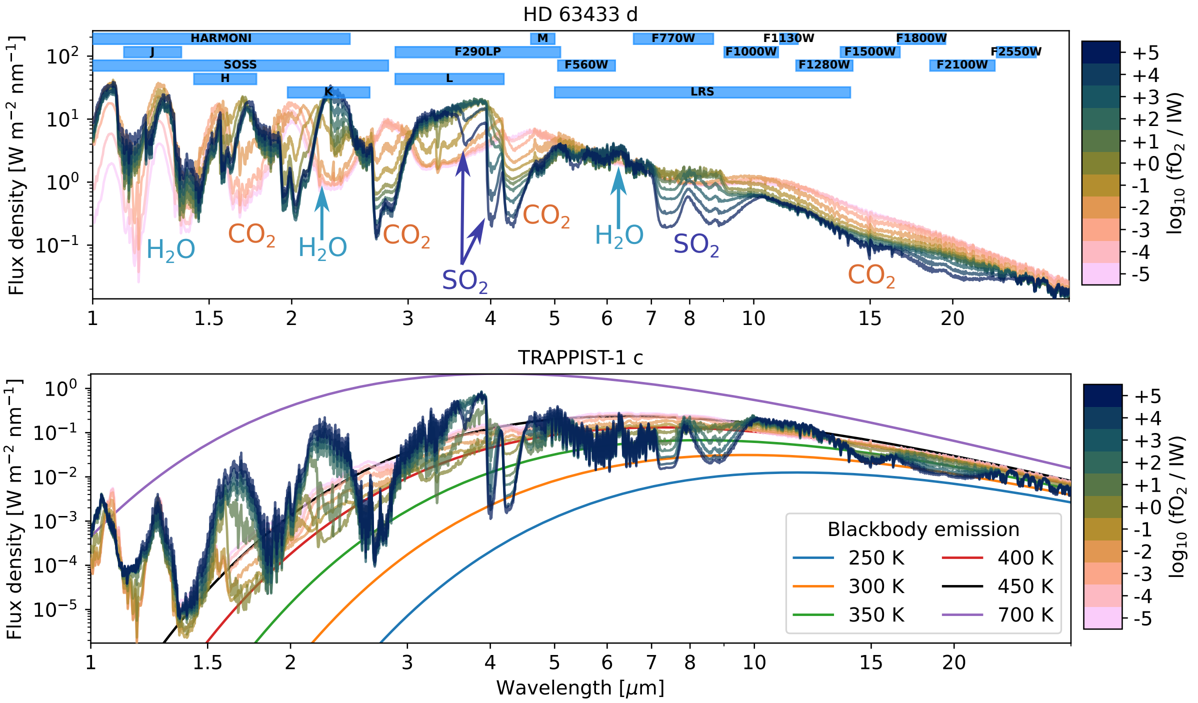
HD 63433 d

TRAPPIST-1 c

Figure 3.9: Top-of-atmosphere planet-averaged outgoing radiation at model termination. Modelled for HD 63433 d and a young TRAPPIST-1 c, versus mantle fO_2 relative to IW (colourbar). For HD 63433 d (**top panel**) this corresponds to the planet at radiative equilibrium at an early stage of its life. For TRAPPIST-1 c (**bottom panel**) this corresponds to the planet at the point of magma ocean solidification. Radiative transfer is calculated at a finer spectral resolution (4096 bands) using the same opacities as in the evolutionary calculations. Outgoing radiation includes thermal emission, back-scattered stellar radiation, and surface reflection. Blue rectangles in the top panel indicate some of the bandpasses for MIRI, NIRSpec, HARMONI, and common high-resolution bands. Legend lines in the bottom panel plot the blackbody emission at various brightness temperatures.

3.6 The 1D thermochemical speciation of an oxidised atmosphere

How does inhomogeneous equilibrium chemistry impact the compositional profile of atmospheres on recently solidified planets? In this section, I couple FastChem and AGNI in order to probe the answer to this question. As described in Section 3.6, this assumption of chemical equilibrium neglects the role of diffusive and photochemical processes in setting the composition of the atmosphere. However, the results presented in Section 3.5.2 have shown that it is possible for the atmospheres on these planets to be stable to convection, so atmospheric composition could be set primarily by chemical processes, rather than being quenched through dynamical mixing and/or strong molecular diffusion. For the case of TRAPPIST-1 c at IW+5, which is shown to be entirely stable to convection, I use the outgassed composition and T_m calculated at the point of solidification (Figure 3.7) to re-calculate the gas-phase composition profile and temperature structure of the atmosphere together self-consistently. Simulations with PROTEUS (Figure 3.6) indicate that the magma ocean solidifies in this case, so volatile dissolution plays a negligible role in setting the atmospheric composition.

Under this calculation, the new atmospheric composition is plotted with solid lines in Figure 3.10 as volume mixing ratio (x-axis) versus total pressure (y-axis). The composition determined during the time-evolved calculation, which assumes that the atmosphere is isochemical, is indicated with the dashed lines. The corresponding temperature profiles are plotted as black lines.

The maximum relative difference in the temperature profile arising from this coupled chemical-climate calculation is 38.75 K (4.36%) between the original (dashed black line) and self-consistent (solid black line) models. This maximum difference occurs at a pressure level of approximately 36 bar. The difference in outgoing longwave radiation is 0.02 W m^{-2}, which is small because the temperature profiles and abundances of three major gases (H_2O, CO_2, SO_2) are effectively identical between the two models in the upper atmosphere. The maximum relative difference in the atmospheric mean molecular weight is 1.10% between the two models.

The calculations with AGNI/FastChem (solid lines) show that the abundances of H_2 (green line) and CO (yellow line) decline to less than 10^{-8} in the upper atmosphere. The hydrogen atoms are instead favourably speciated into H_2O, and condensation remains absent. Production of S_8 (magenta line) is also predicted in this region (magenta line), with a corresponding minor decrease in the abundance of SO_2.

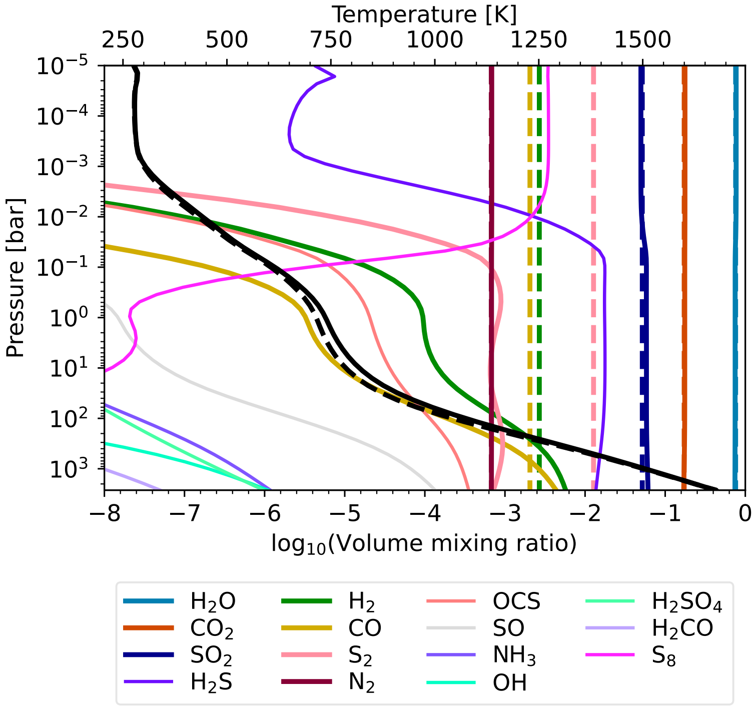

Figure 3.10: Composition and temperature versus pressure in the model atmosphere of a young TRAPPIST-1 c (IW+5). Elemental abundances are derived from time-evolution simulation with AGNI/PROTEUS (dashed lines) and then used to determine gas volume mixing ratios recalculated self-consistently with AGNI/FastChem (solid lines) at the point of magma ocean solidification. The coloured lines plot volume mixing ratios (bottom x-axis). The black lines plot temperature (top x-axis). Species with volume mixing ratios $< 10^{-8}$ are not plotted.

3.7 Chapter discussion

3.7.1 Importance of convective stability

Evolution models of HD 63433 d show that it is possible for atmospheres of mixed volatile composition overlying magma oceans to be stable to convection (Figure 3.8). This fits with the predictions of Section 2.6 based on radiative heating rates in mixed atmospheres, and with those of Selsis et al. (2023) for pure-steam atmospheres. Convective stability occurs in the model atmospheres of HD 63433 d when radiative transport is sufficient to carry the approximately zero net outgoing energy flux F^{atm} that exists at radiative equilibrium. This small F^{atm} does not itself induce temperature gradients sufficient for triggering convection. The square scatter points in the top panel of Figure 3.8 show that oxidising cases maintain convection in the middle atmosphere ($p < 1$ bar), which is triggered by the absorption of downwelling shortwave radiation from the host star and not by transport of heat from a cooling interior. In these regions, convection transports energy upwards to offset the net downward transport of energy by radiation (c.f. the middle panel of Figure 3.3). The reducing cases of HD 63433 d are fully radiative in part due to backscattering of downwelling stellar radiation enabled by the large Rayleigh scattering cross-sections, per unit mass, of H_2 and CO (Pierrehumbert 2010). While the surface temperatures predicted by AGNI are $\sim$ 2000 K lower than those predicted by JANUS, the upper atmosphere temperatures are up to 1000 K larger due to radiative heating by absorption of stellar radiation. This means that, despite the shallower lapse rate in radiative regions, the surface temperatures remain sufficient to sustain a permanent magma ocean (Figure 3.6). Convective shutdown does not *necessarily* preclude a permanent magma ocean on terrestrial-mass exoplanets, so the findings of Selsis et al. (2023) obtained with pure-H_2O atmospheres cannot be extended to real planets generally. My results here, and in particular the sensitivity of atmospheric convection to the presence of particular gas species, are supported by a later-published analysis which uses line-by-line radiative transfer calculations (Cmiel et al. 2025).

Time-evolved simulations of a young TRAPPIST-1 c with AGNI and PROTEUS never reach radiative equilibrium and instead cool until the magma ocean solidifies. I do not simulate the post-solidification evolution of TRAPPIST-1 c, but these models all have a non-zero net upward heat fluxes F^{atm} at the point of solidification: 4.9 W m^{-2} at IW-5, decreasing monotonically to 0.6 W m^{-2} at IW+5. A point of model termination corresponds with convection being maintained under reducing conditions, at larger F^{atm}. In comparison, these atmospheres become purely radiative under oxidising conditions, with smaller F^{atm}. These trends are opposite to the trend seen for HD 63433 d, since convection in the atmosphere of TRAPPIST-1 c is triggered primarily by upward transport of energy from the cooling magma ocean, rather than by the absorption of downwelling stellar radiation in the case of HD 63433 d. Additionally, the lower photospheric temperature of the host star and smaller instellation of TRAPPIST-1 c also means that the amount of optical radiation readily available to trigger convection is reduced compared to HD 63433 d. The temperature structures of the reducing TRAPPIST-1 c cases effectively reproduce the canonical model for the structure of these atmospheres: a deep dry troposphere and an approximately-isothermal stratosphere (Chapter 2; Hamano et al.

2015; Lichtenberg 2021). Further time-evolution and cooling of the surface may see the deep isothermal layers form, as the planet approaches radiative equilibrium. The near-isothermal stratosphere formed under reducing conditions has a temperature approximately consistent with the planet's equilibrium temperature (508 K). The stark contrast between the JANUS and AGNI simulation outcomes demonstrates the necessity of using a more realistic atmosphere when theoretically studying young rocky planets.

3.7.2 Observational prospects for HD 63433 d and TRAPPIST-1 c

Since HD 63433 d is currently only 414 Myr old, it may be possible that it still maintains a permanent magma ocean beneath an outgassed volatile atmosphere with a composition set by equilibrium chemistry and dissolution into the melt. This would allow observations of HD 63433 d to be used to place constraints on the redox state of the magma ocean through absorption features viewed in an emission geometry. Detection of SO_2 or CO_2 within the atmosphere of HD 63433 d might then imply a similar redox history to the Earth, whose mantle has been oxidised since the Hadean eon. Attempting to constrain atmospheric composition with a single photometric point gives rise to various degeneracies; Figure 3.9 shows that MIRI LRS and NIRISS SOSS simultaneously span multiple features which are sensitive to fO_2, so observations with these instruments could alternatively provide deeper insight into these atmospheres compared to photometry (Zieba et al. 2023; August et al. 2025; Hammond et al. 2025). However, a quantitative estimate upper-mantle redox from the inferred presence of atmosphereic SO_2 and CO_2 would be degenerate with planetary S and C inventories. Such degeneracies could potentially be lifted by quantifying molecular abundance *pairings*; e.g. the abundances ratio of CO_2 to CH_4.

The modelled absorption features in the case of TRAPPIST-1 c are comparable with those of HD 63433 d for the most oxidising cases (>IW+2). However, the near-isothermal upper atmosphere generated by TRAPPIST-1 c for the scenario of a reducing mantle instead yields a near-blackbody emission spectrum with comparatively small absorption features. The outgoing radiation continuum for $fO_2 \leq \mathrm{IW} + 1$ closely matches the blackbody curves, which corresponds to the isothermal stratospheres. The oxidising cases yield stratospheric temperatures of approximately 300 K (Figure 3.8), which corresponds to the $\sim$ 300 K brightness temperature in the CO_2 and SO_2 absorption bands in the emission spectra at $fO_2 > \mathrm{IW} + 1$. The extended age of the TRAPPIST-1 system compared to the HD 63433 system means that the planets orbiting TRAPPIST-1 were/are subject to several processes not modelled in this chapter, such as atmospheric escape, which could make direct comparisons between these models and future JWST observations of these planets invalid. Atmospheres on TRAPPIST-1 c could be entirely removed by escape processes, as indicated by recent JWST observations, or at least strongly fractionated by the escape of low molecular weight species to leave behind an O_2-rich composition (Owen 2019). Additionally, the composition of any remaining atmosphere would be influenced by ongoing disequilibrium volcanic outgassing enabled by radiogenic or tidal heating (Tyler et al. 2015b; Matsuyama et al. 2022; Seligman et al. 2024; Walbecq et al. 2025). I explicitly investigate the role of tidal heating in Chapter 4 and atmospheric escape in Chapter 5. The physical processes modelled in this chapter are not unique to TRAPPIST-1 c and HD 63433 d, so it is quite possible that the results of these simulations may be consistent with future observations of younger exoplanets with masses and host stars similar to these two (Diamond-Lowe et al. 2023; Alam et al. 2024; Scarsdale et al. 2024).

3.7.3 Compositional inhomogeneity in early atmospheres

I have generally assumed that these atmospheres can be modelled with well-mixed compositions set by outgassing from an underlying magma ocean. This assumption is consistent with previous work (Elkins-Tanton 2008; Hamano et al. 2015). However, the results presented in Section 3.6 indicate that gas-phase equilibrium chemistry may be sufficient to generate compositional inhomogeneity due to variation in the local pressure and temperature (methods Section 3.2.5; results Section 3.6). The three most abundant gases produced by the outgassing model (H_2O, CO_2, SO_2) remain approximately isochemical when the speciation is re-calculated by FastChem. However, H_2 and CO are found to have significantly reduced abundances in the upper atmosphere. This has a negligible impact on the energy balance of the atmosphere (outgoing longwave radiation differs by 0.02 W m^{-2} between the models) because the abundances differ only in regions of low pressure, which are optically thin. At the surface, the most abundant species unmodelled in the main evolutionary simulations is H_2S. The opacity of H_2S is included in the radiative transfer calculations, but the small change in outgoing radiation associated with the self-consistent chemistry model shows that it has a very minor impact on the energy balance of the atmosphere. However, H_2S could be observable in infrared emission spectra alongside SO_2 and S_2 (Janssen et al. 2023). The formation of S_8 in the upper atmosphere could lead to the production of hazes which dampen absorption features generated deeper in the atmosphere and complicate the characterisation of these planets from observations (Pavlov and Kasting 2002; Gao et al. 2017; Tsai et al. 2024a). I explicitly investigate the potential photochemical formation of SO_2 against a reducing background atmosphere in Section 5.9.

Alongside radiative heating, convection could additionally be inhibited by compositional gradients induced by chemistry and condensation, particularly for atmospheres where low molecular weight species (e.g. H_2) dominate the gas composition (Guillot 1995; Gabriel et al. 2014; Innes et al. 2023; Habib and Pierrehumbert 2024). Compositional inhibition of convection would then more commonly correspond to atmospheres formed in equilibrium with reducing mantles, or those with large gas envelopes captured from the stellar nebula, or hot atmospheres containing high-molecular weight rock vapours near the surface (van Buchem et al. 2023; Zilinskas et al. 2023; Hakim et al. 2025). In the absence of strong atmospheric mixing, photochemistry is expected to stratify the atmospheric composition and could complicate inferences of the conditions in the deeper atmosphere (Venot et al. 2012; Goyal et al. 2020; Piette et al. 2023). Future work should explore the location of the quench point in these atmospheres under various mixing scenarios with the view of understanding its impact on observables. This may require hydrodynamic models to resolve the convection (Habib and Pierrehumbert 2024), or global circulation models to resolve day-night differences (Komacek and Abbot 2019; Komacek et al. 2019a; Roth et al. 2021; Koll 2022).

3.7.4 Limitations and future work

Introduction of additional interior heating processes, such a tidal heating, could allow for permanent magma oceans in cases which would otherwise solidify. Energy dissipated in the mantles of these planets would ultimately have to be transported upwards through their atmospheres and into space. For TRAPPIST-1 c, this could stall further cooling and prolong convection in its atmosphere. Although I do not model tidal heating in this chapter, numerical simulations of tides in the TRAPPIST-1 system suggest that planet-star interactions may dissipate significant amounts of energy into their interiors (Hay and Matsuyama 2019). The maximal estimates for the power dissipated in TRAPPIST-1 c by Hay and Matsuyama (2019) are $\sim 1 \times 10^{18}$ W. Globally averaged over the surface of the planet, this corresponds to a heat flux $\sim 1000\,\mathrm{W\,m^{-2}}$. Similarly, the terrestrial exoplanet L 98-59 d exists within a system of five planets and has been suggested to host an atmosphere containing SO_2 and H_2S; this may be consistent with a permanent magma ocean enabled by planet-planet tidal interactions (Banerjee et al. 2024). The following chapters of this thesis deal with the potential for tidal and escape processes on these planets.

Atmospheric escape may play a role in setting the evolution of these planets, as it removes the blanketing introduced by atmospheric opacity. Models have shown that thermal radiation from the deep atmosphere alone may be sufficient to drive the escape of the upper atmosphere (Guo 2024). This may be particularly important for older planets as escape can continue to take place long after a magma ocean has solidified. Compositional fractionation through the preferential escape of lighter elements would also influence atmospheric composition and act to oxidise the atmosphere and magma ocean over time (Hunten et al. 1987; Kaye 1987; Wordsworth and Pierrehumbert 2014; Luger and Barnes 2015; Zahnle and Kasting 2023). Under reducing conditions with AGNI, the TRAPPIST-1 c models support H_2-CH_4 dominated atmospheres at the point of solidification. The hydrogen in these species would be preferentially lost to space through escape processes, which could yield a thin carbon-rich atmosphere and/or eventually yield a sooty bare-rock surface. However, under oxidising conditions the atmosphere is instead H_2O+CO_2 dominated, which could prove more difficult to escape than the reducing atmosphere due to the decreased scale height for larger mean molecular weight compositions. Recent hydrodynamic modelling of H_2-rich atmospheres on Earth-mass planets has shown that thermal cooling by dilute CO_2 and CO can reduce the efficiency of atmospheric escape by up to an order of magnitude (Yoshida et al. 2024). Observational indications of a reducing atmosphere (e.g. one with a raised CH_4/CO_2 ratio) *could* suggest incomplete core segregation, since remnant metal in the mantle would buffer the surface of the magma ocean towards reducing conditions (Lichtenberg and Miguel 2025). It is also worth noting that, because HD 63433 is a relatively high-mass star, its X-ray saturation timescale would have been shorter than that of TRAPPIST-1 (Johnstone et al. 2021). This means that the time-integrated exposure of HD 63433 d to the high-energy photons necessary to drive atmospheric escape would have been comparatively small, thereby potentially allowing the planet to retain an atmosphere to this day (Owen 2019; Yoshida et al. 2024).

Observations by Hu et al. (2024) of the ultra short period super-Earth 55 Cancri e have suggested the presence of a volatile-rich atmosphere, with subsequent re-visits by JWST showing substantial variation in the derived spectrum (Section 1.2.2; Rasmussen et al. 2023; Patel et al. 2024; Loftus et al. 2025). It is likely that this planet maintains a permanent magma ocean due to intense stellar heating. Detection of SO_2 in its atmosphere, or constraints on the relative abundances of CO_2 and CO (see trends in Figures 3.7 and 3.7), would indicate that 55 Cancri e currently has an oxidised interior through the same analysis applied to the synthetic spectra of HD 63433 d (Figure 3.9). While the 8 Gyr age of 55 Cancri e likely provides ample time for escape processes to strip the planet of volatiles, it is possible that its current atmosphere could be supplied by continued outgassing from its interior, which buffers the remaining volatile reservoir against escape processes (Heng 2023; Meier et al. 2023).

Future observations of TRAPPIST-1 c and HD 63433 d may be able to provide further constraints on their atmospheres and composition. Zieba et al. (2023) used a single photometric point to infer that TRAPPIST-1 c may have only a tenuous atmosphere, but phase curve observations would more directly probe the (lack of) heat redistribution occurring on the planet (Hammond et al. 2025). The small transit depth ($\sim$ 100 ppm) and correspondingly small radius of HD 63433 d measured by Capistrant et al. (2024) could indicate that HD 63433 d has already lost its atmosphere or is dominated by high-mean molar mass gases. This could be tested by radial-velocity measurements of the mass of HD 63433 d, which would allow for estimations of its bulk density. Phase curve observations may further constrain the planets' day-side temperatures and/or heat redistribution efficiency (Koll 2022; Hammond et al. 2025). If future observations indeed reveal HD 63433 d to be a bare rock, despite my models suggesting the presence of a permanent magma ocean, this would indicate that efficient escape processes have acted to strip the planet of its atmosphere despite the buffering of volatiles by dissolution into the underlying melt (Owen 2019; Zahnle and Kasting 2023). Confirmation of a volatile atmosphere on HD 63433 d would suggest that the atmospheres of rocky exoplanets can be buffered against escape by volatile dissolution into magma oceans (Dorn and Lichtenberg 2021; Lichtenberg and Miguel 2025).

3.8 Chapter conclusions

I have extended upon the PROTEUS framework with the introduction of a new radiative-convective atmosphere model. In this chapter, I used PROTEUS to simulate the early evolution of the exoplanets HD 63433 d and TRAPPIST-1 c.

From this modelling and analysis, my conclusions are as follows.

1. Atmospheres generated by magma ocean degassing can be stable to convection, depending on their gaseous composition and the spectrum of incoming stellar radiation. Even with the shutdown of deep convection, it is still possible to maintain a permanent magma ocean for warm planets, which means that the predictions of Selsis et al. (2023) cannot be directly extended to atmospheres beyond the H_2O end-member scenario. Reducing atmospheres ($fO_2 < \text{IW} + 1$) overlying permanent magma oceans have favourable prospects for being entirely stable to convection, while more oxidising atmospheres can maintain convection far above – but detached from – their surfaces, triggered by absorption of stellar radiation. It is also possible to maintain atmospheric convection from the surface of a planet upwards by the release of heat from its interior.
2. HD 63433 d may readily maintain a permanent magma ocean. The amount of melt

within the interior is strongly linked to the composition of the overlying atmosphere, which introduces a physical coupling which can only be accessed by time-integrated modelling. Future observations of this planet's infrared emission spectrum would allow for the characterisation of its atmosphere, which may constrain the redox state of its mantle through the (non-)detections of CO_2 and SO_2.

3. Reduced H_2-dominated atmospheres may exhibit isothermal upper-atmospheres which generate relatively featureless emission spectra that are well-matched by a blackbody. Secondary-eclipse photometry may not be a reliable discriminator between planets with thin or non-existent atmospheres versus those with isothermal profiles that extend into optically thick regions.

Given the indications of sustained convection in these models of TRAPPIST-1 c, in the next chapter I consider mantle tides as a potential source for internal heating, and their relationship to atmospheric convection and climate states.

Chapter 4

Tides regulated by atmospheres and rheology

Observations of specific multi-planet systems provide opportunities for insight into the physics of planetary environments, marginalising over uncertain differences between star systems. Here, I investigate the planets of the L 98-59 system in detail, following recent JWST transmission spectroscopy of planets b and d. Introduction of tidal heating into PROTEUS reveals a generalised feedback between atmospheric energy transport – including convection – and the tidal heating within planetary mantles. I present a characterisation of the early histories of these three exoplanets, which provides context for upcoming observations as part of the JWST Cycle 4 and the ongoing Hot Rocks Survey (Diamond-Lowe et al. 2023). A portion of the research presented in this chapter is published in the Mon. Not. R. Astron. Soc (Nicholls et al. 2025a).

4.1 Introduction

I have motivated that rocky planets form in a hot state, in which their interiors are largely molten (Chapter 1.1). These early magma oceans subsequently cool through thermal radiation, and in many cases will solidify (e.g. the Earth). However, in some cases the interiors of rocky planets could be sustained in a permanently (semi-)molten state through the continuous input of energy alongside potential blanketing by an overlying atmosphere (Herath et al. 2024). One factor in a planet's energy budget is the heat generated within its interior. This could be from radioactive decay, but also from tidal effects due to planet-planet and planet-star gravitational interactions (Driscoll and Barnes 2015; Hay and Matsuyama 2019; Quick et al. 2020).

Tidal theory is an established field of research, so there are fruitful models to draw upon for the purposes of this thesis. Tidal theories see application to the Earth (Kaula 1964; Zahnle et al. 2015), the Galilean moons (Spencer et al. 1990; Hay et al. 2020; Park et al. 2024), and recently to exoplanets (Hay and Matsuyama 2019; Seligman et al. 2024; Farhat et al. 2025). Tides may be negligible for many planets, but sufficiently large tidal heating within the interiors of close-in exoplanets could keep their mantles molten or allow for ongoing volcanic activity (Henning et al. 2009; Kaltenegger et al. 2010; Ostberg et al. 2023; Seligman et al. 2024). Here, I will focus only on tides raised within a planet due to an eccentric orbit around its host star, ignoring explicit planet-planet gravitational interactions. Significant eccentricities may be present during the earlier stages of a planet's lifetime when the stabilising effect of gas drag is lost due to dispersal of the stellar nebula (Gomes et al. 2005; Nesvorny 2018), and eccentricity may be maintained through gravitational perturbations by neighbouring planets (Barr et al. 2018; Hay and Matsuyama 2019). A planet on an eccentric orbit will pass through a changing gravitational potential over time due to the changing distance from its star, with a gradient in the potential existing across the planet at each point of its orbit. More eccentric and faster orbits generate a larger potential difference, so tides can dissipate large amounts of heat. In general, the power per unit volume dissipated by tides scales as

$$\dot{E}_v \propto R_p^5 P^{-5} e^2 \tag{4.1}$$

where P is the orbital period and e the eccentricity (Segatz et al. 1988). The power also depends strongly on the viscosity of the planet's mantle; for short-period rocky planets, it is generally maximised for a mantle viscosity $\eta \sim 10^{14}$ Pa s (Barr et al. 2018; Hay and Matsuyama 2019).

The physical relationship between tidal heat dissipation and the rheology of the mantle raises the prospect of a self-limiting feedback. As a young rocky planet cools from its initially molten state – and its viscosity increases correspondingly – the amount of tidal heat dissipation within the mixed phase part of its mantle will increase (Kaula 1964; Moore 2003). This additional heating due to tides could slow the solidification of the planet's mantle. Since it is atmospheric blanketing which regulates the rate at which a young planet can radiatively cool to space, it might then be expected that the makeup and structure and composition of an overlying atmosphere plays a role in controlling the amount of interior tidal heating: a potential self-regulating feedback between radiative cooling, tidal heating, and mantle rheology which I refer to as a 'radiation-tide-rheology feedback'.

Whatever its origin, the recession of our Moon is a consequence of tidal phase lag interactions, which transport potential energy from the Moon's orbit to heat energy within the Earth's mantle (Williams and Boggs 2015; Lock et al. 2018). Crystallisation ages of lunar zircons indicate that the Moon undertook multiple re-melting events, ostensibly due to encounters with tidal resonant states (Ćuk et al. 2016; Nimmo et al. 2024) during its outward recession. Zahnle et al. (2015) previously suggested that a thick atmosphere slowed the cooling of the early Earth shortly following the canonical Moon-forming impact (Canup and Asphaug 2001). Prolonging Earth's molten state, with a low viscosity, would have made tidal dissipation within the Earth's interior inefficient, significantly slowing the orbital recession of the Moon (Zahnle et al. 2015). It should be noted that Zahnle et al. (2015) assume that a primordial atmosphere blanketing the early Earth would be composed of 270 bar H_2O and 50 bar CO_2. However, the favourable dissolution of H_2O into an underlying magma ocean makes this initially large partial pressure of H_2O unphysical; in reality, such an atmosphere may have been thinner and composed of additional gas species. I have previously shown that steam-dominated and otherwise binary mixtures are not the theoretically-expected composition of outgassed atmospheres (Sections 2.4.1 and 3.4). More recent modelling of tidal heating within the Hadean Earth (Korenaga 2023) has similarly shown the tidal heating within the planet's interior would have significantly impacted the recession of the Moon. This feedback is a different mechanism to the negative feedback between tidal heating and mantle convection proposed to occur within Io and some exoplanets which have been presumed to start in a solid state and then melt from the core-mantle boundary upwards (Peale et al. 1979; Segatz et al. 1988; Fischer and Spohn 1990; Moore 2003; Henning et al. 2009; Matsuyama et al. 2022; Seligman et al. 2024).

In Chapter 3, I showed studied whether exoplanetary atmospheres can become convectively stable. In these cases, atmospheric convection was triggered by the absorption of short-wave stellar radiation in the optically thick regions of the atmosphere. However, atmospheric convection may also be triggered by the net upward transport of heat generated within a planet's interior. It is therefore possible that tidal heating, by its associated geothermal heat flux, could sustain atmospheric convection, thereby also influencing the atmospheric temperature structure and compositional mixing processes. It was well-known from analytic solutions and global climate models that internal heat production can drive convection, usually parametrised by some internal or 'intrinsic'

Planet	L 98-59 b	L 98-59 c	L 98-59 d
Mass [$M_\oplus$]	0.47	2.25	2.14
Semi-major axis [AU]	0.02191	0.0304	0.0486
Eccentricity	0.167	0.049	0.098
Orbital period [days]	2.271	3.705	7.490
Measured radius [$R_\oplus$]	0.850	1.385	1.521
Instellation [$S_\oplus$]	24.7	12.8	5.01
Equilibrium temp. [K]	560.55	475.89	376.38

Table 4.1: Variables pertaining to the three planets considered in this chapter. Data derived from the NASA Exoplanet Archive (Demangeon et al. 2021; Engle and Guinan 2023; Rajpaul et al. 2024). The top part tabulates measured quantities which are used as input parameters to my model. The bottom part provides additional context about other observed quantities, which are not used directly as input parameters to my models, but will be calculated as dependent variables as part of my simulations. The present-day radiative equilibrium temperatures in this table are calculated for a Bond albedo of 30%.

temperature $T_{\rm int}$ (Guillot 2010; Parmentier et al. 2015). Yet, in many studies $T_{\rm int}$ is usually chosen on an *ad-hoc* basis for lack of constraints (Seager 2011; Hu et al. 2025). Here, I am able to self-consistently calculate the heat production within a rocky planet due to tides.

4.2 Outline of modelling approach and case studies

I consider the three transiting inner planets of the L 98-59 system as test cases for atmosphere-interior-tidal interactions. This system was introduced in Section 1.2.2. Previous estimates of the tidal heat dissipation within L 98-59 b/c/d indicate that these planets could experience significant ongoing interior heating due to their eccentric orbits (Quick et al. 2020). Seligman et al. (2024) calculated globally-averaged heat fluxes of 61.1, 24.7, and 0.6 kW m^{-2} for planets b/c/d respectively.

Observations of these three transiting planets have been made with TESS, JWST, HST, HARPS, and ESPRESSO. The HST transit depth constraints placed on the innermost planet (b, a sub-Venus) rule out an extended envelope (Demangeon et al. 2021; Damiano et al. 2022; Zhou et al. 2022). Recent observations with JWST NIRSpec (Bello-Arufe et al. 2025) have been used to infer an SO_2-rich secondary atmosphere on planet b, suggested to be supplied by outgassing from an oxidised $f{\rm O}_2 \gtrsim$ IW + 2.7 subsurface magma ocean which is permanently sustained by tidal heating in a situation analogous to Io. Although an SO_2-rich atmosphere is favoured, a ‘wide range of lower SO_2 abundances' and a bare rock scenario where the planet is lacking an atmosphere are both also consistent with their observations of planet b. The presence of hazes/clouds are disfavoured for this planet. Observational constraints on the second planet (c, a super-Earth) also disfavour H_2-dominated atmospheres, suggesting that it may host a high molecular weight secondary atmosphere or no atmosphere (Barclay et al. 2023; Zhou et al. 2023; Scarsdale et al. 2024). In comparison, transmission spectroscopy of planet d has hinted at a $\sim 10\,\mathrm{g\,mol^{-1}}$ 'hybrid' atmosphere containing sulphur-bearing compounds SO_2 and H_2S in a background of H_2, which is also consistent with planet d's relatively low bulk density (Banerjee et al. 2024; Gressier et al. 2024). Table 4.1 outlines relevant physical parameters for these three planets.

I have broken my investigation into the role of tidal heating within the interiors of these planets into three stages.

- Firstly, I apply a semi-analytic thermal evolution model. This simplified model allows me to probe my suggested radiation-tide-rheology feedback, as well as potential hysteresis behaviours. This simple model is described in Section 4.3 and is similar to the thermal evolution model applied in Zahnle et al. (2015) in that the planet is treated as a 'box model'.
- Secondly, I apply PROTEUS under the baseline scenario in which no tidal heating occurs. These cases without provide control scenarios in which the planetary evolution pathways of these three planets are primarily set by the blanketing effect from their overlying atmospheres and irradiation by their star.
- Thirdly, I simulate the evolution of these three planets using PROTEUS while self-consistently accounting for tidal heating alongside the other aforementioned physics. My tidal heating model is described in Section 4.4.

For the latter two parts, I run a range of simulations which vary the oxygen fugacity fO_2 at the magma ocean surface relative to the iron-wüstite buffer (IW$-$5 to IW$+$5) and the radius fraction r_c of the metallic Fe core (50% to 90%) relative to the radius of the magma ocean-atmosphere interface R_{int}. In reality, fO_2 and r_c are likely correlated, but the wide range considered for these two input variables allows for unknown and unmodelled complexities in the redox evolution of these planets (Wade and Wood 2005; Lichtenberg et al. 2023). A trend between fO_2 and r_c is seen in the Solar System (Trønnes et al. 2019): Mercury has a highly reducing surface environment between IW − 6.5 and IW − 3.5 with a large metallic core fraction $r_c \approx 0.82$ (Namur et al. 2016; Cartier and Wood 2019), while Earth has had an upper mantle oxygen fugacity of approximately IW + 4 with a core radius fraction of $r_c \approx 0.55$ since the Hadean (Lodders and Fegley 1998; Rollinson et al. 2017). It has been suggested that the planets in the L 98-59 system have small metallic core fractions due to the host star's relatively low Fe/(Mg + Si) ratio, but this quantity is poorly constrained (Demangeon et al. 2021). For the purposes of this chapter, a nominal radius of the rocky interior R_{int} is approximated for each planet from its measured mass (Table 4.1) via the equation of state and hydrostatic integration in SPIDER. This structure calculation is the same approach used in Chapter 3. Similarly, the initial abundances of CHNS in the modelled magma oceans are nominally set equal to estimates for the volatile composition of Earth's primitive mantle (Wang et al. 2018).

The L 98-59 semi-empirical spectrum from the MUSCLES Extension is used in this chapter as a template for the stellar emission (Behr et al. 2023), and is evolved self-consistently alongside the evolution of the planet using MORS as described in Section 2.2.10. The current age of L 98-59 is estimated by Engle and Guinan (2023) to be 4.94 ± 0.28 Gyr, so I adopt this median value as the current age of L 98-59 when generating the historical stellar spectra used in my simulations. As discussed in Section 2.2.10, it should be noted once-more that ageing M-type stars is always indirect and generally uncertain (Soderblom 2010; Kippenhahn et al. 2012; Reiners et al. 2012). It has been suggested that the ±0.28 Gyr uncertainty on the age of L 98-59 represents an under-estimate (Demangeon et al. 2021).

Multiple estimates have been placed on the mass of L 98-59:

- $0.273 \pm 0.030\ \mathrm{M}_\odot$ (Demangeon et al. 2021),
- $0.312 \pm 0.031\ \mathrm{M}_\odot$ (Cloutier et al. 2019), and
- $0.313 \pm 0.014\ \mathrm{M}_\odot$ (Kostov et al. 2019)

For this investigation, I adopt a recent estimate of $0.273\ \mathrm{M}_\odot$ from Table A3 of Demangeon et al. (2021). Higher stellar masses correspond to larger planetary tidal heating rates, all else equal. I use a constant solar zenith angle of $\cos^{-1}(1/\sqrt{3}) = 54.74^\circ$ and scale the stellar spectrum by a factor of $1/4$ as in Chapter 3, with the assumption that these three planets approximately oscillate about a state of synchronous axial-orbital rotation due to tidal effects. The goal of this current chapter is not to reproduce present-day atmosphere observations of these planets, but to test the effects of tidal heating coupled to magma ocean evolution.

4.3 Simulations with a semi-analytic thermal model

4.3.1 Evolutionary tracks and hysteresis

I have hypothesised that negative feedback between tidal heating, mantle viscosity, and radiative cooling could extend the lifetimes of primordial magma oceans or extend them indefinitely. This complex picture involves a number of potentially strong physical interactions, so here I first apply a zero-dimensional semi-analytic thermal evolution model. In doing so, I am not exposed to the uncertainties inherent to a more complex model, and instead aim to capture the physical interactions in an intuitive manner. This particular semi-analytic modelling does not aim to make quantitative predictions of tidal heating rate and planetary evolution timescales, but to capture the core essence of the proposed interactions and their qualitative behaviour.

In this simplified evolution model, the planet is considered a homogeneous sphere with a constant density ($\rho = 4550\,\mathrm{kg\,m^{-3}}$), heat capacity ($c_p = 1250\,\mathrm{J\,kg^{-1}\,K^{-1}}$), solidus ($T_s = 1500\,\mathrm{K}$), and liquidus ($T_l = 2000\,\mathrm{K}$). These values are sufficiently representative to mimic a 'real' physical model, and are chosen to be broadly consistent with the properties of Earth's mantle (Stixrude and Lithgow-Bertelloni 2005). In reality, T_s and T_l both depend on pressure and minerology (Katz et al. 2003; Andrault et al. 2011). Given a mass m, the radius can be simply calculated as

$$R = (3m/4\pi\rho)^{1/3}. \tag{4.2}$$

The short-wave surface albedo α is set to 0.2 and the long-wave emissivity ε is set to unity (Essack et al. 2020; Fortin et al. 2024; Hammond et al. 2025). The planet is irradiated on its day-side with a bolometric flux F_{ins}, and its surface emits radiation directly into space isotropically as a greybody according to the Stefan-Boltzmann law

$$F_u = \sigma \varepsilon T^4. \tag{4.3}$$

The net power P_n entering the planet as a function of its temperature T can then be expressed as an energy balance between the absorbed, internal, and emitted fluxes:

$$P_n(T) = \pi R^2 (1-\alpha) F_{\text{ins}} + 4\pi R^2 F_i - 4\pi R^2 \sigma \varepsilon T^4, \tag{4.4}$$

where F_i is the internal heat flux (such as from tidal or radiogenic heating). This expression for the thermal evolution of the planet is identical to the interior evolution model of the young Earth set out by Zahnle et al. (2015). Through the chain rule, Equation 4.4 can be converted to a bulk heating rate

$$\frac{\mathrm{d}T}{\mathrm{d}t} = \frac{4\pi R^2}{m c_p}\left(\frac{1-\alpha}{4} F_{\text{ins}} + F_i - \sigma \varepsilon T^4\right). \tag{4.5}$$

If we were to take $F_i = 0$, the solution to equation 4.5 is that of planetary radiative equilibrium. However, the inclusion of F_i as a function of temperature T permits a calculation which parametrises the effects of interior heating, which is conceptually derived from tides here. Maxwellian models of tidal heat dissipation demonstrated by more physical calculations generally yield a unimodal relationship between the amount of heat dissipated and the mantle melt fraction (Henning et al. 2009; Driscoll and Barnes 2015; Hay and Matsuyama 2019). For the purposes of this initially simplified modelling, I heuristically parametrise the tidal heat flux with a Gaussian function

$$F_i(T) = F_c \exp\left[-\left(\frac{T - T_c}{T_w}\right)^2\right], \tag{4.6}$$

where T_w characterises the temperature range sensitive to tides, T_c is the temperature at which tidal heating is maximised, and F_c is the amplitude of the tidal heating. I centre this heating function between the solidus and liquidus of the material. In reality, the amount of heat dissipated by tidal stresses depends on a number of factors which are robustly accounted-for in my PROTEUS simulations in the following sections. A Gaussian function is an appropriate choice for the level of complexity desired of this semi-analytic model, as it has a single global maximum which decreases monotonically to zero at ±∞ (qualitatively representing a negligible amount of heat dissipated by tides in the fully-solid and fully-molten regimes).

These simplifications allow me to express the complete form of my semi-analytic evolution model as a single equation:

$$\frac{dT}{dt} = \frac{4\pi R^2}{m c_p}\left(\frac{1-\alpha}{4}F_{\text{ins}} + F_c \exp\left[-\left(\frac{T-T_c}{T_w}\right)^2\right] - \sigma\varepsilon T^4\right). \tag{4.7}$$

which is nominally integrated over time from $(T, t) = (T_0, 0)$ up to $t = 20$ kyr, which provides sufficient time for the modelled cases to reach steady-state (see Figure 4.1). I adopt the geometry of L 98-59 b for this example scenario, taking its present-day instellation of $24.7S_\oplus$ and a mass of $0.47M_\oplus$ (Rajpaul et al. 2024).

Figure 4.1 plots the modelled evolution tracks with this toy planet, calculated using my semi-analytic model at various tidal heat flux amplitudes F_c (line colours), and two different initial temperatures T_0 (solid/dashed line styles). In the cases of zero tidal heating (blue lines), the planet cools rapidly to its purely-radiative equilibrium temperature within 20 kyr, regardless of whether it started hot at 2500 K or cold at 1500 K. This short timescale is a result of the simplified interior model and lack of atmosphere. In comparison, under the most extreme cases of tidal heating amplitude (pink lines) the planet sustains a high steady-state temperature corresponding to a permanent magma ocean. For more intermediate cases (red and purple lines) the steady-state is sensitive to its initial conditions. Consider $F_c = 15F_{\text{ins}}$: a cold-start (dashed red line) leads to an evolution pathway in which the planet solidifies without experiencing significant tidal heating (analogous to a large viscosity on the far right of Figure 4.3). The equivalent hot-start case (solid red line) leads to significant heating, which keeps the planet in a hot state indefinitely (analogous to a low viscosity on the far left of Figure 4.3). A hot-start 'birth' scenario is considered the typical starting point of rocky planet evolution following formation due to the large amounts of energy delivered during accretion, by radioactive decay, and from impacts (Wyatt 2008; Schaefer and Elkins-Tanton 2018; Lichtenberg and Miguel 2025).

Whilst the thermal evolution model applied in this section is highly simplified, it is able to generate the behaviour that I hypothesised in Section 4.1: tidal heating can yield negative feedback on temperature, which can prevent magma ocean solidification. How much these results extend to my more physically representative evolution model with atmosphere blanketing to modulate the planet's cooling is explored in the following sections.

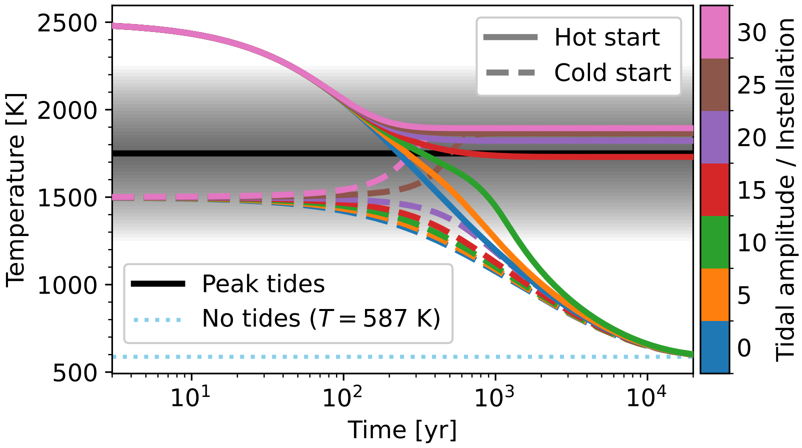

Figure 4.1: Simulated evolution tracks for a toy analogue of L 98-59 b calculated with my semi-analytic model. Temperature is plotted over time for different initial temperatures T_0 (line style) and tidal heating amplitudes F_c (line colour). The shaded region shows the temperature regime in which tidal heating is significant, via Equation 4.6. The black line shows the temperature at which tidal heating is maximised. The dotted blue line shows the pure-radiative equilibrium temperature.

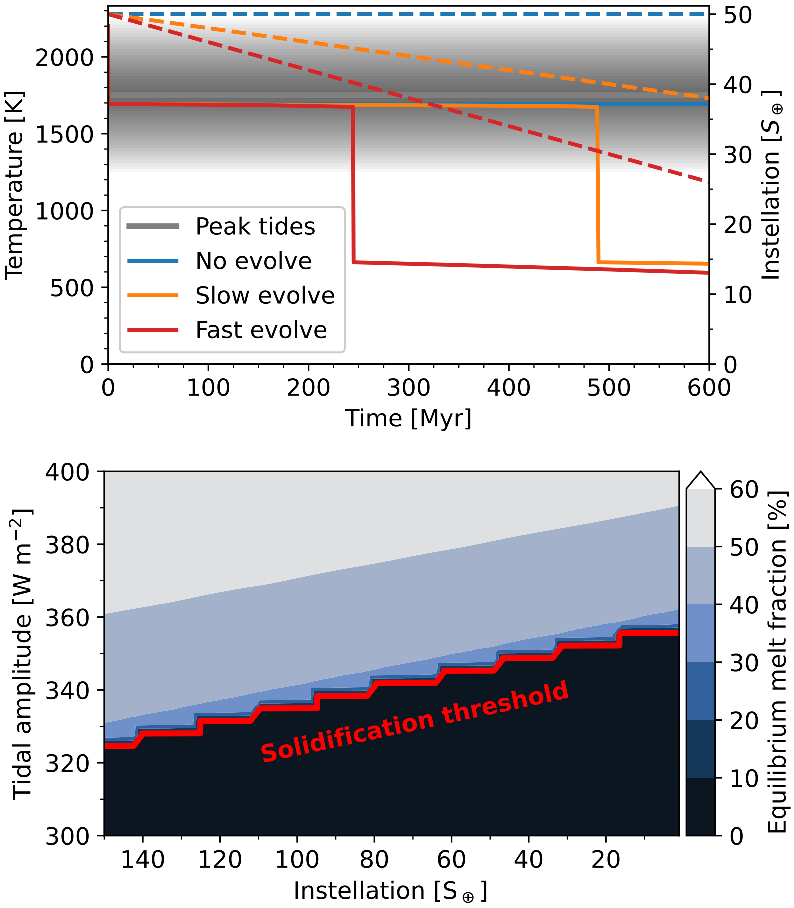

Figure 4.2: Thermal evolution of a toy planet subject to tidal heating alongside co-evolution of its star. Top: solid lines plot the planet's temperature over time for three cases of stellar evolution (line colours). Dashed lines plot the correspondingly evolving instellations. The thick black line indicates the temperature at which tidal heating is maximised. **Bottom**: Equilibrium melt fractions Φ for a toy planet calculated with my semi-analytic thermal evolution model, for a wide range of instellations F_{ins} and tidal heating amplitudes F_c. The red contour line divides the space at $\Phi = 1\%$.

4.3.2 A 'blue sky catastrophe' at later ages

Abrupt transitions of a system from one state to another, such as state bifurcations, are well-studied phenomena in the context of Earth's past and current climate (Lorenz 1963; Ghil 1976; Steffen et al. 2018; Boers et al. 2022). There is potential for planets with otherwise stable conditions to be disrupted by external factors such as orbital perturbations (Riechers et al. 2022) and stellar evolution (Kasting 1988; Goldblatt et al. 2013; Turbet et al. 2023).

We might wish to consider whether planets that find themselves in seemingly stable steady-states (Figure 4.1), through the suggested feedback mechanism, could later solidify. This could occur for situations in which tidal heating is initially sufficient to sustain a permanent magma ocean, but only in combination with intense stellar irradiation and/or a sufficiently large atmosphere. The slowly decreasing luminosity of an M-type host star raises the possibility of a planet sustaining a magma ocean for a substantial period of time, until the stellar luminosity decreases below some tipping point, causing the planet to rapidly solidify: a type of 'blue sky catastrophe'[1] (Meca et al. 2004; Zhou 2013).

I now apply my semi-analytic toy model to a test planet with a fixed arbitrary tidal heating amplitude F_c. This is done under the consideration of three scenarios for how the instellation F_{ins} could evolve: constant, slowly decreasing, or rapidly decreasing in time. Figure 4.2 presents these three additional simulations, with the different simple stellar evolution scenarios indicated by the line colours. The case without stellar evolution (blue lines) remains in radiation-tide-rheology equilibrium with a hot surface. The cases in which F_{ins} decreases undergo a bifurcation when the F_{ins} drops below a critical value (approximately 80% of its initial value in this case). This bifurcation represents the point at which tidal heating is no longer able to sustain global energy balance with a molten interior, causing the planet to rapidly cool to a lower temperature which can be sustained by the instellation alone.

The particular values of F_{ins} considered in this section are not important because I

---

[1] A 'blue sky catastrophe' is a state bifurcation that occurs when a system – which appears to be in a stable state – rapidly changes state *out of the blue*, due to the effects of an otherwise slowly-changing variable.

consider here a toy thermal evolution model in which F_{ins} and the albedo α are effectively degenerate in forcing the thermal evolution of the planet. Any decrease to F_{ins} could be compensated by some decrease to α; quantitatively modelling potential planetary evolution pathways necessitates a comprehensive modelling tool such as PROTEUS. Figure 4.2 shows that it is, however, still important to consider that rapid changes to a planet's thermal state may occur later in its lifetime, potentially triggered by slow changes to external forcings, such as the amount of radiation received from its host star.

Figure 4.2a reveals that bifurcations to a cool state may indeed be triggered once the instellation drops below some critical value. To elucidate how this compares against the strength of my (parametrised) tidal heating within the semi-analytic model, I simulated the evolution of the toy planet under different tidal heating amplitudes F_c and instellations F_{ins} (constant in time). Figure 4.2b represents the equilibrium states of these simulations, plotting the mantle melt fraction versus F_c and F_{ins}. For a given tidal heat flux amplitude, a planet would evolve from the left side to the right side of the plot. Unless the tidal heating is particularly efficient (large F_c), a wide range of these toy planets undergo a bifurcation upon intersection with the red line. Their melt fraction decreases from $> 30\%$ on the left side to less than 1% on the right side of the red line.

4.4 Simulations with viscoelastic mantle tidal heating

4.4.1 Implementation within PROTEUS

To introduce the effects of mantle tidal heating into PROTEUS, I use the LovePy[2] code previously developed by Hay and Matsuyama (2019) and Hay et al. (2020). This calculation ignores direct planet-planet tidal interactions which would be present in multi-planet system states, such as TRAPPIST-1 and L 98-59. A full derivation may be found in Sabadini et al. (2016) and Padovan et al. (2018); here I outline the most important parts of the formulation used in LovePy.

In brief, a planet orbiting around its host star with a non-zero eccentricity is subject to a time-dependent *external* gravitational potential due to continuously changing planet-star separation (Kaula 1964). The differing potential across a planet will act to

---

[2] `https://github.com/nichollsh/lovepy`

deform it from a perfect sphere, inducing an additional *internal* potential. Together, these potentials hydrostatically support the planet in a state of momentum force balance. Work done during the deformation, dissipated as friction, is the source of tidal heat energy.

More specifically, the external gravitational potential due to tides acting on a planet can be written as

$$W(r,\psi) = \frac{GM_p}{a} \sum_{n=2}^{\infty} \left(\frac{r}{a}\right)^n \mathcal{P}_n(\cos\psi) \tag{4.8}$$

where ψ is the angle between a point on the planet and the perturber, which in my case is the host star, and r is the radial distance from the centre of the planet, and $\mathcal{P}$ is the Legendre polynomial of spherical harmonic degree n (Murray and Dermott 1999; Sabadini et al. 2016).

The external tidal potential W induced by the perturber gives rise to an internal potential V due to the resulting deformation of the planet's surface from a spherical shape. These two potentials are related as:

$$V_n(r) = k_n W_n(r) \tag{4.9}$$

where k_n is the n^{th}-order Love number (Love 1911), describing the rheological properties of the planet, and in particular how its shape at order n deforms according to the external potential (Segatz et al. 1988; Sabadini et al. 2016). Since the deformation tidal heating calculations are projected onto Legendre polynomials, we can neglect order $n = 0$ and $n = 1$ terms. The first-order Legendre polynomial describes a circle, and the second-order polynomial an ellipsoid:

$$r_{\text{int}}(\theta) = R_{\text{int}}[1 + \varepsilon\mathcal{P}_2(\cos\theta)] \tag{4.10}$$

So the first-order relationship between tidal potential on planetary deformation are captured by the k_2 Love number. As in Hay and Matsuyama (2019), here I do not include higher-order terms in the potentials or in the deformation vector (Renaud et al. 2021).

The amount of radial displacement – the deformation $\mathbf{u}$ from a sphere to an ellipsoid – at each layer must satisfy the external potential W (from the eccentricity) and the induced internal potential V (from the deformation itself) according to force balance. It is through the time-variation of this displacement $\mathbf{u}$ that heat is generated, as tides apply stress to do work on the mantle, which deforms while dissipating some of the work energy as friction.

The volumetric power density required to do work to deform each layer is then

$$\dot{E}_v^{\text{tide}}(t) = \rho \frac{\mathrm{d}\mathbf{u}}{\mathrm{d}t} \cdot \nabla(V + W) \tag{4.11}$$

The radial displacement **u** can be analytically written in terms of the external and internal potentials (Segatz et al. 1988). A simultaneous solution for the displacement, and shear stresses, and internal potential, together wrapped into a length-6 vector solution $\mathbf{y}$, is obtained by invoking conservation of momentum (Sabadini et al. 2016). In LovePy, this problem is solved as a system of differential equations with respect to radial distance r from the centre of the planet,

$$\mathrm{d}\mathbf{y}/\,\mathrm{d}r = \mathbf{A}(r)\mathbf{y} - \mathbf{f}(r) \tag{4.12}$$

where the matrix **A** analytically expresses the rheological properties of the material making-up the mantle at each layer: its bulk and shear moduli, viscosity, etc. The term $\mathbf{f} = 0$ could incorporate the additional forcing of other massive bodies, but I ignore this contribution at the present time.

To calculate the bulk tidal dissipation rate for a *homogeneous* mantle, we would first time-average Equation 4.11 over one orbital period, and then apply the divergence theorem to re-write the volume integral in terms of a closed surface (Segatz et al. 1988; Hay and Matsuyama 2019). The power dissipated within the mantle in this somewhat simplified homogenous-mantle scenario is then

$$\dot{E}_m^{\text{tide}} = \frac{-21}{2G} \mathrm{Im}(k_2) \cdot (\omega R_{\text{int}})^2 \tag{4.13}$$

where ω is the angular frequency of the external perturbation (i.e. that of the planet's orbit).

In practice, LovePy calculates the tidal heating power density (W kg^{-1}) at each layer of the mantle according to the properties of each layer. Numerically, this system of equations is solved via a 'matrix propagator method' using non-dimensionalised variables following Padovan et al. (2018). The displacement is calculated at each discrete layer of the mantle while integrating radially outwards from the core-mantle boundary, determining the amount of work done to deform each layer of the mantle, and the heat dissipated therein. The shear viscosity η, bulk modulus κ, and density ρ of each layer are all calculated based on the local melt fraction, temperature, and pressure in the mantle

(Wolf and Bower 2018; Kervazo et al. 2021) and assuming some bulk material composition (Section 2.2.5). Regions with a melt fraction above the critical melt fraction Φ_c are approximated as low shear strength solids with rigidity $\mu = 1$ Pa (Bierson and Nimmo 2016).

The viscous and elastic response of the mantle to the tidal stresses, by which the terms of **A** are evaluated, follows the Maxwell viscoelastic model (Peltier 1974; Murray and Dermott 1999). The Maxwell model is a simplified description of a fluid where viscous flow is permitted on timescales longer than the Maxwell time τ_M (e.g. mantle convection) but elastic behaviour is exhibited on shorter timescales (e.g. orbital perturbations). This picture is mechanically analogous to an elastic spring and viscous damper connected in series.

Under the Maxwell model we can then directly express the imaginary part of the Love number k_2 as

$$\mathrm{Im}(k_2) = \frac{-3\bar{\mu}\omega\tau_M}{2 + 2[(1+\bar{\mu})\omega\tau_M]^2} \tag{4.14}$$

where $\bar{\mu} = 19\mu/(2\rho g r)$ is the effective rigidity of each homogeneous layer, and $\tau_M = \eta/\mu$ is the Maxwell timescale (Henning et al. 2009).

Within PROTEUS, this tidal heating calculation with LovePy is performed self-consistently with the time-evolution of the mantle melt fraction and temperature profiles determined by SPIDER. The depth-dependent rheological parameters are updated as the planet's temperature structure evolves.

4.4.2 Expectations for the tidal power-density

To understand the expected behaviour of this more realistic interior tidal heating model, I now calculate the tidal heat flux arising through the surface of a homogeneous planet orbiting with Earth-like rheology and geometry, at a range of shear viscosities and orbital periods around a Solar-mass star. The results of these calculations are shown in Figure 4.3. Heating increases for shorter orbital periods, exceeding 1 MW m^{-2} at orbital periods shorter than 1 day. Of greater importance in determining the tidal heating rate is the shear viscosity η. In the limits of largely inviscid ($\eta < 10^9$ Pa s) and highly viscous ($\eta > 10^{21}$ Pa s) cases, it is clear from Figure 4.3 that the tidal heating rate can be considered negligible except for orbital periods shorter than 1 day. The tidal heating rate is instead maximised for $\eta \sim 10^{15}$ Pa s, although the exact point at which maximum heating is induced shifts to larger η for longer orbital periods as the Maxwell time increases. These behaviours compare well with previous literature (Segatz et al. 1988; Henning et al. 2009; Driscoll and Barnes 2015). For comparison, Earth's current geothermal heat flux is 0.07 $\mathrm{W\,m^{-2}}$ and Io's is approximately 2.5 $\mathrm{W\,m^{-2}}$ (Korenaga 2008; Park et al. 2024).

Over-plotted on Figure 4.3 are the estimated orbital periods and eccentricities of the three L 98-59 planets of interest. It can be seen that we should expect these planets to undergo significant tidal heating when their viscosities are greater than $\sim 10^9$ to $\sim 10^{12}$ Pa s. A comprehensive understanding of how tidal heating impacted their early evolution requires the tides within the PROTEUS framework. It should also be noted that the eccentricity estimates for these planets come with significant relative uncertainties (Demangeon et al. 2021; Rajpaul et al. 2024); noting the log-scaling in the bottom panel of Figure 4.3, it is quite possible that these planets experience different tidal heat fluxes in reality compared to those modelled here and in the literature, solely as a result of their uncertain orbital configurations (Quick et al. 2020; Seligman et al. 2024; Farhat et al. 2025). I test the sensitivity of my modelling to orbital eccentricity in Section 4.6.

4.5 Emergence of tidally-supported worlds

4.5.1 Evolution neglecting tides

In this section, I first apply PROTEUS to simulate the time-evolution of planets b/c/d *without* tidal heating under different initial scenarios potential arising from planet formation; proxied by varying the oxygen fugacity $f\mathrm{O}_2$ relative to the iron-wüstite buffer and metallic core radius fraction r_c. In previous chapters I held r_c constant at an Earth-like 55%; here it is varied because r_c controls the mantle depth, and therefore the conditions under which tidal stresses are acting. This corresponds to 100 simulations per planet. Following a hot-start, Figure 4.4 presents the calculated solidification time for these three planets.

All the evolution scenarios that neglect tidal heating are found to result in mantle solidification within 100 Myr, despite blanketing by their overlying atmospheres. Their

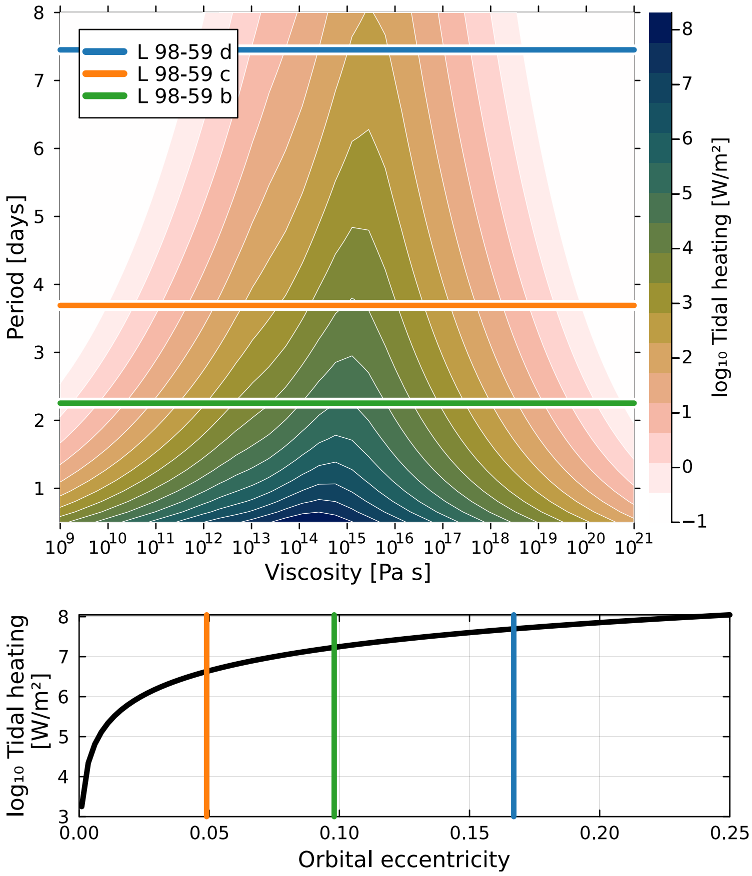

Figure 4.3: Surface tidal heat flux under a Maxwell viscoelastic rheology calculated with LovePy. For the illustrative purposes of this plot, the shear modulus ($\mu = 60\,\mathrm{GPa}$) and bulk modulus ($\kappa = 200\,\mathrm{GPa}$) are held constant. **Top**: heat flux versus shear viscosity and orbital period; the eccentricity is fixed at 0.05. **Bottom**: heat flux versus orbital period; the viscosity is set to 10^{15} Pa s and the orbital period to 1.5 days. Over-plotted are the estimated orbital periods and eccentricities of the L 98-59 planets (Table 4.1).

solidification time depends on both the oxygen fugacity of the mantle (through its control over atmospheric composition) and the relative size of the metallic core. By comparing the top and middle panels of Figure 4.4, it can be seen that planet b generally solidifies more rapidly and readily than planet c, despite its higher equilibrium temperature (Table 4.1). These comparatively different outcomes are partially a result of the square-cube law, which allows the sub-Venus planet (b) to radiate its internal energy to space more easily than the larger planets (c and d). Planet c (middle panel) generally takes the longest time to solidify. Cases with larger r_c solidify more rapidly, simply due to there being a smaller mass of melt to begin with. A solidification timescale of 100 Myr in the absence of tidal heating is consistent with previous work (Lebrun et al. 2013; Hamano et al. 2015; Lichtenberg et al. 2021). At all but the most reducing conditions ($fO_2 > \mathrm{IW} - 2$) these simulations also evolve close to the point of radiative equilibrium, where the net energy flux F^{atm} through the atmosphere is approximately equal to the total heat production within the interior, which is zero in this case without tidal heating.

Uncertainties inherent to my modelling of the stellar evolution and gas opacities could reasonably account for a small net heat flux, which means that, even in the absence of tidal heating, it is possible that these planets could retain shallow magma oceans for periods longer than 100 Myr. The luminosity of L 98-59 (an M3 star) will have decreased as it aged through the pre-main sequence and along its main sequence track. The Baraffe et al. (2015) evolution tracks, used here, predict that the bolometric stellar flux impinging upon these planets would decrease by $\sim$ 20% between the endpoint of my simulations and the estimated current age of the system. This means that even if these planets had at some point reached radiative equilibrium while maintaining a partial magma ocean, any residual melt is likely to have solidified before the present day unless heat is continually provided by some other mechanism. I adopt a null hypothesis that the primordial magma oceans on L 98-59 b/c/d would have solidified within 100 Myr after their formation in the absence of tidal heating.

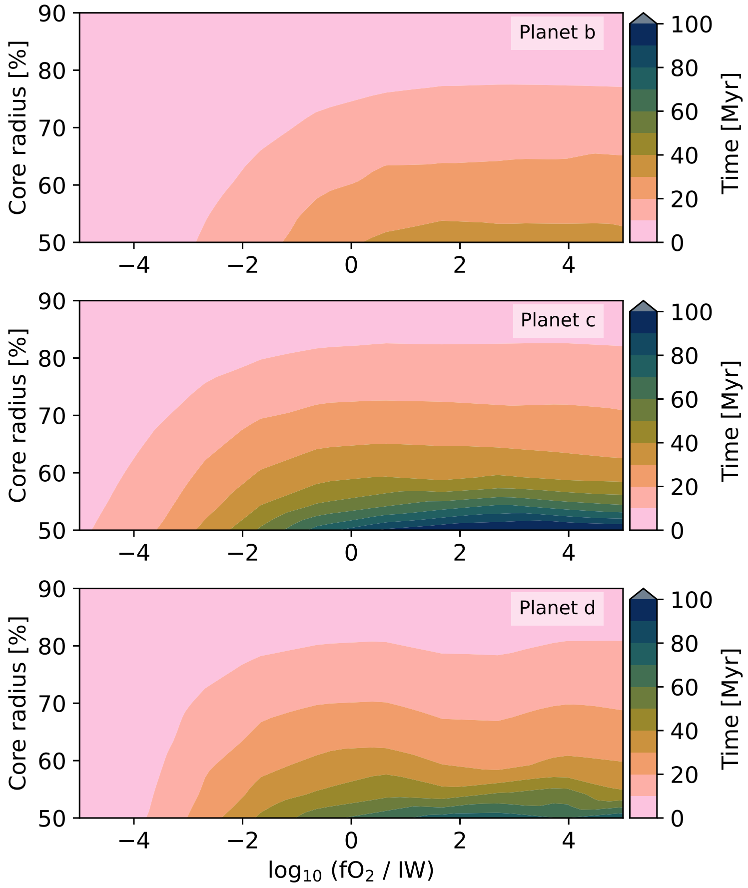

Figure 4.4: Solidification time for L 98-59 b/c/d in the absence of tidal heating. Solidification time modelled by PROTEUS (colour bars) varies between the planets, and also varies by metallic core radius fraction r_c (y-axes) and surface fO_2 (x-axes).

4.5.2 Evolution with tides

In this section, I present results of modelling the evolution of L 98-59 b/c/d with PROTEUS while self-consistently accounting for tidal heating within their mantles. As in Section 4.5.1 I initialise each planet into a fully-molten state, and explore a range of surface oxygen fugacities fO_2 and core radius fractions r_c.

The evolution pathways of melt fraction over time for of these PROTEUS simulations with and without tides are plotted in Figure 4.5. All 600 simulations first cool from their hot-start ($\Phi = 1$, $T_\text{surf} \sim 3500$ K), with a correspondingly large net heat flux F^atm. The cases without tidal heating (300 cases, cyan lines) all evolve until the mantle melt fraction is effectively zero and do not achieve global energy balance (radiative equilibrium). Initially, tidally-heated cases evolve similarly to the no-tides cases, but their pathways diverge once efficient tidal dissipation begins. The tidally-heated cases reach global energy balance ($F^\text{atm} = F_\text{tide}$) without mantle solidification, generally within 10 Myr of evolution. This difference in evolutionary outcome means that tidal heating and atmospheric blanketing are together able to slow the planets' cooling, and prevent complete solidification. The tidally-heated cases show a limiting behaviour towards equilibrium states in the vicinity of the critical melt fraction ($\Phi \gtrsim \Phi_c$, grey lines in Figure 4.5), which is similar and directly analogous to the behaviour demonstrated by the semi-analytic model in Figure 4.1. Atmospheric compositions depend strongly on mantle oxygen fugacity fO_2, as demonstrated in Chapters 2 and 3. These differences in atmospheric composition – and correspondingly their capacity to transport energy to space – lead to a range of evolutionary outcomes for a given r_c, which are visually distinct in Figure 4.5.

For planet b (top panel of Figure 4.5) the melt fraction Φ does not depend strongly on r_c or fO_2, and has a median value of $38.3\% \pm 0.1\%$ at equilibrium. For planet c (middle panel of Figure 4.5) the melt fraction depends primarily on r_c, with smaller metallic cores yielding Φ of up to 45.1%. Due to the radiative effects of the atmospheric greenhouse – which becomes more important at lower instellations – the melt fraction of planet d is sensitive to fO_2 as well as r_c. It is only for planet d that Φ ever becomes less than Φ_c in these models; this planet attains the lowest simulated melt fraction across all the tidally heated scenarios ($\Phi = 4.8\%$, for $r_c \approx 50\%$ and $fO_2 \approx \text{IW} - 5$), although this region of parameter space could be less likely to arise if $f\mathrm{O}_2$ and r_c are negatively correlated (Trønnes et al. 2019).

Together, the results presented in Figure 4.5 demonstrate that tidal heating was sufficient to sustain their primordial magma oceans on L 98-59 b/c/d for at least 10 Myr following their formation. As in Section 4.5.1, planets modelled with larger core radii r_c generally cool sooner. The median surface temperatures at the point of global energy balance in my models are: $1721.9^{+22.6}_{-23.1}$, $1771.0^{+59.4}_{-70.1}$, and $1755.4^{+47.4}_{-96.4}$ K for planets b/c/d respectively. The ranges on these values represent the full spread of surface temperatures arising from my consideration of a range of $f\mathrm{O}_2$. That these planets converge upon similar surface temperatures – despite their different instellations – is a physical outcome of the mantle dynamics modelled by SPIDER. These $T_s \approx$ 1750 K correspond to melt-fraction regime in which mantle convection balances tidal dissipation, modulated by the atmospheric blanketing at steady-state.

The corner plot presented in Figure 4.6 visualises the phase space of tidal heat flux and mantle melt fraction for the simulated outcomes of planets b/c/d. All three populations of results have unimodal distributions of mantle melt fraction (top panel), with median values greater than Φ_c. The distributions of tidal heat flux (right panel) are also unimodal. The median heat flux for planet b is the smallest of the three planets, and is smaller than the predictions made by Quick et al. (2020) and Seligman et al. (2024). In comparison, the modelled median heat flux of planet c compares well with Quick et al. (2020).

The simulations presented in Figure 4.5 and Figure 4.6 account for the greenhouse effect introduced by a range of outgassed atmospheres. For a more direct comparison with previous works (Seligman et al. 2024), I also ran simulations of these three planets under the limiting scenario in which they entirely lack atmospheres following their formation. Despite the loss of atmospheric blanketing, this additional scenario for L 98-59 b is still able to maintain a permanent magma ocean with a mantle melt fraction of 34.3% and large tidal heat flux of 1.08×10^5 W m^{-2}. This is broadly comparable to the heat flux of 6.11×10^4 W m^{-2} derived by Seligman et al. (2024) given our different mantle and tidal models. In contrast, my simulations of planets c/d in the absence of an overlying atmosphere are found to completely solidify, resulting in small tidal heat fluxes of 5.98×10^1 and $4.26\,\mathrm{W\,m^{-2}}$ respectively due to their large mantle viscosities. The stark contrast between these three no-atmosphere scenarios and those presented in Figure 4.6 highlights the important role of the atmosphere within the radiation-tide-rheology feedback, and therefore its ability to shape the thermal evolution of rocky planets. Atmospheres allow the mantles to more readily remain molten, with correspondingly lower viscosities.

4.6 Sensitivity of outcomes to orbital eccentricity

Tidal interactions can lead to changes in the orbits of planets and moons over time: damping their eccentricity and potentially leading to circularisation (Bolmont et al. 2011; Bolmont et al. 2014; Driscoll and Barnes 2015). Continual forcing, such as in the case of mean-motion resonances between planets, acts to sustain orbital eccentricities on long timescales. This interaction is seen in the Galilean satellites Ganymede and Io (Peale et al. 1979; Yoder 1979). I have thus-far modelled the evolution L 98-59 b/c/d under the assumption of orbital steady state, although telescope observations have placed relatively poor constraints on their eccentricities (Demangeon et al. 2021; Rajpaul et al. 2024). The difficulties of constraining planetary masses and orbital parameters were reviewed in Section 1.2.1.

In this section, I test the sensitivity of the planets' modelled thermal evolution to their orbital eccentricity by performing simulations similar to those presented in Section 4.4. To do this, I fix $r_c = 0.55$ and $f\mathrm{O}_2 = \mathrm{IW} + 0$, and instead vary the orbital eccentricities e between 0.001 and 0.2 with logarithmic spacing. These new calculations are done with the same orbital periods as in Table 4.1. Models within this smaller grid of simulations are evolved past the point at which they first approach equilibrium (global energy balance), and instead terminate either at solidification or when the integration time reaches 200 Myr.

Figure 4.7 presents the results of additional tests by plotting mantle melt fraction Φ versus time. All three planets are able to achieve global energy balance with large melt fractions when the orbital eccentricity is large. Planet b (top panel of Figure 4.7) retains a large amount of melt even for relatively small eccentricities; its small orbital period

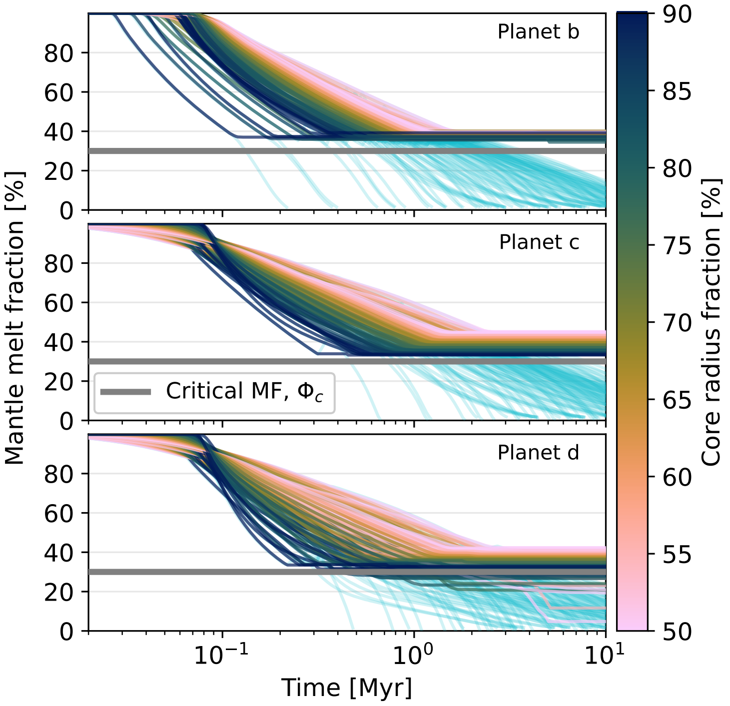

Figure 4.5: Evolution of whole-mantle melt fraction Φ for the three planets modelled. The colour bar indicates the metallic core radius fraction r_c for cases with tidal heating. Cases without tidal heating are shown in cyan lines, and all tend to $\Phi = 0\%$. The thick grey horizontal lines indicate the critical melt fraction $\Phi_c = 30\%$. I perform sensitivity tests to orbital eccentricity in Section 4.6.

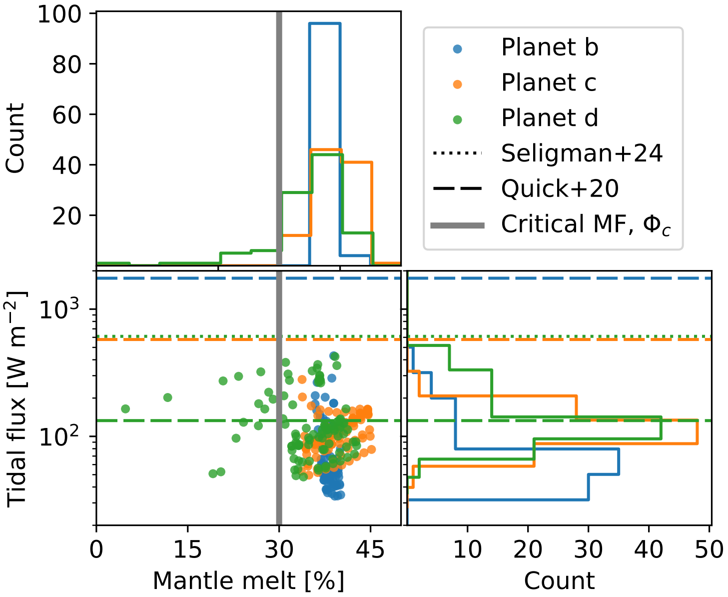

Figure 4.6: Corner plot of tidal heat flux F_{tide} versus mantle melt fraction Φ. Showing all tidally heated cases for L 98-59 b/c/d (colours). Markers represent the point at which these simulations reach global energy balance, which is never later than 10 Myr. Dashed lines indicate tidal heat flux estimates from Quick et al. (2020). The single dotted line indicates the heat flux estimate for planet d from Seligman et al. (2024); their estimates for planets b and c exceed $2 \times 10^3\,\text{W}\,\text{m}^{-2}$. The median melt fractions [%] and tidal heat fluxes [$\text{W}\,\text{m}^{-2}$] are (38.3, 52), (39.2, 101), and (36.5, 113) for planets b/c/d respectively.

enables large tidal heat production, combined with a relatively high instellation – noting that the tidal power density roughly scales as period P^{-5} compared to eccentricity e^2 (Equation 4.1). These results show that planet b is likely to have sustained its primordial magma ocean for at least 200 Myr and potentially up to the present day, even when allowing for more moderate e. Simulations of planet c (middle panel) yield many permanently-molten cases, but are able to solidify when $e \leq 0.0026$. Most of the planet d models (bottom panel) are also able to retain a large amount of melt, but cases for which $e \leq 0.0069$ are able to solidify.

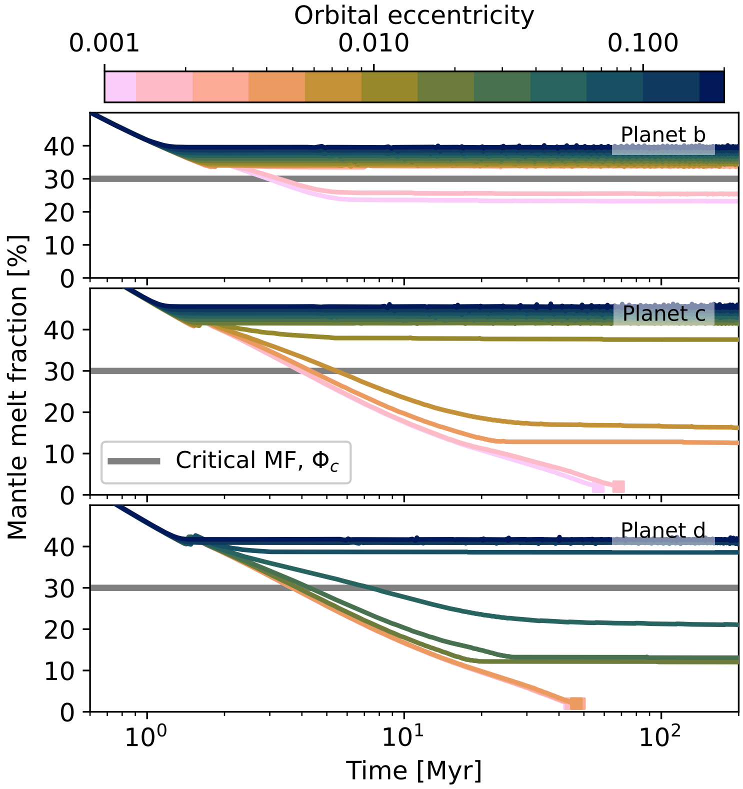

Figure 4.7: Simulated mantle melt fraction Φ over time for L 98-59 b/c/d. I plot each planet's modelled evolution at different orbital eccentricities (colour bar) with fixed ΔIW and r_c. The simulation endpoints are marked with squares. The thick grey line indicates the critical melt fraction Φ_c.

4.7 Sensitivity of atmospheric convection to interior heating

I suggested in Section 4.1 that interior heat production could drive atmospheric convection. The AGNI atmosphere model of the PROTEUS framework permits an assessment of this convective (in)stability. Simulations produced as part of the 600 simulations in Section 4.5 demonstrate convective instability to varying degrees depending on atmospheric composition and the tidal heat flux F_{tide}. In this section, I calculate test profiles of atmospheric temperature and convective heat flux for a collection of atmospheric scenarios to directly assess how internal heat production influences atmospheric convection.

Here, I perform nine calculations across three groups of scenarios:

- an absence of internal heating ($F_{\text{net}} = 0$),
- a small internal heat flux ($F_{\text{net}} = 0.1\ \text{W m}^{-2}$, comparable to Earth's present surface-averaged heat flux 0.07 W m^{-2} (Korenaga 2008)), and
- an interior heat production rate informed by my evolutionary calculations ($F^{\text{atm}} = 113\ \text{W m}^{-2}$, median in Figure 4.6).

Within each of these groups, I consider three observationally-motivated gas compositions: H_2+25%H_2S, H_2+13%SO_2, and pure SO_2. The first two mixtures are consistent with the observational mean molecular weight constraints on L 98-59 d (Banerjee et al. 2024; Gressier et al. 2024), and broadly correspond to atmospheric compositions produced by outgassing from a magma ocean containing dissolved sulfur and hydrogen. These 'hybrid' compositions are formed under relatively reducing conditions in my Section 4.5 grid. The pure-SO_2 case represents an additional end-member case which probes the pure-SO_2 atmospheric compositions suggested for L 98-59 b (Bello-Arufe et al. 2025), although their observations do not constrain the surface pressure on this planet. The pure-SO_2 scenario is included as an end-member to probe the behaviour of SO_2. I perform these atmospheric calculations stand-alone from the coupled PROTEUS framework, decoupled from outgassing and interior processes, just using AGNI stand-alone.

Figure 4.8 shows that these example atmospheres are stable to deep surface-arising convection for all the combinations of net heat flux F_{net} and composition considered in this section. This can be seen from the right panel of Figure 4.8, in which strong convective fluxes only occur at pressure levels $p < 60$ bar. For the hybrid atmospheres (olive and cyan lines) consistent with free chemistry retrievals (Gressier et al. 2024), the strength of atmospheric convection scales with the heat flux F_{net} as predicted. For a pure-SO_2 composition, the convective regime is relatively insensitive to F^{atm} – the three red profiles overlap except in the deep atmosphere. It should be noted that the pure-SO_2

cases are likely much thicker than any realistic scenario for planet b; here I am testing the capacity of SO_2 to efficiently transport energy by radiation in the potential absence of convection, in light of its observationally informed inference. All of these modelled cases intersect the planet's equilibrium temperature (grey line in Figure 4.8) at pressures less than 1 bar where the atmospheres absorb most of the incoming stellar radiation. The T-P ranges explored by the modelled profiles probe the vapour and supercritical regimes, and do not condense any volatiles. Although this modelling shows that reasonable values for the interior heat flux resulting from tidal dissipation (at equilibrium) are unlikely to trigger convection at the base of the atmosphere, a positive F^{atm} can nonetheless increase the middle-atmosphere convective heat flux for an H_2-rich composition. It can be seen that H_2-dominated hybrid atmospheres (cyan and olive lines) are compatible with permanent magma oceans (solidus $T_{\mathrm{sol}} \sim 1400$ K; Wolf and Bower (2018)) when tidal heating generates a modest flux $F_{\mathrm{tide}} = 113\ \mathrm{W\,m^{-2}}$.

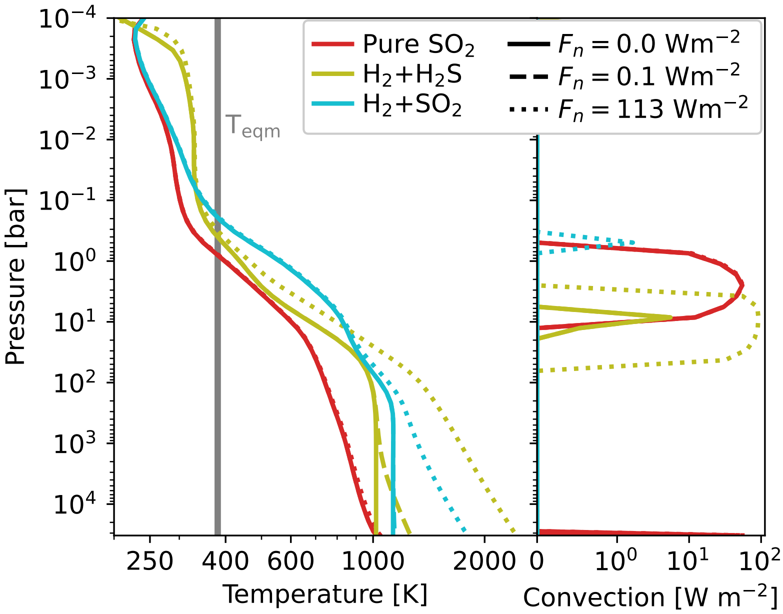

Figure 4.8: Test profiles of atmospheric temperature (left) and convective heat flux (right) modelled for L 98-59 d. I consider three observationally-motivated atmospheric gas compositions (line colour) and three values for the internal heat flux (line style). Note the log scaling applied to both x-axes. The three SO_2 cases (red lines) generally overlap in both panels. The vertical grey line indicates the radiative equilibrium temperature of this planet (see Table 4.1).

4.8 Discussion on tides and their role

4.8.1 Negative feedback and stable equilibria

Results from my simple semi-analytic modelling of L 98-59 b (Section 4.3) demonstrated a general negative feedback between the tidal heating of planetary interiors, their temperature-dependent rheological properties, and radiative cooling to space. Self-regulating feedbacks occurring within the interiors of rocky bodies have been previously suggested to occur within the Earth, on Io (Ojakangas and Stevenson 1986; Moore 2003), and indeed within exoplanetary interiors (Henning et al. 2009), although none of these works simultaneously addressed the physics of magma ocean evolution and atmospheric blanketing. When initialised with a hot-start, my semi-analytic calculations approach a thermal steady-state with super-solidus temperatures given sufficiently large tidal heat fluxes. In cold-start models, tidal heating may never be sufficient to trigger a permanent magma ocean because tides are less efficient at high viscosities, though more realistic non-Maxwellian rheological models may counter this (Moore 2003; Driscoll and Barnes 2015; Bierson 2024). These results also show that limit-cycles are permissible near these stable equilibria. I have also shown that this behaviour extends to the physically-representative PROTEUS models, which are initialised with a hot-start (Section 4.5.2). The robustness of this feedback suggests the emergence of 'tidally-supported' molten worlds within the exoplanet population: planets able to sustain magma oceans permanently, or at least with their solidification timescales extended.

Present day planetary luminosity differences arising from cold- versus hot-start formation scenarios have been discussed within the gas-giant literature (Baraffe et al. 2003; Marley et al. 2007; Molliere et al. 2022). Recent work has gone as far as to numerically constrain the entropy of the exoplanet β Pic b shortly following its formation (Marleau and Cumming 2013). I emphasise that a hot-start initial condition is the more justifiable scenario for most rocky planets (Section 1.1), where they form with fully molten interiors and then cool monotonically. However, we might consider the possibility that young planets can be *partially* re-melted by multiple giant impact events, such that secondary magma oceans are 'reset' to only semi-molten conditions, with somewhat lower entropies. With increasingly precise characterisations being inferred for rocky exoplanets, the radiation-tide-rheology feedback mechanism discussed in this chapter could be used to probe the phase space of initial conditions for a range of exoplanets (given sufficiently large orbital eccentricities).

Exoplanets which find themselves near stable equilibria resulting from the radiation-tide-rheology feedback (above the grey line in Figure 4.1, right of it in Figure 4.6) could remain in this stable state indefinitely, given a fixed instellation and atmospheric greenhouse. Given that my PROTEUS simulations (Section 4.5.2) reproduce the tide-radiative feedback exhibited by the semi-analytic modelling, it is possible that the late bifurcations presented in Section 4.3.2 could extend to physically representative simulations, and thus to reality. For observations of some exoplanets consistent with the absence of tidally heated interiors, it could be the case that this is a late-stage characteristic of their evolution, having previously spent several Gyr of time with an interior kept molten by tides. The decreasing luminosity of M-type stars on Gyr timescales means that borderline-stable cases (e.g. red and purple lines in Figure 4.1, several planet d cases in Figure 4.5) could eventually undergo a 'blue sky catastrophe' bifurcation leading to rapid mantle solidification (Meca et al. 2004; Zhou 2013). My results show that these stable equilibria are also in part shaped by atmospheric composition (Figure 4.6), so it is also possible that the loss of a greenhouse effect resulting from atmospheric escape could also induce such a bifurcation.

The mass – and therefore the luminosity – of L 98-59 is not precisely constrained. The stellar evolution model employed in my simulations suggests that the bolometric instellation of L 98-59 b would decrease from 24.1 $S_\oplus$ at 100 Myr to 19.4 $S_\oplus$ at the present day (a change of -19.5%). An instellation of 24.1 $S_\oplus$ is close to the median estimate of L 98-59 b's *current* instellation of $24.7^{+5.0}_{-4.1}$ $S_\oplus$ (Demangeon et al. 2021). This discrepancy arises from uncertainties in the star's current rotation rate. Given, then, that my estimates on the instellation of these planets are conservative, permanent magma oceans arising from my evolution models are robust to uncertainties in the luminosity of L 98-59.

In this chapter I have considered the time evolution of L 98-59 b/c/d. However, the modelled physics can be equally applied to other systems of rocky exoplanets. Barr et al. (2018) and Hay and Matsuyama (2019) found that tidal heating within the TRAPPIST-1 planets could yield large tidal heat fluxes of up to 1.57×10^4 W m^{-2}, although these estimates were not made through an evolutionary calculation. By invoking the radiation-tide-rheology feedback process discussed in this chapter, it may be possible to discriminate between cold- versus hot-start formation scenarios for a range of planetary systems. Accurately characterising the tidal heating within the TRAPPIST-1 planets may also help assess the plausibility of the multiple scenarios which are consistent with current JWST observations of TRAPPIST-1 b/c (Krissansen-Totton and Fortney 2022; Zieba et al. 2023; Ducrot et al. 2024; Maurel et al. 2025). For example, if an atmosphere on L 98-59 b is confirmed at high significance, while further constraints establish TRAPPIST-1 b as a bare rock, one of several explanations may be that TRAPPIST-1 b failed to reach a tidally-supported equilibrium magma ocean state, catastrophically outgassed upon early solidification, and thus exposed itself to desiccation by the active young star.

4.8.2 Evolution of L 98-59 b/c/d

Turning to my PROTEUS models, hot-start simulations of L 98-59 b/c/d *in the absence* of tidal heating all result in complete mantle solidification within 100 Myr of evolution (Section 4.5.1). If I instead simulate the evolution of b, c, and d self-consistently with the tidal heating model LovePy, it is found that all three planets were likely to have instead attained global energy balance whilst their mantles were still partially-molten. Long-lived magma oceans on the L 98-59 planets are quite possible, considering that my simulations of the L 98-59 planets are based on conservatively-low estimates of their instellations and are somewhat less sensitive to their orbital eccentricity. To better understand and constrain the early evolution of rocky planets and their forming atmospheres, it will be important to further observe young planetary systems; e.g. TOI-2076, TOI-1227, and HD 63433 (Bonati et al. 2019; Capistrant et al. 2024; Barber et al. 2025; Varga et al. 2025). Here, I model only the early evolution of the L 98-59 planets; if they have maintained sufficiently thick atmospheres against escape, radiation-tide-rheology feedback may potentially cause these planets to sustain magma oceans up to the present-day.

In this chapter, I cannot speak directly to the presence or absence of *present day* magma oceans on these planets because their initial (and current) volatile inventories are unknown. In this chapter I only have considered initial volatile inventories consistent with concordant estimates of volatile concentrations within Earth's primitive mantle (Wang et al. 2018). Yet, the lifetimes of these primordial magma oceans could potentially have been extended if the planets formed with a larger initial volatile content inherited from planetary formation (Venturini et al. 2020; Lichtenberg and Clement 2022; Burn et al. 2024). The outcome of magma ocean cooling depends on the planet's total volatile inventory, in part due to the collisional continuum absorption of H_2 in the atmosphere and greenhouse properties of oxidising gas species (Chapter 2). These much larger envelopes would be subject to escape processes during the $\sim$ 5 Gyr period up to the present day. The entire hydrogen inventory of the planet may not be lost, however, given the potential of the interior as a large reservoir for volatile storage (Nikolaou et al. 2019; Dorn and Lichtenberg 2021; Bower et al. 2022; Guimond et al. 2023b; Sossi et al. 2023). The complete evolution of L 98-59 d is considered in Chapter 5.

For the parameter space of r_c and $f\text{O}_2$ adopted in this chapter, the simulated mantle of planet b tends towards a narrow range of values for the mantle melt fraction ($\sim$ 38.3%, top panel of Figure 4.5), which is slightly larger than the adopted critical melt fraction Φ_c of 30%. The limiting feedback near $\Phi \gtrsim \Phi_c$ is key to understanding the early behaviour of planets like these, and cannot be captured by the steady-state modelling of Quick et al. (2020) and Seligman et al. (2024). The coolest surface temperature arising from my tidally-heated simulations of L 98-59 b is 1699 K. This temperature is only 150 K hotter than the $\sim$ 1549 K surface temperature retrieved from observations by Bello-Arufe et al. (2025), although they note that the surface is poorly constrained due to the upper atmosphere being near-isothermal – an issue I highlighted in Chapter 3. The equilibrium melt fractions modelled for planet b produce a unimodal distribution (blue colours in Figure 4.6), a direct result of the strong negative feedback between tidal heating and radiative cooling which prevents Φ from decreasing below the critical melt fraction Φ_c. Results presented in the top panel of Figure 4.7 indicate that even with an orbital eccentricity as low as 0.007 (consistent within 1 standard deviation from radial velocity measurements; Rajpaul et al. 2024) tidal heating within this planet could prevent a primordial magma ocean from solidifying. Furthermore, an additional calculation under the limiting scenario in which planet b has always lacked an atmosphere results in a non-zero mantle melt fraction at the point of global energy balance.

My models of planet b attain global energy balance with slightly lower surface temperatures than those retrieved by Bello-Arufe et al. (2025) while simultaneously maintaining significantly smaller tidal heat fluxes than those predicted at equilibrium by

Quick et al. (2020) and Seligman et al. (2024). A key difference between my modelling and these previous works is that they do not account for the modulated radiative cooling introduced by an overlying atmosphere, nor the expectation that these planets are likely to have achieved some form of energetic quasi-equilibrium during their $\sim$ 5 Gyr lifetimes. Additionally, Seligman et al. (2024) assume that a potential outer lithosphere is mechanically decoupled from the deeper interior due to an internal magma ocean. This assumed decoupling enhances the amplitude of tidal deformation in the deep mantle, increasing the heating rate (Labrosse et al. 2007; Sabadini et al. 2016). If I were to make an *ad hoc* assumption as to the interior conditions of these planets (viscosity, density, etc.) then it is quite possible to predict large tidal heat fluxes with my tidal model, but these states would not necessarily be the equilibrium conditions of these planets, nor representative of any true late stage in their evolution. The net heat flux F^{atm} transported through the atmosphere is defined as

$$F^{\text{atm}} = F_{\text{opr}} - F_{\text{ins}} f_s \cos\theta_z \tag{4.15}$$

where F_{ins} is the instellation and F_{opr} is the outgoing planetary radiation (thermal LW plus scattered SW), which is itself set by the atmospheric temperature structure and composition. The presence of an atmosphere will yield F_{opr} values less than those of a bare rock directly emitting to space for a given surface temperature, since $T(p)$ will generally decrease with height (e.g. Figure 4.8). *At equilibrium*, it must be the case that all the heat dissipated within the interior of a planet is eventually transported through its atmosphere, which requires that the tidal heat flux F_{tide} be equal to F^{atm}. Equation 4.15 does not have a single solution for F^{atm} and F_{opr} for a given F_{ins}, so there can be multiple different interior states for a given F_{ins}, with consequently different F^{atm} associated with different atmospheric compositions. This is precisely why Figure 4.6 reveals a range of possible tidal heat fluxes and melt fractions for a given planet: I have considered a range of atmospheric compositions and temperature structures, which do not presume an adiabatic temperature structure nor direct cooling of the planet's interior to space. It is the combined physics of atmospheric energy transport and interior tidal heat dissipation that simultaneously determines F_{tide}, F^{atm}, and the equilibrium state which makes these two fluxes equal. My models of planet b are thereby able to achieve global energy balance with relatively cool – although still partially molten – interiors, and consequently mantle viscosities less than critical. These low viscosities lead to much smaller tidal heat fluxes than predicted by Quick et al. (2020) and Seligman et al. (2024). This explanation also extends to my models of L 98-59 c and d. Zahnle et al. (2015), Korenaga (2023), and Korenaga (2025) modelled the coupled thermal and orbital evolution of a young Earth and Moon, and also found that atmospheric blanketing of the Earth likely exerted significant control over tidal dissipation within its mantle, yielding consequently slower lunar recession.

Planet c is the most massive of the three modelled in this chapter, and as a result takes the longest to solidify in the absence of tides (Figure 4.4). This proclivity for heat retention also extends to the tidally heated models (non-cyan lines, centre panel of Figure 4.5) in which planet c is able to maintain mantle melt fractions of up to 45.1% with an atmosphere, depending on the relative size r_c of its metallic core. Smaller r_c yield larger mantle melt fractions and a deeper magma ocean on this planet. The mantle of planet c closely approaches – but remains strictly larger than – the critical melt fraction (Figure 4.6). The similar evolutionary behaviour between planets b and c – also exhibited by my semi-analytic model – is a result of the negative radiation-tide-rheology feedback in the vicinity of Φ_c (Figure 4.5), indicating that the thermal evolution of these planets is relatively less sensitive to their particular interior structure and atmospheric chemistry compared to planet d.

Observed differences in the present-day nature of planets b and c could be attributed to processes not explicitly modelled in this chapter, such as variable initial volatile inventories or the formation of hazes in the atmosphere of planet c. If L 98-59 b has been able to retain an atmosphere in spite of its lower escape velocity, we should therefore expect planet c to also have retained an atmosphere, all else equal. Low-confidence detections of a high molecular-weight atmosphere on planet c (Barclay et al. 2023; Zhou et al. 2023) may be confirmed by future observations as part of the Hot Rocks survey (Diamond-Lowe et al. 2023) and other JWST programmes. If future observations indicate that L 98-59 c lacks an atmosphere entirely, this would also point to a bare-rock explanation for L 98-59 b unless there is some continuous resupply mechanism, such as volcanism.

The evolutionary behaviour of planet d is the most varied of the three planets modelled in this chapter. Even in the absence of tidal heating, it can be seen from Figure 4.4 that its thermal evolution fundamentally depends on the oxygen fugacity of the mantle (through its effect on the outgassed atmospheric composition), as well as on the radius of its metallic core. Planets b and c sit within a 'simpler' regime in which they are simultaneously highly irradiated (large F_{ins}) and have large eccentricities (large F_{tide}), while planet d has a radiative equilibrium temperature of only 376 K. Figure 4.5 shows that simulations of planet d are able to maintain a molten interior in the presence of tidal heating and an overlying atmosphere. In some cases, this occurs with melt fractions $\Phi < \Phi_c$; these few cases are comparable to the solid red line in Figure 4.1. Having surpassed the point of maximum tidal heat dissipation (Figure 4.3), some of the green scatter points in Figure 4.6 reveal a positive relationship between tidal heat flux F_{tide} and mantle melt fraction Φ. This relationship is simply a result of higher temperatures arising from higher internal heating rates; equivalently, that higher surface temperatures yield larger F_{opr} all else equal. Multiple independent observations of L 98-59 d indicate that this planet currently has a thick volatile envelope, avoiding the bare-rock scenario under which I predict that it would rapidly solidify regardless of its orbital eccentricity.

Being less irradiated and having a longer orbital period, the thermal evolution of planet d is also more sensitive to its orbital eccentricity e. Rajpaul et al. (2024) estimate the eccentricity of L 98-59 d to be $e = 0.0980^{+0.0270}_{-0.0960}$. These large uncertainties make an eccentricity as small as 0.002 consistent with radial velocity measurements (1σ). The bottom panel of Figure 4.7 shows that it is possible for planet d to solidify for $e \leq 0.0069$, even in the presence of tidal heating, indicating that there remains some probability that the primordial magma ocean of L 98-59 d solidified within 50 Myr given an initial volatile content comparable to the Earth's (Wang et al. 2018).

Alternatively, a thick atmosphere on planet d could be explained by it having only recently undergone a blue sky bifurcation. Tidal heating may have historically kept its volatiles dissolved into a molten interior, protecting them from escape (Dorn and Lichtenberg 2021; Farhat et al. 2025), but eventually the luminosity of its star (which is not well constrained) could have decreased below the threshold for maintaining a tidally-supported magma ocean, leading to catastrophic outgassing, and resulting in a recently-formed but significant H_2 envelope.

4.8.3 Tidally-driven atmospheric convection

It has been previously shown that outgassed secondary atmospheres at pure radiative equilibrium (net heat flux $F_{\text{net}} = 0$) exhibit deep radiative layers which are stable to convection (Chapter 3; Selsis et al. 2023). In addition to short-wave heating, atmospheric convection can be sustained by ongoing heating within a planet's interior. Inferences of SO_2 and H_2S in the upper atmosphere of L 98-59 d have been suggested to be caused by surface volcanism (Gressier et al. 2024), necessitating upward transport of gas to the level probed by transmission spectroscopy. While all the simulations in this chapter assume isochemically composed atmospheres, Section 4.7 provides context and motivation for future work by assessing the potential for convective transport in atmospheres like these.

Figure 4.8 shows that interior heating could trigger and/or strengthen convection in the atmosphere of L 98-59 d. Under atmospheric scenarios consistent with the retrievals on recent JWST observations, my modelled temperature and convection profiles within optically thick regions are sensitive to F_{net}. For the H_2+H_2S cases (olive lines), a small net heat flux of 0.1 W m^{-2} is able to raise the surface temperature by 244 K. A larger heat flux (olive dotted line) informed by my tidal heating models raises the surface temperature by +1421 K. The temperature profiles of the red and cyan lines in Figure 4.8 converge upon each other in the upper atmosphere, where the opacity of H_2 becomes negligible and SO_2 remains the primary absorber of radiation. The strength of atmospheric convection increases with F_{net}, which could also act to increase compositional mixing. However, it is unclear whether tidally-enabled atmospheric convection could lift species outgassed at the surface to the observed level, as the convection does not extend immediately from the surface upwards. Other mixing processes – Rossby waves, gravity waves, synoptic eddies, molecular diffusion, etc. – will need to be invoked to explain the transport of outgassed volatiles to the observable regions of these atmospheres. *In situ* photochemical production may explain tentative detections of SO_2, since the large molecular weight of this molecule combined with a shallow lapse rate (Figure 4.8) would make its diffusion into the upper atmosphere highly inefficient (Seinfeld and Pandis 2006; Venot et al. 2012; Tsai et al. 2023).

4.9 Chapter conclusions

In this chapter, I investigated the role of tidal heating within the interiors of rocky planets and its relationship to outgassed atmospheres. To do this, I simulated the early evolution of the sub-Venus L 98-59 b and the super-Earths L 98-59 c/d. Evolutionary modelling with a self-consistent implementation of tidal heating, mantle rheology, and atmospheric energy transport indicates that the primordial magma oceans of these three planets could have been sustained for some time after their formation. This is possible, despite the sub-solidus radiative equilibrium temperatures of these planets, due to a robust negative feedback mechanism and atmospheric greenhouse properties.

My conclusions from this chapter are summarised as follows.

1. A radiation-tide-rheology feedback is central to controlling the early evolution of rocky planets on eccentric orbits, as it introduces stable equilibria which may indefinitely prevent their interiors from completely solidifying. This behaviour extends upon previous indications that the early Earth was strongly heated by lunar tides.
2. Mixed-phase mantle tides played an important role in the early thermal evolution of L 98-59 b/c/d and likely prolonged the lifetimes of their primordial magma oceans. Across a wide parameter space, my models find that L 98-59 b may have a permanent magma ocean to this day, whether it has retained a substantial atmosphere or not. Permanent magma oceans could also extend to planets c and d for as long as they retain atmospheres, which subject to other processes; e.g. atmospheric escape.
3. When considering tidal heating within a coupled framework, atmospheric energy regulation reduces planetary tidal heat fluxes by up to two orders of magnitude compared to previous estimates. Coupled models are key to understanding the behaviour of these non-linear systems; previous works may have over-estimated tidal heat fluxes.

Further theoretical and observational studies of the L 98-59 system are merited. Modelling must tackle the complete evolution of these planets with a self-consistent representation of atmospheric escape and longer term stellar evolution, up to the present day. Future observations of these planets will constrain their dayside surface temperatures and upper atmospheric compositions, potentially allowing inferences as to their internal melt state. The L 98-59 will be observed with the Pandora SmallSat[3], which will help characterise the activity of the planets' host star, and enable more accurate characterisations of their atmospheric compositions (Barclay et al. 2025). Although not yet published, recent ground based spectroscopy of L 98-59 d has independently detected H_2S in its atmosphere, reinforcing the JWST observations. In the next chapter, I model the complete evolution of L 98-59 d up to the present day, and make a direct comparison with recent observations of this important planet.

---

[3] `https://pandorasat.com/`

Chapter 5

The life and times of L 98-59 d

Recent and upcoming observations motivate detailed study of the super-Earth exoplanet L 98-59 d. Here, with the incorporation of atmospheric escape into the PROTEUS modelling framework, I investigate the complete evolution of L 98-59 d from shortly after its formation up to the present. I reproduce telescope observations of its atmospheric composition and bulk properties, which provides a perspective on this planet's long-term transformation from an early inflated state towards that observed today. This planet must have formed with a significant inventory of volatiles, relatively exceeding that of the inner Solar System planets. My modelling of this planet through deep time highlights properties of its evolution which are unexplained by the classical gas-dwarf and water-world categorisations that are frequently adopted within the exoplanet literature. Using a chemical kinetics analysis, I suggest that photochemistry is necessary to explain the observed presence of SO_2 in the atmosphere of this planet.

A portion of the research presented in this chapter has been accepted *in principle* for publication in Nature Astronomy (Nicholls et al. 2026). Several months after producing the main models and results presented in this chapter, new observations and analyses of the L 98-59 system became available (Cadieux et al. 2025; Schwarz et al. 2025). The revised planetary masses and radii in these new analyses suggest a lower bulk density for L 98-59 d ($R = 1.63 R_\oplus$, $M = 1.64 M_\oplus$, $\rho_p = 2.2\,\mathrm{g\,cm^{-3}}$). This update strengthens my assessment that it formed volatile-rich with a reducing interior, and overall increases the relevance of my findings, since this new (larger) radius estimate places L 98-59 d within the radius valley of M-dwarf exoplanets.

5.1 Introduction

I highlighted in Chapter 1 that the super-Earth (radii $\lesssim 1.7 R_\oplus$) and sub-Neptune (radii $\sim 1.7 - 4 R_\oplus$) exoplanet populations are particularly interesting, because we have no analogues in the Solar-System for planets of this size, while these populations are highly amenable to spectroscopic characterisation with current instruments (Kempton and Knutson 2024; Lichtenberg and Miguel 2025). On a population level, these two categories are distinguished in radius-period phase space by the ‘radius valley’ (Fulton and Petigura 2018; David et al. 2021). The origin of the radius valley and these populations may result from a common set of physical processes, so two competing scenarios are often considered to explain the observed populations (Zeng et al. 2019; Valencia et al. 2025). On one hand, super-Earths and sub-Neptunes may form jointly from a common origin *gas-dwarf* scenario, where they had large H_2/He envelopes around rocky interiors (Rogers 2025). The populations would then later diverge from each other due to longer-term atmospheric escape processes – photoevaporation or core-powered mass loss (Lopez 2017; Owen 2019; Tang et al. 2024). This first scenario is argued on the basis that young planets might accrete large primordial envelopes from the stellar nebula (Lichtenberg and Miguel 2025). On the other hand, these populations could both be *water-worlds* composed of silicate cores overlain my high-pressure ice phases and steam atmospheres; argued from the perspective that formation beyond the ice line would endow them with significant water inventories (Bitsch et al. 2019; Burn et al. 2024). The two populations would then differ in their H_2O content (Mousis et al. 2020; Lacedelli et al. 2022; Luque and Palle 2022). At the same time, estimates of stellar ages suggest that sub-Neptune planets tend to be younger, while super-Earth exoplanets tend to be older. This observed age-radius trend lends an empirical basis to the gas-dwarf origin scenario in which the planets diverge due to long-term photoevaporation (David et al. 2021; Fernandes et al. 2025). Turning to individual case-studies can provide insight into these types of exoplanet.

The M3V-type red dwarf star L 98-59 hosts five confirmed exoplanets, three of which are transiting (Demangeon et al. 2021; Cadieux et al. 2025). I undertook an investigation of planets b/c/d in Chapter 4. Transmission spectroscopy with JWST has been used to infer the presence of SO_2 on planet b, which is suggested to arise from tidally-driven volcanism akin to that on Io. HST observations of the outermost transiting planet (L 98-59 d) have also ruled out a *purely* H_2-He atmosphere (Zhou et al. 2023). Yet, L 98-59 d’s low bulk-density of $3.45\,\mathrm{g\,cm^{-3}}$ is inconsistent with a purely silicate-and-iron composition (Figure 1.3), and is instead consistent with this planet currently hosting an atmosphere rich in volatiles (Demangeon et al. 2021; Rajpaul et al. 2024). By its location on the edge of the small planet radius valley, planet d stands out as a prime case-study for tracing the physics of rocky planet formation and evolution (Parc et al. 2024). Retrievals on the JWST transit spectrum of planet d point to an atmosphere of sulfur-bearing volatiles (H_2S, SO_2) within a background of H_2. Free-chemistry models fit with a significance of 5.6σ, yielding an upper atmosphere mean molecular weight of $9.18^{+2.51}_{-2.41}$ g mol^{-1} and a median estimate H_2S volume mixing ratio of $10^{-0.74^{+0.14}_{-0.49}}$ (Gressier et al. 2024). However, thermochemical equilibrium models fit with a mean molecular weight of $32.13^{+1.50}_{-8.31}$ g mol^{-1}, at a lower significance of only 2.7σ. These retrievals also placed weak constraints on H_2O, CO_2, and CH_4 (Banerjee et al. 2024). Recently, although yet to be published, observations from ground-based telescope facilities have independently detected the presence of H_2S in the atmosphere of this planet.

Table 5.1 outlines recent estimates for the orbital and bulk parameters of L 98-59 d, derived from the NASA Exoplanet Archive. Note that the planet radius R_p represents the observable radius of the planet at the level probed photometrically during transit; R_p is not equal to the radius of the surface, because this planet has an atmosphere which absorbs some of the stellar radiation directed at the observer (Figure 1.2). This planet has a zero-albedo equilibrium temperature of 416 K, far below the solidus temperature of silicate rock, although in Chapter 4 I noted that it may be sustained in a semi-molten state due to the effects of tidal heating.

Parameter	Demangeon et al. (2021)	Rajpaul et al. (2024)	Luque and Palle (2022)	Cloutier et al. (2019)
a [0.01 AU]	$4.86^{+0.18}_{-0.19}$	–	–	5.06 ± 0.02
Eccentricity	$0.074^{+0.057}_{-0.046}$	$0.098^{+0.027}_{-0.096}$	–	< 0.09
$R_p/R_\oplus$	$1.521^{+0.119}_{-0.098}$	$1.521^{+0.119}_{-0.098}$	1.58 ± 0.08	1.57 ± 0.14
$M_p/M_\oplus$	1.94 ± 0.28	$2.14^{+0.25}_{-0.29}$	$2.31^{+0.46}_{-0.45}$	$2.31^{+0.46}_{-0.45}$
ρ_p [g cm^{-3}]	$2.95^{+0.79}_{-0.51}$	$3.45^{+0.25}_{-0.29}$	$3.17^{+0.85}_{-0.73}$	$3.3^{+1.3}_{-0.9}$

Table 5.1: Literature estimates for the pertinent parameters of the planet L 98-59 d. Tabulating semi-major axis a, orbital eccentricity e, planet radius R_p, planet mass R_p, and bulk-density ρ_p. Mass and density (Rajpaul et al. 2024) were obtained through a combined re-analysis of HARPS (Cloutier et al. 2019) and ESPRESSO datasets (Demangeon et al. 2021). The extreme $\pm 1\sigma$ range on the bulk-density across these four works is 2.4 to 4.6 g cm^{-3}.

5.2 A more realistic atmospheric height structure

Atmospheric temperature $T(p)$ and height $r(p)$ structure is known to be an important factor in setting the escape rates of primary envelopes shortly following planet formation (Lopez and Fortney 2014; Kubyshkina et al. 2020). The small molar mass of H_2 alongside high temperatures mean that sub-Neptune atmospheres are initially inflated, allowing for efficient 'boil-off' and rapid loss of volatiles (Ginzburg et al. 2018; Tang et al. 2024). This propensity for early volatile loss suggested for Neptunes and sub-Neptunes could also extend to lower mass planets (Lehmer and Catling 2017), especially those orbiting pre-main sequence stars which have large XUV luminosities during their saturated phase (Section 2.2.10; Johnstone et al. 2021).

An accurate representation of atmospheric structure is therefore important for comparing models to observations, and for accurately calculating atmospheric escape rates which scale super-linearly with planet radius. Most prior studies on early atmospheric structural evolution and escape have assumed convective or isothermal temperature profiles (e.g. Wordsworth and Pierrehumbert 2013; Rogers 2015; Lehmer and Catling 2017; Krissansen-Totton et al. 2024; Cherubim et al. 2025; Rogers 2025). However, in Chapter 3 I established that convectively-stable deep radiative layers can form. Compared to an adiabatic profile, the shallow lapse rates $(\mathrm{d}T / \mathrm{d}p)$ of radiative layers yield *cooler* surfaces and hotter upper atmospheres for a given instellation. But, for a given surface temperature T_s, radiative layers will instead yield comparatively *warmer* upper atmospheric temperatures due to the smaller lapse rate. This latter scenario is applicable to the period in which a young planet is cooling down, before it has reached radiative equilibrium and while T_s is large.

In this section, I further develop AGNI to enable realistic calculations of the atmosphere radius-density structure under extreme temperature-pressure conditions. Previous chapters were primarily concerned with planetary temperature profiles in pressure-space, since I did not make direct comparisons between calculated and observed planetary radii.

The bottom boundary condition on the atmospheric structure is set by the interior radius $r = R_{\text{int}}$ and gravity $g(R_{\text{int}})$ calculated using SPIDER; as in the previous chapters, SPIDER achieves this by solving for the planet's internal structure using the equation of state for a silicate mantle and a metallic core (Bower et al. 2018; Wolf and Bower 2018).

Assuming that the model atmosphere is hydrostatically self-supported by pressure against gravity above the interior, I relate the pressure and radius as

$$\mathrm{d}p = -\rho(p, T) g(r)\, \mathrm{d}r, \tag{5.1}$$

where $\rho(p, T)$ is the mass-density of the gas at pressure p and temperature T, $g(r)$ is the gravitational acceleration, and r is the radial distance from the planet centre. Equation 5.1 is then integrated from the surface pressure p_s to the top of atmosphere p_t to obtain the $r(p)$ profile. The first development made to AGNI in this chapter is to express the gravity $g(r)$ at each atmospheric layer as

$$g(r) = \frac{G}{r^2} M(r) \tag{5.2}$$

where $M(r)$ is now the *total* mass enclosed within r, now accounting for the gravitational attraction of the upper atmosphere layers to the atmosphere layers below (as well as to the planet interior). Self-attraction within the atmosphere (Biolcati et al. 2012) is important for massive envelopes which comprise percentage-fractions of the total planet mass. To perform this hydrostatic and gravitational integration, AGNI now implements a 4$^{\mathrm{th}}$ order Runge-Kutta scheme to integrate Equation 5.1. Several sublevels are used within each of the main atmosphere layers, such that 6000 Runge-Kutta steps are performed across the $\log_{10}(\mathrm{pressure})$ grid.

The second improvement here is the implementation of a real-gas equation of state (EOS), which is used to evaluate $\rho(p, T)$ in Equation 5.1 and in the adiabatic lapse rate ∇_{ad}. The ideal gas equation assumes that molecules have negligible volume and neglects inter-molecular forces; these idealisations break-down at high pressures and low temperatures. The ideal gas EOS uses a single fitting coefficient, the ideal gas constant R. Real-gas EOS go further by including additional 'fitting' coefficients which capture additional physics.

Whenever the atmospheric composition or temperature is updated, the individual densities ρ_j of each gas component j are re-evaluated separately using their appropriate EOS, and then combined using Amagat's ideal additive volume law (Noggle 1996) to obtain the total mass-density ρ at each layer:

$$\frac{1}{\rho(p,T)} = \sum_j \frac{1}{y_j \rho_j(p,T)}, \tag{5.3}$$

where y_j are mass mixing ratios[1]. This construction permits non-ideal behaviour for each gas component individually, but assumes that they mix without interacting. Ideal volume-additive mixing has long been applied in stellar physics (Dorman et al. 1991; Saumon et al. 1995; Baraffe et al. 2015) and to models of hydrogen-dominated planetary atmospheres (Paxton et al. 2011; Kubyshkina et al. 2020; Young et al. 2024). Laboratory experiments and DFT simulations have shown that Amagat's ideal mixing is robust and provides the flexibility necessary for modelling gas mixtures of various compositions at extreme conditions (Root et al. 2013; Magyar et al. 2014; Magyar et al. 2015; Bradley et al. 2018). In AGNI, the EOS for water is interpolated from AQUA (Haldemann et al. 2020) and the EOS for hydrogen is interpolated from Chabrier et al. (2019). The Van der Waals EOS is applied for CO_2, CH_4, CO, N_2, NH_3, SO_2, H_2S, and O_2[2] (Haynes 2016). Any other gases are treated as ideal.

The Van der Waals EOS is empirical and cannot be 'nicely' derived. However, compared to the ideal gas EOS, it provides a better approximation of gas behaviour through its introduction a volume term and an inter-molecular attraction/repulsion term (Kontogeorgis et al. 2019). The empirical Redlich-Kwong and Peng–Robinson cubic equations of state provide further accuracy for supercritical mixtures (Valderrama 2003). I do not directly adopt these two formulations in this thesis, although higher-order deviations from ideality are implicitly accounted-for through my use of Chabrier et al. (2019) for hydrogen and AQUA for water.

My calculation of ∇_{ad} is still partially idealised, since its derivation should account for the non-ideal compressibility of the gas parcel as it rises (Appendix E). Here, non-ideal effects only factor into ∇_{ad} through ρ in the hydrostatic assumption. It is possible to analytically derive a non-idealised adiabatic lapse rate for the Van der Waals EOS (Diaz and Ramirez 2020; Hernandez et al. 2026), but for more complex tabulated EOSs it must be obtained from calculations of the internal energy of each gas individually. On this

---

[1] Converted from volume mixing ratios χ_j with the relation $y_j = \chi_j \mu_j / \bar{\mu}$ where $\bar{\mu} = \sum_j [\mu_j \chi_j]$ is the mean molecular weight of the mixture.

[2] `https://en.wikipedia.org/wiki/Van_der_Waals_constants_(data_page)`

point, it should be noted that the AQUA H_2O EOS tabulates incorrect values (Aguichine et al. 2025) for the internal energy of and convective lapse rate of pure-H_2O, so I leave a *fully* non-ideal calculation of $\nabla_{\rm ad}$ for future work.

To validate this updated atmospheric structure calculation, I first apply AGNI to a range of binary H_2-H_2O mixtures. While the atmosphere of L 98-59 d is thought to be mainly composed of H_2 with volatiles of higher mean molecular weight (MMW) mixed-in, in this section I use H_2O as a proxy for heavy species because of its particular potential for non-ideal behaviour (Figure 4b of Spycher and Reed 1988; Wagner and Pruß 2002). The analysis of atmospheric structure here can be later applied to other extreme volatile-rich environments. Figure 5.1 plots my calculated atmospheric structures for a range of H_2-H_2O mixtures (line colour), EOS formulations (rows), and temperature profile assumptions (line style). Solid lines are radiative-convective models where an energy conserving solution is obtained for a fixed instellation, and fixed surface temperature T_s (3000 K) and pressure p_s (1000 bar). As a baseline, the dashed lines are defined by the dry adiabat until they intersect the H_2O saturation curve.

The left panels, (a) and (b), of Figure 5.1 show that the radiative-convective profiles (solid lines) are not always on the corresponding adiabat (dashed lines). Stellar radiation heats the upper layers, while thermal radiative diffusion efficiently carries the energy flux in deeper regions – this follows from Chapter 3. The profiles converge on similar stratospheric profiles, where the atmosphere is radiative and optically-thin. The corresponding radius profiles are plotted in the right panels, (c) and (d), with H_2-rich low MMW models yielding more extended envelopes.

Panel (c) shows that assuming a fully-convective structure (dashed lines) acts to deflate the atmosphere, while energy conserving solutions (solid lines) are more inflated for the given T_s. In H_2O-poorest scenarios (red lines), radiative heating inflates the top-of-atmosphere radius from $\sim$ 4000 to $\sim$ 7300 km (+83%), whereas the H_2O-richest case is inflated by +33%. Hydrodynamic gas escape rates are closely linked to atmospheric radius through equation 5.4, so my radiative-convective model captures a potential enhancement to photoevaporation here due to non-convective regions.

Panel (b) shows real-gas $T(p)$ profiles corresponding to the ideal-gas equivalents in panel (a) above it. Negligible differences between panels show that the EOS formu-

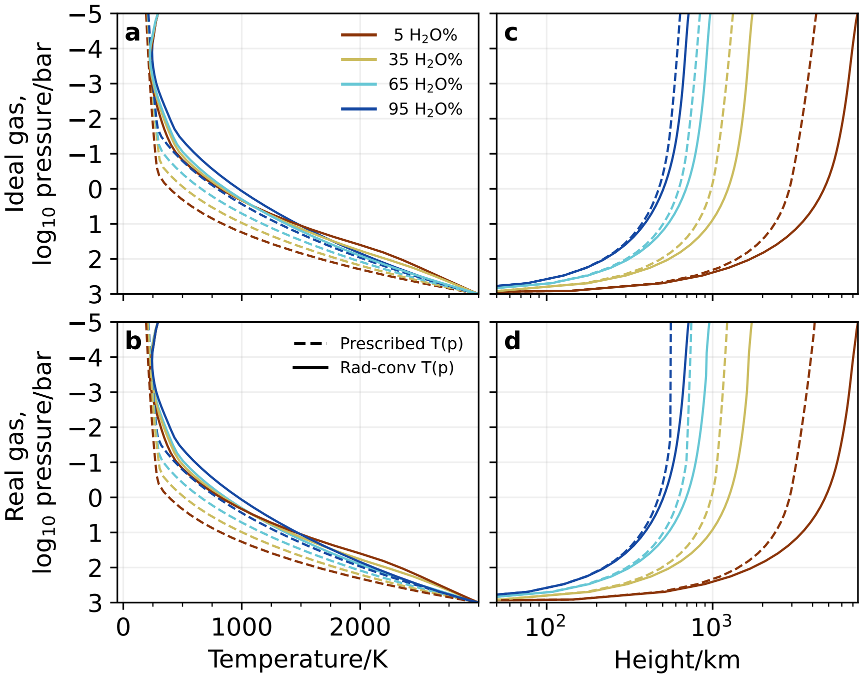

Figure 5.1: Atmospheric temperature (left) and radius (right) structures calculated by AGNI, with a fixed surface temperature of 3000 K. Line colours indicate gas composition, considering a range of H_2-H_2O mixtures. The top row uses the ideal gas EOS, while the bottom row uses the real gas EOS formulation described in the text. Line style indicates whether a prescribed or energy-conserving temperature solution was obtained.

lation only marginally impacts the temperature structure. The choice of real-gas EOS only matters when a simplified adiabatic temperature structure is assumed; compare dashed lines between panels (c) and (d) because adiabatic profiles enter into a non-ideal regime at high p and low T (Spycher and Reed 1988). Radiative-convective solutions remain sufficiently hot for the gas mixtures to behave almost ideally throughout the columns. Correspondence between my real and ideal EOS formulations where expected also demonstrates that my real-gas EOS formulation is behaving correctly.

5.3 Parametrisation of hydrodynamic escape

To model the evolution of rocky planets over billions of years, I must necessarily treat atmospheric escape processes. I now incorporate energy-limited escape into PROTEUS, which removes tracked CHNS atoms from the planet during each time-step. The bulk unfractionating escape rate is calculated using the classic energy-limited formulation:

$$\Phi_{\text{hyd}}(t) = \frac{\eta\pi[R_{\text{XUV}}(t)]^3 F_{\text{XUV}}(t)}{GM_p}, \tag{5.4}$$

which assumes that stellar XUV flux F_{XUV} absorbed by an optically-thick disk of radius R_{XUV} deposits energy to lift mass at an instantaneous rate $\Phi_{\text{hyd}}(t)$ [kg/s] out of the gravitational well with efficiency η, at each point in time t. The time-dependent $F_{\text{XUV}}(t)$ is calculated with MORS as described in Section 2.2.10. The radius R_{XUV} at which XUV radiation is absorbed is determined from the atmospheric temperature structures calculated by AGNI, taking the radius at which $p_{\mathrm{XUV}} = 5$ Pa (Lehmer and Catling 2017).

A fully-self consistent calculation of p_{XUV} is not feasible because X-ray absorption cross-sections of gases are only sparsely available (Kubyshkina et al. 2018; Owen 2019). However, my results are not strongly sensitive to p_{XUV} because the modelled upper-atmosphere scale heights are small in this low-temperature region of the atmosphere (Figure 5.5). Furthermore, any sensitivity to p_{XUV} is degenerate with the escape efficiency η by construction (Figure 5.9).

Alternatively, some existing works take the approach of defining the escaping layer R_{XUV} relative to the infrared photosphere R_p according to the XUV optical depth between the two layers, which is calculated from the mass-path and XUV opacity of the gas (Owen and Schlichting 2024). Data on XUV cross-sections sparse and imprecise when available (Zahnle and Kasting 1986; Odert et al. 2018; Owen and Schlichting 2024), so here I simply define R_{XUV} by my constant p_{XUV}.

Escape is incorporated into PROTEUS alongside the volatile outgassing calculation (Section 2.2.4). The elemental composition of the escaping gas is set equal to that of the outgassed atmosphere. To calculate the loss rate of each element from the planet's *total* volatile inventory, I proportion the bulk escape rate (Equation 5.4) by the *atmospheric* mass mixing ratios of each CHNS element. So, while the escape process itself is treated as non-fractionating, it acts upon an *atmospheric* elemental composition different to the *total* planetary volatile content. Volatile loss can thereby fractionate the planet's elemental inventories as a result of the volatile interior-atmosphere partitioning in my calculations.

Unfractionating escape is a simplifying assumption. However, it is possible that the atmosphere would escape without fractionating when the bulk escape rate is large, as the hydrodynamic outflow of H atoms will also drag off heavier elements (Zahnle and Kasting 1986; Odert et al. 2018; Johnstone 2020). Including fractionation via escape would not change my major conclusions below, as it would only enhance the S/H ratio of the atmosphere by preferentially removing H relative to S. I also use a fixed $\eta = 10\%$ escape efficiency (Lehmer and Catling 2017; Owen 2019) which agrees with simulations from

Yoshida et al. (2024) that directly account for molecular line cooling. Sensitivity tests to η are performed in Section 5.8.

5.4 H_2S, and NH_3, kinetics, and photochemistry

Considering the prior observational indications of H_2S in the atmosphere of L 98-59 d and the important capacity of sulfur to dissolve into reducing melts (Zolotov et al. 2013; Namur et al. 2016; Cartier and Wood 2019; Boulliung and Wood 2022), here I update my volatile outgassing scheme to include the thermochemical formation of H_2S. The partial pressure formed by the exothermic net reaction

$$S_2 + 2\,H_2 \rightleftharpoons 2\,H_2S \tag{5.5}$$

is determined by K_{eq} at thermochemical equilibrium (Section 2.2.4). The inclusion of this equation into my outgassing model accounts for the speciation of sulfur and hydrogen into H_2S within the atmosphere, under the assumption that chemical equilibrium has been achieved. The equilibrium constant of this reaction is well-fitted with

$$K_{\mathrm{eq}}(T) = \exp[a/T - b] \tag{5.6}$$

following Sossi et al. (2023), using tabulated free energies $\Delta G^\circ(T)$ for S_2 and H_2S in the NIST-JANAF database (Chase 1986). I find that coefficient values of $a = 6731.02$ K and $b = 3.62273$ reasonably approximate the empirical data in the temperature range from 200 to 4000 K.

Hydrogen-rich atmospheres could also allow for the formation of NH_3. Non-detection of NH_3 in the sub-Neptune K2-18 b is central to the ongoing discussion as to its surface conditions; NH_3 could be readily dissolved in either a magma ocean or water ocean (Madhusudhan et al. 2023b; Shorttle et al. 2024). I therefore also include the formation of ammonia through the reaction $3\,H_2 + N_2 \rightleftharpoons 2\,NH_3$. This reaction is well-fitted with the same equation using coefficients $a = 2664.02$ K and $b = 5.99238$ (Appendix A).

Chemical kinetics models offer an alternative approach to determining the composition of an atmosphere, with a significant performance cost compared to equilibrium models (e.g. FastChem; Section 3.6). Provided with a set of chemical species and a network of reactions connecting them, a kinetics code time-steps the abundances of all species until they numerically approach a compositional steady-state. A key advantage of kinetics models is that they can include processes which are fundamentally out-of-equilibrium: photochemistry, diffusion and advection, escape and rain-out, haze formation, and quench chemistry (Venot et al. 2012; Madhusudhan et al. 2016; Tsai et al. 2021a; Piette et al. 2023). VULCAN[3] is a numerical model for the chemical kinetics of planetary atmospheres, which has been validated against Solar System planets and other similar codes (Tsai et al. 2021a; Tsai et al. 2022). At the core of VULCAN is the Eulerian continuity equation,

$$\frac{\partial N_j}{\partial t} = P_j - L_j - \frac{\partial \Phi_j}{\partial z} \tag{5.7}$$

which represents the change in the number density N_j of a species j at a given level of the atmosphere. Abundances N_j evolve over time t according to the production P_j and loss L_j rates [molecules $\mathrm{cm}^{-3}\,\mathrm{s}^{-1}$] of the species, as well as its vertical transport flux Φ_j in to and out of each model layer. In VULCAN, production and loss terms are calculated by taking the weighted sum of the rates of all reactions involving j, including both thermo- and photo-reactions. Transport flux Φ_j includes parametrisations of advection, eddy diffusion, molecular diffusion, thermal diffusion, and settling. Equation 5.7 is then numerically integrated over time, for each species j and model level l, using a second-order Rosenbrock method applicable for sensitive ('stiff') systems of partial differential equations (Press 2007; Dallerit et al. 2024). VULCAN terminates when compositional steady state is achieved – where $\partial N_j/\partial t$ are approximately constant for all j. We should expect that kinetics models and equilibrium chemistry models resolve to the same state in regimes dominated by thermochemistry (e.g. at high temperatures) given that the system has sufficient time to attain a steady state (Seinfeld and Pandis 2006; Pierrehumbert 2010; Venot et al. 2012; Madhusudhan et al. 2016).

5.5 Neither a gas-dwarf nor a water-world

I now model various potential evolutionary pathways for L 98-59 d, to test which cases are compatible with the present-day observational constraints on the planet's density and atmospheric mean molecular weight. Cases consistent with the recent observational estimates are those with a calculated bulk-density ρ_p comparable with 3.45 g cm^{-3} to

---

[3] https://github.com/FormingWorlds/VULCAN

$\pm 1\sigma$ (Rajpaul et al. 2024). The calculated bulk-density $\rho_p = 3M_\mathrm{p}/4\pi R_p^3$ depends on the total planet mass M_p and the observable radius R_p that would be photometrically probed in transit. The observable radius R_p is determined by the radius corresponding to the 20 mbar pressure level (Lehmer and Catling 2017). The total planet mass M_p includes the mantle, metallic core, dissolved volatiles, and atmosphere.

The metallic core radius is nominally fixed at 55% of the interior radius, consistent with the relative size of Earth's core, and with Chapters 2 and 3 (see sensitivity test in Figure 5.8). The radius R_int of the planet's interior is calculated using SPIDER by solving for the structure with a given interior mass $M_\mathrm{int} = M_p - M_\mathrm{atm}$. For this planet's $M_p = 2.14 M_\oplus$, I typically obtain $M_\mathrm{core} = 3.9 \times 10^{24}$ kg $= 0.66 M_\oplus$ and $M_\mathrm{mant} = 8.85 \times 10^{24}$ kg $= 1.48 M_\oplus$.

5.5.1 Description of parameter grid

The planet's *initial* inventory of HCNS volatiles is defined in my model by their total mass. In this chapter, I quantify these inventories in terms of:

- H_ppmw, the total mass of hydrogen relative to the mass of the mantle.
- S/H, the amount of sulfur in the planet relative to H by mass.
- N/H, the amount of nitrogen in the planet relative to H by mass.
- C/H, the amount of carbon in the planet relative to H by mass.

The first two variables are incorporated into the main grid of simulations. Defining the initial SNC abundances relative to H means that H_ppmw acts as a measure of the initial *total* volatile endowment. To maintain a computationally feasible parameter space, the C/H and N/H are fixed based on Earth's primitive mantle (Wang et al. 2018).

I will now define the bounds of my parameter space in order to perform a grid-search against the observational constraints. We may expect that this planet contained relatively more H than Earth's primitive mantle did after boil-off, given the observational indications of its low bulk density at the present day. A wide range of initial H inventories are covered by my main grid: from 1000 ppmw (approximately ten times that estimated for Earth's primitive mantle; (Wang et al. 2018)) up to 16000 ppmw (i.e. 1.6 wt% relative to the mantle mass). This upper limit on hydrogen content is a numerically-tractable value informed by the literature (Lopez and Fortney 2014; Tang et al. 2024). Recent modelling of the initial mass loss of early envelopes has suggested that no more than 1.79 wt% of hydrogen (relative to the total mass) may be retained by a planet with approximately this mass and instellation (Tang et al. 2024). My modelled mantles typically correspond to 68% of the planet's total mass, so comparing with this estimated upper limit of 1.79 wt% from Tang et al. (2024), the maximum hydrogen content at birth then corresponds to $H_{\mathrm{ppmw}} \sim 26000$ relative to the mass of the *mantle*.

As in previous chapters, I fix oxygen fugacity fO_2 at the magma ocean surface relative to IW for the course of each simulation. I instead attempt to bracket a wide range ΔIW and S/H ratios by comparing against the recent observations. To do this, Figure 5.2 plots calculated contours of outgassed volume mixing ratios (solid lines) and the atmospheric MMW (dotted line) for a range of S/H and ΔIW. The 9.18 $\mathrm{g\,mol^{-1}}$ contour in Figure 5.2, equal to the molar mass inferred from retrievals, broadly rules out conditions $fO_2 <$ IW $- 4$ and $fO_2 >$ IW. This *suggests* that L 98-59 d must have an interior more reducing than Earth's mantle ($\Delta\mathrm{IW} \approx 4$; Nicklas et al. 2018) but more oxidising than Mercury's surface ($\Delta\mathrm{IW} \approx -5.4$; Namur et al. 2016). The bulk S/H ratio is not well constrained by Figure 5.2. At reducing conditions, all S/H are compatible with the retrieved MMW and H_2S depending on magma ocean fO_2. SO_2 remains a minor constituent of the bulk atmosphere throughout this phase space because speciation of S into H_2S is preferred by the chemistry. Abundances of nearby stars and models of protoplanetary disk chemistry together indicate that a range of planet formation scenarios can reasonably allow rocky planets to form with more than 2% sulfur by mass, with some theoretical formation scenarios exterior to the ice line yielding up to 10 wt% of sulfur in rocky planets (Jorge et al. 2022; Oosterloo et al. 2025).

In summary: applying Figure 5.2 alongside reasoning from established cosmochemistry and planet formation constraints provides broad bounds on the initial volatile inventory. The grid domain spans expected post-accretion scenarios since birth volatile endowment can vary substantially depending on when and where the planet formed (Zeng et al. 2019; Venturini et al. 2020) in addition to differences in magma ocean redox and mineralogical composition (Schlichting and Young 2022; Guimond et al. 2023a; Lichtenberg and Miguel 2025). I construct a grid of simulations with four axes:

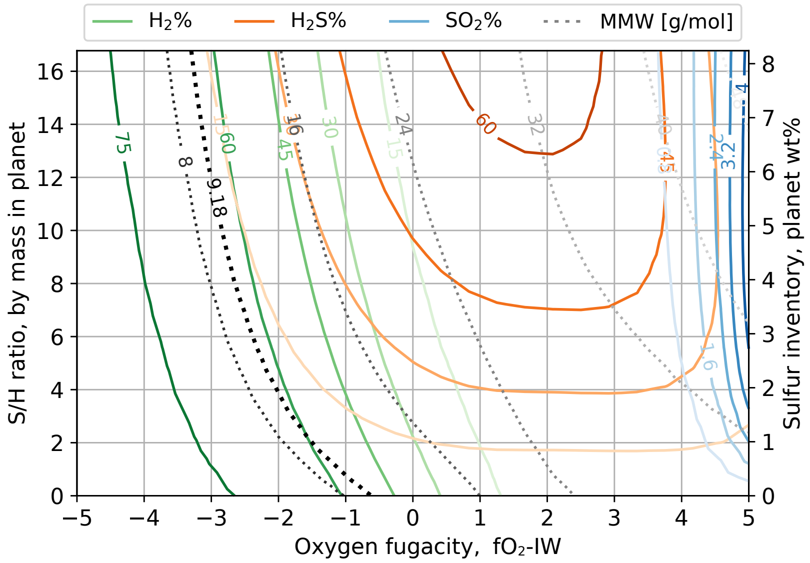

Figure 5.2: Outgassed atmospheric compositions in equilibrium with an underlying magma ocean. Solid contours plot the volume mixing ratios of H_2, H_2S, and SO_2 versus bulk S/H mass ratio and oxygen fugacity. The dotted contour shows the atmospheric MMW. The conditions in this plot are fixed at $T_m = 1850\,\mathrm{K}$, $\Phi = 40\%$, $\mathrm{H_{ppmw}} = 7150$, and $M = 2.14 M_\oplus$.

- oxygen fugacity, $\mathrm{IW} - 4.5 \leq f\mathrm{O_2} \leq \mathrm{IW}$
- hydrogen inventory, $1000 \leq \mathrm{H_{ppmw}} \leq 16000$
- bulk S/H mass ratio, $2 \leq \mathrm{S/H} \leq 10$
- total planet mass, $1.85 \leq M_p \leq 2.39$

Additionally, the total planet mass M_p is varied across the $\pm 1\sigma$ range corresponding to recent radial velocity analyses (Rajpaul et al. 2024). This parameter space results in 900 different scenarios with total volatile inventories between 0.1% and 10.9% relative to the planet's total mass (median of 2.7%).

5.5.2 Modelled evolutionary tracks

PROTEUS is used to simulate the planet's potential evolution for each scenario in the grid, from an initial stellar age of 50 Myr, under the assumption that boil-off has completed (Section 5.8, Tang et al. (2024)) and further delivery processes are negligible compared to the physics that I have included in these models (Lichtenberg et al. 2023). Simulations terminate when the simulated age reaches the 4.94 Gyr median estimated age of L 98-59 (Engle and Guinan 2023) or when the mantle solidifies (melt-fraction $\Phi < 0.5\%$). I do not simulate mantle evolution post-solidification since solid-phase volatile partitioning and volcanic outgassing are not yet included in PROTEUS (Gaillard et al. 2021; Liggins et al. 2022; Lichtenberg and Miguel 2025). Simulation end-points are then compared with observational constraints on the planet's density and atmospheric MMW, enabling the inference of the planet's possible thermal and compositional histories.

My calculated evolutionary tracks, plotted in Figure 5.3, show that the bulk-density ρ_p of L 98-59 d must have decreased significantly over its lifetime. For the larger initial volatile inventories (blue lines), ρ_p is typically less than 2 g cm^{-3} during the first several Myr of the modelled evolution. The planet's observable radius R_p initially exceeds the $1.7R_\oplus$ value often taken as the transition between the super-Earth and sub-Neptune regimes (Lopez 2017). Some of my cases stay within the canonical sub-Neptune density regime for up to 950 Myr after planet formation. Radiative energy lost to space ($F^{\text{atm}} > 0$) leads to cooling of the planet and contraction of its atmosphere, causing the planet's radius R_p to evolve beyond the sub-Neptune edge of the radius valley (dotted line, Figure 5.3a). After several Gyr of evolution up to the present day, modelled scenarios in which the planet was born volatile rich with $\text{H}_{\text{ppmw}} \gtrsim 13000$ (CNHOS volatiles $\gtrsim 1.8\%$ of the planet's mass) fall within estimates of this planet's present bulk-density, and thereby reproduce the observations.

The mantle solidifies under volatile-poor formation scenarios (Figure 5.3, maroon lines) from 70 Myr onwards. Surface cooling and near-complete escape of degassed volatiles leads to a finally rapid increase in ρ_p towards that of a rocky composition within 650 Myr. These volatile-stripped scenarios are not compatible with the observed ρ_p despite starting with likely larger H endowments than the inner Solar System planets (Krijt et al. 2023). These cases reflect prior suggestions that airless planets may be the stripped interiors of evolved sub-Neptunes (Lopez 2017; Owen and Wu 2017).

5.5.3 Scenarios constrained by JWST observations

Which of my modelled scenarios are compatible with the observational constraints? Figure 5.4 plots ρ_p at times corresponding to the estimated current age of the planet. Values of ρ_p are projected over the grid axes (panels a, b, c, d) and two output variables. All cases compatible with the observed ρ_p (orange points) exhibit MMWs from 7 to 24 g mol^{-1} (panel e). This spread in MMW values is wider than the $\pm 1\sigma$ range of $9.18^{+2.51}_{-2.41}$ g mol^{-1}

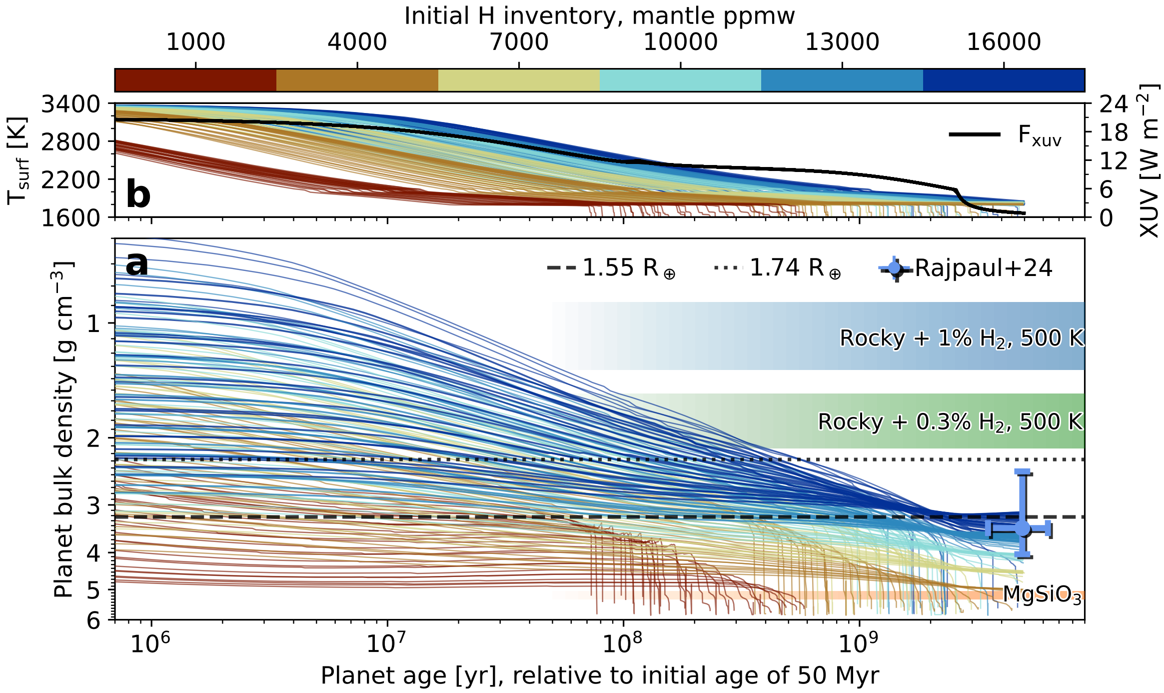

Figure 5.3: Modelled planetary bulk-density over time. The initial hydrogen inventory of each bulk-density evolution track is shown by the line colour. Blue/green shaded regions are reference densities for a planet of this mass (Zeng et al. 2019). Black dashed/dotted lines demarcate edges of the radius valley at this orbital period for low-mass stars (Ho et al. 2024). The region $\pm 1\sigma$ compatible with the estimated bulk-density of this planet is indicated by the blue errorbar (Demangeon et al. 2021; Rajpaul et al. 2024). **Top**: evolution of surface temperature (coloured) and stellar XUV energy flux (black). For clarity of visualisation, this figure only shows cases with S/H=8 by mass.

(purple line) derived with JWST transmission spectroscopy. Simultaneously applying the density and MMW constraints to my models yields the smaller cluster of blue points.

Formation with $H_{\text{ppmw}} < 10000$ can be ruled-out on the basis of ρ_p alone (grey points, Figure 5.4a). I conservatively compare my model against the maximum estimate of ρ_p in the literature, and am thus not sensitive to its quoted uncertainty. Lower densities would necessitate even more volatile-rich birth scenarios to satisfy the present-day ρ_p (Table 5.1).

Figure 5.4b shows that magma ocean oxygen fugacity $f\text{O}_2$ must be between IW $-$ 4 and IW $-$ 1 to reproduce the observed ρ_p and MMW. More oxidising conditions favour gas speciation towards O-bearing species, increasing the atmospheric MMW. Larger MMW atmospheres are either over-dense or inconsistent with the JWST transit depths (or both). A modest MMW ($\sim 9\,\text{g}\,\text{mol}^{-1}$) lowers the atmosphere's propensity for escape through a decreased radius. The full range of *initial* S/H mass ratio considered is compatible with the observed ρ_p. Planet mass itself has little impact on ρ_p compared to the other parameters considered here.

It is interesting to note that magma ocean scenarios simulated with more oxidising conditions – which generate atmospheric compositions of larger MMW – correspond to a wider range of bulk densities at the present day, compared to more reducing scenarios (Figure 5.4b). This is explained by lower MMW compositions readily escaping, and thus solidifying, because of their increased radii through the scale height relation. A corollary of the large emergent spread in ρ_p under oxidised conditions is that the least-dense scenarios correspond to the most oxidised mantles.

All outcomes compatible with the observed ρ_p fall into a tidally-heated regime with a strong atmospheric greenhouse effect. This result suggests that L 98-59 d presently retains a permanent magma ocean ($\sim$ 45% melt fraction, Figure 5.4f). A solidified mantle is ruled-out by ρ_p alone, without invoking the MMW constraint, making this result insensitive to uncertainties on the JWST observations and retrievals. The narrow range of mantle melt fractions corresponding to the observed ρ_p is a physical outcome: mantle viscosity increases strongly for melt fractions $\lesssim$ 45% (Costa et al. 2009), making energy transport through the planet's interior inefficient, and thereby allowing atmospheric blanketing and tides to keep a permanent magma ocean (Section 2.3.3; Chapter 4). Insufficiently thick atmospheres lead to mantle solidification.

5.6 Thermo-compositional case study

Many of my modelled scenarios for this planet suggest that it had an *initially* large radius and low density, on the sub-Neptune side of the radius valley (Figure 5.3). To understand how volatile loss and thermal contraction drive the marked increase in ρ_p over time, crossing through the radius valley, I study a case compatible with the observations in detail. The case study in Figure 5.5 shows L 98-59 d losing 26% of its total volatile inventory whilst retaining a large surface pressure of 30 kbar (pink bars) at the present-day. Some volatiles are outgassed, but due to incomplete mantle solidification, the majority of them remain dissolved in the planet's semi-molten mantle. The *atmosphere* S/H mass ratio increases by a factor of 8.2 during its evolution because S, which is more sol-

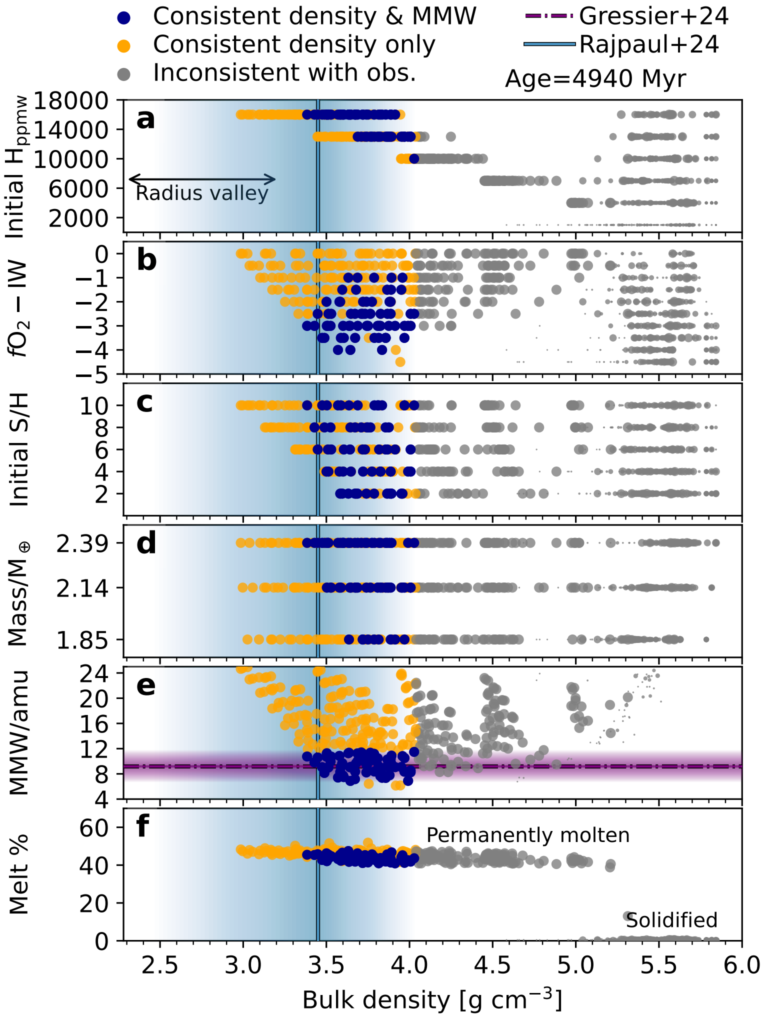

Figure 5.4: Projection of planetary bulk-density ρ_p against several variables. Point sizes represent the age of the planet at simulation end-points; largest sizes correspond to the present day. Vertical blue line and shaded region ($\pm 1\sigma$) highlights the observationally estimated ρ_p. Horizontal purple line show estimates on MMW (with $\pm 1\sigma$ shaded) from free chemistry retrievals. Blue points are consistent with the observed density and MMW, orange points are only consistent with the observed density.

uble than H, is outgassed as the magma ocean crystallises from the bottom up (Namur et al. 2016; Gaillard et al. 2022).

Thermal contraction explains large changes in ρ_p, visualised by the evolving temperature-radius profile for this case study in Figure 5.5b. The surface cools from 3360 K to 1830 K over the first 1.2 Gyr after planet formation, corresponding to the planet's photospheric radius deflating from $> 2.2R_\oplus$ to $\sim 1.74R_\oplus$ during that period. Early contraction is an established theoretical behaviour of H_2-dominated envelopes and is important in regulating the rate of photoevaporative volatile loss (Lopez and Fortney 2014; Kubyshkina et al. 2020). The atmosphere has a deep radiative layer, up to $\sim$ 5000 km thick, above which it undergoes dry convection and is then weakly inverted. Radiative layers in the deep atmosphere decreases the lapse rate compared to an adiabat (Selsis et al. 2023), acting to inflate the atmospheric radius *for a given surface temperature* during the planet's evolution (Figures 5.1 and 5.5b). I have established that many models in the literature assume (pseudo-)adiabatic profiles, neglecting this important region of the atmosphere, and its impact on energy transport and atmospheric structure.

After the planet reaches the radius valley, tidal forces deposit heat energy into the semi-solid part of its mantle (Chapter 4) while hydrodynamic escape continues to remove volatiles and reduce its radius down to the present-day observed value. Favourable dissolution of sulfur (Figure 5.5a) enables the planet's S inventory to be retained across Gyr timescales. It has been previously suggested for H_2O (Dorn and Lichtenberg 2021) and N-compounds (Shorttle et al. 2024) that retention of volatiles in deep magma oceans buffers atmospheric escape over deep time; synthetic analogues of Mercurian lavas have established the capacity for reducing melts to take up large sulfur inventories (Namur et al. 2016).

Here, I consider conditions more reducing than the IW buffer, which yield scenarios consistent with this planet's present-day bulk density and spectroscopy. In this reducing regime, sulfur primarily dissolves as S^{2-}. However, when the total sulfur content is large and the mantle is more oxidising, sulfur can also be stored as SO_4^{2-} at sulfide saturation (Moretti and Neuville 2021; Gaillard et al. 2022). My calculations represent a conservative estimate on deep sulfur storage; larger S contents, arising from planet formation, may be required to explain the present-day measurements of L 98-59 d.

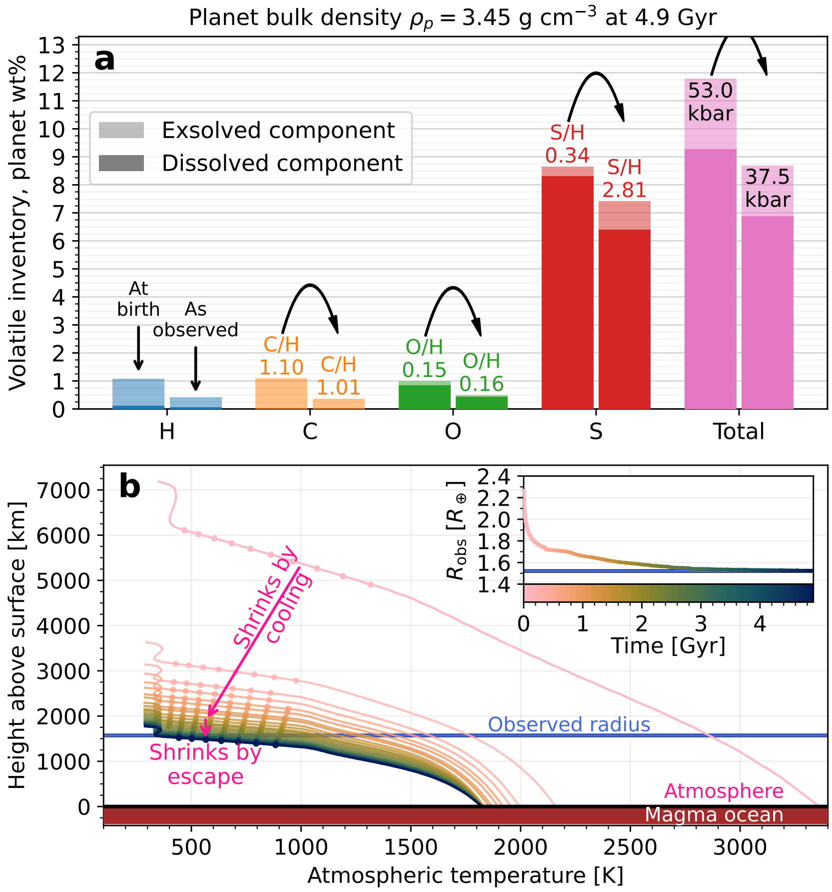

Figure 5.5: Volatile loss and envelope contraction over time. **Top**: bar heights show volatile element inventories at 'birth' (following boil-off) and 'observation' (present day) measured in percentage units relative to M_p. Bar opacity shows the relative partitioning between the interior and atmosphere. Atmospheric mass ratios relative to H are labelled. **Bottom**: atmospheric $T(r)$ over time, showing initial and then later-stage contraction phases. Convection is indicated with dots.

5.7 Which physics drives the evolution of observables?

My simulations show that cooling of a hot interior and atmosphere is the primary driver of initial atmospheric contraction (Figure 5.5b). A decreasing atmospheric height over time corresponds to a decrease in the radius R_p observed by transmission measurements, and corresponds to an increase in ρ_p over time. Figure 5.5b illustrates with pink arrows the two regimes in which atmospheric height decreases over time: first primarily by thermal evolution, and later due to photoevaporative hydrodynamic mass loss. However, both processes act simultaneously.

To quantify how these different physical processes act to shape planetary evolution, in Figure 5.6 I compare variables which trace the physics driving changes in observable properties (solid lines). These correspond to the same simulation as Figure 5.5. Thermal evolution is demonstrated to map to a decrease in atmospheric height, and thus planetary radius (purple and green lines in Figure 5.6). This behaviour is due to the atmospheric scale height decreasing with temperature, through the temperature-dependence of the gas EOS. Furthermore, the partial-solidification of the mantle (brown line) also drives a decrease in R_p for three reasons: (i) solidification causes volatiles to be degassed into the atmosphere – substantially raising its MMW (blue line) and depressing its scale height, (ii) the thermochemical formation of H_2S and CH_4 is exothermic – meaning that these species are favourably generated at cooler temperatures at later times, and (iii) the preferential removal of H atoms from the planet leads to an enhancement in heavier volatiles – because H is the dominant element in the atmosphere.

Cooling is thus the main reason for substantial radius contraction during the first ~ 1.4 Gyr (green line), since photoevaporative mass-loss is unable to drive a decrease in surface pressure against the effects of volatile outgassing during this time (red line). It is only when the planet attains a thermal steady state (after ~ 1.4 Gyr) that the surface pressure decreases over time due to photoevaporative mass-loss, which leads to a slow decrease in planet radius (green line) towards the observational estimate.

Overall, Figure 5.6 shows that both thermal evolution (cooling) and compositional evolution (escape and outgassing) have shaped this planet towards the state observed at the present. Different physical processes dominate during each phase of the planet's lifetime, which highlights the importance of comprehensively tracing the Gyr-scale evolutionary behaviour of planets when comparing physical predictions to telescope observations.

Figure 5.6 shows a substantial increase in atmospheric MMW (blue line) as volatiles are degassed from the mantle and escape preferentially removes H atoms from the planet. This evolution in MMW is not solely due to photoevaporation, as I model mass-loss as a bulk escape process which is not in-itself fractionating. However, since the escaping outflow equals the *atmospheric* elemental composition, volatile loss fractionates the planet's *bulk* volatile inventories via the different interior-atmosphere partitioning of CHNOS elements. It is therefore important to understand how atmospheric MMW varies more generally – beyond this case study – and to understand how changes in atmospheric MMW correlate to changes in mantle melting state, and to changes in the effective radius of the planet over time. Since all of these quantities vary, I compare them by plotting empirical isochrones in Figure 5.7, derived from my main grid of models (Section 5.5.2).

The isochrone at $t = 0$ (blue points) corresponds to an initial planet age of 50 Myr, at which point the mantle is assumed to be entirely molten. The initially low MMW and high temperature yields a large planetary radius, as expected from the scale height relation. At intermediate times near $t \approx 1.4$ Gyr (orange points), many of these cases approach a thermal steady state where the mantle is kept semi-molten by atmospheric blanketing and tidal heating (as per Figures 5.5 and 5.6). The cooling leads to outgassing of heavier elements and the thermochemical formation of heavier species (Kite et al. 2016; Chapter 2), which increases the spread of MMW across the models. Cases which solidify (green points near $\Phi = 0\%$) have a large spread of MMWs, up to a maximum of 64 g/mol where the atmosphere is dominated by S_2 due to the removal of all volatile elements from the planet while S is preferentially retained.

Overall, Figure 5.7 isochrones show that atmospheric MMW varies substantially in time across a range of possible scenarios. A large radius is generally correlated with a small MMW, but it is important to consider that a range of physics factors into the radius R_p probed by transmission measurements. Maintenance of a semi-molten state restricts the spread of atmospheric MMW, since it means that atmospheric composition is buffered by dissolution of volatiles into the underlying melt.

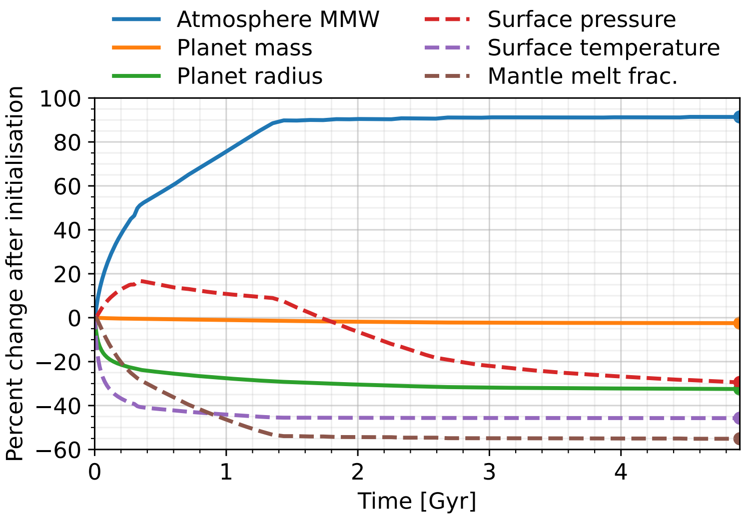

Figure 5.6: Evolution of modelled variables shows that various physical processes drive an overall decrease in planetary radius. Coloured lines trace the relative change of six variables, starting from the point of model initialisation at 50 Myr after planet formation, up to the estimated 4.94 Gyr present-day age of L 98-59 d.

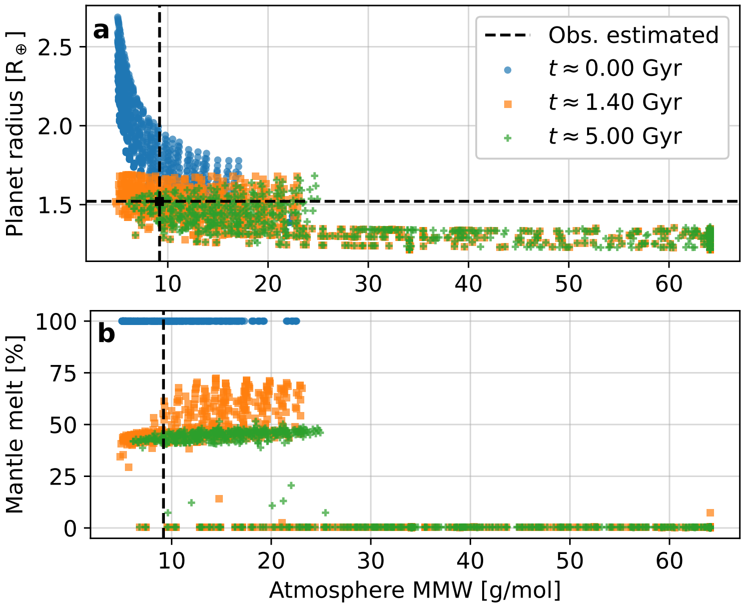

Figure 5.7: Isochrones of planet radius, melt fraction, and atmospheric mean molecular weight. Coloured points show the values of these quantities at three points in time, measured relative to model initialisation 50 Myr after planet formation.

5.8 Sensitivity tests to other physics

In this section, I test the sensitivity of these results to several parameters not included within my main grid. To do this, I take one of the scenarios from the grid that reproduces the present-day bulk-density and atmospheric MMW as a base-case, and then vary: orbital eccentricity e, escape efficiency η, metallic core radius fraction r_c, and the number of SOCRATES correlated-k bands.

Sensitivity tests plotted in Figure 5.8 show that my main conclusions are robust. Panels (a) and (b) reveal a weak dependence on orbital eccentricity; only the zero-eccentricity case tends towards complete mantle solidification, which follows from Chapter 4. Orbital evolution, not modelled here, would correspond to larger initial eccentricities and an initially increased tidal heating rate (Driscoll and Barnes 2015). Changes to escape efficiency η have the largest impact on modelled evolution (panels b and f) across the four test variables here. Increasing η to 20% leads to smaller radii and melt-fractions. Escape efficiencies of >20% – unrealistic due to the effects of atomic line cooling (Yoshida et al. 2024) – cause the planet to lose its volatile envelope in this case. Panels (c) and (g) of Figure 5.8 show that my model has only minor sensitivity to core radius fractions r_c for values up to 80%. The largest r_c end-members correspond to shallow magma oceans which are readily saturated in volatiles, and thereby yield larger atmospheres for a given total volatile inventory in the planet. A core compressed to $\rho_c = 15.3\,\mathrm{g\,cm^{-3}}$ by overburden forces (Hirose et al. 2021) would have a radius $r_c = 49\%$ for the same mass as my nominal core configuration ($r_c = 55\%$ with $\rho_c = 10.738\,\mathrm{g\,cm^{-3}}$). The nominal choice of 48 correlated-k SOCRATES bands in this chapter does not bias the calculated observable radii and mantle melt fractions (panels d and h), which is consistent with my previous sensitivity tests in Section 2.3.1.

Figure 5.8f suggests that some of my modelled outcomes are sensitive to the choice of escape efficiency $\eta = 10\%$. The total volatile loss is influenced by several physical processes which depend on the star's rotational evolution, high-energy emission spectrum, and magnetic environment (Fowler and Hoyle 1960; Johnstone et al. 2021; Namekata et al. 2023). The escape processes themselves also depend on 3D non-thermal star-planet interactions and non-LTE line cooling processes (Brain et al. 2016; Gronoff et al. 2020; Johnstone 2020). I parametrise these effects through the thermal energy-limited escape efficiency η. In my models, modest sensitivity to η can be offset by variations in the planet's initial volatile inventory. To illustrate this degeneracy, I run an additional grid of simulations which span a wide range of relevant parameters: $8000 \leq \mathrm{H_{ppmw}} \leq 30000$ and $5\% \leq \eta \leq 25\%$, also varying $fO_2 = \{\mathrm{IW}-2, \mathrm{IW}-3\}$ for completeness. A plausible upper-value on this planet's H inventory after boil-off is ~ 26000ppmw (Tang et al. 2024).

Contours of modelled bulk-density versus $\mathrm{H_{ppmw}}$ and η are plotted in Figure 5.9 for two values of the mantle oxygen fugacity relative to iron-wüstite (panels). The observed median-estimate on the planet's bulk density is indicated by the solid blue contour, with $\pm 1\sigma$ ranges shown by the dashed blue lines. Diagonal bands show that larger escape efficiencies necessitate larger initial volatile inventories in order to obtain a given present-day ρ_p. Taking an enhanced 15% efficiency, following the solid blue line in the top panel ($fO_2 = \mathrm{IW} - 3$) shows that an initial volatile inventory $\mathrm{H}_{\mathrm{ppmw}} = 26000$ still results in a modelled present-day ρ_p that is consistent with the observations. Uncertainties in the observed density (dashed lines) are a more significant factor in inferring $\mathrm{H}_{\mathrm{ppmw}}$ than my choice of η. Considering $\pm 1\sigma$ contours (dashed lines), both large ($\eta \approx 20\%$) and small ($\eta \approx 8\%$) escape efficiencies yield simulation outcomes (at $\mathrm{IW} - 3$) within the observational constraints for reasonable volatile-rich scenarios. With a less reducing $\mathrm{IW} - 2$ mantle, escape efficiencies of 20% result in present-day ρ_p falling within the observational uncertainty for a reasonable range of $\mathrm{H}_{\mathrm{ppmw}}$. These tests show that my main results are robust, in that the $\mathrm{H}_{\mathrm{ppmw}}$ considered in Figure 5.9 all represent volatile-rich formation scenarios.

5.9 Indication of sulfur photochemistry

The in-situ formation of SO_2 from H_2S, in the presence of OH radicals from photolysis H_2O, can explain the detections of SO_2 within the upper atmosphere of the hot-Jupiter exoplanet WASP-39 b (Tsai et al. 2023; Powell et al. 2024). I suggest that this same mechanism is acting within the atmosphere of L 98-59 d to form the SO_2 suggested by free retrievals on JWST transmission spectroscopy (Gressier et al. 2024). To test this here, I make a comparison between calculations from VULCAN photochemical kinetics models and the JWST free-chemistry retrievals. Figure 5.10 plots atmospheric mixing ratios for this case study as in the Section 5.6 case study, under three chemical paradigms:

- CHNOS photochemical kinetics (solid lines),
- CHNOS kinetics without photochemistry (dashed lines),
- equilibrium volatile outgassing used in my evolutionary calculations (triangle markers).

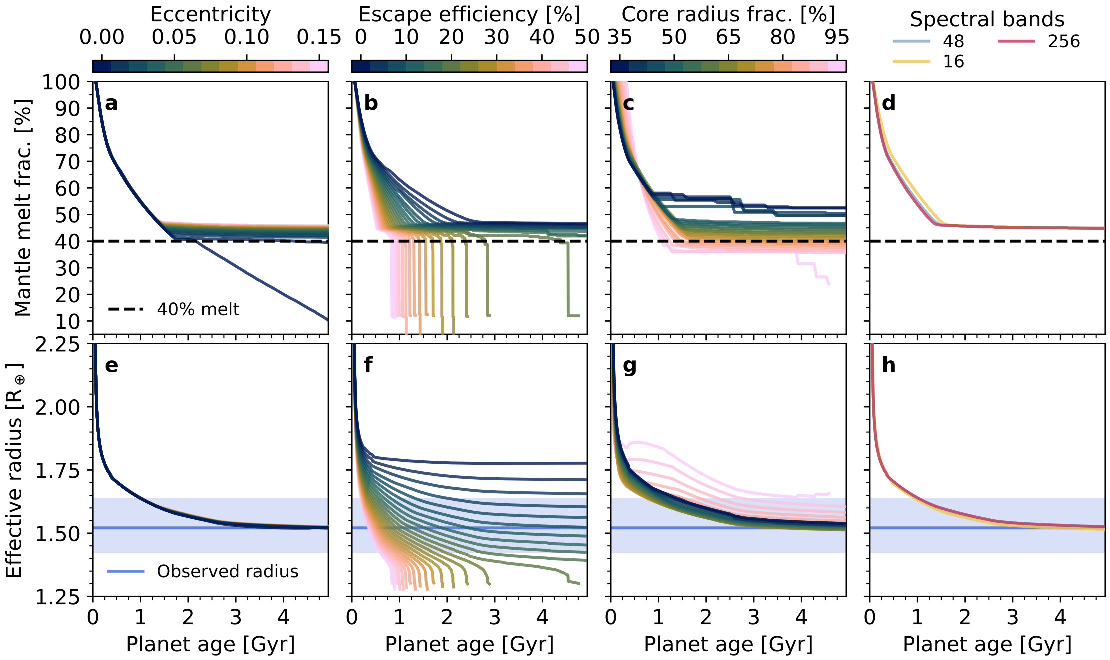

Figure 5.8: Sensitivity of mantle melt-fraction and observable radius to model parameters. Model parameters (columns): orbital eccentricity, atmospheric escape efficiency, metallic core radius fraction, and the number of spectral bands. Sensitivity is assessed by the evolutionary differences in mantle melt-fraction (top row) and the observable radius of the planet (bottom row).

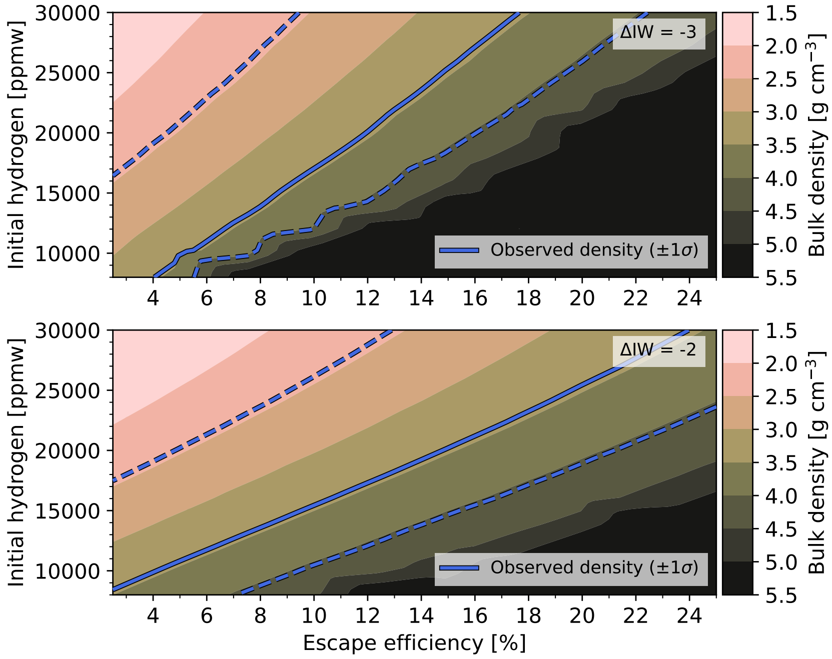

Figure 5.9: Contour plots of bulk density versus initial volatiles and escape efficiency shows a trade-off between these model parameters. Modelled planet bulk-density at its present age is indicated by the colour-bar. The observed density contour is shown by the blue line (solid) with its uncertainty (dashed). Calculated for two values of oxygen fugacity (top and bottom panels).

The mixing ratio of SO_2 (solid blue line) increases with altitude for $p < 6\,\mathrm{bar}$, while the equivalent case without photochemistry (dashed blue line) quenches at negligible abundance. Photochemical production of SO_2 is necessary to raise its abundance in the upper atmosphere to that consistent with the JWST transmission observations (scatter points). Lime-coloured mixing ratio profiles show that H_2S abundance is consistent with the observational constraints under all three chemical paradigms, because H_2S is thermochemically favoured to carry sulfur in the reducing H_2-rich background. Correspondence between the different modelled H_2S abundance profiles also indicates that the net thermochemical reaction applied in my outgassing model (Equation 5.5) is sufficient to capture its production from outgassed S_2 and H_2, since it independently reproduces the same composition as the full VULCAN chemical kinetics network (Tsai et al. 2021a).

Detections of SO_2 cannot be explained by volcanism at the surface, which would require SO_2 to be transported into the observable upper atmosphere without being thermochemically reduced. Transport of SO_2 ($64\,\mathrm{g\,mol^{-1}}$) would have to take place in the absence of deep convection (Figure 5.5b) and therefore only by diffusion through the H_2 background. This physically unlikely scenario instead points to the formation of SO_2 in-situ, requiring only the presence of otherwise poorly-constrained H_2O. This finding represents the first indication of active sulfur photochemistry occurring on a super-Earth exoplanet, and highlights the chemical interactions which link deep planetary interiors and their observable atmospheres. Here I perform these kinetics calculations 'offline' from the main simulations, however, it is possible that photochemical effects would feed back on the climate and change the cooling rate of the planet (Venot et al. 2016; Nicholls et al. 2023). Furthermore, the application of kinetics models can provide more accurate estimates of the upper atmospheric composition, which disequilibrium effects are important, and so better determine the nature of the escaping outflow driven by photoevaporation. Future modelling should incorporate photochemistry self-consistently into these evolutionary calculations, with the view of connecting the observable upper atmosphere to particular deep-atmosphere and planetary interior conditions.

I do not explicitly consider condensation processes in this planet's upper atmosphere because all modelled species exist at temperatures above their dew point. However, it is foreseeable that native sulfur species – not modelled here – may condense in the upper atmosphere because they have relatively low dew point temperatures (Gao et al. 2017; Janssen et al. 2023). Sulfur condensates could sustain clouds and act as condensation nuclei for other species, thereby modulating the radiation environment of the whole column and influencing the transmission spectrum of the planet (Helling 2019).

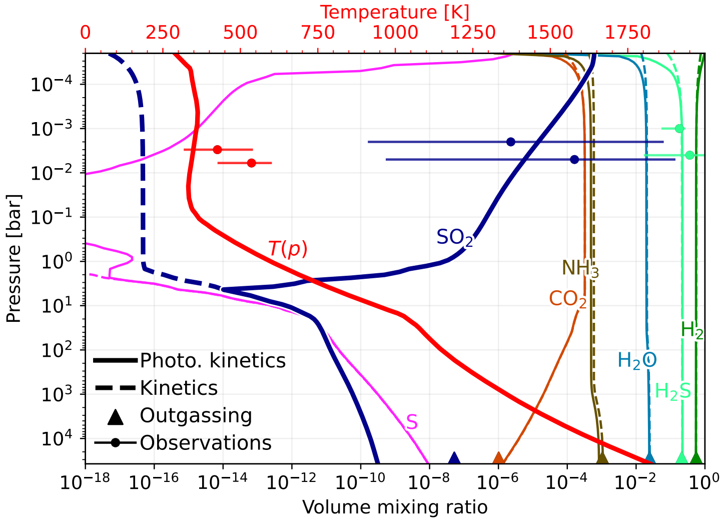

Figure 5.10: Atmospheric composition and temperature profiles. Solid lines plot the volume mixing ratios for a selection of gases calculated with VULCAN's CHNOS photochemical kinetic network. Dashed lines plot mixing ratios calculated without photoreactions. Scatter points show retrieved abundances and temperatures near the photosphere (Banerjee et al. 2024; Gressier et al. 2024). I assume a modest K_{zz} of $10^5\,\mathrm{cm^2\,s^{-1}}$ and use the radiative-convective temperature solution obtained by AGNI (thick red line).

5.10 Chapter conclusions

L 98-59 d is an important planet because its present-day properties allow us to trace its complete history, thereby providing insight into rocky planetary evolution more generally. This planet's observed radius is too small for it to be classified as a prototypical sub-Neptune, although my models suggest that, had it been observed at an age of $\lesssim$ 1 Gyr, we may have confidently labelled it as one (Figure 5.3a). The slow transition towards the super-Earth regime occurs only after several Gyr of evolution, suggesting that even relatively old sub-Neptunes with ages $\gtrsim$ 1 Gyr may exist in a transient state towards becoming what would be classified as super-Earths. Gyr-scale evolution has previously been suggested to explain radius-age trends in the Kepler survey (David et al. 2021) as an alternative to the secondary atmosphere 'loss and revival' mechanism (Kite and Barnett 2020). Super-Earths born rich with volatiles/metals may represent our best prospects for detecting retained atmospheres within the Rocky Worlds DDT survey (Ji et al. 2025). At the same time, my models provide a framework for interpreting future observations of L 98-59 d and similar targets of this survey. For example, GJ 806 b also has a bulk-density consistent with a substantial volatile atmosphere (Palle et al. 2023) and represents an additional opportunity for probing the thermal and compositional evolution of super-Earths.

Future observations could target ‘smoking gun’ tracers of a volatile-rich birth scenario. One such direction might be to observationally-constrain atmospheric D/H or He/H ratios, since a measurement of relatively enhanced D/H or He/H ratios at the present day – compared to planetary building blocks – would suggest that hydrogen-rich planets have been subject to long term fractionating escape processes (Way et al. 2016; Lammer et al. 2020; Cherubim et al. 2024; McCreery et al. 2025). Isotopic constraints on exoplanet atmospheres are already accessible to large high-resolution telescopes (Snellen 2025).

L 98-59 d currently has a radius commensurate with a canonical super-Earth planet, while, at the same time, we know that it must comprise a large mass-fraction of volatiles. A modestly large atmospheric MMW means that it is not well-described by an evolved gas-dwarf scenario. Simultaneously, my models show that a water-world composition is not required to explain its current bulk-density. Forming significant quantities of H_2O also requires oxidising conditions that are incompatible with the observed JWST transmission spectrum.

My modelled interior-atmosphere evolution pathways connect the observed bulk-density of L 98-59 d to a narrow range of conditions at birth. Conditions compatible with observations are those in which the planet initially had at least 100 times the estimated hydrogen content of the early Earth (Krijt et al. 2023). The majority of this planet’s H and C are stored in its atmosphere, whilst its S remains primarily dissolved within its chemically-reducing magma ocean. Fractionation of planetary HCS inventories between their interiors and atmospheres presents an opportunity for testing whether small, low-density exoplanets have underlying magma oceans through measurements of their atmospheric composition (Kite et al. 2016; Dorn and Lichtenberg 2021; Shorttle et al. 2024). Atmospheric thermal contraction, volatile dissolution into a planet-scale magma ocean, mantle tidal heating, and photoevaporation have shaped the observable radius and composition of L 98-59 d over its lifetime – and may continue doing so for billions of years.

Chapter 6
Conclusions

6.1 How atmospheric physics shapes rocky planets

Substantial differences between planets of the inner Solar System are yet to be fully explained. These differences proliferate in light of the third decade of exoplanetary science: observations of exoplanet systems continue to raise manifold questions about how planets form, how they evolve, and exactly why they differ from each other (Lammer and Blanc 2018; Lichtenberg et al. 2025). I have adopted a numerical approach to simulate the Gyr-scale evolution of both real and theoretical planets. By rigorously representing the underlying physics, this numerical approach has – and will continue to – explain the observed properties of surveyed exoplanets and the environments which we directly explore within the Solar System. So, in this thesis, I have advanced our understanding of how planets change through deep time and highlighted the governing role of their atmospheres.

In Chapter 2, I introduced PROTEUS: a modular numerical framework for simulating the evolution of rocky (exo)planets by resolving their vertical structure from core to space. Building on methods developed in prior literature, Chapter 2 provided a new perspective on the important interactions between the interiors and atmospheres of Earth-sized planets. I showed that a range of volatile mixtures can be degassed from primordial magma oceans: a universal period in the early lifetimes of rocky planets. I showed how the outgassed atmospheric composition varies by mantle redox state and volatile content with which a planet is endowed following its formation. The radiative properties of these atmospheric gases – particularly H_2 and H_2O – control the thermal evolution of young planets by slowing or preventing the cooling of their mantles through a strong greenhouse effect. Understanding whether a planet is expected to solidify, and the timescale of magma ocean crystallisation set by atmospheric blanketing, is essential for interpreting measurements of *all* rocky planets. The modelling in this chapter also indicated the potential for atmospheric convective stability.

I further developed my modelling in Chapter 3 to test when and where early outgassed atmospheres are convective or radiatively-stabilised. I developed AGNI – a new atmosphere module integrated into the PROTEUS framework – to perform this test. AGNI applies a suite of numerical optimisation methods to rapidly obtain energy conserving solutions for atmospheric temperatures and radii, and is designed to be applicable to a wide range of climate scenarios. In Chapter 3, I showed that convective shutdown can readily occur in early volatile atmospheres, but also for planets which maintain permanent magma oceans, depending on their composition and radiation environment. This result builds upon the findings of Selsis et al. (2023) and directly appeals to the Decadal Survey question of 'what fundamental planetary parameters and processes determine the complexity of planetary atmospheres?' Furthermore, my results show that commonly adopted fully-convective atmospheric structures are not universally valid. I also suggest that the observable absorption features of atmospheric SO_2 and CO_2 can trace mantle redox state via emission spectroscopy.

Chapter 4 applied PROTEUS to model three exoplanets within the L 98-59 system. Recent observations of these planets have lead to multiple inferences of sulfur-bearing species in their atmospheres, which are suggested to be sustained against escape processes by volcanism and tidal heating of their interiors. So, adopting this system as a case study, I investigated the role of orbital eccentricity tides in shaping the early thermal evolution of these three planets. In doing so, I assessed the nuanced relationship between tidal heating and atmospheric energy transport. With comparisons against a simple semi-analytic thermal model, I showed that from the interactions between tidal dissipation, mantle rheology, and atmospheric blanketing emerges a self-sustaining feedback with the potential to support permanent magma oceans on warm exoplanets. My models indicated that the L 98-59 planets may have molten interiors at the present-day, further highlighting the controls that thick atmospheres can exert over planetary interiors and secular evolution.

Continuing with the L 98-59 system, Chapter 5 focused specifically on the super-Earth exoplanet L 98-59 d. With a parametrisation of atmospheric escape introduced to PROTEUS, I simulated the full course of this planet's thermal and compositional evolution from its birth – shortly after its formation – up to the present-day state recently measured by JWST transmission spectroscopy. My modelled evolution tracks revealed a pathway by which this planet transitioned from an early inflated state, to later having the characteristics of a prototypical sub-Neptune, and then eventually to become a super-Earth. In being constrained by the physics, my modelling pointed to a volatile-rich birth scenario: L 98-59 d must have accreted at least 100 times more volatiles than Earth did during its formation, raising questions as to *where* and *how* this planet formed. JWST observations suggest that L 98-59 d's H_2-dominated atmosphere is abundant in H_2S and SO_2; with this constraint, my models illustrated that L 98-59 d fits into neither of the ‘water world’ or ‘gas dwarf’ scenarios often adopted in the literature. Furthermore, Chapter 5 also showed that photochemical production of SO_2 can explain its suggested detection in the atmosphere of L 98-59 d. This marks the first robust inference of active photochemistry occurring within the atmosphere of a rocky body beyond the Solar System.

Chapters 4 and 5 focused on the L 98-59 planets in particular. Yet, while individual planets may have unique characteristics, the governing physics is universal. We must carefully consider planet-scale interactions – such as feedback between atmospheric blanketing and mantle tides – in setting the observable states of *all* planets that we measure: both as individual entities and as members of larger populations. Chapter 5 inferred the lifetime history of L 98-59 d, which points to its membership of a diffuse exoplanet population with properties that outside the suggested categories of water-world and gas-dwarf planets. These two categories are probably not distinct populations of planets. Instead, there may exist a continuum of scenarios emergent from the processes of planetary formation and evolution.

6.2 Suggested lines of further investigation

I have presented my conclusions as resulting from a holistic and physically-justified modelling framework. At the same time, I have adopted many simplifying and limiting assumptions. Future work must rigorously scrutinise these assumptions and relax them where necessary. I outline some of them below.

Chapter 3 highlighted the frequent potential for some planets to develop convectively-stable layers in their volatile atmospheres, depending on the gas composition and planet energy-balance. Shutdown of convection, and the absence of vigorous dynamical mixing, may allow strong vertical stratification of molecular and elemental compositions within the atmosphere. Disconnect between upper- and lower-atmospheric abundances would complicate observational inferences (Zhang and Showman 2018a; Zhang and Showman 2018b; Komacek et al. 2019b). For example: sufficiently hot surfaces may generate atmospheres composed largely of vaporised mineral species (van Buchem et al. 2023; Seidler et al. 2024) but it is unclear whether these heavy species would be well-mixed and observable. SiO vapour is particularly important because its large optical cross-section can yield thermal inversions, which have observable signatures in both transmission and emission viewing geometries (Zilinskas et al. 2023; Seidler et al. 2024). Future work should directly investigate the role of atmospheric dynamics and chemical processes in relating upper atmospheric composition to the deep atmosphere and interior; e.g. by explicitly resolving the fluid dynamics (Habib and Pierrehumbert 2024).

Planets are three-dimensional objects, yet my results are predicated upon 1D column calculations: an approach ubiquitously adopted in similar research (e.g. Elkins-Tanton 2008; Schaefer et al. 2016; Herath et al. 2024; Krissansen-Totton et al. 2024). While column models are necessary for computational flexibility and feasibility (Manners 2024), they may not accurately parametrise some important physical and dynamical processes; especially on tidally locked planets where stark zonal gradients are expected. Snapshots from my 1D evolutionary calculations should be compared against 3D global models to assess the atmospheric dynamical regime and efficiency of heat redistribution (Koll 2022; Chen et al. 2025). A multi-column calculation (e.g. Tsai et al. 2024b) could be integrated within these evolutionary calculations, which would also permit direct comparisons with phase curve observations of exoplanets (Challener et al. 2025; Hammond et al. 2025).

I have applied the semi-empirical MT_CKD model to simulate the continuum absorption of H_2O (Mlawer et al. 2012; Mlawer et al. 2023). Although MT_CKD is only calibrated at temperate conditions, its application to extreme environments remains commonplace throughout the literature for lack of alternative prescriptions (Hamano et al. 2015; Boukrouche et al. 2021; Selsis et al. 2023; Krissansen-Totton et al. 2024). This known-unknown factor could be a significant source of error in radiative transfer calculations, which motivates laboratory experiments or molecular dynamics simulations on the collisional continua of H_2O (and H_2) across temperatures and pressures (Fortney et al. 2016; Wiesenfeld et al. 2025). The upcoming HITRAN2024 release will provide new continuum absorption data.

I have not modelled stochastic erosion and delivery processes, such as those from giant impacts. However, these processes are thought to have contributed to the final volatile budget of the Solar System planets (Schlichting and Mukhopadhyay 2018). Estimates of volatile losses by impact erosion differ by many orders of magnitude so it is unclear how late-accreting planetesimals and cometary delivery would influence my results (Kegerreis et al. 2020; Denman et al. 2022; Lock and Stewart 2024).

I have conceptually divided planets into two main components: atmospheres and interiors. This seems like a natural assumption – we see such a divide for Earth – and it is usually adopted in the literature. However, recent works have raised the possibility of *miscibility* between planetary interiors and atmospheres for high temperatures: where we may not readily distinguish between these regions with a 'hard' boundary because they do not phase-separate (Benneke et al. 2024; Young et al. 2025). Ideally, observational markers should be established to test for the presence and location of these immiscibly-stratified regimes (Rogers et al. 2025). Similarly, the partitioning of oxygen at high pressures and temperatures favours the formation of FeO as the primary bearer of Fe, as opposed to metallic Fe. This additional effect of Fe speciation could inhibit – or entirely preclude – forming metallic cores in exoplanets with masses $> 3.5M_\oplus$ (Huang et al. 2021; Huang and Dorn 2025). Thirdly, the mineral equations of state, mantle melting properties, and volatile solubility laws adopted in this thesis are targeted at Earth-like conditions (Bower et al. 2018; Wolf and Bower 2018). A more accurate treatment of the mineral physics may be necessary for modelling super-Earths and sub-Neptunes (Gupta et al. 2025). Together, these concerns motivate empirical investigations at high-temperatures, across a wide range of pressures, for mineralogical compositions beyond Bulk Silicate Earth (Putirka and Rarick 2019; Guimond et al. 2023a; Thompson et al. 2025).

I have shown that mantle redox state plays a key role in regulating the behaviour of early magma oceans through the corresponding atmospheric compositions. To account for these effects, I proxied mantle redox state with oxygen fugacities fixed relative to the iron-wüstite buffer – modelled using a temperature-dependent prescription that does not conserve oxygen atoms. In reality: oxygen fugacity is not a conserved quantity, but oxygen atoms and electrons are. For example, fO_2 would vary due to inhomogeneous changes in mantle Fe, Cr, and C content (Hirschmann 2022; Itcovitz et al. 2022). Future work should study the influence of evolving fO_2 and ΔIW during the magma ocean cooling and crystallisation processes, and their relationship to fractionating escape mechanisms. Escape is suggested to oxidise planetary interiors over time, which is applicable to Earth and Venus (Wade and Wood 2005; Frost and McCammon 2008; Wordsworth et al. 2018).

The CALLIOPE outgassing model presented in Chapter 2 is applied to the majority of my modelling. However, this model has since given rise to the development of the new Atmodeller[1] code. Atmodeller can account for phase condensation at the magma ocean-atmosphere interface; e.g. graphite flotation crusts (Sossi et al. 2020). Atmodeller also permits deviation from ideal-gas behaviour, where activity coefficients $a_i \neq 1$, which is thought to influence the composition of atmospheres formed in equilibrium with a deep magma ocean (Bower et al. 2025). Future developments to PROTEUS will incorporate Atmodeller as an additional implementation of the `outgas` module as an alternative to CALLIOPE.

Rocky planets are the subject of this thesis, yet processes known to be active on *solidified* planets are not treated here. For example: the formation of water oceans, disequilibrium volcanic outgassing, geochemical weathering, and biology (Lodders and Fegley 1998). I have instead focused on the processes dominant before and during mantle solidification, and on cases in which planets remain within these particular regimes. Modelling planetary evolution post-solidification will require a treatment of volatile storage within the solid phase of the mantle (e.g. via melt trapping, Sim et al. 2024), disequilibrium volcanic outgassing (Walbecq et al. 2025), and volatile in-gassing processes (e.g. weathering; Pierrehumbert 2010). These physics could be implemented within the PROTEUS modelling framework, which would allow comparative studies of Earth, Venus, Mars, and solidified exoplanets (e.g. TRAPPIST-1 e/f).

---

[1] `https://github.com/ExPlanetology/atmodeller`

The commissioning of new space missions and the advent of sophisticated modelling motivates the adoption of consistent and clear language when communicating research (Forgan et al. 2017). This rapid pace of exoplanetary science provides fertile ground for new jargon, which can be a useful tool, but we currently find ourselves in a situation where the *meanings* of new technical words are fractured across the community. For example, the terms 'mini-Neptune', 'sub-Neptune', 'water-world', 'Earth-like', 'lava world', and 'interior' are applied liberally without consensus on their meaning. These semantic differences necessitate the directed near-term consolidation of technical language (Bibas and Vidal 2025).

6.3 A perspective on the future

In-situ measurements arising from the Space Age have expanded our horizons across the Solar System. These measurements necessitated the development of models to explain how rocky bodies change over billions of years. For example, early observations of Mars appeared to feature forests and straight artificially-constructed canals (Lowell 1907; Lyot 1929), while early works suggested that Venus hosts a 'swampy' habitable surface, which was later ruled-out by the Venera missions (Gillmann et al. 2022; Bibas and Vidal 2025). Similarly, the architecture of the Solar System with its inner (rocky) planets and outer (giant) planets was thought to be a common configuration. Yet, modern exoplanet surveys shown this not to be the case; e.g. the TRAPPIST-1 system features a 'peas in a pod' configuration unlike the Solar System, with seven similarly sized rocky planets (Millholland et al. 2017; Agol et al. 2021). There is historical precedent for an overturn in our understanding of planetary environments and architectures, when faced with new generations of instrumentation.

We are primed to make theoretical predictions of the present states of highly-observable exoplanets, such as those targeted by the Rocky Worlds DDT Survey (Redfield et al. 2024). JWST is already detecting unexpected spectroscopic chemical signatures which are yet to be explained by theory (e.g. K2-18 b). Upcoming space missions such as PLATO (launching 2026) and Ariel (launching 2029) will survey thousands more exoplanets, allowing systematic characterisations of their compositions and thermal properties. Advances in our observational capabilities of exoplanets are creating additional opportunities to test and (re-)develop planetary science. These imminent data raise the need for modelling frameworks capable of interpreting these observations, thereby extracting meaningful insights about planetary formation and their evolution processes.

It is now timely to directly address some of the most prominent outstanding questions in the field of (exo)planetary science. What are sub-Neptunes? Are they a single category of planet, or a family of smaller groups? Which planets are molten, and are there observational markers to distinguish these states? Which processes shape the radius valley, radius cliff, and other demographic features? Under what conditions do rocky planets retain atmospheres? How do the interior and atmospheric compositions of particular planets change over time? Is atmospheric retention shaped primarily by the stellar environment or by planetary formation processes? When did oceans first form on the Earth? In what environment did Earth's life arise? How unique is the Earth? From the perspective of physical processes, we might ask: how do clouds/aerosols modulate magma ocean lifetimes? And what role does atmospheric dynamics play in maintaining permanent dayside magma oceans on tidally locked exoplanets? It would be possible to directly approach these questions by incorporating additional physics into PROTEUS.

Computer models allow us to virtually capture the physics and chemistry of these environments and the contexts in which they exist. By carefully leveraging a comprehensive treatment of the relevant physics, alongside a new wealth of observational data, we will unpick the evolutionary pathways that shape the atmospheres observed and experienced today. Our understanding of how planets are structured, composed, and related to one another will continue to develop – incrementally surpassing our prior notions, until one day, soon, we will explain what happened to rocky planets.

Bibliography

Waterson, J. J. (1851). "On the Physics of media that are composed of free and perfectly elastic molecules in a state of motion". In: *Proc. R. Soc. Lond.* 5, p. 604.

John, T. (1869). "IV. On the blue colour of the sky, the polarization of skylight, and on the polarization of light by cloudy matter generally". In: *Proc. R. Soc. Lond.* 17, pp. 223–233.

Lord Rayleigh, F. R. S. (1881). "X. On the electromagnetic theory of light". In: *London, Edinburgh, and Dublin Philosophical Magazine and Journal of Science*.

Jeans, J. (1904). *The Dynamical Theory of Gases*. Cambridge, England, UK: Cambridge University Press.

Lowell, P. (1907). "Mars in 1907 - Nature". In: *Nature* 76, p. 446.

Love, A. E. H. (1911). *Some Problems of Geodynamics: Being an Essay to which the Adams Prize in the University of Cambridge was Adjudged in 1911*. Oxford, England, UK: University Press.

Maunder, E. W. (1913). *Are the planets inhabited?* London: Harper and Brothers.

Aston, F. W. (1924). "Atomic Species and their Abundance on the Earth - Nature". In: *Nature* 113, pp. 393–395.

Prandtl, L. (1925). "7. Bericht über Untersuchungen zur ausgebildeten Turbulenz". In: *Zeitschrift Angewandte Mathematik und Mechanik* 5.2, pp. 136–139.

Lyot, B. (1929). "Recherches sur la polarisation de la lumière des planètes et de quelques substances terrestresRecherches sur la polarisation de la lumière des planètes et de quelques substances terrestresResearch on polarization of light from planets and some terrestrial substances;" PhD thesis. Universite Pierre et Marie Curie (Paris VI), France.

Von Karman, T. (1930). "Mechanische Ähnlichkeit und Turbulenz". In: *Nachrichten von der Gesellschaft der Wissenschaften zu Göttingen* 1930, pp. 58–76.

Elsasser, W. M. (1938). "Mean Absorption and Equivalent Absorption Coefficient of a Band Spectrum". In: *Phys. Rev.* 54.2, pp. 126–129.

Daly, R. A. (1946). "Origin of the Moon and Its Topography". In: *Proceedings of the American Philosophical Society* 90.2, pp. 104–119.

Parthasarathy, S. (1951). "Light scattering in gases". In: *Indian Journal of Physics* 25, pp. 21–24.

Vitense, E. (1953). "Die Wasserstoffkonvektionszone der Sonne. Mit 11 Textabbildungen". In: *Zeitschrift fur Astrophysik* 32, p. 135.

Burbidge, E. M., Burbidge, G. R., Fowler, W. A., and Hoyle, F. (1957). "Synthesis of the Elements in Stars". In: *Rev. Mod. Phys.* 29.4, pp. 547–650.

Eugster, H. (1957). "Heterogeneous reactions involving oxidation and reduction at high pressures and temperatures". In: *The Journal of Chemical Physics* 26.6, pp. 1760–1761.

Fowler, W. A. and Hoyle, F. (1960). "Nuclear cosmochronology". In: *Ann. Phys.* 10.2, pp. 280–302.

Hayashi, C. (1961). "Stellar evolution in early phases of gravitational contraction." In: *Publications of the Astronomical Society of Japan* 13, pp. 450–452.

Hayashi, C. and Hoshi, R. (1961). "The Outer Envelope of Giant Stars with Surface Convection Zone". In: *Publications of the Astronomical Society of Japan* 13, pp. 442–449.

Ledoux, P., Schwarzschild, M., and Spiegel, E. A. (1961). "On the Spectrum of Turbulent Convection." In: *Astrophysical Journal* 133, p. 184.

Blackadar, A. K. (1962). "The vertical distribution of wind and turbulent exchange in a neutral atmosphere". In: *Journal of Geophysical Research* 67.8, pp. 3095–3102.

Lorenz, E. N. (1963). "Deterministic Nonperiodic Flow". In: *Journal of Atmospheric Sciences* 20.2, pp. 130–141.

Dole, S. (1964). *Habitable Planets for Man*. Blaisdell book on the pure and applied sciences. Blaisdell Publishing Company.

Kaula, W. M. (1964). "Tidal Dissipation by Solid Friction and the Resulting Orbital Evolution". In: *Reviews of Geophysics* 2.4, p. 661.

Klein, M. J. (1965). "Einstein, Specific Heats, and the Early Quantum Theory". In: *Science* 148.3667, pp. 173–180.

Wilson, J. T. (1965). "A new class of faults and their bearing on continental drift". In: *Nature* 207.4995, pp. 343–347.

Komabayasi, M. (1967). "Discrete Equilibrium Temperatures of a Hypothetical Planet with the Atmosphere and the Hydrosphere of One Component-Two Phase System under Constant Solar Radiation". In: *Journal of the Meteorological Society of Japan. Ser. II* 45.1, pp. 137–139.

Ingersoll, A. P. (1969). "The Runaway Greenhouse: A History of Water on Venus". In: *J. Atmos. Sci.* 26.6, pp. 1191–1198.

Kaula, W. M. (1969). *An introduction to planetary physics. The terrestrial planets.*

Shemansky, D. E. (1969). "N2 Vegard-Kaplan System in Absorption". In: *The Journal of Chemical Physics* 51.2, pp. 689–700.

Wood, J. A., Dickey Jr., J. S., Marvin, U. B., and Powell, B. N. (1970). "Lunar anorthosites and a geophysical model of the moon". In: *Geochimica et Cosmochimica Acta Supplement* 1, p. 965.

Sagan, C. and Mullen, G. (1972). "Earth and Mars: Evolution of Atmospheres and Surface Temperatures". In: *Science* 177.4043, pp. 52–56.

Teller, J. A. (1973). "EARLY EVOLUTION OF PLANET EARTH". Copyright - Database copyright ProQuest LLC; ProQuest does not claim copyright in the individual underlying works; Last updated - 2023-08-10. PhD thesis. Yeshiva University, p. 94.

Peltier, W. R. (1974). "The impulse response of a Maxwell Earth". In: *Rev. Geophys.* 12.4, pp. 649–669.

Pollack, J. B. and Young, R. (1975). "Calculations of the Radiative and Dynamical State of the Venus Atmosphere". In: *J. Atmos. Sci.* 32.6, pp. 1025–1037.

Box, G. E. P. (1976). "Science and Statistics". In: *Journal of the American Statistical Association* 71.356, pp. 791–799.

Cameron, A. G. W. and Ward, W. R. (1976). "The Origin of the Moon". In: *Lunar and Planetary Science Conference*. Vol. 7. Lunar and Planetary Science Conference, p. 120.

Ghil, M. (1976). "Climate Stability for a Sellers-Type Model". In: *Journal of Atmospheric Sciences* 33.1, pp. 3–20.

Joseph, J. H., Wiscombe, W. J., and Weinman, J. A. (1976). "The Delta-Eddington Approximation for Radiative Flux Transfer". In: *J. Atmos. Sci.* 33.12, pp. 2452–2459.

Lee, T., Papanastassiou, D. A., and Wasserburg, G. J. (1976). "Demonstration of 26 Mg excess in Allende and evidence for 26 Al". In: *Geophysical Research Letters* 3.1, pp. 41–44.

Moody, J. B. (1976). "Serpentinization: a review". In: *Lithos* 9.2, pp. 125–138.

Peale, S. J., Cassen, P., and Reynolds, R. T. (1979). "Melting of Io by Tidal Dissipation". In: *Science* 203.4383, pp. 892–894.

Smith, B. A. et al. (1979). "The Jupiter System Through the Eyes of Voyager 1". In: *Science* 204.4396, pp. 951–957.

Yoder, C. F. (1979). "How Tidal Heating in Io Drives the Galilean Orbital Resonance Locks". In: *Nature* 279.5716, pp. 767–770.

Gough, D. (1980). "The pre-main-sequence evolution of the sun". In: *The Ancient Sun: Fossil Record in the Earth, Moon and Meteorites*. Ed. by R. O. Pepin, J. A. Eddy, and R. B. Merrill, pp. 533–550.

Zdunkowski, W., Welch, R., and Kork, G. (1980). "AN INVESTIGATION OF THE STRUCTURE OF TYPICAL TWO STREAM-METHODS FOR THE CALCULATION OF SOLAR FLUXES AND HEATING RATES IN CLOUDS". In: *BEITR. PHYS. ATMOSPH.; DEU; DA. 1980; VOL. 53; NO 2; PP. 147-166; ABS. GER/FRE; BIBL. 16 REF.*

Denbigh, K. G. (1981). *The Principles of Chemical Equilibrium: With Applications in Chemistry and Chemical Engineering*. Cambridge, England, UK: Cambridge University Press.

Clark, W. C. (1982). New York: Oxford University Press, p. 469.

Lange, M. A. and Ahrens, T. J. (1982). "The evolution of an impact-generated atmosphere". In: *Icarus* 51.1, pp. 96–120.

Slingo, A. and Schrecker, H. M. (1982). "On the shortwave radiative properties of stratiform water clouds". In: *Q. J. R. Meteorolog. Soc.* 108.456, pp. 407–426.

Cameron, A. (1983). "Origin of the atmospheres of the terrestrial planets". In: *Icarus* 56.2, pp. 195–201.

Eggleton, P. P. (1983). "Towards consistency in simple prescriptions for stellar convection". In: *Mon. Not. R. Astron. Soc* 204.2, pp. 449–461.

Kasting, J. F., Pollack, J. B., and Ackerman, T. P. (1984). "Response of Earth's atmosphere to increases in solar flux and implications for loss of water from Venus". In: *Icarus* 57.3, pp. 335–355.

Abe, Y. and Matsui, T. (1985). "The formation of an impact-generated H2O atmosphere and its implications for the early thermal history of the Earth". In: *Journal of Geophysical Research: Solid Earth* 90.S02, pp. C545–C559.

Warren, P. H. (1985). "THE MAGMA OCEAN CONCEPT AND LUNAR EVOLUTION". In: *Annual Review of Earth and Planetary Sciences* 13.Volume 13, 1985, pp. 201–240.

Zdunkowski, W. and Korb, G. (1985). "Numerische methoden zur lösung der strahlungsübertragungsgleichung". In: *Promet* 2.3, p. 1985.

Abe, Y. and Matsui, T. (1986). "Early evolution of the Earth: Accretion, atmosphere formation, and thermal history". In: *Journal of Geophysical Research: Solid Earth* 91.B13, E291–E302.

Chase, M. W. (1986). *JANAF thermochemical tables*. New York: American Chemical Society.

López-Puertas, M., Rodrigo, R., Molina, A., and Taylor, F. W. (1986). "A non-LTE radiative transfer model for infrared bands in the middle atmosphere. I. Theoretical basis and application to CO_2 15 μm bands." In: *Journal of Atmospheric and Terrestrial Physics* 48, pp. 729–748.

Matsui, T. and Abe, Y. (1986). "Evolution of an impact-induced atmosphere and magma ocean on the accreting Earth". In: *Nature* 319, pp. 303–305.

Ojakangas, G. W. and Stevenson, D. J. (1986). "Episodic Volcanism of Tidally Heated Satellites with Application to Io". In: *Icarus* 66.2, pp. 341–358.

Zahnle, K. J. and Kasting, J. F. (1986). "Mass fractionation during transonic escape and implications for loss of water from Mars and Venus". In: *Icarus* 68.3, pp. 462–480.

Chan, K. L. and Sofia, S. (1987). "Validity Tests of the Mixing-Length Theory of Deep Convection". In: *Science* 235.4787, pp. 465–467.

Hunten, D. M., Pepin, R. O., and Walker, J. C. (1987). "Mass fractionation in hydrodynamic escape". In: *Icarus* 69.3, pp. 532–549.

Kaye, J. A. (1987). "Mechanisms and observations for isotope fractionation of molecular species in planetary atmospheres". In: *Reviews of Geophysics* 25.8, pp. 1609–1658.

Högström, U. (1988). "Non-dimensional wind and temperature profiles in the atmospheric surface layer: A re-evaluation". In: *Boundary-Layer Meteorology* 42.1-2, pp. 55–78.

Kasting, J. F. (1988). "Runaway and moist greenhouse atmospheres and the evolution of Earth and Venus". In: *Icarus* 74.3, pp. 472–494.

Segatz, M., Spohn, T., Ross, M. N., and Schubert, G. (1988). "Tidal Dissipation, Surface Heat Flow, and Figure of Viscoelastic Models of Io". In: *Icarus* 75.2, pp. 187–206.

Spycher, N. F. and Reed, M. H. (1988). "Fugacity coefficients of H2, CO2, CH4, H2O and of H2O-CO2-CH4 mixtures: A virial equation treatment for moderate pressures and temperatures applicable to calculations of hydrothermal boiling". In: *Geochim. Cosmochim. Acta* 52.3, pp. 739–749.

Zahnle, K. J., Kasting, J. F., and Pollack, J. B. (1988). "Evolution of a steam atmosphere during earth's accretion". In: *Icarus* 74.1, pp. 62–97.

Bertout, C. (1989). "T Tauri stars: wild as dust." In: *Annu. Rev. Astron. Astrophys.* 27, pp. 351–395.

Goody, R. M. and Yung, Y. L. (1989). *Atmospheric Radiation: Theoretical Basis*. Publication Title: Atmospheric Radiation. Cary: Oxford University Press, Incorporated.

Chyba, C. F. (1990). "Impact delivery and erosion of planetary oceans in the early inner Solar System". In: *Nature* 343, pp. 129–133.

Fischer, H. .-. and Spohn, T. (1990). "Thermal-orbital histories of viscoelastic models of Io (J1)". In: *Icarus* 83.1, pp. 39–65.

Spencer, J. R. et al. (1990). "Discovery of hotspots on Io using disk-resolved infrared imaging". In: *Nature* 348.6302, pp. 618–621.

Borysow, A. and Frommhold, L. (1991). "Pressure-induced absorption in the infrared: A data base for the modelling of planetary atmospheres". In: *Journal of Geophysical Research: Planets* 96.E2, pp. 17501–17506.

Canuto, V. M. and Mazzitelli, I. (1991). "Stellar Turbulent Convection: A New Model and Applications". In: *Astrophysical Journal* 370, p. 295.

Dorman, B., Irwin, A. W., and Pedersen, B. B. (1991). "On Equation of State Interpolation Errors in Stellar Interior Calculations". In: *Astrophysical Journal* 381, p. 228.

Frost, B. R. (1991). "INTRODUCTION TO OXYGEN FUGACITY AND ITS PETROLOGIC IMPORTANCE". In: *Petrologic and Magnetic Significance*. Ed. by D. H. Lindsley. Berlin, Boston: De Gruyter, pp. 1–10.

Kress, V. C. and Carmichael, I. S. E. (1991). "The compressibility of silicate liquids containing Fe2O3 and the effect of composition, temperature, oxygen fugacity and pressure on their redox states". In: *Contrib. Mineral. Petrol.* 108.1, pp. 82–92.

Lacis, A. A. and Oinas, V. (1991). "A description of the correlatedkdistribution method for modeling nongray gaseous absorption, thermal emission, and multiple scattering in vertically inhomogeneous atmospheres". In: *Journal of Geophysical Research* 96.D5. Publisher: American Geophysical Union (AGU), p. 9027.

Gehlen, K. von (1992). "Sulfur in the Earth's Mantle – A Review". In: *Early Organic Evolution*. Berlin, Germany: Springer, pp. 359–366.

Nakajima, S., Hayashi, Y.-Y., and Abe, Y. (1992). "A study on the 'runaway greenhouse effect' with a one-dimensional radiative-convective equilibrium model". In: *Journal of the Atmospheric Sciences* 49.23, pp. 2256–2266.

Ritter, B. and Geleyn, J.-F. (1992). "A Comprehensive Radiation Scheme for Numerical Weather Prediction Models with Potential Applications in Climate Simulations". In: *Mon. Weather Rev.* 120.2, pp. 303–325.

Rothman, L. S., Hawkins, R. L., Wattson, R. B., and Gamache, R. R. (1992). "Energy levels, intensities, and linewidths of atmospheric carbon dioxide bands". In: *Journal of Quantitative Spectroscopy and Radiative Transfer* 48.5-6. Publisher: Elsevier BV, pp. 537–566.

Taylor, G. J. and Norman, M. D. (1992). "Evidence for Magma Oceans on Asteroids, the Moon, and Earth". In: *Physics and Chemistry of Magma Oceans from 1 Bar to 4 Mbar*. Ed. by C. B. Agee and J. Longhi, p. 58.

Trenberth, K. E. (1992). *Climate system modeling*. Cambridge University Press.

Abe, Y. (1993). "Thermal Evolution and Chemical Differentiation of the Terrestrial Magma Ocean". In: *Evolution of the Earth and Planets*. American Geophysical Union (AGU), pp. 41–54.

Frommhold, L. (1993). *Collision-induced absorption in gases*. Publication Title: Collision-induced absorption in gases. Cambridge.

Grinspoon, D. H. (1993). "Implications of the high D/H ratio for the sources of water in Venus' atmosphere". In: *Nature* 363, pp. 428–431.

Kasting, J. F., Eggler, D. H., and Raeburn, S. P. (1993a). "Mantle redox evolution and the oxidation state of the Archean atmosphere". In: *The Journal of geology* 101.2, pp. 245–257.

Kasting, J. F., Whitmire, D. P., and Reynolds, R. T. (1993b). "Habitable Zones around Main Sequence Stars". In: *Icarus* 101.1, pp. 108–128.

Parker, E. N. (1993). "A Solar Dynamo Surface Wave at the Interface between Convection and Nonuniform Rotation". In: *Astrophysical Journal* 408, p. 707.

Solomatov, V. S. and Stevenson, D. J. (1993a). "Nonfractional crystallization of a terrestrial magma ocean". In: *Journal of Geophysical Research* 98.E3, pp. 5391–5406.

— (1993b). "Suspension in convective layers and style of differentiation of a terrestrial magma ocean". In: *Journal of Geophysical Research* 98.E3, pp. 5375–5390.

Tonks, W. B. and Melosh, H. J. (1993). "Magma ocean formation due to giant impacts". In: *Journal of Geophysical Research: Planets* 98.E3, pp. 5319–5333.

Allard, F. and Hauschildt, P. H. (1995). "Model Atmospheres for M (Sub)Dwarf Stars. I. The Base Model Grid". In: *Astrophysical Journal* 445, p. 433.

Ballhaus, C. (1995). "Is the upper mantle metal-saturated?" In: *Earth Planet. Sci. Lett.* 132.1, pp. 75–86.

Guillot, T. (1995). "Condensation of Methane, Ammonia, and Water and the Inhibition of Convection in Giant Planets". In: *Science* 269.5231, pp. 1697–1699.

Mayor, M. and Queloz, D. (1995). "A Jupiter-mass companion to a solar-type star". In: *Nature* 378.6555, pp. 355–359.

Saumon, D., Chabrier, G., and van Horn, H. M. (1995). "An Equation of State for Low-Mass Stars and Giant Planets". In: *Astrophysical Journal Supplement Series* 99, p. 713.

Canuto, V. M., Goldman, I., and Mazzitelli, I. (1996). "Stellar Turbulent Convection: A Self-consistent Model". In: *Astrophys. J.* 473.1, p. 550.

Carr, M. H. (1996). *Water On Mars*. Oxford University Press.

Chassefiere, E. (1996). "Hydrodynamic escape of hydrogen from a hot water-rich atmosphere: The case of Venus". In: *Journal of Geophysical Research: Planets* 101.E11, pp. 26039–26056.

Dreibus, G. and Palme, H. (1996a). "Cosmochemical constraints on the sulfur content in the Earth's core". In: *Geochim. Cosmochim. Acta* 60.7, pp. 1125–1130.

— (1996b). "Cosmochemical constraints on the sulfur content in the Earth's core". In: *Geochim. Cosmochim. Acta* 60.7, pp. 1125–1130.

Edwards, J. M. (1996). "Efficient Calculation of Infrared Fluxes and Cooling Rates Using the Two-Stream Equations". In: *J. Atmos. Sci.* 53.13, pp. 1921–1932.

Edwards, J. M. and Slingo, A. (1996). "Studies with a flexible new radiation code. I: Choosing a configuration for a large-scale model". In: *Quarterly Journal of the Royal Meteorological Society* 122.531, pp. 689–719.

Grossman, S. A. (1996). "A theory of non-local mixing-length convection - III. Comparing theory and numerical experiment". In: *Mon. Not. R. Astron. Soc* 279.2, pp. 305–336.

Noggle, J. H. (1996). *Physical Chemistry, Part 1*. HarperCollins College Publishers.

Williams, Q. and Garnero, E. J. (1996). "Seismic Evidence for Partial Melt at the Base of Earth's Mantle". In: *Science* 273.5281, pp. 1528–1530.

Abe, Y. (1997). "Thermal and chemical evolution of the terrestrial magma ocean". In: *Physics of the Earth and Planetary Interiors* 100.1. Physical and Chemical Evolution of the Earth, pp. 27–39.

Benvenuto, O. G. and Althaus, L. G. (1997). "DB white dwarf evolution in the frame of the full spectrum turbulence theory". In: *Mon. Not. R. Astron. Soc* 288.4, pp. 1004–1014.

Dixon, J. E. (1997). "Degassing of alkalic basalts". In: *American Mineralogist* 82.3-4, pp. 368–378.

Karato, S.-i. and Rama Murthy, V. (1997). "Core formation and chemical equilibrium in the Earth I. Physical considerations". In: *Phys. Earth Planet. Inter.* 100.1, pp. 61–79.

McCammon, C. (1997). "Perovskite as a Possible Sink for Ferric Iron in the Lower Mantle". In: *Nature* 387.6634, pp. 694–696.

McQuarrie, D. A. and Simon, J. D. (1997). *Physical Chemistry: A Molecular Approach*. University Science Books.

Sagan, C. and Chyba, C. (1997). "The early faint sun paradox: Organic shielding of ultraviolet-labile greenhouse gases". In: *Science* 276, pp. 1217–1221.

Shen, A. H. and Keppler, H. (1997). "Direct observation of complete miscibility in the albite–H2O system". In: *Nature* 385, pp. 710–712.

Williams, D. M., Kasting, J. F., and Wade, R. A. (1997). "Habitable moons around extrasolar giant planets". In: *Nature* 385, pp. 234–236.

Lodders, K. and Fegley, B. (1998). *The planetary scientist's companion / Katharina Lodders, Bruce Fegley.*

McPhee, J. (1998). *Annals of the Former World*. Annals of the Former World. Farrar, Straus and Giroux.

Charbonneau, D., Brown, T. M., Latham, D. W., and Mayor, M. (1999). "Detection of Planetary Transits Across a Sun-like Star". In: *The Astrophysical Journal* 529.1, p. L45.

Guillot, T. (1999). "A comparison of the interiors of Jupiter and Saturn". In: *Planet. Space Sci.* 47.10, pp. 1183–1200.

Murray, C. D. and Dermott, S. F. (1999). *Solar System Dynamics*. Cambridge, England, UK: Cambridge University Press.

Herzberg, C., Raterron, P., and Zhang, J. (2000). "New experimental observations on the anhydrous solidus for peridotite KLB-1". In: *Geochemistry, Geophysics, Geosystems* 1.11.

Pepin, R. O. (2000). "On the Isotopic Composition of Primordial Xenon in Terrestrial Planet Atmospheres". In: *Space Sci. Rev.* 92.1, pp. 371–395.

Solomatov, V. S. (2000). "Fluid Dynamics of a Terrestrial Magma Ocean". In: *Origin of the Earth and Moon*. Ed. by R. M. Canup, K. Righter, and et al., pp. 323–338.

Whittaker, J. (2000). "What is software testing? And why is it so hard?" In: *IEEE Software* 17.1, pp. 70–79.

Canup, R. M. and Asphaug, E. (2001). "Origin of the Moon in a giant impact near the end of the Earth's formation". In: *Nature* 412.6848, pp. 708–712.

Catling, D. C., Zahnle, K. J., and McKay, C. P. (2001). "Biogenic Methane, Hydrogen Escape, and the Irreversible Oxidation of Early Earth". In: *Science* 293.5531, pp. 839–843.

Dalrymple, G. B. (2001). "The age of the Earth in the twentieth century: a problem (mostly) solved". In: *Geological Society of London Special Publications* 190.1, pp. 205–221.

Korotev, R. L. and Gillis, J. J. (2001). "A new look at the Apollo 11 regolith and KREEP". In: *Journal of Geophysical Research: Planets* 106.E6, pp. 12339–12353.

Schubert, G., Turcotte, D. L., and Olson, P. (2001). *Mantle convection in the Earth and planets*. Cambridge University Press.

Sleep, N. H., Zahnle, K., and Neuhoff, P. S. (2001). "Initiation of clement surface conditions on the earliest Earth". In: *Proc. Natl. Acad. Sci. U.S.A.* 98.7, pp. 3666–3672.

Wadhwa, M. (2001). "Redox State of Mars' Upper Mantle and Crust from Eu Anomalies in Shergottite Pyroxenes". In: *Science* 291.5508, pp. 1527–1530.

Wilde, S. A., Valley, J. W., Peck, W. H., and Graham, C. M. (2001). "Evidence from detrital zircons for the existence of continental crust and oceans on the Earth 4.4 Gyr ago". In: *Nature* 409, pp. 175–178.

Yi, S. et al. (2001). "Toward Better Age Estimates for Stellar Populations: The Y2 Isochrones for Solar Mixture". In: *Astrophys. J. Suppl. Ser.* 136.2, p. 417.

Bonanno, A., Schlattl, H., and Paternò, L. (2002). "The age of the Sun and the relativistic corrections in the EOS". In: *Astronomy & Astrophysics* 390, pp. 1115–1118.

Goldstein, H., Poole, C. P., and Safko, J. L. (2002). *Classical Mechanics*. Harlow, England, UK: Addison Wesley.

O'Neill, H. S. C. and Mavrogenes, J. A. (2002). "The Sulfide Capacity and the Sulfur Content at Sulfide Saturation of Silicate Melts at 1400°C and 1 bar". In: *J. Petrol.* 43.6, pp. 1049–1087.

Pavlov, A. A. and Kasting, J. F. (2002). "Mass-Independent Fractionation of Sulfur Isotopes in Archean Sediments: Strong Evidence for an Anoxic Archean Atmosphere". In: *Astrobiology* 2.1, pp. 27–41.

Schoenberg, R., Kamber, B. S., Collerson, K. D., and Eugster, O. (2002). "New W-isotope evidence for rapid terrestrial accretion and very early core formation". In: *Geochim. Cosmochim. Acta* 66.17, pp. 3151–3160.

Turcotte, D. L. and Schubert, G. (2002). *Geodynamics - 2nd Edition*.

Wagner, W. and Pruß, A. (2002). "The IAPWS Formulation 1995 for the Thermodynamic Properties of Ordinary Water Substance for General and Scientific Use". In: *Journal of Physical and Chemical Reference Data* 31.2, pp. 387–535.

Baraffe, I., Chabrier, G., Barman, T. S., Allard, F., and Hauschildt, P. H. (2003). "Evolutionary models for cool brown dwarfs and extrasolar giant planets. The case of HD 209458". In: *Astronomy & Astrophysics* 402, pp. 701–712.

Kasting, J. F. and Catling, D. (2003). "Evolution of a habitable planet". In: *Annu. Rev. Astron. Astrophys.* 41.1, pp. 429–463.

Katz, R. F., Spiegelman, M., and Langmuir, C. H. (2003). "A new parameterization of hydrous mantle melting". In: *Geochemistry, Geophysics, Geosystems* 4.9.

Lodders, K. (2003). "Solar System Abundances and Condensation Temperatures of the Elements". In: *Astrophys. J.* 591.2, p. 1220.

Lunine, J. I., Chambers, J., Morbidelli, A., and Leshin, L. A. (2003). "The origin of water on Mars". In: *Icarus* 165.1, pp. 1–8.

Moore, W. B. (2003). "Tidal heating and convection in Io". In: *Journal of Geophysical Research: Planets* 108.E8.

Valderrama, J. O. (2003). "The State of the Cubic Equations of State". In: *Ind. Eng. Chem. Res.* 42.8, pp. 1603–1618.

Borg, L. E., Shearer, C. K., Asmerom, Y., and Papike, J. J. (2004). "Prolonged KREEP magmatism on the Moon indicated by the youngest dated lunar igneous rock". In: *Nature* 432.7014, pp. 209–211.

Browning, M. K., Brun, A. S., and Toomre, J. (2004). "Simulations of Core Convection in Rotating A-Type Stars: Differential Rotation and Overshooting". In: *Astrophys. J.* 601.1, p. 512.

Gueymard, C. A. (2004). "The sun's total and spectral irradiance for solar energy applications and solar radiation models". In: *Solar Energy* 76.4, pp. 423–453.

Meca, E., Mercader, I., Batiste, O., and Ramírez-Piscina, L. (2004). "Blue Sky Catastrophe in Double-Diffusive Convection". In: *Phys. Rev. Lett.* 92 (23), p. 234501.

Renard, J. J., Calidonna, S. E., and Henley, M. V. (2004). "Fate of ammonia in the atmosphere-a review for applicability to hazardous releases". In: *Journal of Hazardous Materials* 108.1, pp. 29–60.

Stahler, S. W. and Palla, F. (2004). "Young Stellar Systems". In: *The Formation of Stars*. John Wiley & Sons, Ltd. Chap. 4, pp. 88–133.

Baker, J., Bizzarro, M., Wittig, N., Connelly, J., and Haack, H. (2005). "Early planetesimal melting from an age of 4.5662Gyr for differentiated meteorites". In: *Nature* 436.7054, pp. 1127–1131.

Cavosie, A. J., Valley, J. W., Wilde, S. A., and F., E. I. M. (2005). "Magmatic 18O in 4400-3900 Ma detrital zircons: A record of the alteration and recycling of crust in the Early Archean". In: *Earth Planet. Sci. Lett.* 235.3, pp. 663–681.

Gomes, R., Levison, H. F., Tsiganis, K., and Morbidelli, A. (2005). "Origin of the cataclysmic Late Heavy Bombardment period of the terrestrial planets". In: *Nature* 435, pp. 466–469.

Hindmarsh, A. C. et al. (2005). "SUNDIALS: Suite of nonlinear and differential/algebraic equation solvers". In: *ACM Transactions on Mathematical Software (TOMS)* 31.3, pp. 363–396.

Javoy, M. (2005). "Where do the oceans come from?" In: *Comptes Rendus Geoscience* 337.1, pp. 139–158.

Jørgensen, B. R. and Lindegren, L. (2005). "Determination of stellar ages from isochrones: Bayesian estimation versus isochrone fitting". In: *Astron. Astrophys.* 436.1, pp. 127–143.

Miesch, M. S. (2005). "Large-Scale Dynamics of the Convection Zone and Tachocline". In: *Living Rev. Sol. Phys.* 2.1, pp. 1–139.

Salaris, M. and Cassisi, S. (2005). *Evolution of Stars and Stellar Populations*. Chichester, England, UK: Wiley.

Stixrude, L. and Lithgow-Bertelloni, C. (2005). "Thermodynamics of mantle minerals - I. Physical properties". In: *Geophysical Journal International* 162.2, pp. 610–632.

Wade, J. and Wood, B. J. (2005). "Core formation and the oxidation state of the Earth". In: *Earth Planet. Sci. Lett.* 236.1, pp. 78–95.

Barber, R. J., Tennyson, J., Harris, G. J., and Tolchenov, R. N. (2006). "A high-accuracy computed water line list". In: *Mon. Not. R. Astron. Soc* 368.3, pp. 1087–1094.

Cooper, C. S. and Showman, A. P. (2006). "Dynamics and Disequilibrium Carbon Chemistry in Hot Jupiter Atmospheres, with Application to HD 209458b". In: *Astrophys. J.* 649.2, p. 1048.

Feistel, R. and Wagner, W. (2006). "A New Equation of State for H_2O Ice Ih". In: *Journal of Physical and Chemical Reference Data* 35.2, pp. 1021–1047.

Harris, G. J., Tennyson, J., Kaminsky, B. M., Pavlenko, Y. V., and Jones, H. R. A. (2006). "Improved HCN/HNC linelist, model atmospheres and synthetic spectra for WZ Cas". In: *Mon. Not. R. Astron. Soc* 367.1, pp. 400–406.

Ikoma, M. and Genda, H. (2006). "Constraints on the Mass of a Habitable Planet with Water of Nebular Origin". In: *The Astrophysical Journal* 648.1, p. 696.

Keppler, H. and Bolfan-Casanova, N. (2006). "Thermodynamics of Water Solubility and Partitioning". In: *Rev. Mineral. Geochem.* 62.1, pp. 193–230.

Nicholson, L. and Benn, D. I. (2006). "Calculating ice melt beneath a debris layer using meteorological data". In: *J. Glaciol.* 52.178, pp. 463–470.

Seinfeld, J. H. and Pandis, S. N. (2006). *Atmospheric chemistry and physics : from air pollution to climate change*. 2nd ed. Hoboken, N.J.: Wiley.

Skilling, J. (2006). "Nested sampling for general Bayesian computation". In: *ba* 1.4, pp. 833–859.

Allendorf, M. D. and Besmann, T. (2007). *Thermodynamics Resource Data Base.* Tech. rep. Sandia National Lab.(SNL-CA), Livermore, CA (United States).

Coker, A. (2007). *Ludwig's Applied Process Design for Chemical and Petrochemical Plants*. Burlington: Gulf Professional Publishing.

Gudel, M. (2007). "The Sun in Time: Activity and Environment". In: *Living Rev. Sol. Phys.* 4.1, pp. 1–137.

Labrosse, S., Hernlund, J. W., and Coltice, N. (2007). "A crystallizing dense magma ocean at the base of the Earth's mantle". In: *Nature* 450, pp. 866–869.

Lammer, H. et al. (2007). "Coronal Mass Ejection (CME) Activity of Low Mass M Stars as An Important Factor for The Habitability of Terrestrial Exoplanets. II. CME-Induced Ion Pick Up of Earth-like Exoplanets in Close-In Habitable Zones". In: *Astrobiology* 7.1, pp. 185–207.

Marley, M. S., Fortney, J. J., Hubickyj, O., Bodenheimer, P., and Lissauer, J. J. (2007). "On the Luminosity of Young Jupiters". In: *The Astrophysical Journal* 655.1, p. 541.

Mosenfelder, J. L., Asimow, P. D., and Ahrens, T. J. (2007). "Thermodynamic properties of Mg2SiO4 liquid at ultra-high pressures from shock measurements to 200 GPa on forsterite and wadsleyite". In: *J. Geophys. Res. Solid Earth* 112.B6.

Pikuta, E. V., Hoover, R. B., and Tang, J. (2007). "Microbial Extremophiles at the Limits of Life". In: *Crit. Rev. Microbiol.*

Press, W. H. (2007). *Numerical Recipes 3rd Edition: The Art of Scientific Computing*. Numerical Recipes: The Art of Scientific Computing. Cambridge University Press.

Rubie, D. C., Nimmo, F., and Melosh, J. (2007). "Formation of Earth's Core". In: *Evolution of the Earth*. Ed. by G. Schubert. Vol. 9, pp. 51–90.

Sharp, C. M. and Burrows, A. (2007). "Atomic and Molecular Opacities for Brown Dwarf and Giant Planet Atmospheres". In: *The Astrophysical Journal Supplement Series* 168.1. Publisher: American Astronomical Society, pp. 140–166.

Solomatov, V. (2007). "9.04 - Magma Oceans and Primordial Mantle Differentiation". In: *Treatise on Geophysics*. Ed. by G. Schubert. Amsterdam: Elsevier, pp. 91–119.

Stefels, J., Steinke, M., Turner, S., Malin, G., and Belviso, S. (2007). "Environmental constraints on the production and removal of the climatically active gas dimethylsulphide (DMS) and implications for ecosystem modelling". In: *Biogeochemistry* 83.1-3, pp. 245–275.

Valencia, D., Sasselov, D. D., and O'Connell, R. J. (2007). "Radius and Structure Models of the First Super-Earth Planet". In: *The Astrophysical Journal* 656.1, p. 545.

Zahnle, K. et al. (2007). "Emergence of a Habitable Planet". In: *Space Sci. Rev.* 129.1, pp. 35–78.

Elkins-Tanton, L. (2008). "Linked magma ocean solidification and atmospheric growth for Earth and Mars". In: *Earth and Planetary Science Letters* 271.1, pp. 181–191.

Fortney, J. J., Lodders, K., Marley, M. S., and Freedman, R. S. (2008). "A Unified Theory for the Atmospheres of the Hot and Very Hot Jupiters: Two Classes of Irradiated Atmospheres". In: *Astrophysical Journal* 678.2, pp. 1419–1435.

Frost, D. J. and McCammon, C. A. (2008). "The Redox State of Earth's Mantle". In: *Annual Review of Earth and Planetary Sciences* 36, pp. 389–420.

Genda, H. and Ikoma, M. (2008). "Origin of the ocean on the Earth: Early evolution of water D/H in a hydrogen-rich atmosphere". In: *Icarus* 194.1, pp. 42–52.

Grossman, L., Beckett, J. R., Fedkin, A. V., Simon, S. B., and Ciesla, F. J. (2008). "Redox Conditions in the Solar Nebula: Observational, Experimental, and Theoretical Constraints". In: *Reviews in Mineralogy and Geochemistry* 68.1, pp. 93–140.

Korenaga, J. (2008). "Urey ratio and the structure and evolution of Earth's mantle". In: *Reviews of Geophysics* 46.2.

O'Neil, J., Carlson, R. W., Francis, D., and Stevenson, R. K. (2008). "Neodymium-142 Evidence for Hadean Mafic Crust". In: *Science* 321.5897, pp. 1828–1831.

Wyatt, M. C. (2008). "Evolution of Debris Disks". In: *Annu. Rev. Astron. Astrophys.* 46.Volume 46, 2008, pp. 339–383.

Costa, A., Caricchi, L., and Bagdassarov, N. (2009). "A model for the rheology of particle-bearing suspensions and partially molten rocks". In: *Geochemistry, Geophysics, Geosystems* 10.3.

Dasgupta, R., Buono, A., Whelan, G., and Walker, D. (2009). "High-pressure melting relations in Fe-C-S systems: Implications for formation, evolution, and structure of metallic cores in planetary bodies". In: *Geochim. Cosmochim. Acta* 73.21, pp. 6678–6691.

Debaille, V., Brandon, A. D., O'Neill, C., Yin, Q.-Z., and Jacobsen, B. (2009). "Early martian mantle overturn inferred from isotopic composition of nakhlite meteorites". In: *Nature Geoscience* 2.8, pp. 548–552.

Gonzalez-Galindo, F., Forget, F., Lppez-Valverde, M. A., Coll, M. A. i., and Millour, E. (2009). "A ground-to-exosphere Martian general circulation model: 1. Seasonal, diurnal, and solar cycle variation of thermospheric temperatures". In: *J. Geophys. Res. Planets* 114.E4.

Henning, W. G., O'Connell, R. J., and Sasselov, D. D. (2009). "TIDALLY HEATED TERRESTRIAL EXOPLANETS: VISCOELASTIC RESPONSE MODELS". In: *The Astrophysical Journal* 707.2, p. 1000.

Kleine, T. et al. (2009). "Hf–W chronology of the accretion and early evolution of asteroids and terrestrial planets". In: *Geochim. Cosmochim. Acta* 73.17, pp. 5150–5188.

Knutson, H. A. et al. (2009). "Multiwavelength Constraints on the Day-Night Circulation Patterns of HD 189733b". In: *Astrophysical Journal* 690.1, pp. 822–836.

Madhusudhan, N. and Seager, S. (2009). "A TEMPERATURE AND ABUNDANCE RETRIEVAL METHOD FOR EXOPLANET ATMOSPHERES". In: *Astrophys. J.* 707.1, p. 24.

Mosenfelder, J. L., Asimow, P. D., Frost, D. J., Rubie, D. C., and Ahrens, T. J. (2009). "The $MgSiO_3$ system at high pressure: Thermodynamic properties of perovskite, postperovskite, and melt from global inversion of shock and static compression data". In: *Journal of Geophysical Research (Solid Earth)* 114.B1, B01203, B01203.

Reif, F. (2009). *Fundamentals of Statistical and Thermal Physics*. Prospect Heights, IL, USA: Waveland Press.

Reiners, A. and Basri, G. (2009). "On the magnetic topology of partially and fully convective stars". In: *Astronomy & Astrophysics* 496.3, pp. 787–790.

Davies, J. H. and Davies, D. R. (2010). "Earth's surface heat flux". In: *Solid Earth* 1.1, pp. 5–24.

Guillot, T. (2010). "On the radiative equilibrium of irradiated planetary atmospheres". In: *Astronomy & Astrophysics* 520, A27.

Ichikawa, H., Labrosse, S., and Kurita, K. (2010). "Direct numerical simulation of an iron rain in the magma ocean". In: *J. Geophys. Res. Solid Earth* 115.B1.

Kaltenegger, L., Henning, W. G., and Sasselov, D. D. (2010). "Detecting Volcanism on Extrasolar Planets". In: *Astronomical Journal* 140.5, pp. 1370–1380.

Kaltenegger, L. and Sasselov, D. (2010). "Detecting Planetary Geochemical Cycles on Exoplanets: Atmospheric Signatures and the Case of SO_2". In: *Astrophysical Journal* 708.2, pp. 1162–1167.

Pierrehumbert, R. T. (2010). *Principles of planetary climate*. Cambridge New York: Cambridge University Press.

Reiners, A., Bean, J. L., Huber, K. F., Dreizler, S., Seifahrt, A., and Czesla, S. (2010). "DETECTING PLANETS AROUND VERY LOW MASS STARS WITH THE RADIAL VELOCITY METHOD". In: *The Astrophysical Journal* 710.1, p. 432.

Rothman, L. et al. (2010). "HITEMP, the high-temperature molecular spectroscopic database". In: *Journal of Quantitative Spectroscopy and Radiative Transfer* 111.15. XVIth Symposium on High Resolution Molecular Spectroscopy (HighRus-2009), pp. 2139–2150.

Soderblom, D. R. (2010). "The Ages of Stars". In: *Annu. Rev. Astron. Astrophys.* Volume 48, 2010, pp. 581–629.

Swain, M. R. et al. (2010). "A ground-based near-infrared emission spectrum of the exoplanet HD 189733b". In: *Nature* 463.7281, pp. 637–639.

Abel, M., Frommhold, L., Li, X., and Hunt, K. L. C. (2011). "Collision-Induced Absorption by H2 Pairs: From Hundreds to Thousands of Kelvin". In: *The Journal of Physical Chemistry A* 115.25. PMID: 21207941, pp. 6805–6812.

Adelberger, E. G. et al. (2011). "Solar fusion cross sections. II. The pp chain and CNO cycles". In: *Reviews of Modern Physics* 83.1, pp. 195–246.

Agol, E. (2011). "Transit Surveys for Earths in the Habitable Zones of White Dwarfs". In: *Astrophysical Journal Letters* 731.2, L31, p. L31.

Andrault, D., Bolfan-Casanova, N., Nigro, G. L., Bouhifd, M. A., Garbarino, G., and Mezouar, M. (2011). "Solidus and liquidus profiles of chondritic mantle: Implication for melting of the Earth across its history". In: *Earth Planet. Sci. Lett.* 304.1, pp. 251–259.

Bolmont, E., Raymond, S. N., and Leconte, J. (2011). "Tidal evolution of planets around brown dwarfs". In: *Astronomy & Astrophysics* 535, A94.

Chen, G., Laane, J., Wheeler, S. E., and Zhang, Z. (2011). "Greenhouse gas molecules: a mathematical perspective". In: *Notices of the AMS* 58.10, pp. 1421–1434.

Ebel, D. S. (2011). "Sulfur in Extraterrestrial Bodies and the Deep Earth". In: *Rev. Mineral. Geochem.* 73.1, pp. 315–336.

Khurana, K. K., Jia, X., Kivelson, M. G., Nimmo, F., Schubert, G., and Russell, C. T. (2011). "Evidence of a Global Magma Ocean in Io's Interior". In: *Science* 332.6034, pp. 1186–1189.

Kopp, G. and Lean, J. L. (2011). "A new, lower value of total solar irradiance: Evidence and climate significance". In: *Geophysical Research Letters* 38.1.

Paxton, B., Bildsten, L., Dotter, A., Herwig, F., Lesaffre, P., and Timmes, F. (2011). "Modules for Experiments in Stellar Astrophysics (MESA)". In: *Astrophysical Journal Supplement Series* 192, 3, p. 3.

Perryman, M. (2011). "Imaging". In: *The Exoplanet Handbook*. Cambridge University Press, pp. 149–180.

Pierrehumbert, R. and Gaidos, E. (2011). "HYDROGEN GREENHOUSE PLANETS BEYOND THE HABITABLE ZONE". In: *The Astrophysical Journal Letters* 734.1, p. L13.

Schneider, J., Dedieu, C., Le Sidaner, P., Savalle, R., and Zolotukhin, I. (2011). "Defining and cataloging exoplanets: the exoplanet.eu database". In: *A&A* 532, A79.

Seager, S. (2011). *Exoplanets*. Tucson: University of Arizona Press.

Spera, F. J., Ghiorso, M. S., and Nevins, D. (2011a). "Structure, thermodynamic and transport properties of liquid MgSiO3: Comparison of molecular models and laboratory results". In: *Geochim. Cosmochim. Acta* 75.5, pp. 1272–1296.

— (2011b). "Structure, thermodynamic and transport properties of liquid MgSiO3: Comparison of molecular models and laboratory results". In: *Geochim. Cosmochim. Acta* 75.5, pp. 1272–1296.

Trail, D., Watson, E. B., and Tailby, N. D. (2011). "The oxidation state of Hadean magmas and implications for early Earth's atmosphere". In: *Nature* 480.7375, pp. 79–82.

Walsh, K. J., Morbidelli, A., Raymond, S. N., O'Brien, D. P., and Mandell, A. M. (2011). "A low mass for Mars from Jupiter's early gas-driven migration". In: *Nature* 475, pp. 206–209.

Biolcati, E., Svitlov, S., and Germak, A. (2012). "Self-attraction effect and correction on three absolute gravimeters". In: *Metrologia* 49.4, p. 560.

Carr, M. H. (2012). "The fluvial history of Mars". In: *Philos. Trans. Royal Soc. A* 370.1966, pp. 2193–2215.

Connelly, J. N., Bizzarro, M., Krot, A. N., Nordlund, Å., Wielandt, D., and Ivanova, M. A. (2012). "The Absolute Chronology and Thermal Processing of Solids in the Solar Protoplanetary Disk". In: *Science* 338.6107, p. 651.

Elkins-Tanton, L. T. (2012). "Magma Oceans in the Inner Solar System". In: *Annual Review of Earth and Planetary Sciences* 40.Volume 40, 2012, pp. 113–139.

Freytag, B., Steffen, M., Ludwig, H.-G., Wedemeyer-Bohm, S., Schaffenberger, W., and Steiner, O. (2012). "Simulations of stellar convection with CO5BOLD". In: *J. Comput. Phys.* 231.3, pp. 919–959.

Hirschmann, M. M. (2012). "Magma ocean influence on early atmosphere mass and composition". In: *Earth and Planetary Science Letters* 341, pp. 48–57.

Kippenhahn, R., Weigert, A., and Weiss, A. (2012). *Stellar Structure and Evolution*. Berlin, Germany: Springer.

Korenaga, J. (2012). "Plate tectonics and planetary habitability: current status and future challenges". In: *Annals of the New York Academy of Sciences* 1260.1, pp. 87–94.

Mlawer, E. J., Payne, V. H., Moncet, J. .-., Delamere, J. S., Alvarado, M. J., and Tobin, D. C. (2012). "Development and recent evaluation of the MT_CKD model of continuum absorption". In: *Philosophical Transactions of the Royal Society of London Series A* 370.1968, pp. 2520–2556.

Reiners, A., Joshi, N., and Goldman, B. (2012). "A CATALOG OF ROTATION AND ACTIVITY IN EARLY-M STARS". In: *Astronomical Journal* 143.4, p. 93.

Robinson, T. D. and Catling, D. C. (2012). "AN ANALYTIC RADIATIVE-CONVECTIVE MODEL FOR PLANETARY ATMOSPHERES". In: *The Astrophysical Journal* 757.1, p. 104.

Tennyson, J. and Yurchenko, S. N. (2012). "ExoMol: molecular line lists for exoplanet and other atmospheres". In: *Mon. Not. R. Astron. Soc* 425.1, pp. 21–33.

Venot, O. et al. (2012). "A chemical model for the atmosphere of hot Jupiters". In: *Astronomy & Astrophysics* 546, A43.

Yaxley, G. M., Berry, A. J., Kamenetsky, V. S., Woodland, A. B., and Golovin, A. V. (2012). "An oxygen fugacity profile through the Siberian Craton — Fe K-edge XANES determinations of Fe3+/∑Fe in garnets in peridotite xenoliths from the Udachnaya East kimberlite". In: *Lithos* 140-141, pp. 142–151.

Ardia, P., Hirschmann, M. M., Withers, A. C., and Stanley, B. D. (2013). "Solubility of CH4 in a synthetic basaltic melt, with applications to atmosphere–magma ocean–core partitioning of volatiles and to the evolution of the Martian atmosphere". In: *Geochim. Cosmochim. Acta* 114, pp. 52–71.

Barber, R. J. et al. (2013). "ExoMol line lists - III. An improved hot rotation-vibration line list for HCN and HNC". In: *Mon. Not. R. Astron. Soc* 437.2, pp. 1828–1835.

Barnes, R. and Heller, R. (2013). "Habitable Planets Around White and Brown Dwarfs: The Perils of a Cooling Primary". In: *Astrobiology* 13.3, pp. 279–291.

Beeck, B., Cameron, R. H., Reiners, A., and Schssler, M. (2013). "Three-dimensional simulations of near-surface convection in main-sequence stars - II. Properties of granulation and spectral lines". In: *Astron. Astrophys.* 558, A49.

Bolmont, E. et al. (2013). "Tidal dissipation and eccentricity pumping: Implications for the depth of the secondary eclipse of 55 Cancri e". In: *Astronomy & Astrophysics* 556, A17, A17.

Cates, N. L., Ziegler, K., Schmitt, A. K., and Mojzsis, S. J. (2013). "Reduced, reused and recycled: Detrital zircons define a maximum age for the Eoarchean (ca. 3750-3780Ma) Nuvvuagittuq Supracrustal Belt, Quebec (Canada)". In: *Earth and Planetary Science Letters* 362, pp. 283–293.

Foreman-Mackey, D., Hogg, D. W., Lang, D., and Goodman, J. (2013). "emcee: The MCMC Hammer". In: *Publ. Astron. Soc. Pac.* 125.925, p. 306.

Goldblatt, C., Robinson, T. D., Zahnle, K. J., and Crisp, D. (2013). "Low simulated radiation limit for runaway greenhouse climates". In: *Nature Geoscience* 6.8, pp. 661–667.

Halliday, A. N. (2013). "The origins of volatiles in the terrestrial planets". In: *Geochimica et Cosmochimica Acta* 105, pp. 146–171.

Hamano, K., Abe, Y., and Genda, H. (2013). "Emergence of Two Types of Terrestrial Planet on Solidification of Magma Ocean". In: *Nature* 497.7451, pp. 607–610.

Husser, T.-O. et al. (2013). "A new extensive library of PHOENIX stellar atmospheres and synthetic spectra". In: *Astronomy & Astrophysics* 553, A6.

Kopparapu, R. K. et al. (2013). "HABITABLE ZONES AROUND MAIN-SEQUENCE STARS: NEW ESTIMATES". In: *The Astrophysical Journal* 765.2, p. 131.

Lebrun, T. et al. (2013). "Thermal evolution of an early magma ocean in interaction with the atmosphere: MAGMA OCEAN AND ATMOSPHERE EVOLUTION". In: *Journal of Geophysical Research: Planets* 118.6, pp. 1155–1176.

Leconte, J., Forget, F., Charnay, B., Wordsworth, R., and Pottier, A. (2013). "Increased insolation threshold for runaway greenhouse processes on Earth-like planets". In: *Nature* 504.7479, pp. 268–271.

Lopez, E. D. and Fortney, J. J. (2013). "The Role of Core Mass in Controlling Evaporation: The Kepler Radius Distribution and the Kepler-36 Density Dichotomy". In: *Astrophysical Journal* 776.1, 2, p. 2.

Marleau, G.-D. and Cumming, A. (2013). "Constraining the initial entropy of directly detected exoplanets". In: *Mon. Not. R. Astron. Soc* 437.2, pp. 1378–1399.

Parmentier, V., Showman, A., and Lian, Y. (2013). "3D mixing in hot Jupiters atmospheres - I. Application to the day/night cold trap in HD 209458b". In: *Astronomy & Astrophysics* 558, A91.

Root, S., Cochrane, K. R., Carpenter, J. H., and Mattsson, T. R. (2013). "Carbon dioxide shock and reshock equation of state data to 8 Mbar: Experiments and simulations". In: *Phys. Rev. B* 87.22, p. 224102.

Seager, S. (2013). "Exoplanet Habitability". In: *Science* 340.6132, pp. 577–581.

Spada, F., Demarque, P., Kim, Y. .-., and Sills, A. (2013). "THE RADIUS DISCREPANCY IN LOW-MASS STARS: SINGLE VERSUS BINARIES". In: *The Astrophysical Journal* 776.2, p. 87.

Wordsworth, R. D. and Pierrehumbert, R. T. (2013). "WATER LOSS FROM TERRESTRIAL PLANETS WITH CO2-RICH ATMOSPHERES". In: *The Astrophysical Journal* 778.2, p. 154.

Zhou, T. (2013). "Bifurcation". In: *Encyclopedia of Systems Biology*. New York, NY: Springer New York, pp. 79–86.

Zolotov, M. Y., Sprague, A. L., Hauck, S. A., Nittler, L. R., Solomon, S. C., and Weider, S. Z. (2013). "The redox state, FeO content, and origin of sulfur-rich magmas on Mercury". In: *J. Geophys. Res. Planets* 118.1, pp. 138–146.

Zsom, A., Seager, S., de Wit, J., and Stamenković, V. (2013). "Toward the Minimum Inner Edge Distance of the Habitable Zone". In: *Astrophysical Journal* 778.2, 109, p. 109.

Amundsen, D. et al. (2014). "Accuracy tests of radiation schemes used in hot Jupiter global circulation models". In: *Astronomy & Astrophysics* 564, A59.

Bolmont, E. et al. (2014). "FORMATION, TIDAL EVOLUTION, AND HABITABILITY OF THE KEPLER-186 SYSTEM". In: *The Astrophysical Journal* 793.1, p. 3.

Borg, L. E., Gaffney, A. M., and Shearer, C. K. (2014). "A review of lunar chronology revealing a preponderance of 4.34-4.37 Ga ages". In: *Meteorit. Planet. Sci.* 50.4, pp. 715–732.

Brown, S. M., Elkins-Tanton, L. T., and Walker, R. J. (2014). "Effects of magma ocean crystallization and overturn on the development of 142Nd and 182W isotopic heterogeneities in the primordial mantle". In: *Earth and Planetary Science Letters* 408, pp. 319–330.

Catling, D. (2014). "6.7 - The Great Oxidation Event Transition". In: *Treatise on Geochemistry (Second Edition)*. Ed. by H. D. Holland and K. K. Turekian. Second Edition. Oxford: Elsevier, pp. 177–195.

Cronin, T. W. (2014). "On the Choice of Average Solar Zenith Angle". In: *Journal of the Atmospheric Sciences* 71.8, pp. 2994–3003.

Fischer, D. A. et al. (2014). "Exoplanet Detection Techniques". In: *Protostars and Planets VI*. University of Arizona Press.

Gabriel, M., Noels, A., Montalbn, J., and Miglio, A. (2014). "Proper use of Schwarzschild Ledoux criteria in stellar evolution computations". In: *Astron. Astrophys.* 569, A63.

Gorshelev, V., Serdyuchenko, A., Weber, M., Chehade, W., and Burrows, J. P. (2014). "High spectral resolution ozone absorption cross-sections Part 1: Measurements, data analysis and comparison with previous measurements around 293 K". In: *Atmospheric Measurement Techniques* 7.2, pp. 609–624.

Haywood, R. D. et al. (2014). "Disentangling planetary orbits from stellar activity in radial-velocity surveys". In: *International Journal of Astrobiology* 13.2, pp. 155–157.

Kreidberg, L. et al. (2014). "Clouds in the atmosphere of the super-Earth exoplanet GJ\hspace0.167em1214b". In: *Nature* 505.7481. Publisher: Springer Science and Business Media LLC, pp. 69–72.

Lopez, E. D. and Fortney, J. J. (2014). "UNDERSTANDING THE MASS-RADIUS RELATION FOR SUB-NEPTUNES: RADIUS AS A PROXY FOR COMPOSITION". In: *The Astrophysical Journal* 792.1, p. 1.

Mackwell, S. J., Simon-Miller, A. A., Harder, J. W., and Bullock, M. A. (2014). *Comparative Climatology of Terrestrial Planets*. University of Arizona Press.

Magyar, R. J., Root, S., and Mattsson, T. R. (2014). "Equations of state for mixtures: results from density-functional (DFT) simulations compared to high accuracy validation experiments on Z". In: *Journal of Physics: Conference Series* 500.16, p. 162004.

Ramirez, R. M. and Kaltenegger, L. (2014). "THE HABITABLE ZONES OF PRE-MAIN-SEQUENCE STARS". In: *The Astrophysical Journal Letters* 797.2, p. L25.

Reiners, A., Schüssler, M., and Passegger, V. M. (2014). "Generalized Investigation of the Rotation-Activity Relation: Favoring Rotation Period instead of Rossby Number". In: *Astrophysical Journal* 794.2, 144, p. 144.

Robinson, T. D. and Catling, D. C. (2014). "Common 0.1 bar tropopause in thick atmospheres set by pressure-dependent infrared transparency". In: *Nat. Geosci.* 7, pp. 12–15.

Robinson, T. D. and Marley, M. S. (2014). "TEMPERATURE FLUCTUATIONS AS A SOURCE OF BROWN DWARF VARIABILITY". In: *The Astrophysical Journal* 785.2, p. 158.

Sleep, N. H., Zahnle, K. J., and Lupu, R. E. (2014). "Terrestrial aftermath of the Moon-forming impact". In: *Philosophical Transactions of the Royal Society A: Mathematical, Physical and Engineering Sciences* 372.2024, p. 20130172.

Taylor, F. W. and Hunten, D. M. (2014). "Chapter 14 - Venus: Atmosphere". In: *Encyclopedia of the Solar System (Third Edition)*. Ed. by T. Spohn, D. Breuer, and T. V. Johnson. Third Edition. Boston: Elsevier, pp. 305–322.

Wordsworth, R. and Pierrehumbert, R. (2014). "ABIOTIC OXYGEN-DOMINATED ATMOSPHERES ON TERRESTRIAL HABITABLE ZONE PLANETS". In: *The Astrophysical Journal* 785.2, p. L20.

Yurchenko and Tennyson (2014). "ExoMol line lists - IV. The rotation-vibration spectrum of methane up to 1500K". In: *Mon. Not. R. Astron. Soc* 440.2, pp. 1649–1661.

Al Derzi, A. R., Furtenbacher, T., Tennyson, J., Yurchenko, S. N., and Csaszar, A. G. (2015). "MARVEL analysis of the measured high-resolution spectra of 14NH3". In: *Journal of Quantitative Spectroscopy and Radiative Transfer* 161, pp. 117–130.

Armstrong, L. S., Hirschmann, M. M., Stanley, B. D., Falksen, E. G., and Jacobsen, S. D. (2015). "Speciation and solubility of reduced COHN volatiles in mafic melt: Implications for volcanism, atmospheric evolution, and deep volatile cycles in the terrestrial planets". In: *Geochim. Cosmochim. Acta* 171, pp. 283–302.

Baraffe, I., Homeier, D., Allard, F., and Chabrier, G. (2015). "New evolutionary models for pre-main sequence and main sequence low-mass stars down to the hydrogen-burning limit". In: *Astronomy & Astrophysics* 577, A42.

Bonan, G. (2015). *Ecological Climatology: Concepts and Applications*. Cambridge, England, UK: Cambridge University Press.

Driscoll, P. and Barnes, R. (2015). "Tidal Heating of Earth-like Exoplanets around M Stars: Thermal, Magnetic, and Orbital Evolutions". In: *Astrobiology* 15.9. PMID: 26393398, pp. 739–760.

Ehrenreich, D. et al. (2015). "A giant comet-like cloud of hydrogen escaping the warm Neptune-mass exoplanet GJ 436b". In: *Nature* 522.7557, pp. 459–461.

Farmer, D. K., Cappa, C. D., and Kreidenweis, S. M. (2015). "Atmospheric Processes and Their Controlling Influence on Cloud Condensation Nuclei Activity". In: *Chem. Rev.* 115.10, pp. 4199–4217.

Gallet, F. and Bouvier, J. (2015). "Improved angular momentum evolution model for solar-like stars. II. Exploring the mass dependence". In: *Astronomy & Astrophysics* 577, A98, A98.

Hamano, K., Kawahara, H., Abe, Y., Onishi, M., and Hashimoto, G. L. (2015). "LIFETIME AND SPECTRAL EVOLUTION OF A MAGMA OCEAN WITH A STEAM ATMOSPHERE: ITS DETECTABILITY BY FUTURE DIRECT IMAGING". In: *The Astrophysical Journal* 806.2, p. 216.

Huebner, W. F. and Mukherjee, J. (2015). "Photoionization and photodissociation rates in solar and blackbody radiation fields". In: *Planetary and Space Science* 106, pp. 11–45.

Li, G. et al. (2015). "ROVIBRATIONAL LINE LISTS FOR NINE ISOTOPOLOGUES OF THE CO MOLECULE IN THE X1+ GROUND ELECTRONIC STATE". In: *The Astrophysical Journal Supplement Series* 216.1, p. 15.

Luger, R. and Barnes, R. (2015). "Extreme Water Loss and Abiotic O_2 Buildup on Planets Throughout the Habitable Zones of M Dwarfs". In: *Astrobiology* 15.2, pp. 119–143.

Magyar, R. J., Root, S., Cochrane, K., Mattsson, T. R., and Flicker, D. G. (2015). "Ethane-xenon mixtures under shock conditions". In: *Phys. Rev. B* 91 (13), p. 134109.

Marley, M. and Robinson, T. (2015). "On the Cool Side: Modeling the Atmospheres of Brown Dwarfs and Giant Planets". In: *Annu. Rev. Astron. Astrophys.* 53.1, pp. 279–323.

Matt, S. P., Brun, A. S., Baraffe, I., Bouvier, J., and Chabrier, G. (2015). "The Mass-dependence of Angular Momentum Evolution in Sun-like Stars". In: *Astrophysical Journal Letters* 799.2, L23, p. L23.

Parmentier, V., Guillot, T., Fortney, J. J., and Marley, M. S. (2015). "A non-grey analytical model for irradiated atmospheres - II. Analytical vs. numerical solutions". In: *Astronomy & Astrophysics* 574, A35.

Rogers, L. A. (2015). "Most 1.6 Earth-radius Planets Are Not Rocky". In: *The Astrophysical Journal* 801.1, p. 41.

Tremblin, P. et al. (2015). "FINGERING CONVECTION AND CLOUDLESS MODELS FOR COOL BROWN DWARF ATMOSPHERES". In: *The Astrophysical Journal* 804.1. Publisher: American Astronomical Society, p. L17.

Tyler, R. H., Henning, W. G., and Hamilton, C. W. (2015a). "Tidal heating in a magma ocean within Jupiter's moon Io". In: *The Astrophysical Journal Supplement Series* 218.2, p. 22.

— (2015b). "TIDAL HEATING IN A MAGMA OCEAN WITHIN JUPITER'S MOON Io". In: *The Astrophysical Journal Supplement Series* 218.2, p. 22.

Wakeford, H. R. and Sing, D. K. (2015). "Transmission spectral properties of clouds for hot Jupiter exoplanets". In: *Astron. Astrophys.* 573, A122.

Williams, J. G. and Boggs, D. H. (2015). "Tides on the Moon: Theory and determination of dissipation". In: *J. Geophys. Res. Planets* 120.4, pp. 689–724.

Winn, J. N. and Fabrycky, D. C. (2015). "The Occurrence and Architecture of Exoplanetary Systems". In: *Annu. Rev. Astron. Astrophys.* Volume 53, 2015, pp. 409–447.

Zahnle, K. J., Lupu, R., Dobrovolskis, A., and Sleep, N. H. (2015). "The tethered Moon". In: *Earth and Planetary Science Letters* 427, pp. 74–82.

Aulbach, S. and Stagno, V. (2016). "Evidence for a reducing Archean ambient mantle and its effects on the carbon cycle". In: *Geology* 44.9, pp. 751–754.

Azzam, A. A. A., Tennyson, J., Yurchenko, S. N., and Naumenko, O. V. (2016). "ExoMol molecular line lists - XVI. The rotation-vibration spectrum of hot H2S". In: *Mon. Not. R. Astron. Soc* 460.4, pp. 4063–4074.

Barklem, P. and Collet, R. (2016). "Partition functions and equilibrium constants for diatomic molecules and atoms of astrophysical interest". In: *Astronomy & Astrophysics* 588, A96.

Barnes, R. et al. (2016). "The Habitability of Proxima Centauri b I: Evolutionary Scenarios". In: *arXiv e-prints*, arXiv:1608.06919, arXiv:1608.06919.

Barr, A. C. (2016). "On the origin of Earth's Moon". In: *Journal of Geophysical Research: Planets* 121.9, pp. 1573–1601.

Bierson, C. J. and Nimmo, F. (2016). "A Test for Io's Magma Ocean: Modeling Tidal Dissipation with a Partially Molten Mantle". In: *Journal of Geophysical Research: Planets* 121.11, pp. 2211–2224.

Brain, D. A., Bagenal, F., Ma, Y. .-., Nilsson, H., and Stenberg Wieser, G. (2016). "Atmospheric escape from unmagnetized bodies". In: *Journal of Geophysical Research (Planets)* 121.12, pp. 2364–2385.

Cronin, T. W. and Jansen, M. F. (2016). "Analytic radiative-advective equilibrium as a model for high-latitude climate". In: *Geophys. Res. Lett.* 43.1, pp. 449–457.

Ćuk, M., Hamilton, D. P., Lock, S. J., and Stewart, S. T. (2016). "Tidal evolution of the Moon from a high-obliquity, high-angular-momentum Earth". In: *Nature* 539.7629, pp. 402–406.

Demory, B.-O. et al. (2016). "A map of the large day-night temperature gradient of a super-Earth exoplanet". In: *Nature* 532.7598, pp. 207–209.

Ding, F. and Pierrehumbert, R. T. (2016). "CONVECTION IN CONDENSIBLE-RICH ATMOSPHERES". In: *The Astrophysical Journal* 822.1, p. 24.

Drummond, B. et al. (2016). "The effects of consistent chemical kinetics calculations on the pressure-temperature profiles and emission spectra of hot Jupiters". In: *Astronomy & Astrophysics* 594, A69.

Fischer, D. A. et al. (2016). "State of the Field: Extreme Precision Radial Velocities". In: *Publications of the Astronomical Society of the Pacific* 128.964, p. 066001.

Fortney, J. J. et al. (2016). "The Need for Laboratory Work to Aid in The Understanding of Exoplanetary Atmospheres". In: *arXiv White Paper*.

France, K. et al. (2016). "THE MUSCLES TREASURY SURVEY. I. MOTIVATION AND OVERVIEW". In: *The Astrophysical Journal* 820.2, p. 89.

Gaetani, G. A. (2016). "The behavior of Fe3+/∑Fe during partial melting of spinel lherzolite". In: *Geochim. Cosmochim. Acta* 185, pp. 64–77.

Ginzburg, S., Schlichting, H. E., and Sari, R. (2016). "SUPER-EARTH ATMOSPHERES: SELF-CONSISTENT GAS ACCRETION AND RETENTION". In: *The Astrophysical Journal* 825.1, p. 29.

Haynes, W. M. (2016). *CRC Handbook of Chemistry and Physics*. Andover, England, UK: Taylor & Francis.

Kite, E. S., Jr., B. F., Schaefer, L., and Gaidos, E. (2016). "ATMOSPHERE-INTERIOR EXCHANGE ON HOT, ROCKY EXOPLANETS". In: *The Astrophysical Journal* 828.2, p. 80.

Madhusudhan, N., Agundez, M., Moses, J. I., and Hu, Y. (2016). "Exoplanetary Atmospheres-Chemistry, Formation Conditions, and Habitability". In: *Space Science Reviews* 205.1-4, pp. 285–348.

Mazeh, T., Holczer, T., and Faigler, S. (2016). "Dearth of short-period Neptunian exoplanets: A desert in period-mass and period-radius planes". In: *A&A* 589, A75.

Namur, O., Charlier, B., Holtz, F., Cartier, C., and McCammon, C. (2016). "Sulfur solubility in reduced mafic silicate melts: Implications for the speciation and distribution of sulfur on Mercury". In: *Earth and Planetary Science Letters* 448, pp. 102–114.

Sabadini, R., Vermeersen, B., and Cambiotti, G. (2016). *Global dynamics of the Earth*. Springer.

Schaefer, L., Wordsworth, R. D., Berta-Thompson, Z., and Sasselov, D. (2016). "PREDICTIONS OF THE ATMOSPHERIC COMPOSITION OF GJ 1132b". In: *The Astrophysical Journal* 829.2, p. 63.

Underwood, D. S. et al. (2016). "ExoMol molecular line lists - XIV. The rotation-vibration spectrum of hot SO2". In: *Mon. Not. R. Astron. Soc* 459.4, pp. 3890–3899.

Vazan, A., Helled, R., Podolak, M., and Kovetz, A. (2016). "THE EVOLUTION AND INTERNAL STRUCTURE OF JUPITER AND SATURN WITH COMPOSITIONAL GRADIENTS". In: *Astrophys. J.* 829.2, p. 118.

Venot, O., Rocchetto, M., Carl, S., Hashim, A. R., and Decin, L. (2016). "INFLUENCE OF STELLAR FLARES ON THE CHEMICAL COMPOSITION OF EXOPLANETS AND SPECTRA". In: *The Astrophysical Journal* 830.2, p. 77.

Way, M. J. et al. (2016). "Was Venus the first habitable world of our solar system?" In: *Geophysical Research Letters* 43.16, pp. 8376–8383.

Amundsen, D. S., Tremblin, P., Manners, J., Baraffe, I., and Mayne, N. J. (2017). "Treatment of overlapping gaseous absorption with the correlated-k method in hot Jupiter and brown dwarf atmosphere models". In: *Astron. Astrophys.* 598, A97.

Bezanson, J., Edelman, A., Karpinski, S., and Shah, V. B. (2017). "Julia: A fresh approach to numerical computing". In: *SIAM Review* 59.1, pp. 65–98.

Bolmont, E. et al. (2017). "Water loss from terrestrial planets orbiting ultracool dwarfs: implications for the planets of TRAPPIST-1". In: *Mon. Not. R. Astron. Soc* 464.3, pp. 3728–3741.

Burgasser, A. J. and Mamajek, E. E. (2017). "On the Age of the TRAPPIST-1 System". In: *Astrophysical Journal* 845.2, 110, p. 110.

Catling, D. C. and Kasting, J. F. (2017). *Atmospheric Evolution on Inhabited and Lifeless Worlds*. Cambridge University Press.

Dauphas, N. (2017). "The isotopic nature of the Earth's accreting material through time". In: *Nature* 541, pp. 521–524.

Deamer, D. and Damer, B. (2017). "Can Life Begin on Enceladus? A Perspective from Hydrothermal Chemistry". In: *Astrobiology* 17.9, pp. 834–839.

Dudhia, A. (2017). "The Reference Forward Model (RFM)". In: *J. Quant. Spectrosc. Radiat. Transfer* 186, pp. 243–253.

Forgan, D., Purkamo, L., and Watkins, A. (2017). "Cooking up exoplanet collaboration". In: *Astron. Geophys.* 58.6, pp. 6.22–6.23.

Fulton, B. J. et al. (2017). "The California-Kepler Survey. III. A Gap in the Radius Distribution of Small Planets∗". In: *Astronomical Journal* 154.3, p. 109.

Gao, P., Marley, M. S., Zahnle, K., Robinson, T. D., and Lewis, N. K. (2017). "Sulfur Hazes in Giant Exoplanet Atmospheres: Impacts on Reflected Light Spectra". In: *Astronomical Journal* 153.3, p. 139.

Gillon, M. et al. (2017). "Seven temperate terrestrial planets around the nearby ultracool dwarf star TRAPPIST-1". In: *Nature* 542.7642, pp. 456–460.

Goyal, J. et al. (2017). "A library of ATMO forward model transmission spectra for hot Jupiter exoplanets". In: *Mon. Not. R. Astron. Soc* 474.4. Publisher: Oxford University Press (OUP), pp. 5158–5185.

Hier-Majumder, S. and Hirschmann, M. M. (2017). "The origin of volatiles in the Earth's mantle". In: *Geochemistry, Geophysics, Geosystems* 18.8, pp. 3078–3092.

Kislyakova, K. G. et al. (2017). "Magma oceans and enhanced volcanism on TRAPPIST-1 planets due to induction heating". In: *Nature Astronomy* 1.12, pp. 878–885.

Leconte, J., Selsis, F., Hersant, F., and Guillot, T. (2017). "Condensation-inhibited convection in hydrogen-rich atmospheres - Stability against double-diffusive processes and thermal profiles for Jupiter, Saturn, Uranus, and Neptune". In: *Astron. Astrophys.* 598, A98.

Lehmer, O. R. and Catling, D. C. (2017). "Rocky Worlds Limited to 1.8 Earth Radii by Atmospheric Escape during a Star's Extreme UV Saturation". In: *The Astrophysical Journal* 845.2, p. 130.

Lopez, E. D. (2017). "Born dry in the photoevaporation desert: Kepler's ultra-short-period planets formed water-poor". In: *Mon. Not. R. Astron. Soc* 472.1, pp. 245–253.

Malik, M. et al. (2017). "HELIOS: AN OPEN-SOURCE, GPU-ACCELERATED RADIATIVE TRANSFER CODE FOR SELF-CONSISTENT EXOPLANETARY ATMOSPHERES". In: *Astronomical Journal* 153.2, p. 56.

Manners, J. et al. (2017). *SOCRATES Technical Guide: Suite Of Community RAdiative Transfer Codes Based on Edwards and Slingo*. Tech. rep. Met Office, Exeter, UK.

Martinez, A. O. et al. (2017). "Stellar and Planetary Parameters for K2's Late-type Dwarf Systems from C1 to C5". In: *Astrophys. J.* 837.1, p. 72.

Millholland, S., Wang, S., and Laughlin, G. (2017). "Kepler Multi-planet Systems Exhibit Unexpected Intra-system Uniformity in Mass and Radius". In: *Astrophys. J. Lett.* 849.2, p. L33.

Norris, C. A. and Wood, B. J. (2017). "Earth's volatile contents established by melting and vaporization". In: *Nature* 549, pp. 507–510.

Owen, J. E. and Wu, Y. (2017). "The Evaporation Valley in the Kepler Planets". In: *The Astrophysical Journal* 847.1, p. 29.

Peslier, A. H., Schonbachler, M., Busemann, H., and Karato, S.-I. (2017). "Water in the Earth's Interior: Distribution and Origin". In: *Space Sci. Rev.* 212.1, pp. 743–810.

Ramirez, R. M. and Kaltenegger, L. (2017). "A Volcanic Hydrogen Habitable Zone". In: *The Astrophysical Journal Letters* 837.1, p. L4.

Rollinson, H., Adetunji, J., Lenaz, D., and Szilas, K. (2017). "Archaean chromitites show constant Fe3+/Fe in Earth's asthenospheric mantle since 3.8 Ga". In: *Lithos* 282, pp. 316–325.

Ruedas, T. (2017). "Radioactive heat production of six geologically important nuclides". In: *Geochemistry, Geophysics, Geosystems* 18.9, pp. 3530–3541.

Salvador, A., Massol, H., Davaille, A., Marcq, E., Sarda, P., and Chassefière, E. (2017). "The relative influence of H_2O and CO_2 on the primitive surface conditions and evolution of rocky planets". In: *Journal of Geophysical Research (Planets)* 122.7, pp. 1458–1486.

Schaefer, L. and Fegley, B. (2017). "Redox States of Initial Atmospheres Outgassed on Rocky Planets and Planetesimals". In: *The Astrophysical Journal* 843.2, p. 120.

Sharp, Z. D. (2017). "Nebular ingassing as a source of volatiles to the Terrestrial planets". In: *Chemical Geology* 448, pp. 137–150.

Shestakov, A. V., Stepanov, R. A., and Frick, P. G. (2017). "On Cascade Energy Transfer in Convective Turbulence". In: *J. Appl. Mech. Tech. Phys.* 58.7, pp. 1171–1180.

Stamnes, K., Thomas, G. E., and Stamnes, J. J. (2017). *Radiative Transfer in the Atmosphere and Ocean*. Cambridge University Press.

Way, M. J. et al. (2017). "Resolving Orbital and Climate Keys of Earth and Extraterrestrial Environments with Dynamics (ROCKE-3D) 1.0: A General Circulation Model for Simulating the Climates of Rocky Planets". In: *Astrophys. J. Suppl. Ser.* 231.1, p. 12.

Western, C. M. (2017). "PGOPHER: A program for simulating rotational, vibrational and electronic spectra". In: *Journal of Quantitative Spectroscopy and Radiative Transfer* 186. Satellite Remote Sensing and Spectroscopy: Joint ACE-Odin Meeting, October 2015, pp. 221–242.

Wheatley, P. J., Louden, T., Bourrier, V., Ehrenreich, D., and Gillon, M. (2017). "Strong XUV irradiation of the Earth-sized exoplanets orbiting the ultracool dwarf TRAPPIST-1". In: *Mon. Not. R. Astron. Soc* 465.1, pp. L74–L78.

Wolf, E. T. (2017). "Assessing the Habitability of the TRAPPIST-1 System Using a 3D Climate Model". In: *Astrophys. J. Lett.* 839.1, p. L1.

Young, R. M. B. and Read, P. L. (2017). "Forward and inverse kinetic energy cascades in Jupiter's turbulent weather layer". In: *Nat. Phys.* 13, pp. 1135–1140.

Yurchenko, Amundsen, Tennyson, and Waldmann (2017). "A hybrid line list for CH4 and hot methane continuum". In: *Astronomy & Astrophysics* 605, A95.

Abbot, D. S. et al. (2018). "Decrease in Hysteresis of Planetary Climate for Planets with Long Solar Days". In: *The Astrophysical Journal* 854.1, p. 3.

Barr, A. C., Dobos, V., and Kiss, L. L. (2018). "Interior Structures and Tidal Heating in the TRAPPIST-1 Planets". In: *Astronomy & Astrophysics* 613, A37.

Barragan, O. et al. (2018). "K2-141 b - A 5-ME super-Earth transiting a K7 V star every 6.7 h". In: *Astron. Astrophys.* 612, A95.

Betts, H. C., Puttick, M. N., Clark, J. W., Williams, T. A., Donoghue, P. C. J., and Pisani, D. (2018). "Integrated genomic and fossil evidence illuminates life's early evolution and eukaryote origin". In: *Nat. Ecol. Evol.* 2, pp. 1556–1562.

Birkby, J. L. (2018). "Spectroscopic Direct Detection of Exoplanets". In: *Handbook of Exoplanets*. Cham, Switzerland: Springer International Publishing, pp. 1–24.

Bower, D. J., Sanan, P., and Wolf, A. S. (2018). "Numerical solution of a non-linear conservation law applicable to the interior dynamics of partially molten planets". In: *Physics of the Earth and Planetary Interiors* 274, pp. 49–62.

Bradley, P. A., Loomis, E. N., Merritt, E. C., Guzik, J. A., Denne, P. H., and Clark, T. T. (2018). "Experimental validation of thermodynamic mixture rules at extreme pressures and densities". In: *Physics of Plasmas* 25.1, p. 012710.

Chubb, K. L. et al. (2018). "Marvel analysis of the measured high-resolution rovibrational spectra of H232S". In: *Journal of Quantitative Spectroscopy and Radiative Transfer* 218, pp. 178–186.

Fulton, B. J. and Petigura, E. A. (2018). "The California- *Kepler* Survey. VII. Precise Planet Radii Leveraging *Gaia* DR2 Reveal the Stellar Mass Dependence of the Planet Radius Gap". In: *Astronomical Journal* 156.6, p. 264.

Ginzburg, S., Schlichting, H. E., and Sari, R. (2018). "Core-powered mass-loss and the radius distribution of small exoplanets". In: *Mon. Not. R. Astron. Soc* 476.1, pp. 759–765.

Grimm, Simon L. et al. (2018). "The nature of the TRAPPIST-1 exoplanets". In: *Astronomy & Astrophysics* 613, A68.

Gunell, H. et al. (2018). "Why an intrinsic magnetic field does not protect a planet against atmospheric escape". In: *Astronomy & Astrophysics* 614, L3, p. L3.

Krissansen-Totton, J., Olson, S., and Catling, D. C. (2018). "Disequilibrium biosignatures over Earth history and implications for detecting exoplanet life". In: *Science Advances* 4.1, eaao5747.

Kubyshkina, D. et al. (2018). "Overcoming the Limitations of the Energy-limited Approximation for Planet Atmospheric Escape". In: *Astrophys. J. Lett.* 866.2, p. L18.

Lammer, H. and Blanc, M. (2018). "From Disks to Planets: The Making of Planets and Their Early Atmospheres. An Introduction". In: *Space Science Reviews* 214.2, p. 60.

Li, C., Ingersoll, A. P., and Oyafuso, F. (2018). "Moist Adiabats with Multiple Condensing Species: A New Theory with Application to Giant-Planet Atmospheres". In: *Journal of the Atmospheric Sciences* 75.4, pp. 1063–1072.

Lincowski, A. P. et al. (2018). "Evolved Climates and Observational Discriminants for the TRAPPIST-1 Planetary System". In: *The Astrophysical Journal* 867.1, p. 76.

Lock, S. J. et al. (2018). "The Origin of the Moon Within a Terrestrial Synestia". In: *J. Geophys. Res. Planets* 123.4, pp. 910–951.

Loyd, R. O. P. et al. (2018). "The MUSCLES Treasury Survey. V. FUV Flares on Active and Inactive M Dwarfs". In: *The Astrophysical Journal* 867.1, p. 71.

Madhusudhan, N. (2018). "Atmospheric Retrieval of Exoplanets". In: *Handbook of Exoplanets*. Springer International Publishing, pp. 2153–2182.

Meadows, V. S. et al. (2018). "The Habitability of Proxima Centauri b: Environmental States and Observational Discriminants". In: *Astrobiology* 18.2. PMID: 29431479, pp. 133–189.

Nakajima, M. and Stevenson, D. J. (2018). "Inefficient volatile loss from the Moon-forming disk: Reconciling the giant impact hypothesis and a wet Moon". In: *Earth Planet. Sci. Lett.* 487, pp. 117–126.

Nesvorny, D. (2018). "Dynamical Evolution of the Early Solar System". In: *Annu. Rev. Astron. Astrophys.* Volume 56, 2018, pp. 137–174.

Nicklas, R. W., Puchtel, I. S., and Ash, R. D. (2018). "Redox state of the Archean mantle: Evidence from V partitioning in 3.5-2.4Ga komatiites". In: *Geochimica et Cosmochimica Acta* 222, pp. 447–466.

Odert, P. et al. (2018). "Escape and fractionation of volatiles and noble gases from Mars-sized planetary embryos and growing protoplanets". In: *Icarus* 307, pp. 327–346.

Padovan, S. et al. (2018). "Matrix-propagator approach to compute fluid Love numbers and applicability to extrasolar planets". In: *Astron. Astrophys.* 620, A178.

Pearce, B. K. D., Tupper, A. S., Pudritz, R. E., and Higgs, P. G. (2018). "Constraining the Time Interval for the Origin of Life on Earth". In: *Astrobiology* 18.3, pp. 343–364.

Perryman, M. (2018). *The Exoplanet Handbook*. 2nd ed. Cambridge: Cambridge University Press.

Polyansky, O. L., Kyuberis, A. A., Zobov, N. F., Tennyson, J., Yurchenko, S. N., and Lodi, L. (2018). "ExoMol molecular line lists XXX: a complete high-accuracy line list for water". In: *Mon. Not. R. Astron. Soc* 480.2, pp. 2597–2608.

Postberg, F. et al. (2018). "Macromolecular organic compounds from the depths of Enceladus". In: *Nature* 558, pp. 564–568.

Rackham, B. V., Apai, D., and Giampapa, M. S. (2018). "The Transit Light Source Effect: False Spectral Features and Incorrect Densities for M-dwarf Transiting Planets". In: *Astrophys. J.* 853.2, p. 122.

Schaefer, L. and Elkins-Tanton, L. T. (2018). "Magma oceans as a critical stage in the tectonic development of rocky planets". In: *Philosophical Transactions of the Royal Society A: Mathematical, Physical and Engineering Sciences* 376.2132, p. 20180109.

Schlichting, H. E. and Mukhopadhyay, S. (2018). "Atmosphere Impact Losses". In: *Space Science Reviews* 214.1, 34, p. 34.

Steffen, W. et al. (2018). "Trajectories of the Earth System in the Anthropocene". In: *Proceedings of the National Academy of Sciences* 115.33, pp. 8252–8259.

Stock, J. W., Kitzmann, D., Patzer, A. B. C., and Sedlmayr, E. (2018). "FastChem: A computer program for efficient complex chemical equilibrium calculations in the neutral/ionized gas phase with applications to stellar and planetary atmospheres". In: *Mon. Not. R. Astron. Soc.*

Vazan, A., Ormel, C. W., Noack, L., and Dominik, C. (2018). "Contribution of the Core to the Thermal Evolution of Sub-Neptunes". In: *Astrophysical Journal* 869.2, 163, p. 163.

Wang, H. S., Lineweaver, C. H., and Ireland, T. R. (2018). "The elemental abundances (with uncertainties) of the most Earth-like planet". In: *Icarus* 299, pp. 460–474.

Western, C. M., Carter-Blatchford, L., Crozet, P., Ross, A. J., Morville, J., and Tokaryk, D. W. (2018). "The spectrum of N2 from 4,500 to 15,700cm1 revisited with pgopher". In: *Journal of Quantitative Spectroscopy and Radiative Transfer* 219, pp. 127–141.

Woitke, P. et al. (2018). "Equilibrium chemistry down to 100 K: Impact of silicates and phyllosilicates on the carbon to oxygen ratio". In: *Astronomy & Astrophysics* 614, A1.

Wolf, A. S. and Bower, D. J. (2018). "An equation of state for high pressure-temperature liquids (RTpress) with application to MgSiO3 melt". In: *Physics of the Earth and Planetary Interiors* 278, pp. 59–74.

Wordsworth, R. D., Schaefer, L. K., and Fischer, R. A. (2018). "Redox Evolution via Gravitational Differentiation on Low-mass Planets: Implications for Abiotic Oxygen, Water Loss, and Habitability". In: *Astronomical Journal* 155.5, p. 195.

Zhang, X. and Showman, A. P. (2018a). "Global-mean Vertical Tracer Mixing in Planetary Atmospheres. I. Theory and Fast-rotating Planets". In: *Astrophys. J.* 866.1, p. 1.

Zhang, X. and Showman, A. P. (2018b). "Global-mean Vertical Tracer Mixing in Planetary Atmospheres. II. Tidally Locked Planets". In: *Astrophys. J.* 866.1, p. 2.

Armstrong, K., Frost, D. J., McCammon, C. A., Rubie, D. C., and Ballaran, T. B. (2019). "Deep magma ocean formation set the oxidation state of Earth's mantle". In: *Science* 365.6456, pp. 903–906.

Bitsch, B., Raymond, S. N., and Izidoro, A. (2019). "Rocky super-Earths or waterworlds: the interplay of planet migration, pebble accretion, and disc evolution". In: *Astron. Astrophys.* 624, A109.

Bonati, I., Lichtenberg, T., Bower, D. J., Timpe, M. L., and Quanz, S. P. (2019). "Direct imaging of molten protoplanets in nearby young stellar associations". In: *Astronomy & Astrophysics* 621, A125, A125.

Bower, D. J., Kitzmann, D., Wolf, A. S., Sanan, P., Dorn, C., and Oza, A. V. (2019). "Linking the evolution of terrestrial interiors and an early outgassed atmosphere to astrophysical observations". In: *Astronomy & Astrophysics* 631, A103.

Cartier, C. and Wood, B. J. (2019). "The Role of Reducing Conditions in Building Mercury". In: *Elements* 15.1, pp. 39–45.

Chabrier, G., Mazevet, S., and Soubiran, F. (2019). "A New Equation of State for Dense Hydrogen-Helium Mixtures". In: *The Astrophysical Journal* 872.1, p. 51.

Cloutier, R. et al. (2019). "Characterization of the L 98-59 multi-planetary system with HARPS. Mass characterization of a hot super-Earth, a sub-Neptune, and a mass upper limit on the third planet". In: *Astronomy & Astrophysics* 629, A111, A111.

Coles, P. A., Yurchenko, S. N., and Tennyson, J. (2019). "ExoMol molecular line lists - XXXV. A rotation-vibration line list for hot ammonia". In: *Mon. Not. R. Astron. Soc* 490.4, pp. 4638–4647.

Doyle, A. E., Klein, B., Zuckerman, B., Schlichting, H. E., and Young, E. D. (2019a). "Exoplanetary oxygen fugacities from polluted white dwarf stars". In: *Proceedings of the International Astronomical Union* 15.S357, pp. 28–32.

Doyle, A. E., Young, E. D., Klein, B., Zuckerman, B., and Schlichting, H. E. (2019b). "Oxygen fugacities of extrasolar rocks: Evidence for an Earth-like geochemistry of exoplanets". In: *Science* 366.6463, pp. 356–359.

Froning, C. S. et al. (2019). "A Hot Ultraviolet Flare on the M Dwarf Star GJ 674". In: *Astrophysical Journal Letters* 871.2, L26, p. L26.

Hargreaves, R. J. et al. (2019). "Spectroscopic line parameters of NO, NO2, and N2O for the HITEMP database". In: *Journal of Quantitative Spectroscopy and Radiative Transfer* 232, pp. 35–53.

Harman, C. et al. (2019). "A Balancing Act: Biosignature and Anti-Biosignature Studies in the Next Decade and Beyond". In: *Bulletin of the American Astronomical Society* 51. ADS Bibcode: 2019BAAS...51c.414H, p. 414.

Hay, H. C. F. C. and Matsuyama, I. (2019). "Tides Between the TRAPPIST-1 Planets". In: *Astrophysical Journal* 875.1, 22, p. 22.

Helling, C. (2019). "Exoplanet Clouds". In: *Annu. Rev. Earth Planet. Sci.* Volume 47, 2019, pp. 583–606.

Kahana, A., Schmitt-Kopplin, P., and Lancet, D. (2019). "Enceladus: First Observed Primordial Soup Could Arbitrate Origin-of-Life Debate". In: *Astrobiology* 19.10, pp. 1263–1278.

Karman, T. et al. (2019). "Update of the HITRAN collision-induced absorption section". In: *Icarus* 328, pp. 160–175.

Katyal, N. et al. (2019). "Evolution and Spectral Response of a Steam Atmosphere for Early Earth with a Coupled Climate-Interior Model". In: *Astrophysical Journal* 875.1, 31, p. 31.

Komacek, T. D. and Abbot, D. S. (2019). "The Atmospheric Circulation and Climate of Terrestrial Planets Orbiting Sun-like and M Dwarf Stars over a Broad Range of Planetary Parameters". In: *Astrophys. J.* 871.2, p. 245.

Komacek, T. D., Jansen, M. F., Wolf, E. T., and Abbot, D. S. (2019a). "Scaling Relations for Terrestrial Exoplanet Atmospheres from Baroclinic Criticality". In: *Astrophys. J.* 883.1, p. 46.

Komacek, T. D., Showman, A. P., and Parmentier, V. (2019b). "Vertical Tracer Mixing in Hot Jupiter Atmospheres". In: *Astrophys. J.* 881.2, p. 152.

Kontogeorgis, G. M., Privat, R., and Jaubert, J.-N. (2019). "Taking Another Look at the van der Waals Equation of State–Almost 150 Years Later". In: *J. Chem. Eng. Data* 64.11, pp. 4619–4637.

Kostov, V. B. et al. (2019). "The L 98-59 System: Three Transiting, Terrestrial-size Planets Orbiting a Nearby M Dwarf". In: *Astronomical Journal* 158.1, 32, p. 32.

Kreidberg, L. et al. (2019). "Absence of a thick atmosphere on the terrestrial exoplanet LHS 3844b". In: *Nature* 573.7772, pp. 87–90.

Lichtenberg, T., Keller, T., Katz, R. F., Golabek, G. J., and Gerya, T. V. (2019a). "Magma ascent in planetesimals: Control by grain size". In: *Earth Planet. Sci. Lett.* 507, pp. 154–165.

Lichtenberg, T. et al. (2019b). "A water budget dichotomy of rocky protoplanets from 26Al-heating". In: *Nat. Astron.* 3, pp. 307–313.

Ligrone, R. (2019). "The Great Oxygenation Event". In: *Biological Innovations that Built the World*. Cham, Switzerland: Springer, pp. 129–154.

Line, M. et al. (2019). "The Importance of Thermal Emission Spectroscopy for Understanding Terrestrial Exoplanets". In: *Bulletin of the American Astronomical Society* 51.3.

Madhusudhan, N. (2019). "Exoplanetary Atmospheres: Key Insights, Challenges, and Prospects". In: *Annu. Rev. Astron. Astrophys.* 57.1. Publisher: Annual Reviews, pp. 617–663.

Mai, C. and Line, M. R. (2019). "Exploring Exoplanet Cloud Assumptions in JWST Transmission Spectra". In: *Astrophys. J.* 883.2, p. 144.

Nikolaou, A., Katyal, N., Tosi, N., Godolt, M., Grenfell, J. L., and Rauer, H. (2019). "What Factors Affect the Duration and Outgassing of the Terrestrial Magma Ocean?" In: *The Astrophysical Journal* 875.1, p. 11.

Owen, J. E. (2019). "Atmospheric Escape and the Evolution of Close-In Exoplanets". In: *Annual Review of Earth and Planetary Sciences* 47.Volume 47, 2019, pp. 67–90.

Putirka, K. D. and Rarick, J. C. (2019). "The composition and mineralogy of rocky exoplanets: A survey of >4000 stars from the Hypatia Catalog". In: *American Mineralogist* 104.6, pp. 817–829.

Qaddah, B., Monteux, J., Clesi, V., Bouhifd, M. A., and Le Bars, M. (2019). "Dynamics and stability of an iron drop falling in a magma ocean". In: *Phys. Earth Planet. Inter.* 289, pp. 75–89.

Rackham, B. V., Apai, D., and Giampapa, M. S. (2019). "The Transit Light Source Effect. II. The Impact of Stellar Heterogeneity on Transmission Spectra of Planets Orbiting Broadly Sun-like Stars". In: *Astronomical Journal* 157.3. Publisher: American Astronomical Society, p. 96.

Roueff, Abgrall, Czachorowski, Pachucki, Puchalski, and Komasa (2019). "The full infrared spectrum of molecular hydrogen". In: *Astronomy & Astrophysics* 630, A58.

Thiemens, M. M., Sprung, P., Fonseca, R. O. C., Leitzke, F. P., and Munker, C. (2019). "Early Moon formation inferred from hafnium-tungsten systematics". In: *Nat. Geosci.* 12, pp. 696–700.

Tremblin, P. et al. (2019). "Thermo-compositional Diabatic Convection in the Atmospheres of Brown Dwarfs and in Earth's Atmosphere and Oceans". In: *The Astrophysical Journal* 876.2. Publisher: American Astronomical Society, p. 144.

Trønnes, R. G. et al. (2019). "Core formation, mantle differentiation and core-mantle interaction within Earth and the terrestrial planets". In: *Tectonophysics* 760, pp. 165–198.

Turbet, M., Ehrenreich, D., Lovis, C., Bolmont, E., and Fauchez, T. (2019). "The runaway greenhouse radius inflation effect. An observational diagnostic to probe water on Earth-sized planets and test the habitable zone concept". In: *Astronomy & Astrophysics* 628, A12, A12.

Unterborn, C. T. and Panero, W. R. (2019). "The Pressure and Temperature Limits of Likely Rocky Exoplanets". In: *Journal of Geophysical Research: Planets* 124.7, pp. 1704–1716.

West, R. G. et al. (2019). "NGTS-4b: A sub-Neptune transiting in the desert". In: *Mon. Not. R. Astron. Soc* 486.4, pp. 5094–5103.

Williams, C. D. and Mukhopadhyay, S. (2019). "Capture of nebular gases during Earth's accretion is preserved in deep-mantle neon". In: *Nature* 565.7737, pp. 78–81.

Zeng, L. et al. (2019). "Growth model interpretation of planet size distribution". In: *Proceedings of the National Academy of Science* 116.20, pp. 9723–9728.

Ali, S. Z. and Dey, S. (2020). "The law of the wall: A new perspective". In: *Physics of Fluids* 32.12, p. 121401.

Barnes, R. et al. (2020). "VPLanet: The Virtual Planet Simulator". In: *Publications of the Astronomical Society of the Pacific* 132.1008, 024502, p. 024502.

Barstow, J., Changeat, Q., Garland, R., Line, M., Rocchetto, M., and Waldmann, I. P. (2020). "A comparison of exoplanet spectroscopic retrieval tools". In: *Mon. Not. R. Astron. Soc* 493.4, pp. 4884–4909.

Barstow, J. K. (2020). "Unveiling cloudy exoplanets: the influence of cloud model choices on retrieval solutions". In: *Mon. Not. R. Astron. Soc* 497.4, pp. 4183–4195.

Barstow, J. K. and Heng, K. (2020). "Outstanding Challenges of Exoplanet Atmospheric Retrievals". In: *Space Science Reviews* 216.5. Publisher: Springer Science and Business Media LLC.

Bowman, D. M. et al. (2020). "Photometric detection of internal gravity waves in upper main-sequence stars - II. Combined TESS photometry and high-resolution spectroscopy". In: *Astron. Astrophys.* 640, A36.

Deng, J., Du, Z., Karki, B. B., Ghosh, D. B., and Lee, K. K. M. (2020). "A magma ocean origin to divergent redox evolutions of rocky planetary bodies and early atmospheres". In: *Nature Communications* 11.1, p. 2007.

Diaz, B. and Ramirez, J. E. (2020). "Adiabatic lapse rate of nonideal gases: The role of molecular interactions and vibrations". In: *Phys. Rev. E* 102.4, p. 042107.

Essack, Z., Seager, S., and Pajusalu, M. (2020). "Low-albedo Surfaces of Lava Worlds". In: *The Astrophysical Journal* 898.2, p. 160.

Fleming, D. P., Barnes, R., Luger, R., and VanderPlas, J. T. (2020). "On the XUV Luminosity Evolution of TRAPPIST-1". In: *The Astrophysical Journal* 891.2, p. 155.

Goyal, J. M. et al. (2020). "A library of self-consistent simulated exoplanet atmospheres". In: *Mon. Not. R. Astron. Soc* 498.4. Publisher: Oxford University Press (OUP), pp. 4680–4704.

Graham, R. J. and Pierrehumbert, R. (2020). "Thermodynamic and Energetic Limits on Continental Silicate Weathering Strongly Impact the Climate and Habitability of Wet, Rocky Worlds". In: *The Astrophysical Journal* 896.2, p. 115.

Gronoff, G. et al. (2020). "Atmospheric Escape Processes and Planetary Atmospheric Evolution". In: *Journal of Geophysical Research: Space Physics* 125.8.

Haldemann, J., Alibert, Y., Mordasini, C., and Benz, W. (2020). "AQUA: a collection of H2O equations of state for planetary models". In: *Astronomy & Astrophysics* 643, A105.

Hay, H. C. F. C., Trinh, A., and Matsuyama, I. (2020). "Powering the Galilean Satellites with Moon-Moon Tides". In: *Geophysical Research Letters* 47.15, e88317, e88317.

Johnstone, C. P. (2020). "Hydrodynamic Escape of Water Vapor Atmospheres near Very Active Stars". In: *Astrophysical Journal* 890.1, p. 79.

Kane, S. R., Roettenbacher, R. M., Unterborn, C. T., Foley, B. J., and Hill, M. L. (2020). "A Volatile-poor Formation of LHS 3844b Based on Its Lack of Significant Atmosphere". In: *The Planetary Science Journal* 1.2, 36, p. 36.

Katyal, N. et al. (2020). "Effect of mantle oxidation state and escape upon the evolution of Earth's magma ocean atmosphere". In: *Astronomy & Astrophysics* 643, A81.

Kegerreis, J. A., Eke, V. R., Catling, D. C., Massey, R. J., Teodoro, L. F. A., and Zahnle, K. J. (2020). "Atmospheric Erosion by Giant Impacts onto Terrestrial Planets: A Scaling Law for any Speed, Angle, Mass, and Density". In: *Astrophysical Journal* 901.2, L31, p. L31.

Kimura, T. and Ikoma, M. (2020). "Formation of aqua planets with water of nebular origin: effects of water enrichment on the structure and mass of captured atmospheres of terrestrial planets". In: *Mon. Not. R. Astron. Soc* 496.3, pp. 3755–3766.

Kite, E. S. and Barnett, M. N. (2020). "Exoplanet secondary atmosphere loss and revival". In: *Proceedings of the National Academy of Sciences* 117.31, pp. 18264–18271.

Kite, E. S., Fegley Jr., B., Schaefer, L., and Ford, E. B. (2020). "Atmosphere Origins for Exoplanet Sub-Neptunes". In: *The Astrophysical Journal* 891.2, p. 111.

Kubyshkina, D., Vidotto, A. A., Fossati, L., and Farrell, E. (2020). "Coupling thermal evolution of planets and hydrodynamic atmospheric escape in mesa". In: *Mon. Not. R. Astron. Soc* 499.1, pp. 77–88.

Lammer, H. et al. (2020). "Constraining the early evolution of Venus and Earth through atmospheric Ar, Ne isotope and bulk K/U ratios". In: *Icarus* 339, p. 113551.

Madhusudhan, N., Nixon, M. C., Welbanks, L., Piette, A. A. A., and Booth, R. A. (2020). "The Interior and Atmosphere of the Habitable-zone Exoplanet K2-18b". In: *Astrophysical Journal Letters* 891.1, L7, p. L7.

Mousis, O. et al. (2020). "Irradiated Ocean Planets Bridge Super-Earth and Sub-Neptune Populations". In: *The Astrophysical Journal Letters* 896.2, p. L22.

Ortenzi, G. et al. (2020). "Mantle redox state drives outgassing chemistry and atmospheric composition of rocky planets". In: *Scientific Reports* 10.1, p. 10907.

Piette, A. A. A., Madhusudhan, N., McKemmish, L. K., Gandhi, S., Masseron, T., and Welbanks, L. (2020). "Assessing spectra and thermal inversions due to TiO in hot Jupiter atmospheres". In: *Mon. Not. R. Astron. Soc* 496.3. Publisher: Oxford University Press (OUP), pp. 3870–3886.

Quick, L. C., Roberge, A., Mlinar, A. B., and Hedman, M. M. (2020). "Forecasting Rates of Volcanic Activity on Terrestrial Exoplanets and Implications for Cryovolcanic Activity on Extrasolar Ocean Worlds". In: *Publications of the Astronomical Society of the Pacific* 132.1014, 084402, p. 084402.

Sossi, P. A., Burnham, A. D., Badro, J., Lanzirotti, A., Newville, M., and O'Neill, H. S. (2020). "Redox state of Earth's magma ocean and its Venus-like early atmosphere". In: *Science Advances* 6.48, eabd1387.

Spaargaren, R. J., Ballmer, M. D., Bower, D. J., Dorn, C., and Tackley, P. J. (2020). "The influence of bulk composition on the long-term interior-atmosphere evolution of terrestrial exoplanets". In: *Astronomy & Astrophysics* 643, A44.

Turbet, M. et al. (2020). "Revised mass-radius relationships for water-rich rocky planets more irradiated than the runaway greenhouse limit". In: *Astronomy & Astrophysics* 638, A41.

Venturini, J., Guilera, O. M., Haldemann, J., Ronco, M. P., and Mordasini, C. (2020). "The nature of the radius valley. Hints from formation and evolution models". In: *Astronomy & Astrophysics* 643, L1, p. L1.

Wogan, N. F. and Catling, D. C. (2020). "When is Chemical Disequilibrium in Earth-like Planetary Atmospheres a Biosignature versus an Anti-biosignature? Disequilibria from Dead to Living Worlds". In: *The Astrophysical Journal* 892.2, p. 127.

Yurchenko, Mellor, Freedman, and Tennyson (2020). "ExoMol line lists - XXXIX. Ro-vibrational molecular line list for CO2". In: *Mon. Not. R. Astron. Soc* 496.4, pp. 5282–5291.

Zahnle, K. J., Lupu, R., Catling, D. C., and Wogan, N. (2020). "Creation and Evolution of Impact-generated Reduced Atmospheres of Early Earth". In: *The Planetary Science Journal* 1.1, p. 11.

Agol, E. et al. (2021). "Refining the Transit-timing and Photometric Analysis of TRAPPIST-1: Masses, Radii, Densities, Dynamics, and Ephemerides". In: *The Planetary Science Journal* 2.1, p. 1.

Barth, P., Carone, L., Barnes, R., Noack, L., Molliere, P., and Henning, T. (2021). "Magma Ocean Evolution of the TRAPPIST-1 Planets". In: *Astrobiology* 21.11, pp. 1325–1349.

Boukrouche, R., Lichtenberg, T., and Pierrehumbert, R. T. (2021). "Beyond Runaway: Initiation of the Post-runaway Greenhouse State on Rocky Exoplanets". In: *The Astrophysical Journal* 919.2, p. 130.

Charnay, B., Blain, D., Bzard, B., Leconte, J., Turbet, M., and Falco, A. (2021). "Formation and dynamics of water clouds on temperate sub-Neptunes: the example of K2-18b". In: *Astron. Astrophys.* 646, A171.

Datseris, G. and Stevens, B. (2021). "Earth's Albedo and Its Symmetry". In: *AGU Adv.* 2.3, e2021AV000440.

David, T. J. et al. (2021). "Evolution of the Exoplanet Size Distribution: Forming Large Super-Earths Over Billions of Years". In: *Astronomical Journal* 161.6, p. 265.

Demangeon, O. D. S. et al. (2021). "Warm terrestrial planet with half the mass of Venus transiting a nearby star". In: *Astronomy & Astrophysics* 653, A41, A41.

Dorn, C. and Lichtenberg, T. (2021). "Hidden Water in Magma Ocean Exoplanets". In: *Astrophysical Journal Letters* 922.1, L4, p. L4.

Fortney, J. J., Dawson, R. I., and Komacek, T. D. (2021). "Hot Jupiters: Origins, Structure, Atmospheres". In: *Journal of Geophysical Research: Planets* 126.3. Publisher: American Geophysical Union (AGU).

Gaillard, F. et al. (2021). "The Diverse Planetary Ingassing/Outgassing Paths Produced over Billions of Years of Magmatic Activity". In: *Space Science Reviews* 217.1, p. 22.

Graham, R. J., Lichtenberg, T., Boukrouche, R., and Pierrehumbert, R. T. (2021). "A Multispecies Pseudoadiabat for Simulating Condensable-rich Exoplanet Atmospheres". In: *The Planetary Science Journal* 2.5, p. 207.

Grimm, S. L. et al. (2021). "HELIOS-K 2.0 Opacity Calculator and Open-source Opacity Database for Exoplanetary Atmospheres". In: *The Astrophysical Journal Supplement Series* 253.1, 30, p. 30.

Hakim, K. et al. (2021). "Lithologic Controls on Silicate Weathering Regimes of Temperate Planets". In: *The Planetary Science Journal* 2.2, p. 49.

Hammond, M. and Lewis, N. T. (2021). "The rotational and divergent components of atmospheric circulation on tidally locked planets". In: *Proceedings of the National Academy of Sciences* 118.13. Publisher: Proceedings of the National Academy of Sciences.

Hedges, C. et al. (2021). "TOI-2076 and TOI-1807: Two Young, Comoving Planetary Systems within 50 pc Identified by TESS that are Ideal Candidates for Further Follow Up". In: *Astronomical Journal* 162.2, p. 54.

Hirose, K., Wood, B., and Vočadlo, L. (2021). "Light elements in the Earth's core". In: *Nature Reviews Earth & Environment* 2.9, pp. 645–658.

Hirschmann, M. M. (2021). "Iron-wustite revisited: A revised calibration accounting for variable stoichiometry and the effects of pressure". In: *Geochim. Cosmochim. Acta* 313, pp. 74–84.

Huang, D., Siebert, J., and Badro, J. (2021). "High pressure partitioning behavior of Mo and W and late sulfur delivery during Earth's core formation". In: *Geochim. Cosmochim. Acta* 310, pp. 19–31.

Ito, Y. and Ikoma, M. (2021). "Hydrodynamic escape of mineral atmosphere from hot rocky exoplanet. I. Model description". In: *Mon. Not. R. Astron. Soc* 502.1, pp. 750–771.

Johnstone, C. P., Bartel, M., and Gudel, M. (2021). "The active lives of stars: A complete description of the rotation and XUV evolution of F, G, K, and M dwarfs". In: *Astronomy & Astrophysics* 649, A96.

Kervazo, M., Tobie, G., Choblet, G., Dumoulin, C., and Behounkova, M. (2021). "Solid tides in Io's partially molten interior - Contribution of bulk dissipation". In: *Astronomy & Astrophysics* 650, A72.

Kite, E. S. and Schaefer, L. (2021). "Water on Hot Rocky Exoplanets". In: *The Astrophysical Journal Letters* 909.2, p. L22.

Krissansen-Totton, J., Fortney, J. J., and Nimmo, F. (2021). "Was Venus Ever Habitable? Constraints from a Coupled Interior-Atmosphere-Redox Evolution Model". In: *The Planetary Science Journal* 2.5, p. 216.

Lee, E. K. H. et al. (2021). "Simulating gas giant exoplanet atmospheres with Exo-FMS: comparing semigrey, picket fence, and correlated-k radiative-transfer schemes". In: *Mon. Not. R. Astron. Soc* 506.2, pp. 2695–2711.

Lichtenberg, T. (2021). "Redox Hysteresis of Super-Earth Exoplanets from Magma Ocean Circulation". In: *The Astrophysical Journal Letters* 914.1, p. L4.

Lichtenberg, T. et al. (2021). "Vertically Resolved Magma Ocean-Protoatmosphere Evolution: H_2 , H_2O, CO_2 , CH_4 , CO, O_2 , and N_2 as Primary Absorbers". In: *Journal of Geophysical Research: Planets* 126.2.

Lupu, R., Freedman, R., Gharib-Nezhad, E., Visscher, C., and Molliere, P. (2021). *Correlated k coefficients for H2-He atmospheres; 196 spectral windows and 1460 pressure-temperature points*. Zenodo.

Madhusudhan, N., Piette, A. A. A., and Constantinou, S. (2021). "Habitability and Biosignatures of Hycean Worlds". In: *Astrophys. J.* 918.1, p. 1.

Misener, W. and Schlichting, H. E. (2021). "To cool is to keep: Residual H/He atmospheres of super-Earths and sub-Neptunes". In: *Mon. Not. R. Astron. Soc* 503.4. arXiv:2103.09212 [astro-ph], pp. 5658–5674.

Moretti, R. and Neuville, D. R. (2021). *Magma Redox Geochemistry*. Chichester, England, UK: John Wiley & Sons, Ltd.

Poulton, S. W., Bekker, A., Cumming, V. M., Zerkle, A. L., Canfield, D. E., and Johnston, D. T. (2021). "A 200-million-year delay in permanent atmospheric oxygenation". In: *Nature* 592, pp. 232–236.

Renaud, J. P. et al. (2021). "Tidal Dissipation in Dual-body, Highly Eccentric, and Nonsynchronously Rotating Systems: Applications to Pluto–Charon and the Exoplanet TRAPPIST-1e". In: *The Planetary Science Journal* 2.1, p. 4.

Roth, A., Drummond, B., Hebrard, E., Tremblin, P., Goyal, J., and Mayne, N. (2021). "Pseudo-2D modelling of heat redistribution through H2 thermal dissociation/recombination: consequences for ultra-hot Jupiters". In: *Mon. Not. R. Astron. Soc* 505.3. Publisher: Oxford University Press (OUP), pp. 4515–4530.

Sandoval, A., Contardo, G., and David, T. J. (2021). "The Influence of Age on the Relative Frequency of Super-Earths and Sub-Neptunes". In: *Astrophys. J.* 911.2, p. 117.

Scheibe, L., Nettelmann, N., and Redmer, R. (2021). "Thermal evolution of Uranus and Neptune - II. Deep thermal boundary layer". In: *Astron. Astrophys.* 650, A200.

Tsai, S.-M. et al. (2021a). "A Comparative Study of Atmospheric Chemistry with VULCAN". In: *The Astrophysical Journal* 923.2, p. 264.

Tsai, S.-M. et al. (2021b). "Inferring Shallow Surfaces on Sub-Neptune Exoplanets with JWST". In: *Astrophys. J. Lett.* 922.2, p. L27.

Turbet, M., Bolmont, E., Chaverot, G., Ehrenreich, D., Leconte, J., and Marcq, E. (2021). "Day–night cloud asymmetry prevents early oceans on Venus but not on Earth". In: *Nature* 598.7880, pp. 276–280.

Wilson, D. J. et al. (2021). "The Mega-MUSCLES Spectral Energy Distribution of TRAPPIST-1". In: *The Astrophysical Journal* 911.1, p. 18.

Xu, S. and Bonsor, A. (2021). "Exogeology from Polluted White Dwarfs". In: *Elements* 17.4, pp. 241–244.

Yu, X., Moses, J. I., Fortney, J. J., and Zhang, X. (2021). "How to Identify Exoplanet Surfaces Using Atmospheric Trace Species in Hydrogen-dominated Atmospheres". In: *Astrophysical Journal* 914.1, 38, p. 38.

Anders, E. H. et al. (2022). "Schwarzschild and Ledoux are Equivalent on Evolutionary Timescales". In: *Astrophys. J. Lett.* 928.1, p. L10.

Ashton, G. et al. (2022). "Nested sampling for physical scientists". In: *Nat. Rev. Methods Primers* 2.39, pp. 1–22.

Bajgain, S. K., Ashley, A. W., Mookherjee, M., Ghosh, D. B., and Karki, B. B. (2022). "Insights into magma ocean dynamics from the transport properties of basaltic melt". In: *Nature Communications* 13.1, p. 7590.

Boers, N., Ghil, M., and Stocker, T. F. (2022). "Theoretical and paleoclimatic evidence for abrupt transitions in the Earth system". In: *Environmental Research Letters* 17.9, p. 093006.

Boukaré, C.-É., Cowan, N. B., and Badro, J. (2022). "Deep Two-phase, Hemispherical Magma Oceans on Lava Planets". In: *Astrophysical Journal* 936.2, 148, p. 148.

Boulliung, J. and Wood, B. J. (2022). "SO2 solubility and degassing behavior in silicate melts". In: *Geochimica et Cosmochimica Acta* 336, pp. 150–164.

Bower, D. J., Hakim, K., Sossi, P. A., and Sanan, P. (2022). "Retention of Water in Terrestrial Magma Oceans and Carbon-rich Early Atmospheres". In: *The Planetary Science Journal* 3.4, p. 93.

Crapitto, A. J., Campbell, A., Harris, A., and Goldman, A. D. (2022). "A consensus view of the proteome of the last universal common ancestor". In: *Ecology and Evolution* 12.6, e8930.

Damiano, M. et al. (2022). "A Transmission Spectrum of the Sub-Earth Planet L98-59 b in 1.1-1.7 μm". In: *Astronomical Journal* 164.5, 225, p. 225.

Dasgupta, R., Falksen, E., Pal, A., and Sun, C. (2022). "The fate of nitrogen during parent body partial melting and accretion of the inner solar system bodies at reducing conditions". In: *Geochim. Cosmochim. Acta* 336, pp. 291–307.

Denman, T. R., Leinhardt, Z. M., and Carter, P. J. (2022). "Atmosphere loss in oblique Super-Earth collisions". In: *Mon. Not. R. Astron. Soc* 513.2, pp. 1680–1700.

Gaillard, F. et al. (2022). "Redox controls during magma ocean degassing". In: *Earth and Planetary Science Letters* 577, p. 117255.

Gardner, D. J., Reynolds, D. R., Woodward, C. S., and Balos, C. J. (2022). "Enabling new flexibility in the SUNDIALS suite of nonlinear and differential/algebraic equation solvers". In: *ACM Transactions on Mathematical Software (TOMS)*.

Gillmann, C. et al. (2022). "The Long-Term Evolution of the Atmosphere of Venus: Processes and Feedback Mechanisms". In: *Space Science Reviews* 218.7, 56, p. 56.

Gordon, I. E. et al. (2022a). "The HITRAN2020 molecular spectroscopic database". In: *Journal of Quantitative Spectroscopy and Radiative Transfer* 277. Publisher: Elsevier BV, p. 107949.

Gordon, K. D. et al. (2022b). "The James Webb Space Telescope Absolute Flux Calibration. I. Program Design and Calibrator Stars". In: *Astronomical Journal* 163.6, p. 267.

Hirschmann, M. (2022). "Magma oceans, iron and chromium redox, and the origin of comparatively oxidized planetary mantles". In: *Geochimica et Cosmochimica Acta* 328, pp. 221–241.

Itcovitz, J. P. et al. (2022). "Reduced Atmospheres of Post-impact Worlds: The Early Earth". In: *The Planetary Science Journal* 3, p. 115.

Jorge, D. M., Kamp, I. E. E., Waters, L. B. F. M., Woitke, P., and Spaargaren, R. J. (2022). "Forming Planets Around Stars With Non-Solar Elemental Composition". In: *Astronomy & Astrophysics* 660, A85.

Koll, D. D. B. (2022). "A Scaling for Atmospheric Heat Redistribution on Tidally Locked Rocky Planets". In: *The Astrophysical Journal* 924.2, p. 134.

Kovacevic, T., Gonzalez-Cataldo, F., Stewart, S. T., and Militzer, B. (2022). "Miscibility of rock and ice in the interiors of water worlds". In: *Sci. Rep.* 12.13055, pp. 1–11.

Krissansen-Totton, J. and Fortney, J. J. (2022). "Predictions for Observable Atmospheres of Trappist-1 Planets from a Fully Coupled Atmosphere-Interior Evolution Model". In: *Astrophysical Journal* 933.1, 115, p. 115.

Lacedelli, G. et al. (2022). "Investigating the architecture and internal structure of the TOI-561 system planets with CHEOPS, HARPS-N, and TESS". In: *Mon. Not. R. Astron. Soc* 511.3, pp. 4551–4571.

Lichtenberg, T. and Clement, M. S. (2022). "Reduced Late Bombardment on Rocky Exoplanets around M Dwarfs". In: *The Astrophysical Journal Letters* 938.1, L3, p. L3.

Liggins, P., Jordan, S., Rimmer, P. B., and Shorttle, O. (2022). "Growth and Evolution of Secondary Volcanic Atmospheres: I. Identifying the Geological Character of Hot Rocky Planets". In: *Journal of Geophysical Research: Planets* 127.7.

Luque, R. and Palle, E. (2022). "Density, not radius, separates rocky and water-rich small planets orbiting M dwarf stars". In: *Science* 377.6611, pp. 1211–1214.

Matsuyama, I. N., Steinke, T., and Nimmo, F. (2022). "Tidal Heating in Io". In: *Elements* 18.6, pp. 374–378.

Miyawaki, O., Shaw, T. A., and Jansen, M. F. (2022). "Quantifying Energy Balance Regimes in the Modern Climate, Their Link to Lapse Rate Regimes, and Their Response to Warming". In: *J. Clim.* 35.3, pp. 1045–1061.

Miyazaki, Y. and Stevenson, D. J. (2022). "A Subsurface Magma Ocean on Io: Exploring the Steady State of Partially Molten Planetary Bodies". In: *The Planetary Science Journal* 3.11, p. 256.

Molliere, P. et al. (2022). "Interpreting the Atmospheric Composition of Exoplanets: Sensitivity to Planet Formation Assumptions". In: *The Astrophysical Journal* 934.1, p. 74.

Nakayama, A., Ikoma, M., and Terada, N. (2022). "Survival of Terrestrial N_2-O_2 Atmospheres in Violent XUV Environments through Efficient Atomic Line Radiative Cooling". In: *Astrophysical Journal* 937.2, 72, p. 72.

Peters, J. M., Mulholland, J. P., and Chavas, D. R. (2022). "Generalized Lapse Rate Formulas for Use in Entraining CAPE Calculations". In: *J. Atmos. Sci.* 79.3, pp. 815–836.

Quanz, S. P. et al. (2022). "Large Interferometer For Exoplanets (LIFE) - I. Improved exoplanet detection yield estimates for a large mid-infrared space-interferometer mission". In: *A&A* 664, A21.

Raymond, S. N. and Morbidelli, A. (2022). "Planet Formation: Key Mechanisms and Global Models". In: *Demographics of Exoplanetary Systems, Lecture Notes of the 3rd Advanced School on Exoplanetary Science*. Ed. by K. Biazzo, V. Bozza, L. Mancini, and A. Sozzetti. Vol. 466. Astrophysics and Space Science Library, pp. 3–82.

Riechers, K., Mitsui, T., Boers, N., and Ghil, M. (2022). "Orbital insolation variations, intrinsic climate variability, and Quaternary glaciations". In: *Climate of the Past* 18.4, pp. 863–893.

Schlichting, H. E. and Young, E. D. (2022). "Chemical Equilibrium between Cores, Mantles, and Atmospheres of Super-Earths and Sub-Neptunes and Implications for Their Compositions, Interiors, and Evolution". In: *The Planetary Science Journal* 3.5, 127, p. 127.

Sossi, P. A., Stotz, I. L., Jacobson, S. A., Morbidelli, A., and O'Neill, H. S. C. (2022). "Stochastic accretion of the Earth". In: *Nat. Astron.* 6, pp. 951–960.

Stock, J. W., Kitzmann, D., and Patzer, A. B. C. (2022). "FASTCHEM 2 : an improved computer program to determine the gas-phase chemical equilibrium composition for arbitrary element distributions". In: *Mon. Not. R. Astron. Soc* 517.3, pp. 4070–4080.

Tsai, S.-M., Lee, E. K. H., and Pierrehumbert, R. (2022). "A Mini-Chemical Scheme with Net Reactions for 3D GCMs I.: Thermochemical Kinetics". In: *Astronomy & Astrophysics* 664, A82.

Ware, A., Young, P., Truitt, A., and Spacek, A. (2022). "Continuous Habitable Zones: Using Bayesian Methods to Prioritize Characterization of Potentially Habitable Worlds". In: *The Astrophysical Journal* 929.2, p. 143.

Wordsworth, R. and Kreidberg, L. (2022). "Atmospheres of Rocky Exoplanets". In: *Annu. Rev. Astron. Astrophys.* 60, pp. 159–201.

Zhang, M. et al. (2022). "Detection of Ongoing Mass Loss from HD 63433c, a Young Mini-Neptune". In: *Astronomical Journal* 163.2, 68, p. 68.

Zhou, L., Ma, B., Wang, Y., and Zhu, Y. (2022). "Hubble WFC3 Spectroscopy of the Rocky Planet L 98-59 b: No Evidence for a Cloud-free Primordial Atmosphere". In: *Astronomical Journal* 164.5, 203, p. 203.

Zieba, S. et al. (2022). "K2 and Spitzer phase curves of the rocky ultra-short-period planet K2-141 b hint at a tenuous rock vapor atmosphere". In: *Astron. Astrophys.* 664, A79.

Acuna, L., Deleuil, M., and Mousis, O. (2023). "Interior-atmosphere modelling to assess the observability of rocky planets with JWST". In: Publisher: arXiv Version Number: 1.

Aigrain, S. and Foreman-Mackey, D. (2023). "Gaussian Process Regression for Astronomical Time Series". In: *Annu. Rev. Astron. Astrophys.* Volume 61, 2023, pp. 329–371.

Barclay, T. et al. (2023). "The transmission spectrum of the potentially rocky planet L 98-59 c". In: *arXiv e-prints*, arXiv:2301.10866, arXiv:2301.10866.

Behr, P. R. et al. (2023). "The MUSCLES Extension for Atmospheric Transmission Spectroscopy: UV and X-Ray Host-star Observations for JWST ERS & GTO Targets". In: *Astronomical Journal* 166.1, 35, p. 35.

Bergin, E. A. et al. (2023a). "Exoplanet Volatile Carbon Content as a Natural Pathway for Haze Formation". In: *Astrophys. J. Lett.* 949.1, p. L17.

— (2023b). "Exoplanet Volatile Carbon Content as a Natural Pathway for Haze Formation". In: *The Astrophysical Journal Letters* 949.1, p. L17.

Boley, K. M., Panero, W. R., Unterborn, C. T., Schulze, J. G., Martnez, R. R., and Wang, J. (2023). "Fizzy Super-Earths: Impacts of Magma Composition on the Bulk Density and Structure of Lava Worlds". In: *Astrophys. J.* 954.2, p. 202.

Bonsor, A., Lichtenberg, T., Drazkowska, J., and Buchan, A. M. (2023). "Rapid formation of exoplanetesimals revealed by white dwarfs". In: *Nat. Astron.* 7, pp. 39–48.

Diamond-Lowe, H. et al. (2023). *The Hot Rocks Survey: Testing 9 Irradiated Terrestrial Exoplanets for Atmospheres*. JWST Proposal. Cycle 2, ID. #3730.

Drążkowska, J. et al. (2023). "Planet Formation Theory in the Era of ALMA and Kepler: from Pebbles to Exoplanets". In: *Protostars and Planets VII*. Ed. by S. Inutsuka, Y. Aikawa, T. Muto, K. Tomida, and M. Tamura. Vol. 534. Astronomical Society of the Pacific Conference Series, p. 717.

Ehlers, K. and Moosmuller, H. (2023). "Small and large particle limits of the asymmetry parameter for homogeneous, spherical particles". In: *Aerosol Sci. Technol.*

Engle, S. G. and Guinan, E. F. (2023). "Living with a Red Dwarf: The Rotation-Age Relationships of M Dwarfs". In: *The Astrophysical Journal Letters* 954.2, p. L50.

Greene, T. P., Bell, T. J., Ducrot, E., Dyrek, A., Lagage, P.-O., and Fortney, J. J. (2023). "Thermal Emission from the Earth-sized Exoplanet TRAPPIST-1 b using JWST". In: *Nature*.

Guimond, C. M., Shorttle, O., Jordan, S., and Rudge, J. F. (2023a). "A mineralogical reason why all exoplanets cannot be equally oxidising". In: *Mon. Not. R. Astron. Soc.* arXiv:2308.09505 [astro-ph], stad2486.

Guimond, C. M., Shorttle, O., and Rudge, J. F. (2023b). "Mantle Mineralogy Limits to Rocky Planet Water Inventories". In: *Mon. Not. R. Astron. Soc* 521.2, pp. 2535–2552.

Halliday, A. N. and Canup, R. M. (2023). "The accretion of planet Earth". In: *Nature Reviews Earth & Environment* 4.1, pp. 19–35.

Heng, K. (2023). "The Transient Outgassed Atmosphere of 55 Cancri e". In: *Astrophysical Journal Letters* 956.1, L20, p. L20.

Ho, C. S. K. and Van Eylen, V. (2023). "A deep radius valley revealed by Kepler short cadence observations". In: *Mon. Not. R. Astron. Soc* 519.3, pp. 4056–4073.

Innes, H., Tsai, S.-M., and Pierrehumbert, R. T. (2023). "The Runaway Greenhouse Effect on Hycean Worlds". In: *Astrophysical Journal* 953.2, 168, p. 168.

Janssen, L. J. et al. (2023). "The sulfur species in hot rocky exoplanet atmospheres". In: *Astronomische Nachrichten* 344.10, e20230075, e20230075.

Joyce, M. and Tayar, J. (2023). "A Review of the Mixing Length Theory of Convection in 1D Stellar Modeling". In: *Galaxies* 11.3, p. 75.

Kislyakova, K. G. et al. (2023). "Induction heating of planetary interiors in white dwarf systems". In: *Astronomy & Astrophysics* 677, A109.

Korenaga, J. (2023). "Rapid solidification of Earth's magma ocean limits early lunar recession". In: *Icarus* 400, p. 115564.

Krijt, S. et al. (2023). "Chemical Habitability: Supply and Retention of Life's Essential Elements During Planet Formation". In: *Protostars and Planets VII*. Ed. by S. Inutsuka, Y. Aikawa, T. Muto, K. Tomida, and M. Tamura. Vol. 534. Astronomical Society of the Pacific Conference Series, p. 1031.

Krissansen-Totton, J. (2023). "Implications of Atmospheric Nondetections for Trappist-1 Inner Planets on Atmospheric Retention Prospects for Outer Planets". In: *Astrophysical Journal Letters* 951.2, L39, p. L39.

Lichtenberg, T., Schaefer, L. K., Nakajima, M., and Fischer, R. A. (2023). "Geophysical Evolution During Rocky Planet Formation". In: *Protostars and Planets VII*. Ed. by S. Inutsuka, Y. Aikawa,

T. Muto, K. Tomida, and M. Tamura. Vol. 534. Astronomical Society of the Pacific Conference Series, p. 907.

Madhusudhan, N., Moses, J. I., Rigby, F., and Barrier, E. (2023a). "Chemical conditions on Hycean worlds". In: *Faraday Discussions* 245, pp. 80–111.

Madhusudhan, N., Sarkar, S., Constantinou, S., Holmberg, M., Piette, A. A. A., and Moses, J. I. (2023b). "Carbon-bearing Molecules in a Possible Hycean Atmosphere". In: *Astrophysical Journal Letters* 956.1, L13, p. L13.

Maillard, J. et al. (2023). "Humid Evolution of Haze in the Atmosphere of Super-Earths in the Habitable Zone". In: *Astrobiology* 23.6. PMID: 37229532, pp. 723–732.

Meier, T. G., Bower, D. J., Lichtenberg, T., Hammond, M., and Tackley, P. J. (2023). "Interior dynamics of super-Earth 55 Cancri e". In: *Astronomy & Astrophysics* 678, A29, A29.

Misener, W., Schlichting, H. E., and Young, E. D. (2023). "Atmospheres as windows into sub-Neptune interiors: coupled chemistry and structure of hydrogen-silane-water envelopes". In: *Mon. Not. R. Astron. Soc* 524.1, pp. 981–992.

Mlawer, E. J., Cady-Pereira, K. E., Mascio, J., and Gordon, I. E. (2023). "The inclusion of the MT_-CKD water vapor continuum model in the HITRAN molecular spectroscopic database". In: *Journal of Quantitative Spectroscopy and Radiative Transfer* 306, 108645, p. 108645.

Mukherjee, S., Batalha, N. E., Fortney, J. J., and Marley, M. S. (2023). "PICASO 3.0: A One-dimensional Climate Model for Giant Planets and Brown Dwarfs". In: *The Astrophysical Journal* 942.2, p. 71.

Namekata, K., Toriumi, S., Airapetian, V. S., Shoda, M., Watanabe, K., and Notsu, Y. (2023). "Reconstructing the XUV Spectra of Active Sun-like Stars Using Solar Scaling Relations with Magnetic Flux". In: *Astrophys. J.* 945.2, p. 147.

National Academies of Sciences, Engineering, and Medicine (2023). Washington DC: The National Academies Press, p. 629.

Nicholls, H., Hebrard, E., Venot, O., Drummond, B., and Evans, E. (2023). "Temperature-chemistry coupling in the evolution of gas giant atmospheres driven by stellar flares". In: *Mon. Not. R. Astron. Soc* 523.4, pp. 5681–5702.

Ostberg, C. M. et al. (2023). "The Prospect of Detecting Volcanic Signatures on an ExoEarth Using Direct Imaging". In: *Astronomical Journal* 166.5, p. 199.

Padovani, P. and Cirasuolo, M. (2023). "The Extremely Large Telescope". In: *Contemporary Physics* 64.1, pp. 47–64.

Palle, E. et al. (2023). "GJ 806 (TOI-4481): A bright nearby multi-planetary system with a transiting hot low-density super-Earth". In: *A&A* 678, A80.

Piette, A. A. A. et al. (2023). "Rocky Planet or Water World? Observability of Low-density Lava World Atmospheres". In: *Astrophysical Journal* 954.1, 29, p. 29.

Rasmussen, K. C. et al. (2023). "A Nondetection of Iron in the First High-resolution Emission Study of the Lava Planet 55 Cnc e". In: *Astronomical Journal* 166.4, p. 155.

Salvador, A. et al. (2023). "Magma Ocean, Water, and the Early Atmosphere of Venus". In: *Space Sci Rev* 219.7, 51, p. 51.

Selsis, F., Leconte, J., Turbet, M., Chaverot, G., and Bolmont, e. (2023). "A cool runaway greenhouse without surface magma ocean". In: *Nature* 620.7973, pp. 287–291.

Sergeev, D. E. et al. (2023). "Simulations of idealised 3D atmospheric flows on terrestrial planets using LFRic-Atmosphere". In: *Geoscientific Model Development* 16.19, pp. 5601–5626.

Sossi, P. A., Tollan, P. M. E., Badro, J., and Bower, D. J. (2023). "Solubility of Water in Peridotite Liquids and the Prevalence of Steam Atmospheres on Rocky Planets". In: *Earth and Planetary Science Letters* 601, p. 117894.

Suer, T.-A., Jackson, C., Grewal, D. S., Dalou, C., and Lichtenberg, T. (2023). "The distribution of volatile elements during rocky planet formation". In: *Frontiers in Earth Science* 11, 1159412, p. 1159412.

Tackley, P. J. (2023). "Tectono-Convective Modes on Earth and Other Terrestrial Bodies". In: *Dynamics of Plate Tectonics and Mantle Convection*. Ed. by J. C. Duarte. Elsevier, pp. 159–180.

Tsai, S.-M. et al. (2023). "Photochemically produced SO2 in the atmosphere of WASP-39b". In: *Nature* 617.7961, pp. 483–487.

Turbet, M. et al. (2023). "Water condensation zones around main sequence stars". In: *Astronomy & Astrophysics* 679, A126.

van Buchem, C. P. A., Miguel, Y., Zilinskas, M., and van Westrenen, W. (2023). "LavAtmos: An open-source chemical equilibrium vaporization code for lava worlds". In: *Meteoritics & Planetary Science* 58.8, pp. 1149–1161.

Wolf, A. S., Jaggi, N., Sossi, P. A., and Bower, D. J. (2023). "VapoRock: Thermodynamics of Vaporized Silicate Melts for Modeling Volcanic Outgassing and Magma Ocean Atmospheres". In: *The Astrophysical Journal* 947.2, p. 64.

Wood, M. L. et al. (2023). "TESS Hunt for Young and Maturing Exoplanets (THYME). IX. A 27 Myr Extended Population of Lower Centaurus Crux with a Transiting Two-planet System". In: *Astronomical Journal* 165.3, 85, p. 85.

Zahnle, K. J. and Kasting, J. F. (2023). "Elemental and isotopic fractionation as fossils of water escape from Venus". In: *Geochimica et Cosmochimica Acta* 361, pp. 228–244.

Zhou, L., Ma, B., Wang, Y.-H., and Zhu, Y.-N. (2023). "Hubble WFC3 Spectroscopy of the Terrestrial Planets L 98-59 c and d: No Evidence for a Clear Hydrogen Dominated Primary Atmosphere". In: *Research in Astronomy and Astrophysics* 23.2, 025011, p. 025011.

Zieba, S. et al. (2023). "No thick carbon dioxide atmosphere on the rocky exoplanet TRAPPIST-1 c". In: *Nature* 620, pp. 746–749.

Zilinskas, M., Miguel, Y., Buchem, C. P. A. van, and Snellen, I. A. G. (2023). "Observability of silicates in volatile atmospheres of super-Earths and sub-Neptunes". In: *Astronomy & Astrophysics* 671.

Alam, M. K. et al. (2024). "JWST COMPASS: The first near- to mid-infrared transmission spectrum of the hot super-Earth L 168-9 b". In: *arXiv e-prints*, arXiv:2411.03154, arXiv:2411.03154.

Aygun, B. and Cadek, O. (2024). "Tidal Heating in a Subsurface Magma Ocean on Io Revisited". In: *Geophysical Research Letters* 51.10. e2023GL107869 2023GL107869, e2023GL107869.

Banerjee, A. et al. (2024). "Atmospheric Retrievals Suggest the Presence of a Secondary Atmosphere and Possible Sulfur Species on L98-59 d from JWST Nirspec G395H Transmission Spectroscopy". In: *The Astrophysical Journal Letters* 975.1, p. L11.

Benneke, B. et al. (2024). "JWST Reveals CH_4, CO_2, and H_2O in a Metal-rich Miscible Atmosphere on a Two-Earth-Radius Exoplanet". In: *arXiv e-prints*, arXiv:2403.03325, arXiv:2403.03325.

Bergermann, A., French, M., and Redmer, R. (2024). "Ab initio calculation of the miscibility diagram for mixtures of hydrogen and water". In: *Phys. Rev. B* 109 (17), p. 174107.

Bierson, C. J. (2024). "The Impact of Rheology Model Choices on Tidal Heating Studies". In: *Icarus* 414, p. 116026.

Burn, R. et al. (2024). "A radius valley between migrated steam worlds and evaporated rocky cores". In: *Nature Astronomy* 8, pp. 463–471.

Capistrant, B. K. et al. (2024). "TESS Hunt for Young and Maturing Exoplanets (THYME). XI. An Earth-sized Planet Orbiting a Nearby, Solar-like Host in the 400 Myr Ursa Major Moving Group". In: *Astronomical Journal* 167.2, p. 54.

Cherubim, C., Wordsworth, R., Hu, R., and Shkolnik, E. (2024). "Strong Fractionation of Deuterium and Helium in Sub-Neptune Atmospheres along the Radius Valley". In: *The Astrophysical Journal* 967.2, 139, p. 139.

Dallerit, V., Buvoli, T., Tokman, M., and Gaudreault, S. (2024). "Second-order Rosenbrock-exponential (ROSEXP) methods for partitioned differential equations". In: *Numer. Algorithms* 96.3, pp. 1143–1161.

Davies, A. G., Perry, J. E., Williams, D. A., and Nelson, D. M. (2024). "Io's polar volcanic thermal emission indicative of magma ocean and shallow tidal heating models". In: *Nature Astronomy* 8.1, pp. 94–100.

Ducrot, E. et al. (2024). "Combined analysis of the 12.8 and 15 μm JWST/MIRI eclipse observations of TRAPPIST-1 b". In: *Nature Astronomy*.

Falco, A., Tremblin, P., Charnoz, S., Ridgway, R. J., and Lagage, P.-O. (2024). "Hydrogenated atmospheres of lava planets: Atmospheric structure and emission spectra". In: *Astronomy & Astrophysics* 683, A194, A194.

Feinberg, L. et al. (2024). "The Habitable Worlds Observatory engineering view: status, plans, and opportunities". In: *Proceedings Volume 13092, Space Telescopes and Instrumentation 2024: Optical, Infrared, and Millimeter Wave*. Vol. 13092. SPIE, pp. 548–559.

Fortin, M.-A., Gazel, E., Williams, D. B., Thompson, J. O., Kaltenegger, L., and Ramsey, M. S. (2024). "Lava Worlds Surface Measurements at High Temperatures". In: *The Astrophysical Journal Letters* 974.1, p. L7.

Fromont, E. F. et al. (2024). "Atmospheric Escape From Three Terrestrial Planets in the L 98-59 System". In: *The Astrophysical Journal* 961.1, p. 115.

Gillmann, C., Hakim, K., Lourenco, D., Quanz, S. P., and Sossi, P. A. (2024). "Interior Controls on the Habitability of Rocky Planets". In: *Space: Science & Technology* 4, p. 0075.

Gressier, A. et al. (2024). "Hints of a Sulfur-rich Atmosphere around the 1.6 R $_\oplus$ Super-Earth L98-59 d from JWST NIRspec G395H Transmission Spectroscopy". In: *Astrophysical Journal Letters* 975.1, L10, p. L10.

Grewal, D. S., Nie, N. X., Zhang, B., Izidoro, A., and Asimow, P. D. (2024). "Accretion of the earliest inner Solar System planetesimals beyond the water snowline". In: *Nature Astronomy* 8, pp. 290–297.

Guimond, C. M., Wang, H., Seidler, F., Sossi, P., Mahajan, A., and Shorttle, O. (2024). "From Stars to Diverse Mantles, Melts, Crusts, and Atmospheres of Rocky Exoplanets". In: *Reviews in Mineralogy and Geochemistry* 90.1, pp. 259–300.

Guo, J. H. (2024). "Characterization of the regimes of hydrodynamic escape from low-mass exoplanets". In: *Nature Astronomy* 8.7, pp. 920–928.

Habib, N. and Pierrehumbert, R. T. (2024). "Modeling Noncondensing Compositional Convection for Applications to Super-Earth and Sub-Neptune Atmospheres". In: *Astrophysical Journal* 961.1, 35, p. 35.

Haldemann, J., Dorn, C., Venturini, J., Alibert, Y., and Benz, W. (2024). "BICEPS: An improved characterization model for low- and intermediate-mass exoplanets". In: *A&A* 681, A96.

Hamano, K., Gillmann, C., Golabek, G. J., Lourenco, D., and Westall, F. (2024). "The evolutionary divergence of Mars, Venus and Earth". In: *arXiv*.

Herath, M., Boukare, C.-e., and Cowan, N. B. (2024). "Thermal evolution of lava planets". In: *Mon. Not. R. Astron. Soc* 535.3, pp. 2404–2414.

Ho, C. S. K., Rogers, J. G., Eylen, V. v., Owen, J. E., and Schlichting, H. E. (2024). "Shallower radius valley around low-mass hosts: evidence for icy planets, collisions, or high-energy radiation scatter". In: *Mon. Not. R. Astron. Soc* 531.3, pp. 3698–3714.

Hu, R. et al. (2024). "A secondary atmosphere on the rocky exoplanet 55 Cancri e". In: *Nature* 630.8017, pp. 609–612.

Kempton, E. M. .-. and Knutson, H. A. (2024). "Transiting Exoplanet Atmospheres in the Era of JWST". In: *Reviews in Mineralogy and Geochemistry* 90.1, pp. 411–464.

Kitzmann, D., Stock, J. W., and Patzer, A. B. C. (2024). "FASTCHEM COND: equilibrium chemistry with condensation and rainout for cool planetary and stellar environments". In: *Mon. Not. R. Astron. Soc* 527.3, pp. 7263–7283.

Krissansen-Totton, J., Wogan, N., Thompson, M., and Fortney, J. J. (2024). "The erosion of large primary atmospheres typically leaves behind substantial secondary atmospheres on temperate rocky planets". In: *Nature Communications* 15.1, p. 8374.

Lee, E. K. H., Tan, X., and Tsai, S.-M. (2024). "Dynamically coupled kinetic chemistry in brown dwarf atmospheres - II. Cloud and chemistry connections in directly imaged sub-Jupiter exoplanets". In: *Mon. Not. R. Astron. Soc* 529.3, pp. 2686–2701.

Lee, E. K. H. (2024). "Testing Approximate Infrared Scattering Radiative-transfer Methods for Hot Jupiter Atmospheres". In: *Astrophys. J.* 965.2, p. 115.

Libralato, M. et al. (2024). "High-precision Astrometry and Photometry with the JWST/MIRI Imager". In: *Publ. Astron. Soc. Pac.* 136.3, p. 034502.

Lock, S. J. and Stewart, S. T. (2024). "Atmospheric Loss in Giant Impacts Depends on Preimpact Surface Conditions". In: *Planetary Science Journal* 5.2, 28, p. 28.

Luu, C. N. et al. (2024). "Volatile-rich Sub-Neptunes as Hydrothermal Worlds: The Case of K2-18 b". In: *Astrophys. J. Lett.* 977.2, p. L51.

Lyons, T. W. et al. (2024). "Co-evolution of early Earth environments and microbial life". In: *Nat. Rev. Microbiol.* 22, pp. 572–586.

Malsky, I. et al. (2024). "A Direct Comparison between the Use of Double Gray and Multiwavelength Radiative Transfer in a General Circulation Model with and without Radiatively Active Clouds". In: *Astrophys. J.* 961.1, p. 66.

Manners, J. (2024). "A fast and flexible scheme for photolysis and radiative heating of the whole atmosphere". In: *AIP Conference Proceedings* 2988.1, p. 030002.

Maurice, M., Dasgupta, R., and Hassanzadeh, P. (2024). "Volatile atmospheres of lava worlds". In: *Astron. Astrophys.* 688, A47.

Moody, E. R. R. et al. (2024). "The nature of the last universal common ancestor and its impact on the early Earth system". In: *Nature Ecology & Evolution* 8.9, pp. 1654–1666.

Nicholls, H., Lichtenberg, T., Bower, D. J., and Pierrehumbert, R. (2024). "Magma Ocean Evolution at Arbitrary Redox State". In: *Journal of Geophysical Research: Planets* 129.12. e2024JE008576 2024JE008576, e2024JE008576.

Nimmo, F., Kleine, T., and Morbidelli, A. (2024). "Tidally driven remelting around 4.35 billion years ago indicates the Moon is old". In: *Nature* 636, pp. 598–602.

Noti, P. A. and Lee, E. K. H. (2024). "Effects of the internal temperature on vertical mixing and on cloud structures in ultra-hot Jupiters". In: *Astron. Astrophys.* 691, A139.

Owen, J. E. and Schlichting, H. E. (2024). "Mapping out the parameter space for photoevaporation and core-powered mass-loss". In: *Mon. Not. R. Astron. Soc* 528.2, pp. 1615–1629.

Parc, L., Bouchy, F., Venturini, J., Dorn, C., and Helled, R. (2024). "From super-Earths to sub-Neptunes: Observational constraints and connections to theoretical models". In: *Astronomy & Astrophysics* 688, A59, A59.

Park, R. S. et al. (2024). "Io's Tidal Response Precludes a Shallow Magma Ocean". In: *Nature*, pp. 1–3.

Patel, J. A. et al. (2024). "JWST reveals the rapid and strong day-side variability of 55 Cancri e". In: *Astronomy & Astrophysics* 690, A159.

Pettine, M. et al. (2024). "JIRAM observations of volcanic flux on Io: Distribution and comparison to tidal heat flow models". In: *Geophysical Research Letters* 51.17, e2023GL105782.

Powell, D. et al. (2024). "Sulfur dioxide in the mid-infrared transmission spectrum of WASP-39b". In: *Nature* 626.8001, pp. 979–983.

Rajpaul, V. M., Barragán, O., and Zicher, N. (2024). "A non-zero Doppler amplitude is not enough: revisiting the putative radial velocity detection of sub-Venus exoplanet L 98-59b". In: *Mon. Not. R. Astron. Soc* 530.4, pp. 4665–4675.

Redfield, S. et al. (2024). "Report of the Working Group on Strategic Exoplanet Initiatives with HST and JWST". In: *arXiv e-prints*, arXiv:2404.02932, arXiv:2404.02932.

Rigby, F. E. et al. (2024). "Toward a Self-consistent Evaluation of Gas Dwarf Scenarios for Temperate Sub-Neptunes". In: *Astrophysical Journal* 975.1, 101, p. 101.

Scarsdale, N. et al. (2024). "JWST COMPASS: The 3-5 m Transmission Spectrum of the Super-Earth L 98-59 c". In: *Astronomical Journal* 168.6, p. 276.

Schaefer, L., Pahlevan, K., and Elkins-Tanton, L. T. (2024). "Ferric Iron Evolution During Crystallization of the Earth and Mars". In: *Journal of Geophysical Research (Planets)* 129.9, e2023JE008262, e2023JE008262.

Seidler, F. L., Sossi, P. A., and Grimm, S. L. (2024). "Impact of oxygen fugacity on the atmospheric structure and emission spectra of ultra-hot rocky exoplanets". In: *A&A* 691, A159.

Seligman, D. Z. et al. (2024). "Potential Melting of Extrasolar Planets by Tidal Dissipation". In: *The Astrophysical Journal* 961.1, p. 22.

Shorttle, O., Jordan, S., Nicholls, H., Lichtenberg, T., and Bower, D. J. (2024). "Distinguishing Oceans of Water from Magma on Mini-Neptune K2-18b". In: *The Astrophysical Journal Letters* 962.1, p. L8.

Sim, S. J., Hirschmann, M. M., and Hier-Majumder, S. (2024). "Volatile and Trace Element Storage in a Crystallizing Martian Magma Ocean". In: *Journal of Geophysical Research: Planets* 129.8. e2024JE008346 2024JE008346, e2024JE008346.

Sossi, P. A., Nakajima, M., and Khan, A. (2024). "Composition, structure, and origin of the Moon". In: *Treatise on Geochemistry (Third Edition)* 7.

Tang, Y., Fortney, J. J., and Murray-Clay, R. (2024). "Assessing Core-powered Mass Loss in the Context of Early Boil-off: Minimal Long-lived Mass Loss for the Sub-Neptune Population". In: *The Astrophysical Journal* 976.2, p. 221.

Truong, N., Glein, C. R., and Lunine, J. I. (2024). "A Broad Set of Solar and Cosmochemical Data Indicates High C-N-O Abundances for the Solar System". In: *Astrophys. J.* 976.1, p. 14.

Tsai, S.-M., Innes, H., Wogan, N. F., and Schwieterman, E. W. (2024a). "Biogenic Sulfur Gases as Biosignatures on Temperate Sub-Neptune Waterworlds". In: *Astrophysical Journal Letters* 966.2, L24, p. L24.

Tsai, S.-M. et al. (2024b). "Global Chemical Transport on Hot Jupiters: Insights from the 2D VULCAN Photochemical Model". In: *Astrophys. J.* 963.1, p. 41.

Vach, S. et al. (2024). "The Occurrence of Small, Short-period Planets Younger than 200 Myr with TESS". In: *Astronomical Journal* 167.5, 210, p. 210.

Wogan, N. F., Batalha, N. E., Zahnle, K. J., Krissansen-Totton, J., Tsai, S.-M., and Hu, R. (2024). "JWST Observations of K2-18b Can Be Explained by a Gas-rich Mini-Neptune with No Habitable Surface". In: *The Astrophysical Journal Letters* 963.1, p. L7.

Yan, D., Guo, J., Seon, K.-i., Lopez-Puertas, M., Czesla, S., and Lampon, M. (2024). "A possibly solar metallicity atmosphere escaping from HAT-P-32b revealed by Ha and He absorption". In: *Astron. Astrophys.* 686, A208.

Yoshida, T., Terada, N., and Kuramoto, K. (2024). "Suppression of hydrodynamic escape of an H2-rich early Earth atmosphere by radiative cooling of carbon oxides". In: *Progress in Earth and Planetary Science* 11.1, p. 59.

Young, E. D., Stixrude, L., Rogers, J. G., Schlichting, H. E., and Marcum, S. P. (2024). "Phase Equilibria of Sub-Neptunes and Super-Earths". In: *The Planetary Science Journal* 5.12, 268, p. 268.

Zhang, F. et al. (2024a). "The constant oxidation state of Earth's mantle since the Hadean". In: *Nature Communications* 15.1, p. 6521.

Zhang, H. L. et al. (2024b). "Ferric iron stabilization at deep magma ocean conditions". In: *Sci. Adv.* 10.42.

Zurlo, A. (2024). *Direct imaging of exoplanets*.

Agrawal, R. et al. (2025). "Warm, water-depleted rocky exoplanets with surface ionic liquids: A proposed class for planetary habitability". In: *Proc. Natl. Acad. Sci. U.S.A.* 122.33, e2425520122.

Aguichine, A., Batalha, N., Fortney, J. J., Nettelmann, N., Owen, J. E., and Kempton, E. M.-R. (2025). "Evolution of Steam Worlds: Energetic Aspects". In: *Astrophys. J.* 988.2, p. 186.

Allen, N. H. et al. (2025). "Hot Rocks Survey IV: Emission from LTT 3780 b is consistent with a bare rock". In: *arXiv*.

August, P. C. et al. (2025). "Hot Rocks Survey I: A possible shallow eclipse for LHS 1478 b". In: *Astron. Astrophys.* 695, A171.

Barber, M. G., Mann, A. W., Vanderburg, A., Boyle, A. W., and Lopez Murillo, A. I. (2025). "TESS Investigation—Demographics of Young Exoplanets (TI-DYE). III. An Inner Super-Earth in TOI 2076". In: *Astronomical Journal* 170.1, 32, p. 32.

Barclay, T. et al. (2025). "The Pandora SmallSat: A Low-Cost, High Impact Mission to Study Exoplanets and Their Host Stars". In: *arXiv e-prints*, arXiv:2502.09730, arXiv:2502.09730.

Bello-Arufe, A. et al. (2025). "Evidence for a Volcanic Atmosphere on the Sub-Earth L 98-59 b". In: *Astrophysical Journal Letters* 980.2, L26, p. L26.

Bibas, D. R. and Vidal, C. (2025). "Responsible Discovery in Astrobiology: Lessons from Four Controversial Claims". In: *arXiv*.

Boer, I. D., Nicholls, H., and Lichtenberg, T. (2025). "Absence of a Runaway Greenhouse Limit on Lava Planets". In: *Astrophys. J.* 987.2, p. 172.

Boitard-Crepeau, L., Ceccarelli, C., Beck, P., Vacher, L., and Ugliengo, P. (2025). "Was Earth's Water Acquired Locally during the Earliest Phases of the Solar System Formation?" In: *Astrophys. J. Lett.* 987.2, p. L25.

Bower, D. J., Thompson, M. A., Hakim, K., Tian, M., and Sossi, P. A. (2025). "Diversity of Low-mass Planet Atmospheres in the C–H–O–N–S–Cl System with Interior Dissolution, Non-ideality, and Condensation: Application to TRAPPIST-1e and Sub-Neptunes". In: *Astrophys. J.* 995.1, p. 59.

Bussmann, M. et al. (2025). "The possibility of a giant impact on Venus". In: *Astron. Astrophys.* 702, A106.

Cadieux, C. et al. (2025). "Detailed Architecture of the L 98-59 System and Confirmation of a Fifth Planet in the Habitable Zone". In: *arXiv e-prints*, arXiv:2507.09343, arXiv:2507.09343.

Capelleveen, R. F. van et al. (2025). "WIde Separation Planets In Time (WISPIT): A Gap-clearing Planet in a Multi-ringed Disk around the Young Solar-type Star WISPIT 2". In: *Astrophys. J. Lett.* 990.1, p. L8.

Caro, G., Grocolas, T., Bourgeois, P., Bouilhol, P., Mojzsis, S. J., and Paris, G. (2025). "Early Archaean onset of volatile cycling at subduction zones". In: *Nature Geoscience* 18.5, pp. 436–442.

Challener, R. C. et al. (2025). "Horizontal and vertical exoplanet thermal structure from a JWST spectroscopic eclipse map". In: *Nat. Astron.*, pp. 1–12.

Chen, H., De Luca, P., Hochman, A., and Komacek, T. D. (2025). "Effects of Transient Stellar Emissions on Planetary Climates of Tidally Locked Exo-Earths". In: *Astronomical Journal* 170.1, p. 40.

Cherubim, C., Wordsworth, R., Bower, D. J., Sossi, P. A., Adams, D., and Hu, R. (2025). "An Oxidation Gradient Straddling the Small Planet Radius Valley". In: *Astrophys. J.* 983.2, p. 97.

Close, L. M. et al. (2025). "Wide Separation Planets in Time (WISPIT): Discovery of a Gap Hα Protoplanet WISPIT 2b with MagAO-X". In: *Astrophys. J. Lett.* 990.1, p. L9.

Cmiel, J., Wordsworth, R., and Seeley, J. T. (2025). "Characterizing the Radiative-Convective Structure of Dense Rocky Planet Atmospheres". In: *The Planetary Science Journal* 6.5, p. 123.

Dauphas, N. et al. (2025). "Completion of lunar magma ocean solidification at 4.43 Ga". In: *Proceedings of the National Academy of Sciences* 122.2, e2413802121.

Derras-Chouk, A., Elsaesser, G., Luo, Z. J., Matsui, T., Prein, A. F., and Wu, J. (2025). "Estimating Vertical Velocity in Convective Updrafts from Temperature, Pressure, and Latent Heating". In: *arXiv*.

Donoghue, P. C. J., Lenton, T. M., Okasha, S., Shields, G. A., and Spang, A. (2025). "Chance and purpose in the evolution of biospheres". In: *Philosophical Transactions of the Royal Society B: Biological Sciences* 380.1931, p. 20240085.

Farcy, B. J., Seligman, D. Z., Mandt, K. E., Noonan, J. W., and Anderson, S. E. (2025). "Habitable from the start: How initial planetary formation conditions may create habitable worlds". In: *arXiv*.

Farhat, M., Auclair-Desrotour, P., Boué, G., Lichtenberg, T., and Laskar, J. (2025). "Tides on Lava Worlds: Application to Close-in Exoplanets and the Early Earth–Moon System". In: *Astrophysical Journal* 979.2, 133, p. 133.

Fernandes, R. B. et al. (2025). "Signatures of Atmospheric Mass Loss and Planet Migration in the Time Evolution of Short-period Transiting Exoplanets". In: *Astronomical Journal* 169.4, 208, p. 208.

Fortune, M. et al. (2025). "Hot Rocks Survey - III. A deep eclipse for LHS 1140c and a new Gaussian process method to account for correlated noise in individual pixels". In: *Astron. Astrophys.* 701, A25.

Franco, P., Roig, F., Winter, O. C., Sfair, R., Burger, C., and Schafer, C. M. (2025). "Formation of Mercury by a grazing giant collision involving similar-mass bodies". In: *Nat. Astron.* 9, pp. 1158–1166.

Gillon, M. et al. (2025). "First JWST thermal phase curves of temperate terrestrial exoplanets reveal no thick atmosphere around TRAPPIST-1 b and c". In: *arXiv*.

Gkouvelis, L., Pozuelos, F. J., Drant, T., Farhat, M., Tian, M., and Akın, C. (2025). "Interior redox state effects on the stability of secondary atmospheres and observational manifestations: LP 791-18 d as a case study for outgassing rocky exoplanets". In: *arXiv e-prints*, arXiv:2506.02188, arXiv:2506.02188.

Gupta, A., Stixrude, L., and Schlichting, H. E. (2025). "The Miscibility of Hydrogen and Water in Planetary Atmospheres and Interiors". In: *Astrophys. J. Lett.* 982.2, p. L35.

Hakim, K., Bower, D. J., Seidler, F., and Sossi, P. A. (2025). "Silane-Methane Competition in Sub-Neptune Atmospheres as a Diagnostic of Metallicity and Magma Oceans". In: *arXiv*.

Hammond, M. et al. (2025). "Reliable Detections of Atmospheres on Rocky Exoplanets with Photometric JWST Phase Curves". In: *The Astrophysical Journal Letters* 978.2, p. L40.

Hazra, G. (2025). "Atmospheric escape from exoplanets: recent observations and theoretical models". In: *Rev. Mod. Plasma Phys.* 9.1, pp. 1–44.

Heng, K., Owen, J. E., and Tian, M. (2025). "The Gradient of Mean Molecular Weight Across the Radius Valley". In: *arXiv e-prints*, arXiv:2504.02499, arXiv:2504.02499.

Horn, H. W., Vazan, A., Chariton, S., Prakapenka, V. B., and Shim, S.-H. (2025). "Building wet planets through high-pressure magma–hydrogen reactions". In: *Nature* 646, pp. 1069–1074.

Howard, S., Helled, R., Bergermann, A., and Redmer, R. (2025). "The possibility of hydrogen-water demixing in Uranus, Neptune, K2-18 b and TOI-270 d". In: *Astron. Astrophys.* 703, A154.

Hu, R. et al. (2025). "A water-rich interior in the temperate sub-Neptune K2-18 b revealed by JWST". In: *arXiv*.

Huang, D. and Dorn, C. (2025). "Limits on forming coreless terrestrial worlds in the TRAPPIST-1 system". In: *arXiv*.

Jakosky, B. M. and Byrne, P. K. (2025). "Using Venus, Earth, and Mars to Understand Exoplanet Volatile and Climate Evolution". In: *J. Geophys. Res. Planets* 130.10, e2024JE008882.

Ji, X., Chatterjee, R. D., Coy, B. P., and Kite, E. (2025). "The Cosmic Shoreline Revisited: A Metric for Atmospheric Retention Informed by Hydrodynamic Escape". In: *Astrophys. J.* 992.2, p. 198.

Joiret, S., Morbidelli, A., Sousa Ribeiro, R. de, Avice, G., and Sossi, P. (2025). "A massive primordial atmosphere on early Mars". In: *Earth Planet. Sci. Lett.* 671, p. 119625.

Jordan, S., Shorttle, O., and Quanz, S. P. (2025). "Planetary Albedo Is Limited by the Above-cloud Atmosphere: Implications for Sub-Neptune Climates". In: *Astrophysical Journal* 993.1, 86, p. 86.

Korenaga, J. (2025). "Tidal dissipation within Earth's solidifying magma ocean: III. Effects of matrix compaction". In: *Icarus* 442, p. 116759.

Lammer, H. et al. (2025). "Earth-mass planets with He atmospheres in the habitable zone of Sun-like stars". In: *Nat. Astron.* 9, pp. 1022–1030.

Lee, E. K. H. and Ohno, K. (2025). "Three-dimensional dynamical evolution of cloud particle microphysics in sub-stellar atmospheres - I. Description and exploring Y-dwarf atmospheric variability". In: *Astron. Astrophys.* 695, A111.

Li, J., Bergin, E. A., Hirschmann, M. M., Blake, G. A., Ciesla, F. J., and Kempton, E. M.-R. (2025). "Soot Planets instead of Water Worlds". In: *arXiv*.

Lichtenberg, T. and Miguel, Y. (2025). "Super-Earths and Earth-like Exoplanets". In: *Treatise on Geochemistry* 7, pp. 51–112.

Lichtenberg, T., Shorttle, O., Teske, J., and Kempton, E. M.-R. (2025). "Constraining exoplanet interiors using observations of their atmospheres". In: *Science* 390.6769.

Lin, Z. and Seager, S. (2025). "Carbon-rich Sub-Neptune Interiors Are Compatible with JWST Observations". In: *Astrophys. J. Lett.* 990.2, p. L35.

Liu, J., Christie, D., and Yang, J. (2025). "Three-dimensional transport-induced chemistry on temperate sub-Neptune K2-18b, Part I: the effects of atmospheric dynamics". In: *Mon. Not. R. Astron. Soc* 541.4, pp. 2897–2916.

Loftus, K., Luo, Y., Fan, B., and Kite, E. S. (2025). "Extreme weather variability on hot rocky exoplanet 55 Cancri e explained by magma temperature–cloud feedback". In: *Proc. Natl. Acad. Sci. U.S.A.* 122.17, e2423473122.

Losekoot, A., Balme, M. R., Coe, A. L., Fawdon, P., and Davis, J. M. (2025). "Widespread Depositional Fluvial Systems in Noachis Terra, Mars". In: *J. Geophys. Res. Planets* 130.11, e2025JE009378.

Madhusudhan, N., Constantinou, S., Holmberg, M., Sarkar, S., Piette, A. A. A., and Moses, J. I. (2025). "New Constraints on DMS and DMDS in the Atmosphere of K2-18 b from JWST MIRI". In: *Astrophys. J. Lett.* 983.2, p. L40.

Mak, M. T. (2025). "Advancing the Theory of Haze in Exoplanetary Atmospheres". PhD thesis. University of Exeter.

Maurel, A. et al. (2025). "Constraints on the possible atmospheres on TRAPPIST-1 b: insights from 3D climate modeling". In: *arXiv*.

McCreery, P., Dos Santos, L. A., Espinoza, N., Allart, R., and Kirk, J. (2025). "Tracing the Winds: A Uniform Interpretation of Helium Escape in Exoplanets from Archival Spectroscopic Observations". In: *Astrophysical Journal* 980.1, 125, p. 125.

McDonough, W. F. (2025). "Earth's composition: Origin, energy budget, and insights from geoneutrinos". In: *Geochim. Cosmochim. Acta*.

Nicholls, H., Guimond, C. M., Hay, H. C. F. C., Chatterjee, R. D., Lichtenberg, T., and Pierrehumbert, R. T. (2025a). "Self-limited tidal heating and prolonged magma oceans in the L 98-59 system". In: *Mon. Not. R. Astron. Soc* 541.3, pp. 2566–2584.

Nicholls, H., Pierrehumbert, R., and Lichtenberg, T. (2025b). "AGNI: A radiative-convective model for lava planet atmospheres". In: *Journal of Open Source Software* 10.109, p. 7726.

Nicholls, H., Pierrehumbert, R. T., Lichtenberg, T., Soucasse, L., and Smeets, S. (2025c). "Convective shutdown in the atmospheres of lava worlds". In: *Mon. Not. R. Astron. Soc* 536.3, pp. 2957–2971.

Oosterloo, M., Kamp, I., and Westrenen, W. van (2025). *The effects of transport processes on the bulk composition of the first generation of planetesimals interior to the water iceline*.

Paschek, K. et al. (2025). "Deep Mantle-Atmosphere Coupling and Carbonaceous Bombardment: Options for Biomolecule Formation on an Oxidized Early Earth". In: *The Astrophysical Journal* 985.1, p. 50.

Piaulet-Ghorayeb, C. et al. (2025). "Strict Limits on Potential Secondary Atmospheres on the Temperate Rocky Exo-Earth TRAPPIST-1 d". In: *Astrophys. J.* 989.2, p. 181.

Rauer, H. et al. (2025). "The PLATO mission". In: *Experimental Astronomy* 59.3, p. 26.

Rogers, J. G. (2025). "On the road to the radius valley: distinguishing between gas dwarfs and water worlds with young transiting exoplanets". In: *Mon. Not. R. Astron. Soc.* 539.3, pp. 2230–2241.

Rogers, J. G., Young, E. D., and Schlichting, H. E. (2025). "Redefining interiors and envelopes: hydrogen–silicate miscibility and its consequences for the structure and evolution of sub-Neptunes". In: *Mon. Not. R. Astron. Soc* 544.4, pp. 3496–3511.

Runge, E., Vulpius, S., Herwartz, D., Pack, A., Brachmann, C., and Noack, L. (2025). "The aerobic biosphere as an O2 sink before the Great Oxygenation Event: geobiological feedback to solid Earth and surface oxidation". In: *Geo-Bio Interfaces* 2, e10.

Sahu, C. K., Majumdar, L., Mridha, S., and Krishna, H. (2025). "Unveiling the Interior Structure and Thermal Evolution of Super-Earth GJ 486b". In: *Astrophysical Journal* 981.1, 80, p. 80.

Sanghi, A. et al. (2025). "Worlds Next Door: A Candidate Giant Planet Imaged in the Habitable Zone of α Centauri A. II. Binary Star Modeling, Planet and Exozodi Search, and Sensitivity Analysis". In: *Astrophys. J. Lett.* 989.2, p. L23.

Saracino, F., Charlier, B., Zhang, Y., Lecaille, M., Lin, Y., and Namur, O. (2025). "The role of sulfur on the liquidus temperature and olivine-orthopyroxene equilibria in highly reduced magmas". In: *Chemical Geology* 683, p. 122777.

Savignac, V. and Lee, E. J. (2025). "Constructing Earth Formation History Using Deep Mantle Noble Gas Reservoirs". In: *arXiv*.

Schwarz, P., Dreizler, S., and Heller, R. (2025). "Confirmation of a non-transiting planet in the habitable zone of the nearby M dwarf L 98-59". In: *arXiv*, arXiv:2507.06413.

Snellen, I. A. G. (2025). "Exoplanet Atmospheres at High Spectral Resolution". In: *Annu. Rev. Astron. Astrophys.* Volume 63, 2025, pp. 83–125.

Sole, C., O'Neil, J., Rizo, H., Paquette, J.-L., Benn, D., and Plakholm, J. (2025). "Evidence for Hadean mafic intrusions in the Nuvvuagittuq Greenstone Belt, Canada". In: *Science* 388.6754, pp. 1431–1435.

Spaargaren, R. J., Herbort, O., Wang, H. S., Mojzsis, S. J., and Sossi, P. (2025). "Proto-planetary disk composition-dependent element volatility in the context of rocky planet formation". In: *arXiv*.

Stevenson, K. B. et al. (2025). "K2-18b Does Not Meet the Standards of Evidence for Life". In: *Astronomical Journal* 170.5, p. 257.

Taylor, J. (2025). "Are there Spectral Features in the MIRI/LRS Transmission Spectrum of K2-18b?" In: *arXiv*.

Thompson, M. A., Sossi, P. A., Bower, D. J., Shahar, A., Liebske, C., and Allaz, J. (2025). "Water solubility in silicate melts: The effects of melt composition under reducing conditions and implications for nebular ingassing on rocky planets". In: *Chem. Geol.* 695, p. 123048.

Trapp-Muller, G. et al. (2025). "Earth's silicate weathering continuum". In: *Nat. Geosci.* 18, pp. 691–701.

Valencia, D., Moro-Martin, A., and Teske, J. (2025). "Diversity of exoplanets". In: ed. by A. Anbar and D. Weis, pp. 19–49.

Varga, A., Kastner, J. H., Binks, A. S., Guenther, H. M., and Murphy, S. J. (2025). "The Age and High Energy Environment of the Very Young Transiting Exoplanet TOI 1227b". In: *arXiv e-prints*, arXiv:2506.04440, arXiv:2506.04440.

Walbecq, A., Samuel, H., and Limare, A. (2025). "The effect of out-of-equilibrium outgassing on the cooling of planetary magma oceans". In: *Icarus* 434, p. 116513.

Wang, H. et al. (2025a). "Two-billion-year transitional oxygenation of the Earth's surface". In: *Nature*, pp. 1–7.

Wang, L., Long, F., Yang, H., Dong, R., and Xu, S. (2025b). "Adsorption and condensation of molecules on astrophysical dust grain surfaces: Ab-initio calculalations and kinetic Monte Carlo simulations". In: *arXiv*.

Welbanks, L. et al. (2025). "The Challenges Involved in the Detection of Gases in Exoplanet Atmospheres". In: *arXiv*.

Werlen, A., Dorn, C., Schlichting, H. E., Grimm, S. L., and Young, E. D. (2025). "Atmospheric C/O Ratios of Sub-Neptunes with Magma Oceans: Homemade rather than Inherited". In: *arXiv e-prints*, arXiv:2504.20450, arXiv:2504.20450.

Westall, F. (2025). "What the earliest evidence for life tells us about the early evolution of the biosphere". In: *Phil. Trans. R. Soc. B* 380.1931.

Wiesenfeld, L., Niraula, P., Wit, J. de, Jaidane, N., Gordon, I. E., and Hargreaves, R. J. (2025). "Ab Initio Quantum Dynamics as a Scalable Solution to the Exoplanet Opacity Challenge: A Case Study of CO2 in a Hydrogen Atmosphere". In: *Astrophys. J.* 981.2, p. 148.

Young, E. D., Werlen, A., Marcum, S. P., Stixrude, L., and Dullemond, C. P. (2025). "Differentiation, the Exception, Not the Rule: Evidence for Full Miscibility in Sub-Neptune Interiors". In: *Planet. Sci. J.* 6.11, p. 251.

Zang, W. et al. (2025). "Microlensing events indicate that super-Earth exoplanets are common in Jupiter-like orbits". In: *Science* 388.6745, pp. 400–404.

Zilinskas, M. et al. (2025). "Characterising the atmosphere of 55 Cancri e: 1D forward model grid for current and future JWST observations". In: *Astronomy & Astrophysics* 697, A34, A34.

Hernandez, J. C., Machucho, M. A., and Ramirez, J. E. (2026). "Adiabatic Lapse Rate Estimation Using a Van Der Waals-type Equation of State". In: *Braz. J. Phys.* 56.1, p. 15.

Nicholls, H., Lichtenberg, T., Chatterjee, R., Guimond, C., Postolec, E., and Pierrehumbert, R. (2026). "Volatile-rich evolution of molten super-Earth L 98-59 d". In: *Nature Astronomy*.

Bower, D., Sastre, M., Soucasse, L., Nicholls, H., and Lichtenberg, T. (In prep.). "Title TBD". In.

Postolec, E., Lichtenberg, T., Nicholls, H., Soucasse, L., and Tak, F. van der (Submitted). "Atmospheric evolution through outgassing and escape on young molten rocky exoplanets". In: *Astronomy & Astrophysics*.

Appendix A
Volatile solubilities and thermochemistry

In this appendix, I write-out the thermochemical *net* reactions and solubility laws incorporated into my outgassing model. These reactions are assumed to have attained equilibrium, meaning that sufficient time has passed for the forward and reverse rates to have become equal. Since reaction rates increase with temperature, this is taken to be a valid assumption for the case of magma ocean degassing. Thermochemical equilibrium then permits calculation of reaction equilibrium constants K_{eq}, describing the 'position' of the mixture between a composition composed of reactants versus products. K_{eq} can be calculated from the Gibbs free energy of products and reactants per Equation 2.13. The free energies of species are tabulated as functions of temperature in the JANAF (Chase 1986) and IVANTHERMO databases (Allendorf and Besmann 2007).

$H_2 + 0.5\,O_2 \rightleftharpoons H_2O$ fitted to JANAF in the range $1500 < T/\mathrm{K} < 3000$ (Bower et al. 2019)

$$\log_{10} K_{\mathrm{eq}} = \frac{13152.4778\,\mathrm{K}}{T} + 3.0385 \tag{A.1}$$

$CO + 0.5\,O_2 \rightleftharpoons CO_2$ fitted to JANAF in the range $1500 < T/\mathrm{K} < 3000$ (Bower et al. 2019)

$$\log_{10} K_{\mathrm{eq}} = \frac{-14467.5114\,\mathrm{K}}{T} + 4.3481 \tag{A.2}$$

$CO_2 + {}_2H_2 \rightleftharpoons CH_4 + O_2$ fitted to IVANTHERMO in the range $298 < T/\mathrm{K} < 2000$ (Schaefer and Fegley 2017)

$$\log_{10} K_{\mathrm{eq}} = \frac{-16276\,\mathrm{K}}{T} - 5.4738 \tag{A.3}$$

$0.5\,S_2 + O_2 \rightleftharpoons SO_2$ fitted to JANAF in the range $900 < T/\mathrm{K} < 2000$(Boulliung and Wood 2022)

$$\log_{10} K_{\mathrm{eq}} = \frac{18887\,\mathrm{K}}{T} - 3.8064 \tag{A.4}$$

$N_2 + 3\,H_2 \rightleftharpoons 2\,NH_3$ fitted to JANAF in the range $200 < K < 4000$ (Chapter 5)

$$\log_{10} K_{\mathrm{eq}} = \frac{2664.0156\,\mathrm{K}}{T} - 5.9924 \tag{A.5}$$

$0.5\,S_2 + H_2 \rightleftharpoons 0.5\,H_2S$ fitted to JANAF in the range $200 < K < 4000$ (Chapter 5)

$$\log_{10} K_{\mathrm{eq}} = \frac{6731.0155\,\mathrm{K}}{T} - 3.6227 \tag{A.6}$$

The solubility laws given below are empirical. The typical process for doing this is to pass the gas of interest over molten rock, allowing some part of the gas to dissolve and measuring its pressure. The rock is then rapidly cooled, quenching it into glass and trapping the dissolved species inside the now-solid sample. Measurement of the amount of trapped volatiles compared to the gas pressure provides a measure of the gas solubility (Namur et al. 2016; Sossi et al. 2023). However, it should be noted that experimental practicalities make these measurements difficult, limiting the valid range of any fitted solubility laws and the types of melt which may be considered. For example, the solubility laws devised by Gaillard et al. (2022) come with '50% uncertainties' which 'directly translates into 10-50% uncertainties in the calculated concentrations of species in the melt and gas depending on the species considered'. It should also be noted that, although different types of rock are considered between these solubility laws, they are all (ultra)mafic with low SiO_2 content comparable with Earth's mantle (Lodders and Fegley 1998; Schubert et al. 2001). We may still obtain order of magnitude estimates and study general trends. In the equations below, partial pressures (and fugacities) are given in units of bar. Concentrations are in the dimensionless units of ppm by weight. Units on fitting coefficients are left-off for brevity.

H_2O in peridotite (Bower et al. 2019; Sossi et al. 2023)

$$X_{\mathrm{H_2O}} = 525 \times (p_{\mathrm{H_2O}})^{0.5} \tag{A.7}$$

CO_2 in alkalic basalt, dissolving as carbonate (Dixon 1997)

$$X_{\mathrm{CO_3^-}} = 3.8 \times 10^{-7} \times p e^{\frac{-23(p-1)}{83.15T}} \tag{A.8}$$

$$X_{\mathrm{CO_2}} = 10^4 \times (4400 X_{\mathrm{CO_3^-}})/(36.6 - 44 X_{\mathrm{CO_3^-}}) \tag{A.9}$$

S_2 in peridotite, assuming 10 wt% FeO (Gaillard et al. 2022)

$$X_{\mathrm{SO_2}} = \frac{p}{2 f_{\mathrm{O_2}}} \exp[13.8426 - 26476.0/T + 0.124 X_{\mathrm{FeO}}] \tag{A.10}$$

N_2 in basalt (Dasgupta et al. 2022). Taking $X_{\mathrm{SiO_2}} = 0.56$, $X_{\mathrm{Al_2O_3}} = 0.11$, $X_{\mathrm{TiO_2}} = 0.01$ from the same paper. from same paper.

$$A = \exp[4.67 + 7.11 X_{\mathrm{SiO_2}} - 13.06 X_{\mathrm{Al_2O_3}} - 120.67 X_{\mathrm{TiO_2}}] \tag{A.11}$$

$$X_{\mathrm{N_2}} = (p_{\mathrm{N_2}}/10000)^{0.5} \exp[5908.0 \times (p/10000)^{0.5}/T - 1.6\Delta\mathrm{IW}] + A p_{\mathrm{N_2}}/10000 \tag{A.12}$$

CH_4 in basalt (Ardia et al. 2013)

$$X_{\mathrm{CH_4}} = (p_{\mathrm{CH_4}}/10000) \times \exp[4.93 - 1.93 \times 10^{-8} p] \tag{A.13}$$

CO in basalt (Armstrong et al. 2015)

$$\log_{10} X_{\mathrm{CO}} = -0.738 + 0.876 \log_{10}(p_{\mathrm{CO}}) - 5.44 \times 10^{-5} p \tag{A.14}$$

I have not explicitly included a model for the dissolution of H_2 since it has low solubility, especially when compared to H_2O (Bower et al. 2022; Thompson et al. 2025).

Appendix B
Derivation of time-average orbital separation

Planets travel on elliptical orbits which are described by Kepler's Laws in the non-relativistic limit. We can express the instantaneous planet-star distance r as a function of orbital phase θ as,

$$r(\theta) = \frac{a(1-e^2)}{1+e\cos\theta}, \tag{B.1}$$

where e is the eccentricity and a is the semi-major axis of the orbit. The phase can be written in terms of time using the chain rule: $\mathrm{d}t = \mathrm{d}\theta/\dot{\theta}$.

We wish to evaluate the time-average value,

$$\langle r \rangle = \frac{1}{T}\int_0^T r(t)\,\mathrm{d}t = \frac{1}{T}\int_0^{2\pi} \frac{r(\theta)}{\dot{\theta}}\,\mathrm{d}\theta, \tag{B.2}$$

where T is the orbital period, and I have performed a change of variables from t to θ.

To write $\dot{\theta}$, we can imagine the ellipse being composed of triangular segments of area $\mathrm{d}A$, so

$$\mathrm{d}A = \frac{1}{2}r^2\,\mathrm{d}\theta, \tag{B.3}$$

and then via Kepler's second law, which states that $\mathrm{d}A/\,\mathrm{d}t = A/T =$ constant, we have

$$\dot{\theta} = \frac{2}{r^2 T}A = \frac{2}{r^2 T}\pi a^2\sqrt{1-e^2}. \tag{B.4}$$

Bringing together these equations, we can write the time-average orbital distance in terms of θ only,

$$\langle r \rangle = \frac{1}{2a^2\pi\sqrt{1-e^2}}\int_0^{2\pi} r^3(\theta)\,\mathrm{d}\theta, \tag{B.5}$$

which can be symbolically integrated using a calculator to obtain,

$$\langle r \rangle = a(1 + e^2/2), \tag{B.6}$$

which is our Equation 2.4 from Chapter 2.

Appendix C
Gibbs free energy and the equilibrium constant of reaction

The position of the chemical reaction with two products and two reactants,

$$\alpha A + \beta B \; = \gamma C + \delta D, \tag{C.1}$$

is given by its reaction quotient,

$$Q = \frac{a_C^\gamma a_D^\delta}{a_A^\alpha a_B^\beta} \tag{C.2}$$

where a_i are the activities of each species i. Activity can be thought of as a non-ideal mole fraction χ_i via an activity coefficient $a_i = \psi_i x_i$. Activity is defined by the chemical potential relative to its standard state,

$$\mu_i = \mu_i^\circ + RT \ln a_i \tag{C.3}$$

which is equivalent to the Gibbs free energy when T and p are constant. Gibbs free energy G expresses the amount of work that can be performed by a system at constant pressure p and temperature T.

Taking these points together, the change in Gibbs free energy for the reaction can be written as,

$$\begin{aligned}\Delta G &= G_p - G_r & \text{(C.4)}\\ &= \gamma(\mu_C^\circ + RT\ln a_C) + \delta(\mu_D^\circ + RT\ln a_D) - \alpha(\mu_A^\circ + RT\ln a_A) + \beta(\mu_B^\circ + RT\ln a_B) & \text{(C.5)}\\ &= (G_C^\circ + G_D^\circ) - (G_A^\circ + G_B^\circ) + RT\ln\left(\frac{a_C^\gamma a_D^\delta}{a_A^\alpha a_B^\beta}\right) & \text{(C.6)}\\ &= \Delta G^\circ + RT\ln Q & \text{(C.7)}\end{aligned}$$

In a state of thermochemical equilibrium, Q is the equilibrium constant K_{eq}. This leaves,

$$\Delta G^\circ = \Delta G - RT\ln K_{\mathrm{eq}} \tag{C.8}$$

G is related to enthalpy and entropy as $G = H - TS$, and entropy is maximised at thermochemical equilibrium, so G is minimised. Setting $\Delta G = 0$ yields our final result

$$\Delta G^\circ = -RT\ln K_{\mathrm{eq}}. \tag{C.9}$$

Appendix D
Derivation of the Clapeyron and Clausius-Clapeyron relations

Consider a substance which can change from one phase (A) to another phase (B). For example, water transitioning from a gas to a liquid. At some pressure p and temperature T, the Gibbs free energy must remain unchanged: $G_1 = G_2$.

Consider some infinitesimal change in the pressure and temperature,

$$\mathrm{d}G = \left(\frac{\partial G}{\partial T}\bigg|_p\right)\mathrm{d}T + \left(\frac{\partial G}{\partial p}\bigg|_T\right)\mathrm{d}p \tag{D.1}$$

$$= -S\,\mathrm{d}T + v\,\mathrm{d}p \tag{D.2}$$

Assuming that the phases remain in equilibrium,

$$-S_1\,\mathrm{d}T + v_1\,\mathrm{d}p = -S_2\,\mathrm{d}T + v_2\,\mathrm{d}p, \tag{D.3}$$

which yields the exact Clapeyron equation,

$$\mathrm{d}T\,/\,\mathrm{d}p = \frac{S_2 - S_1}{v_2 - v_1} = \frac{(H_2 - H_1)/T}{v_2 - v_1} = \frac{1}{T}\frac{\Delta H}{\Delta v} \tag{D.4}$$

for some change in enthalpy H and molar volume v.

If we now assume that $v_2 \gg v_1$, we can invoke the ideal gas equation of state ($pv = RT$) and obtain the Clausius-Clapeyron equation,

$$\mathrm{d}T\,/\,\mathrm{d}p = \frac{\Delta H}{T}\frac{p}{RT} = \frac{pL}{RT^2}, \tag{D.5}$$

since the change in enthalpy ΔH is equal the the latent heat L of the phase transition at constant pressure.

Appendix E

Derivation of the dry adiabatic lapse rate

Consider a parcel of atmosphere which is positively buoyant relative to the surrounding gas. Its buoyancy may be driven by the parcel being heated, which increases its temperature and decreases its density. The parcel thus wishes to ascend on a vertical trajectory. I will assume that it ascends in pressure equilibrium, but not thermal equilibrium.

It is most natural to express this process in terms of enthalpy $H = U + pV$, from which the product rule yields,

$$\mathrm{d}H = \mathrm{d}U + p\,\mathrm{d}V + V\,\mathrm{d}p \tag{E.1}$$

or alternatively

$$\mathrm{d}H = C_p\,\mathrm{d}T + V(1 - \alpha_V T)\,\mathrm{d}p \tag{E.2}$$

where C_p is the heat capacity at constant pressure. α_V is the coefficient of thermal expansion. For the ideal gas equation of state,

$$pV = nRT \tag{E.3}$$

we can analytically reduce α_V to a function of temperature

$$\alpha_V := \frac{1}{V}\frac{\partial V}{\partial T}\bigg|_p = \frac{1}{V/n}\left(\frac{R}{p}\right) = \frac{1}{T} \tag{E.4}$$

and so the second term in Equation E.2 goes to zero. For an ideal gas, we are just left with $\mathrm{d}H = C_p\,\mathrm{d}T$, and thus

$$C_p\,\mathrm{d}T = \mathrm{d}U + p\,\mathrm{d}V + V\,\mathrm{d}p \tag{E.5}$$

The energetics of the ascending parcel may be tracked via the First Law of Thermodynamics

$$\mathrm{d}U = \delta Q - \delta W \tag{E.6}$$

to express its change in internal energy U in terms of heat exchange Q and work done W. Let us assumes that the parcel does not exchange heat or mass with its surroundings during the ascent, making this process adiabatic and isentropic. $\delta Q = 0$.

However, work is done by the parcel due to its volume expansion upon ascent, $\delta W = p\,\mathrm{d}V$, so we then have

$$\mathrm{d}U = -p\,\mathrm{d}V \tag{E.7}$$

by substituting this into our Equation E.5, we have

$$C_p\,\mathrm{d}T = (-p\,\mathrm{d}V + p\,\mathrm{d}V) + V\,\mathrm{d}p = V\,\mathrm{d}p \tag{E.8}$$

So then,

$$\frac{\mathrm{d}T}{\mathrm{d}p} = \frac{V}{C_p} \tag{E.9}$$

although the parcel volume V is not a practical quantity, so through the ideal gas equation of state we may instead write

$$\frac{\mathrm{d}T}{\mathrm{d}p} = \frac{nRT/p}{C_p} = \frac{T}{p}\frac{R}{c_p} \tag{E.10}$$

where c_p is now the *molar* heat capacity.

With which I write the dry adiabatic lapse rate in my preferred form,

$$\nabla_{\mathrm{ad}} := \frac{\mathrm{d}\ln T}{\mathrm{d}\ln p} \equiv \frac{p}{T}\frac{\mathrm{d}T}{\mathrm{d}p} = \frac{R}{c_p} \tag{E.11}$$

It is through Equation E.2 that the compressibility of real gases will factor into the adiabatic lapse rate. Note that I have avoided writing this in terms of height z and do not invoke the equation of hydrostatic equilibrium.

Appendix F
Derivation of the convective heat flux with MLT

Let us once more consider a parcel of atmosphere which is positively buoyant relative to the surrounding gas, so that it wishes to ascend on a vertical trajectory in pressure-equilibrium.

During its ascent from a location at a radial distance r to $r + \Delta r$, the temperature of the parcel changes by an amount ΔT relative to the background atmosphere, which as a 1^{st}-order Taylor expansion is

$$\Delta T(\Delta r) = T_{\text{pa}}(r + \Delta r) - T_{\text{bg}}(r + \Delta r) \approx \Delta r \left(\frac{\mathrm{d}T_{\text{pa}}}{\mathrm{d}r} - \frac{\mathrm{d}T_{\text{bg}}}{\mathrm{d}r} \right) \tag{F.1}$$

If we assume that the parcel lapse rate is similar to the background lapse rate over Δr, we can substitute $\mathrm{d}T \rightarrow T \, \mathrm{d} \ln T$ into both fractions,

$$\Delta T(\Delta r) = \Delta r \cdot T \left(\frac{\mathrm{d} \ln T_{\text{pa}}}{\mathrm{d}r} - \frac{\mathrm{d} \ln T_{\text{bg}}}{\mathrm{d}r} \right) \tag{F.2}$$

From the hydrostatic equation where ρ is density and g is gravity,

$$\mathrm{d}p = -\rho g \, \mathrm{d}r \tag{F.3}$$

we can replace the radial coordinate with a pressure coordinate,

$$\mathrm{d}r = \frac{\mathrm{d}p}{-\rho g} = \frac{\mathrm{d} \ln p}{-\rho g / p} \tag{F.4}$$

Giving us,

$$\Delta T = \Delta r \cdot T \left((-\rho g/p) \frac{\mathrm{d} \ln T_{\text{pa}}}{\mathrm{d} \ln p} - (-\rho g/p) \frac{\mathrm{d} \ln T_{\text{bg}}}{\mathrm{d} \ln p} \right) \tag{F.5}$$

$$= \Delta r \frac{\rho g}{p} \, T (\nabla_{\text{bg}} - \nabla_{pa}) \tag{F.6}$$

$$= \Delta r \, T (\nabla_{\text{bg}} - \nabla_{pa}) / H_p \tag{F.7}$$

where in the last line we have identified that the pressure scale height $H_p = p/(\rho g)$. Non-ideal effects may factor into this through the dependence of ρ on p and T.

The heat flux necessary to dissipate the work done during parcel ascent is given by

$$F(r) = \frac{1}{A} \frac{\mathrm{d}E}{\mathrm{d}t} = \frac{c_p \rho}{A} \frac{\mathrm{d}(VT)}{\mathrm{d}t} \approx \rho c_p \lambda \frac{\mathrm{d}T}{\mathrm{d}t} \tag{F.8}$$

where we have assumed that energy is dissipated during ascent over some length scale λ and c_p is the heat capacity of the gas per unit *mass*.

We then have via the chain rule,

$$F(r) = \rho c_p \lambda \frac{\mathrm{d}T}{\mathrm{d}t} = \rho c_p \lambda w \frac{\mathrm{d}T}{\mathrm{d}r} \tag{F.9}$$

where w is the characteristic upward velocity of the parcel.

If we then substitute our $\Delta T / \Delta r$ into this, we obtain

$$F = \rho c_p \lambda w \times T(\nabla_{\mathrm{bg}} - \nabla_{pa})/H_p \tag{F.10}$$

$$= \rho w c_p T(\lambda / H_p)(\nabla_{\mathrm{bg}} - \nabla_{pa}) \tag{F.11}$$

Which does not assume a particular equation of state.

By its definition, the parcel's lapse rate is equal to that of a critically-convective profile. If we assume that the parcel ascends adiabatically, we may take its lapse rate $\nabla_{\mathrm{pa}} = \nabla_{\mathrm{ad}}$ which was derived in Appendix E for an ideal gas. This is the Schwarzschild criterion. We could use an alternative critical lapse rate to account for compositional gradients which may stabilise the parcel's ascent, such as the Ledoux and Guillot criteria (Guillot 1999; Gabriel et al. 2014; Anders et al. 2022).

The lapse rate of the background is that of the atmospheric profile $\nabla_{\mathrm{bg}} = \nabla_T$. Additionally, a factor of 1/2 is introduced to represent the fact that half of the mass in a convective cell is rising while the other half is sinking, while this derivation only considered an ascending parcel. This leaves us with the formulation for convective flux implemented in AGNI:

$$F^{\mathrm{cvt}} = \frac{1}{2} \rho c_p \lambda w T(\nabla_T - \nabla_{ad})/H_p \tag{F.12}$$

The mixing length λ is often expressed as a multiple of the scale height: $\lambda = \alpha H_p$ where α is the 'mixing length parameter'. For stellar models, this quantity is usually calibrated against the Sun or convection-resolving simulations (Kippenhahn et al. 2012; Baraffe et al. 2015).

In my models, I calculate the mixing length λ using $\alpha = 1$ and an asymptotic scaling from the height z above the ground:

$$\lambda(z) = \frac{k_v z}{1 + k_v z/(\alpha H_p)} \tag{F.13}$$

which ensures that $F^{\mathrm{cvt}} \rightarrow 0$ at the ground, consistent with the 'law of the wall' and a no-slip boundary condition (Högström 1988). The quantity k_v is Von Karman's constant, which arises from mass conservation at a solid boundary.

The parcels oscillate in a convective motion according to a balance of buoyant and gravitational forces. The frequency of the parcel's oscillation is the Brunt–Väisälä frequency,

$$N = \sqrt{\frac{g}{\rho}\frac{\partial\rho}{\partial r}} \tag{F.14}$$

from which we can obtain the velocity as

$$w = \lambda\sqrt{(\nabla_T - \nabla_{ad}) \cdot g/H_p} \tag{F.15}$$

Here I have considered only a single convective cell with a particular length and velocity scale. In reality, convection occurs across a range of scales which means that MLT will under-estimate the convective heat and mass fluxes (Canuto and Mazzitelli 1991; Canuto et al. 1996). MLT can be extended to include the effects of parcel overshooting, where a rising parcel penetrates into an otherwise convectively-stable zone due to its inertia, which is important for mass mixing between convective and non-convective layers (Eggleton 1983; Grossman 1996).

Appendix G

Supplementary emission spectra from the JANUS model

The character of a planet's emission spectrum is primarily determined by its atmospheric composition and structure, and the irradiation that it receives from its star (Perryman 2011). It was shown in Section 3.5.2 that the temperature profiles modelled by JANUS differ significantly compared to those modelled by AGNI, especially with respect to the formation of radiative layers in the latter cases. In Figure G.1 below, I additionally present the emission spectra corresponding to the cases simulated with JANUS. These have been calculated at an increased resolution compared to the main simulations, and are analogous to those presented in Figure 3.9 for simulations with AGNI.

The absorption features in these alternative emission spectra of HD 63433 d (top panel of Figure G.1) are common to those in Figure 3.9. This follows from the fact that the composition is calculated in the same manner, although generally at higher surface temperatures. In contrast to the AGNI cases, the temperature profiles are less sensitive to the composition of the atmosphere because they are set only by an analytical moist pseudoadiabat (Graham et al. 2021); this can be clearly seen by the dashed lines in Figure 3.8. The emission spectra presented in Figure G.1 depend less strongly on fO_2 as a result of this partial decoupling between $T(p)$ and fO_2. This indicates that the application of sufficiently comprehensive atmosphere models (e.g. AGNI) can be necessary for calculating accurate emission spectra.

The emission spectra resulting from simulations of these two planets with JANUS are relatively similar to each other: compare the top and bottom panels of Figure G.1. This is also a result of the moist pseudoadiabat prescription within JANUS, which cannot capture key characteristics of the atmospheric temperature. For example, the formation of a near-isothermal stratospheres under reducing conditions on TRAPPIST-1 c (Figure 3.8).

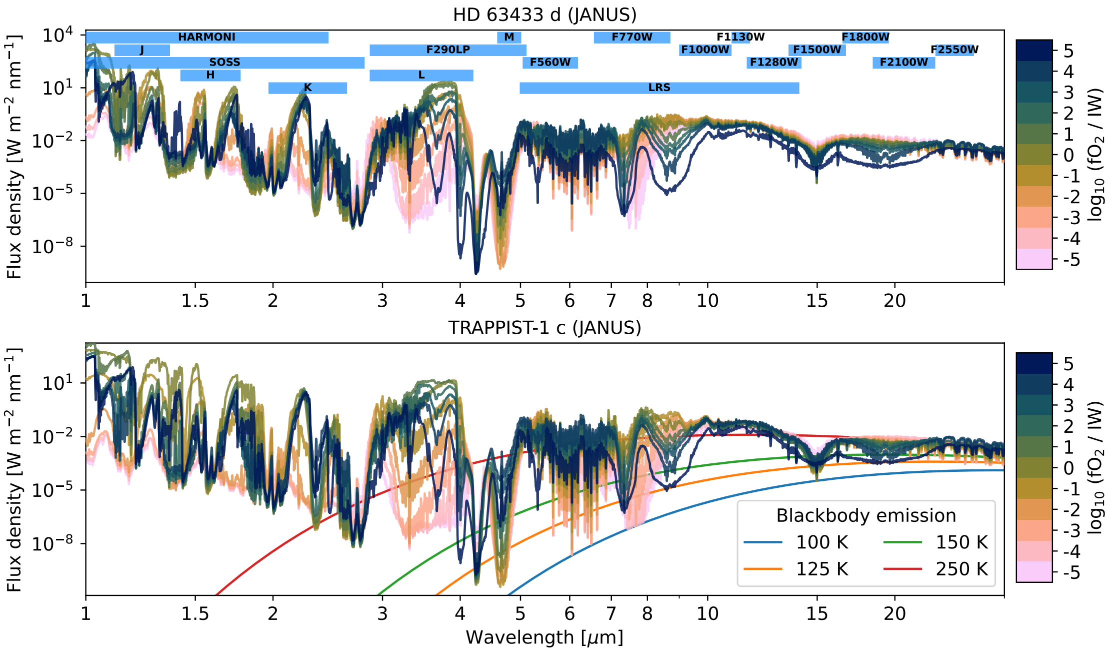

Figure G.1: Top-of-atmosphere flux representative of the planet-averaged outgoing radiation from simulations of young HD 63433 d and TRAPPIST-1 c. This is the same as Figure 3.9, but instead corresponds to the results of simulations coupled to JANUS. All of these cases are at radiative equilibrium and do not solidify within these simulations.